REACTIVITY CONTROLLED COMPRESSION IGNITION (RCCI) COMBUSTION

by

Sage Lucas Kokjohn

A dissertation submitted in partial fulfillment of the
requirements for the degree of

Doctor of Philosophy
(Mechanical Engineering)

at the
University of Wisconsin – Madison
2012

Date of final oral examination: 4/11/2012

The dissertation is approved by the following members of the Final Oral Committee:

Rolf D. Reitz, Professor, Mechanical Engineering
David E. Foster, Professor, Mechanical Engineering
Christopher J. Rutland, Professor, Mechanical Engineering
Jaal B. Ghandhi, Professor, Mechanical Engineering
James J. Schauer, Professor, Civil and Environmental Engineering

Abstract

Premixed Compression Ignition (PCI) combustion strategies are promising methods to achieve low engine out NOx and soot emissions and high-efficiency. However, PCI strategies have failed to see widespread implementation due to difficulties controlling the heat release rate and lack of an adequate combustion phasing control mechanism. In this research, a dual-fuel reactivity controlled compression ignition (RCCI) concept is proposed to address these issues. In the RCCI strategy two fuels with different auto-ignition characteristics are blended inside the combustion chamber. Combustion phasing is controlled by the relative ratios of these two fuels and the combustion duration is controlled by spatial stratification between the two fuels. The study has three primary goals. The first goal of the study is to highlight the development of the RCCI strategy. In this part, CFD modeling is used to propose the RCCI strategy and develop a method to choose the optimal fuel blend and EGR rate for a given operating condition. The CFD modeling is further used to suggest an injection strategy capable of achieving RCCI operation with conventional hardware.

In the second part of the research, CFD modeling and metal engine experiments are used to discuss the performance and emissions characteristics of RCCI combustion. The metal engine experiments confirm that RCCI operation is possible over a wide range of conditions with near zero levels of NOx and soot emissions. Additionally, it is found that RCCI is able to achieve very high indicated efficiency by lowering heat transfer losses and improving the control over the combustion phasing and burn duration. Metal engine experiments are used to compare light- and heavy-duty RCCI operation. The comparisons between the two engine platforms show that RCCI is very scalable. High indicated efficiency and low NOx and soot emissions can be achieved in both engines. However, it is found that the light-duty engine converts 5% less of the fuel energy to work than the heavy-duty engine due to increased heat transfer losses and lower combustion efficiency.

In the third part of this research, optical engine experiments are used to validate model predictions and provide a fundamental explanation for the processes controlling RCCI combustion. The results of the optical engine experiments clarify the mechanisms controlling the RCCI energy release. Chemiluminescence imaging shows that RCCI features a reaction zone that appears to grow by the appearance of small auto-ignition pockets. The fuel tracer fluorescence imaging shows that the ignition locations correspond to the regions with the lowest PRF number and highest equivalence ratio. The rate of reaction zone growth is then controlled by the level of stratification in equivalence ratio and PRF number. Kinetics modeling based on the fuel tracer fluorescence imaging shows that the PRF number has the largest effect on the rate of reaction zone growth. Finally, the results of the optical engine experiments suggests that the current KIVA-CHEMKIN code is capable of capturing the key combustion characteristics without the need to consider flame propagation.

Acknowledgments

First, I would like to thank my advisor, Professor Rolf Reitz, for his support and guidance. I am thankful for the opportunity to work in such a great research facility. Furthermore, I am grateful for the many opportunities Professor Reitz has given me to present the findings of my research. In addition, I would like to thank Dr. Mark Musculus at Sandia National Laboratories for allowing me to spend eight months learning from him in his laboratory. Mark put his own research on hold for my visit and spent almost every day in the lab helping with my work and teaching me about optical diagnostics. Mark's attention to detail is something that I will carry with me through my career. I would also like to thank my other thesis committee members Professor Chris Rutland, Professor Jaal Ghandhi, Professor David Foster, and Professor James Schauer for many useful comments.

This project would not exists if it were not for the financial support from the US Department of Energy (DOE) HCCI contract # DE-FC04-02AL67612 and from the Engine Research Center's Diesel Engine Research Consortium (DERC) member companies. Furthermore, the questions and comments from DERC member companies have been extremely helpful in providing direction for this research.

A debt of gratitude is owed to all of the ERC students, staff, and faculty. In particular, the many insightful conversations with Adam Dempsey, Jessica Brakora, Reed Hanson, Derek Splitter, Ryan Walker, Younchul Ra, Mike Andrie, Yu Shi (currently at ConocoPhillips), Mike Bergin (currently at Wisconsin Engine Research Consultants), and Dave Wickman (currently at Wisconsin Engine Research Consultants) were essential to this research. None of the work at the ERC would be possible without the computer and laboratory support offered by Joshua Leach.

Josh seems to work 24 hours a day keeping all of the computer systems and servers functioning and he deserves many thanks.

The staff and researchers at Sandia made my visit a very rewarding experience. My work at Sandia would not have been possible without the laboratory support from Dave Cicone and Chris Carlen. Additionally, Dave's conversations were always enjoyable and made every day interesting.

The staff and researchers at Oak Ridge National Laboratory provided a significant amount of input into the feasibility of multi-cylinder RCCI combustion. The interaction and discussions with Robert Wagner, Scott Curran, and Tom Briggs (currently at Southwest Research Institute) were vital in the development of the RCCI strategy.

Most importantly, I must thank my family and friends for all of their support. I thank my wife Jennifer Kokjohn for putting up with me during this research and always offering me support when my research was not going as planned. Without her support, this study would not have been possible. Finally, I would like to thank my parents for always encouraging me to follow my dreams and for providing me the means and direction to achieve my goals.

Table of Contents

List of Figures

List of Tables

Nomenclature

Abbreviations

AFR	Air Fuel Ratio
AHRR	Apparent Heat Release Rate
ATAC	Active Thermo-Atmosphere Combustion
ATDC	After Top Dead Center
BDC	Bottom Dead Center
BMEP	Brake Mean Effective Pressure
BPF	Band Pass Filter
BTDC	Before Top Dead Center
CA	Crank Angle
CA10	Crank Angle At 10% Burn
CA50	Crank Angle At 50% Burn
CA90	Crank Angle At 90% Burn
CCD	Charge-Coupled Device
CDC	Conventional Diesel Combustion
CFD	Computational Fluid Dynamics
CH_2O	Formaldehyde
CI	Compression Ignited
CMOS	Complementary Metal Oxide Semiconductor
CO	Carbon Monoxide
COSSO	COmponent Selection And Smoothing Operator
COV	Coefficient Of Variation
CR	Common-Rail
DEF	Diesel Exhaust Fluid
DI	Direct Injection
DOE	Design Of Experiments
DOI	Duration Of Injection
DPF	Diesel Particulate Filter
EGR	Exhaust Gas Recirculation
EI	Emissions Index
EPA	Environmental Protection Agency
EVO	Exhaust Valve Opening
FOV	Field Of View
FSN	Filter Smoke Number
GA	Genetic Algorithm
GDI	Gasoline Direct Injection

GIE	Gross Indicated Efficiency
GRI	Gas Research Institute
HCCI	Homogeneous Charge Compression Ignition
HD	Heavy-Duty
HPLC	High-Performance Liquid Chromatography
HRR	Heat Release Rate
HSC	High Speed Camera
HT	Heat Transfer
HTHR	High Temperature Heat Release
IC	Internal Combustion
IMEP	Indicated Mean Effective Pressure
IS	Indicated Specific
ISFC	Indicated Specific Fuel Consumption
IVC	Intake Valve Closure
LD	Light-Duty
LDEF	Lagrangian-Drop and Eulerian-Fluid
LHV	Lower Heating Value
LIF	Laser Induced Fluorescence
LNT	Lean NOx Trap
LTC	Low Temperature Combustion
LTHR	Low Temperature Heat Release
LWP	Long Wave Pass
MEP	Mean Effective Pressure
MOGA	Multi-Objective Genetic Algorithm
MON	Motor Octane Number
Nd:YAG	Neodymium-Doped: Yttrium Aluminum Garnet
NOx	Nitrogen Oxides
NSGAII	Nondominated Sorting Genetic Algorithm
OH	Hydroxyl Radical
ON	Octane Number
OPO	Optical Parametric Oscillator
PAH	Polycyclic Aromatic Hydrocarbons
PCCI	Premixed Charge Compression Ignition
PCI	Premixed Compression Ignition
PDF	Probability Density Function
PI	Princeton Instruments
PID	Proportional Integral Derivative
PLIF	Planar Laser Induced Fluorescence
PM	Particulate Matter

PPM	Parts Per Million
PRF	Primary Reference Fuel
PRR	Pressure Rise Rate
RCCI	Reactivity Controlled Compression Ignition
RNG	Re-Normalized Group
RON	Research Octane Number
RPM	Revolutions Per Minute
SCR	Selective Catalytic Reduction
SI	Spark Ignited
SOI	Start Of Injection
SS	Single Shot
SWP	Short Wave Pass
TDC	Top Dead Center
TWC	Three Way Catalyst
UHC	Unburned Hydrocarbons
UNIBUS	Uniform Bulky Combustion System
UV	Ultra-Violet
VPP	Variable Pressure Pulse

Arabic Symbols

a,b,c	Parameters/Constants
A	Pre-Exponential Constant In Arrhenius Form Of Reaction Rate
Cp	Specific Heat
D	Diffusivity
D	Diameter
E	Activation Energy
h	Enthalpy
I	Intensity
L	Length Scale
M or m	Mass
MW	Molecular Weight
n	Molar Density
P	Pressure
Q	Heat Transfer
R	Ideal Gas Constant
s	Speed
t	Time
T	Temperature

tke	Turbulent Kinetic Energy
u	Velocity
V	Volume
v	Velocity

Greek Symbols

α, β, γ	Parameters/Constants
ε	Dissipation of Turbulent Kinetic Energy
λ	Heat Conductivity
ρ	Mass Density
τ	Ignition Delay
ϕ	Equivalence Ratio

Chapter 1

Introduction

1.1 Motivation and Background

Modern life would not be possible without the use of combustion technology. In fact, combustion has been the primary means of heating, food preparation, and material processing for several thousand years [1] and combustion of liquid hydrocarbons is the primary energy conversion device used in the transportation sector. However, even with its long history, a detailed understanding of the interactions between fluid flow, mixing, and chemical kinetics is not well understood. To complicate matters further, much of the transportation sector is powered by internal combustion engines where the difficulties associated with turbulent combustion are compounded by interactions with complex flow fields and two-phase mixtures. Finally, mechanical considerations for work extraction and the use of complex turbo-machinery further complicate the analysis of internal combustion engines.

Recently, rising and unstable fuel costs and a focus on reduction of greenhouse gases have driven the need for increased efficiency from the internal combustion engine. This need for increased efficiency has placed the diesel or compression ignition (CI) engine in the spotlight due to its superior fuel efficiency compared to spark-ignited (SI) engines. Although the fuel efficiency of compression ignition engines is generally higher than that of SI engines, controlling NOx and soot emissions is a challenge. Under conventional diesel operation, parts of the combustion chamber pass through both rich- and lean-high temperature regions, forming soot and NOx, respectively. Soot can be effectively reduced with a diesel particulate filter (DPF);

however, DPFs require periodic regeneration (i.e., removal of collected soot), which often increases fuel consumption. Additionally, since diesel engines generally operate lean of stoichiometric, the exhaust oxygen concentrations are too high to reduce NOx to nitrogen using a three-way catalyst (TWC). Several attempts have been made to operate compression ignition engines stoichiometric such that a TWC can be used for NOx reduction [2]; however, these efforts generally resulted in poor fuel economy; thus removing the compression ignition engines advantages over the SI engine. In addition to stoichiometric-TWC NOx reduction, forms of NOx aftertreatment compatible with lean operation exist (i.e., lean NOx traps (LNT) and selective catalytic reduction (SCR)). An LNT is essentially a TWC reformulated to enhance storage of NOx during lean operation [3]. As such, LNTs provide NOx reduction in a very similar manner as a conventional TWC; that is, NOx is reduced to N_2 through reactions with products of rich combustion (CO, UHC, and H_2) [3]. An engine relying on an LNT for NOx reduction must periodically operate rich to reduce the stored NOx; thus, fuel efficiency is reduced. In contrast to LNT technology, SCR technology can be used for NOx reduction without the need to operate rich; thus, the fuel economy benefits of the lean burn compression ignition engine are retained. However, similar to the required periodic rich operation of LNT technology, SCR technology requires the introduction of a reducing agent (urea). The urea is stored on the vehicle and is injected into the exhaust system, providing no useful work; thus, the consumed urea used for NOx reduction can be considered additional “fuel” consumption. Based on the work of Johnson [4], urea consumption can be estimated at 1% of the fuel consumption per g/kW-hr reduction in NOx emissions.

Considering the above discussion, it is clear that to maximize overall engine efficiency an engine should minimize the need for aftertreatment-type emissions reduction. Accordingly, reduction of NOx and soot in-cylinder has been investigated by many researchers. This study presents development and analysis of an advanced compression ignition strategy capable of achieving near zero NOx and soot levels in-cylinder.

1.2 Objectives

There are three primary objectives of this research:

1) Highlight the development of a high-efficiency, dual-fuel reactivity controlled compression ignition (RCCI) concept used to address several of the issues associated with most premixed compression ignition strategies (Chapter 4).
2) Demonstrate and discuss the performance and emissions characteristics of RCCI (Chapter 5-Chapter 7)
3) Develop an in-depth understanding of the key processes controlling RCCI combustion (Chapter 5, Chapter 9, and Chapter 10)

1.3 Approach

In this study a range of tools are used: kinetics modeling, CFD modeling, cycle-simulations, metal engine experiments, and optical engine experiments. Each tool has advantages and disadvantages; accordingly, in this study several tools are combined such that the impact of each specific tool is maximized. For example, the accessibility of information and control over initial and boundary conditions make CFD modeling a very useful tool. However, it is necessary to combine CFD modeling with appropriate engine experiments, such as the metal engine experiments presented in Chapter 6 and the optical engine experiments presented in Chapter 9, to validate the model predictions. Similarly, optical engine experiments are an extremely useful tool for the investigation of the dominant mechanisms controlling a combustion process; however, the robustness of metal engine experiments makes them a much better tool to assess the performance and emissions characteristics. Only by combining these tools can an accurate picture be developed. The specific approaches used to achieve each goal are discussed below:

1.3.1 Highlight the development of a high-efficiency, dual-fuel reactivity controlled compression ignition (RCCI) concept

First, HCCI (kinetics) simulations are performed to demonstrate a method to select the optimal EGR and fuel blend at several operating conditions. Next, detailed computational fluid dynamics (CFD) modeling is used to develop an injection strategy for controlled premixed compression ignition combustion using in-cylinder fuel blending. Then, the HCCI simulations and spray modeling are combined to demonstrate RCCI combustion.

1.3.2 Demonstrate and discuss the performance and emissions characteristics of RCCI

The results of the preliminary RCCI development are used to guide heavy-duty metal engine experiments. The results of the metal engine experiments are used to validate model predictions. The validated models are then used to help explain the observations of the measurements. To gauge the performance and emissions characteristics of RCCI, the CFD modeling is used compare RCCI with conventional diesel combustion.

To demonstrate the scalability of RCCI combustion, single-cylinder metal engine experiments are used to compare the light- and heavy-duty engines. Similar to the approach in the heavy-duty engine RCCI work, the model predictions are used to explain the experimental observations and make comparisons to reference conditions.

1.3.3 Develop an in-depth understanding of the key processes controlling RCCI combustion

The RCCI combustion process is explained using a combination of CFD modeling and optical engine experiments. First, CFD modeling is used to propose a hypothesis of the processes controlling RCCI combustion. This hypothesis is confirmed by applying a suite of optical diagnostics to an engine operating in the RCCI combustion mode. The optical diagnostics are further used to gain a fundamental understanding of ignition and early-stage reaction zone growth. Kinetics and CFD modeling is coupled with the optical diagnostics to aid in interpretation of the images.

Chapter 2

Literature Review

2.1 Advanced Combustion Strategies

In recent years, many advanced combustion strategies have been proposed in order to meet current and future emissions mandates. Most of the current strategies can be lumped into the category of premixed, low temperature combustion (LTC). Lower combustion temperatures result in NOx reduction due to the high activation energy of NO formation reactions [5]. In addition, utilizing long ignition delay times allows adequate time for mixing prior to the start of combustion; thus, rich regions are reduced and soot formation is inhibited. Many researchers have shown that Homogeneous Charge Compression Ignition (HCCI) and Premixed Charge Compression Ignition (PCCI) concepts are promising techniques for simultaneous NOx and soot reduction [6-22]. In addition to significant NOx and soot reductions, premixed LTC operation can provide fuel efficiency advantages due to reduced combustion duration and lower heat transfer losses. Additionally, Caton [23] suggests that LTC engines have the potential for further efficiency gains due to the higher value of the ratio of specific heats, which results in more efficient work extraction.

Neely [24] overlaid the LTC, PCCI, HCCI, and traditional diesel operating regimes in the Φ-T space originally presented by Kamimoto [25], see Figure 2-1. Although the borders of the combustion regimes shown by Figure 2-1 are somewhat arbitrary, the figure is useful to understand the different combustion characteristics. As mentioned in the Introduction, Figure 2-1 shows that the conventional diesel combustion regime encompasses both the NOx and soot islands. PCCI combustion is achieved by increasing the pre-combustion mixing time, such that the peak equivalence ratios are below the soot formation threshold. Further, high-levels of EGR are often used to reduce the oxygen concentration and lower peak flame temperatures. PCCI combustion results in a shift to lower local equivalence ratios (due to the increased pre-combustion mixing time) and lower peak temperature (due to a combination of lower local equivalence ratios and lower oxygen concentrations), resulting in movement out of the soot island and less NOx formation. By further reducing the oxygen concentration, via increased

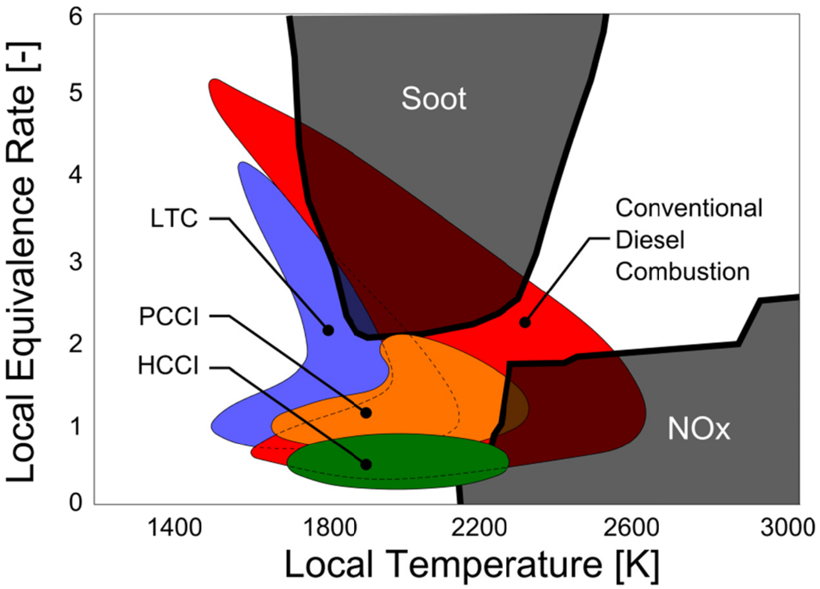

Figure 2-1. (a) LTC, PCCI, HCCI, and conventional diesel operating regimes shown in φ-T space. Adapted from the work of Neely et al. [24].

EGR, low temperature combustion (LTC) is achieved. The reduced oxygen concentration results in higher local equivalence ratios than PCCI combustion. The LTC curve has a similar shape as the conventional diesel curve, but the reduced oxygen concentration results in lower flame temperatures and the combustion process moves out of the NOx island and encompasses significantly less of the soot island than conventional diesel combustion. Akihama et al. [26] showed that when combustion temperatures are significantly reduced, the conversion of PAH to soot does not occur. Therefore, even though rich conditions exist, no soot is formed.

Park et al. [27] expanded on the work of Neely [24] and Kamimoto [25] by adding the regions in ϕ-T space that contribute to incomplete combustion. Figure 2-2 shows a summary of

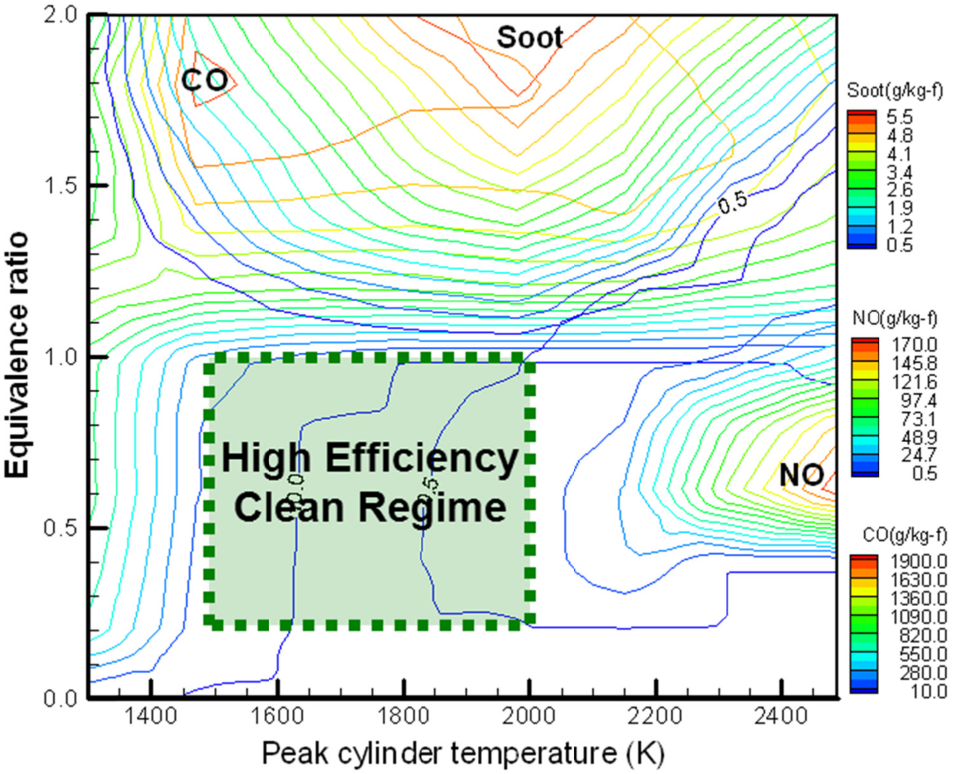

Figure 2-2. High-efficiency clean combustion regime overlaid in φ-T space based on the work of Park et al. [27].

their results indicating a region of high-efficiency (i.e., near 100% combustion efficiency), clean-combustion (i.e., near zero levels of NOx and soot emissions). From Figure 2-2, it is clear that the optimal combustion strategy will have a charge that results in combustion temperatures in the range of 1500 K to 2000 K. The lower temperature limit ensures complete oxidation of carbon monoxide and the upper temperature limit ensures minimal NOx formation.

2.2 HCCI Combustion

As indicated in Figure 2-1, the intent of HCCI combustion is to avoid forming NOx by keeping peak temperatures below ~2000 K and avoid forming soot by eliminating high equivalence ratio regions. Onishi [28] first explored HCCI combustion to improve part load performance of a two-stroke spark-ignited engine. He termed the HCCI combustion process Active Thermo Atmospheric Combustion (ATAC). In the ATAC strategy, the exhaust scavenging process of the two-stroke cycle was controlled to trap a large quantity of hot residuals. The residuals raised the charge temperature enough to achieve auto-ignition of the charge. Several years later, Najt and Foster [29] applied the HCCI concept to a four-stroke engine. Since the introduction of HCCI in the late 1970's, controlling the combustion process has been a challenge and has limited the commercial feasibility. In the mid 1990's, Yamaguchi [30] made a major step towards a commercially viable two-stroke, part-time HCCI engine using an exhaust throttle to control the level of hot residuals. The engine demonstrated the possibility of a production HCCI strategy by competing (and finishing) the Granada-Dakar Rally (an off-road motorcycle race consisting of stages of up to 500 miles per day).

By definition, HCCI is achieved by creating a perfectly premixed charge prior to ignition. However, most highly premixed compression ignition strategies share characteristics with HCCI combustion. Hasegawa and Yanagihara [31] developed a highly premixed compression ignition strategy using multiple injections of diesel fuel. They termed this HCCI-like combustion strategy the uniform bulky combustion system (UNIBUS). An early injection, well before TDC, is used to create a premixed charge. Engine parameters (intake gas temperature, intake valve closure (IVC) timing, fuel quantity, and injection timing) are set such that high-temperature heat release does not occur prior to the start of the second injection. The second injection occurs after TDC (ATDC) and is used to control the start of combustion of the premixed fuel. Using this strategy, they were able to demonstrate near zero levels of NOx and soot emissions at low-load conditions.

Many other strategies can be lumped into the HCCI-like combustion strategy envelope. The present study focuses on a combination of these advanced, low-temperature compression ignition strategies. Thus, they will be lumped together and referred to as premixed compression ignition (PCI).

2.3 Problems Associated with Premixed Compression Ignition (PCI) Strategies

Although PCI strategies have been shown to yield very low NOx and soot levels, two primary problems have limited the use of these strategies. The first issue is combustion phasing control. Even when direct-injection is used as the fuel delivery strategy, the ignition delay must be sufficiently long to allow adequate time for mixing. However, as the ignition delay is extended past the end-of-injection (i.e., positive ignition dwell) the injection and ignition events become decoupled (i.e., changing the injection timing results in small or unpredictable changes in the combustion phasing). Therefore, chemistry time-scales must be controlled such that ignition occurs at the proper time. The second problem is rate of heat release control. Because the combustion rate is no longer limited by the mixing process as in conventional diesel combustion, the heat release can be rapid and result in excessive engine noise and structural damage.

2.3.1 Combustion Phasing Control

Due to the existing fuel infrastructure, most PCI research has been conducted using either strictly gasoline or diesel fuel. However, in their neat forms, each fuel has specific advantages and shortcomings for PCI operation. Recently there has been increasing interest in gasoline compression ignition. There are two primary types of gasoline compression ignition strategies. The first strategy is based on gasoline HCCI and begins with a highly premixed charge of gasoline (i.e., gasoline HCCI-like). Since the combustion efficiency of gasoline drops off quickly below an equivalence ratio of ~0.2 (see e.g., Hwang [12]) the gasoline mixture is partially stratified using an injection of gasoline part way through the compression stroke. This strategy was first introduced by Marriott et al. [32, 33] in 2002. Using a low-pressure, hollow-cone, gasoline direct injector (GDI), they showed that indicated efficiency increases with increasing charge stratification (i.e., injection timing retard), but if the injection timing is retarded beyond ~-150° ATDC, NOx increases rapidly. More recently, Aroonsrisopon et al. [34] and Hwang et al. [12] have further investigated partial fuel stratification as a method to improve combustion efficiency of low-load gasoline HCCI combustion.

The second gasoline compression ignition concept begins with a diesel injection strategy (i.e., near TDC injection) and replaces the diesel fuel with gasoline. In this strategy, a high pressure direct injector (e.g., common-rail injector) is used to deliver gasoline. This strategy has been pioneered by the work of Kalghatgi et al. [35-37]. In their work, gasoline's resistance to auto-ignition (i.e., low cetane number) was exploited to extend the pre-combustion mixing time in order to achieve simultaneous reductions in NOx and soot emissions.

Although the gasoline compression ignition strategies proposed by Marriot et al. [32, 33] and Kalghatgi et al. [35-37] show promise, other researchers (e.g., Liu et al. [38]) have shown that the poor auto-ignition qualities of gasoline can make it difficult to achieve combustion at low-load conditions. Conversely, diesel fuel has superior auto-ignition qualities, making low-load PCI operation easily achievable. However, the high reactivity (cetane number) of diesel fuel can result in difficulty controlling the combustion phasing as engine load is increased. Therefore, when neat diesel fuel is used in a PCI strategy, high levels of exhaust gas recirculation (EGR) are required to phase combustion appropriately [39]. Further, the low-volatility of diesel fuel makes generating a well-mixed charge challenging [40].

Since gasoline-like fuels tend to have difficulty achieving ignition at low-load conditions and diesel-like fuels have difficultly controlling combustion phasing at high load condition, many researchers have investigated PCI operation using fuel blends. Aroonsrisopon et al. [41] compared the HCCI operating range for various combinations of intake temperature and engine speed for four different fuel compositions. Three of the fuels, n-butane, a blend of n-heptane and iso-octane, and a blend of indolene and n-heptane, had research octane numbers (RON) of 91.8. The final fuel, a blend of n-heptane and iso-octane, had a research octane number of 70. They showed that the lower RON fuel (PRF 70) resulted in larger equivalence ratio window for stable HCCI operation (i.e., acceptable combustion phasing and pressure rise rates). However, the peak achievable load was only about half of that of the RON 91.8 indolene blend. Yao et al. [42] investigated HCCI operation using pre-blended iso-octane and n-heptane (PRF). Their study showed that the PRF blend controls combustion phasing and an optimum fuel blend exists at each operating condition. For example, light load operation required a low-octane number fuel and high-load (highest load considered was 4.3 bar IMEP) required a high-octane fuel to achieve optimum combustion phasing.

In a similar set of experiments, Bessonette et al. [43] found that the best fuel for HCCI operation may have autoignition qualities between that of diesel fuel and gasoline. Using a compression ratio of 12:1 and a fuel with a derived cetane number of ~27 (i.e., a gasoline boiling range fuel with an octane number of 80.7), they were able to extend the HCCI operating range to 16 bar BMEP – a 60% increase in the maximum achievable load compared to operation using traditional diesel fuel. Furthermore, consistent with the findings of Yao et al. [42], their results showed that low load operation, below 2 bar BMEP, required a derived cetane number of ~45 (i.e., traditional diesel fuel). Thus, it may be beneficial to explore HCCI operation using fuel blends optimized for specific operating conditions.

Zheng et al. [44] explored HCCI operation using two port fuel injectors (one for methanol and one for DME). With this setup, they were able to change the blend ratio of the two fuels on a cycle-to-cycle basis to control the combustion phasing. Inagaki et al. [45] investigated dual-fuel PCI operation as a means for reducing the EGR requirements of PCI strategies. Using premixed iso-octane and direct-injected diesel fuel, they were able to operate in PCI mode at 12 bar IMEP.

Based on the results of Aroonsrisopon et al. [41], Yao et al. [42], Bessonette et al. [43], Zheng et al. [44] and Inagaki et al. [45], it is likely that different fuel blends will be required at different operating conditions (e.g., a high cetane fuel at light load and a low cetane fuel at high load). Thus, it is desirable to have the capability to operate with fuel blends covering the spectrum from neat gasoline to neat diesel fuel depending on the operating regime. This work proposes port-fuel-injection of gasoline (or another high-octane fuel) and early cycle direct-injection of diesel fuel (or another high-cetane fuel).

To further understand the motivation for investigating in-cylinder fuel blending, Figure 2-3 shows constant volume ignition delay calculations using a primary reference fuel (PRF) mechanism developed by Ra et al. [46] for neat iso-octane, neat n-heptane, and a 50-50 blend of isooctane and n-heptane. For optimum thermal efficiency, the combustion phasing must be precisely controlled and, to maintain high efficiency, an engine must be able to accommodate changes in the operating conditions (e.g., charge temperature) while maintaining the optimum combustion phasing. Figure 2-3 shows that, since each fuel has a unique ignition delay –

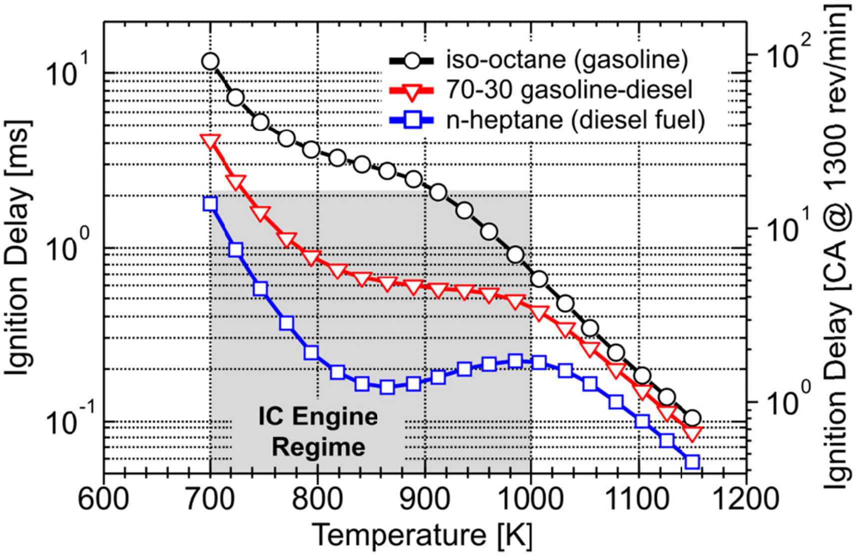

Figure 2-3. Constant volume ignition delay times for neat n-heptane, neat iso-octane, and a 70-30 blend of iso-octane and n-heptane calculated using the SENKIN [47] code and a reduced PRF mechanism [46]. This set of simulations was performed at an initial pressure of 70 bar and an equivalence ratio of 0.5. The shaded area shows TDC temperatures and ignition delay times representative of conditions seen in an internal combustion (IC) engines.

temperature curve, each fuel will be limited to a narrow operating range where peak efficiency can be achieved. In the laboratory, where intake temperature and EGR can be precisely controlled, single fuel HCCI combustion can demonstrate very promising results. However, in practice the charge gas temperature of practical engines depends on many factors and varies with speed, load, and operating environment. For example, if a representative temperature of 725 K is selected and the ignition delay required to achieve optimum combustion phasing is ~8° CA, neat diesel fuel would provide the optimum fuel reactivity to achieve peak efficiency. However, if the operating conditions changed such that the representative temperature increased to 780 K, neat diesel fuel would result in overly advanced combustion phasing, increased heat transfer losses, and reduced thermal efficiency. However, by using in-cylinder fuel blending, peak efficiency could be maintained by moving from neat diesel fuel to a 70-30 blend of diesel and gasoline.

2.3.2 Heat Release Rate Control

Expanding on the partial fuel stratification concept proposed by Marriott and Reitz [32, 33] and Aroonsriopon et al. [34], Sjöberg et al. [15] suggested that partial fuel stratification may be a promising method to control the heat-release rate for HCCI engines. In their work, around 80% of the total fuel was "premixed" by using a direct-injection during the intake stroke and the remaining fuel was injected later in the cycle to introduce stratification in the equivalence ratio distribution. Using this technique with a PRF 80 fuel, they showed that the peak pressure rise rate (PRR) could be reduced from 8.8 bar/deg. to below 5 bar/deg. while maintaining NOx and soot levels below the 2010 heavy-duty limits. Using multi-zone kinetics modeling, they showed that the heat release proceeded in a staged event with the zones igniting sequentially from richest to leanest. However, in the same work, Sjöberg et al. [15] showed that, at naturally aspirated conditions, partial fuel stratification was not effective at controlling the pressure rise rate for neat iso-octane. Again, relying on kinetics modeling they found that the high temperature heat release of iso-octane is not sensitive to equivalence ratio (termed "ϕ-sensitivity" by Dec et al. [10]).

In a more recent work, Yang et al. [11] explored the potential for heat release rate or PRR control using a PRF 73 fuel and found improved results compared to the PRF 80 fuel used in the initial investigation of Sjöberg et al. [15]. Other researchers (e.g., Dahl et al. [48]) showed similar findings to that of Dec's group (i.e., Yang et al. [11] and Sjöberg et al. [15]). Consequently, Dec et al. [10] concluded that, under naturally aspirated conditions, fuels with higher reactivity are more suited for controlling PRR using partial fuel stratification. Alternatively, Dec et al. [10] showed that the auto-ignition reactivity of conventional gasoline (87.6 antiknock index in their work) increases significantly when the intake pressure is increased above atmospheric pressure (i.e., boosted). They showed a moderate ϕ-sensitivity at an intake pressure of 1.6 bar absolute and strong ϕ-sensitivity at an intake pressure of 2 bar absolute. Using an intake pressure of 2 bar absolute and partial fuel stratification with conventional gasoline, Dec et al. [10] operated in the HCCI mode at up to 13 bar gross IMEP, an 11% increase in the maximum achievable load compared to operation without partial fuel stratification.

In addition to partial fuel stratification, Dec et al. [13] showed that even with perfectly homogenous fuel distribution, bulk-gas thermal stratification results in sequential ignition from hotter-to-cooler regions. Using a planar temperature imaging diagnostic, Dec et al. [49] showed that natural thermal stratification increases as the piston reaches TDC and a PDF analysis of their single-shot images showed a thermal width (5 – 95%) of 44 K. Based on the planar-imaging thermometry, they concluded that the source of naturally occurring thermal stratification was wall heat transfer and convection into the bulk gas due to turbulent structures. Finally, Dec et al. [49] concluded that controlling natural thermal stratification may be a promising method to extend the high-load limit of HCCI combustion.

The above discussion of partial fuel stratification and thermal stratification can be summarized as introducing gradients into the auto-ignition characteristics (i.e., the ignition delay) of the charge. Relying on Zel'dovich [50], Chen et al. [51] relate the speed of a propagating subsonic spontaneous ignition front, S_{ig}, to the spatial gradient in ignition delay, $\nabla\tau$, as

$$s_{ig} = \frac{1}{|\nabla\tau|} . \qquad \textbf{(2-1)}$$

The gradient in ignition delay is difficult to define since it will depend not only on the state of the mixture, but also on the state of the surrounding mixtures that interact through transport and compression heating. However, it is clear from Eq. 2-1, that controlling the gradients in ignition delay is critical to control the heat release rate of PCI combustion. Further, it is well known that ignition delay is a function of temperature, pressure, composition, equivalence ratio, and fuel type (see Figure 2-3 for an illustration of the temperature and fuel type effects). Recall that the discussion of combustion phasing control (see Section 2.3.1) suggested that exploring in-cylinder fuel blending may be useful for combustion phasing control. The dependence of ignition delay and likely HRR through Eq. 2-1 on fuel type gives an additional argument to the investigation of in-cylinder fuel blending. That is, in-cylinder fuel blending of two fuels with different auto-ignition characteristics offers the potential to simultaneously control the combustion phasing and heat release characteristics.

Chapter 3

Computational Approach and Preliminary Model Validation

3.1 CFD Model Description

Computations were performed using the KIVA-3v release 2 code [52] with improvements to many physical and chemistry models developed at the Engine Research Center (ERC) [53-59]. This section provides an overview of the physical models important to the present study.

3.1.1 Combustion Models

The CHEMKIN^{TM} II solver is integrated into the KIVA-3v code to couple the chemistry and flow solutions. The RNG k-ε model [59] is used for turbulence calculations; however, sub-grid turbulence-chemistry interactions are not considered. That is, the current implementation of the CHEMKIN^{TM} II solver considers every cell a Well Stirred Reactor (WSR). At each time step, species concentrations and thermodynamic conditions are passed to the chemistry solver for each computational cell. The chemistry solver then integrates the mass and energy equations at constant volume over a period of time equal to the computational time step. The rate of change of each species, k, in each computational cell is given by

$$\frac{dY_k}{dt} = v\dot{\omega}_k W_k \quad , \tag{3-1}$$

where Y_k is the mass fraction of species k, v is the specific volume of the cell, $\dot{\omega}_k$ is the production rate of species k, and W_k is the molecular weight. Although, sub-grid scale turbulent-chemistry interactions are not considered in Eqn. 3-1, by coupling the chemistry solver with the CFD code, the effects of turbulence on combustion are accounted by modeling the effects of turbulence on property transport, heat flux, and mixture preparation.

In this study the chemistry of gasoline and diesel fuel are represented by that of iso-octane and n-heptane, respectively. A reduced reaction mechanism made up of 45 species and 142 reactions [58] describes the combined oxidation of n-heptane and iso-octane. Note that many studies (e.g., Ra et al. [60]) have shown that the combustion characteristics of gasoline and diesel are represented acceptably by iso-octane (i.e., PRF 100) and n-heptane (i.e., PRF 0), respectively. This approach has also been shown to yield acceptable agreement for blends of gasoline and diesel fuel (e.g., Kokjohn et al. [20, 21, 61]). Furthermore, Puduppakkam et al. [62] compared the PRF mechanism used in the present study to a detailed gasoline mechanism (425 species and 3128 reactions) and found similar bulk combustion characteristics.

During conventional and LTC combustion, the reaction zone thickness is approximately 1 mm or larger (see Singh et al. [63]); thus, resolution of the reaction zone is possible with grids on the order ½ mm. However, when the combustion process is controlled by flame propagation, the reaction zone is much thinner. For example, the laminar flame thickness of an iso-octane – air mixture at 600 K and 40 bar (i.e., typical SI engine conditions) is ~10 μm[1]. The thickness of the inner layer (i.e., the fuel consumption layer) is approximately 10 times smaller than the flame thickness [64] – 1 μm for the iso-octane – air mixture discussed above. Obviously, refining the computational grid enough to resolve the flame front is not feasible for engineering-type calculations; thus, a flame propagation model is required to approximate the under-resolved flame front. In this work, flame propagation was considered by the use of a level-set based

---

[1] The flame speed and thickness were estimated using Eqns. 3-8 and 3-9.

model, the G-equation model [64]. The model was developed by Peters [64] and implemented into the KIVA code by Tan [65] to model flame propagation in a spark-ignited engine. Singh et al. [55] applied the flame propagation model to a dual-fuel partially premixed compression-ignition engine operating on premixed natural gas with a small diesel pilot injection. In their work, auto-ignition was calculated using the Shell model [66] and diesel combustion was calculated using the characteristic time combustion (CTC) model [67]. Liang et al. [68] extended this work to consider detailed chemistry calculations in the regions outside of the flame front. Similarly, in the present work, the ignition process and combustion outside of the flame front is predicted using the KIVA-CHEMKIN approach, as previously discussed. Once a flame surface is established through auto-ignition, the flame front is tracked using a level-set approach. A scalar field, G, is used to divide the combustion chamber into burned (G > 0) and unburned regions (G < 0) and the zero level-set (i.e., G = 0) gives the average location of a turbulent flame brush. The present implementation of the G-equation flame propagation model is described in detail by Liang et al [68]; thus, only an abbreviated description is provided here. The transport of the scalar, G, and its variance, G" are given by

$$\begin{aligned}\frac{\partial \tilde{G}}{\partial t} + \left(\tilde{\vec{v}}_{fluid} - \tilde{\vec{v}}_{vertex}\right) \cdot \nabla \tilde{G} = \frac{\bar{\rho}_u}{\bar{\rho}} s_t^0 \left|\nabla \tilde{G}\right| - \\ D_t \tilde{k}_M \left|\nabla \tilde{G}\right| \end{aligned}, \qquad \textbf{(3-2)}$$

$$\begin{aligned}\frac{\partial \tilde{G}''}{\partial t} + \tilde{\vec{u}} \cdot \nabla \tilde{G}''^2 = \nabla_{\parallel} \cdot \left(\frac{\bar{\rho}_u}{\bar{\rho}} D_T \nabla_{\parallel} \tilde{G}''^2 \right) + \\ 2 D_T \left(D_T \nabla \tilde{G} \right)^2 - c_S \frac{\tilde{\varepsilon}}{\tilde{k}} \tilde{G}''^2 \end{aligned}, \qquad \textbf{(3-3)}$$

where $\tilde{\vec{v}}_{fluid}$ is the velocity of the fluid, $\tilde{\vec{v}}_{vertex}$ is the velocity of the cell vertex, $\bar{\rho}_u$ is the density of the unburned mixture, $\bar{\rho}$ is the mean density at the flame front, D$_t$ is the turbulent diffusivity, s_t^0

is the turbulent flame speed, $\nabla_{\|}$ is the tangential gradient operator, c_S is a modeling constant, $\tilde{k}$ is the turbulent kinetic energy, and $\tilde{\varepsilon}$ is the dissipation rate of turbulent kinetic energy. The tilde denotes Favre averaging. The turbulent flame speed, s_T^0, is given by [65]

$$\frac{s_T^0}{s_L^0} = 1 - \frac{a_4 b_3^2}{2b_1}\frac{l_T}{l_F} + \left[\left(\frac{a_4 b_3^2}{2b_1}\frac{l_T}{l_F}\right)^2\right] + a_4 b_3^2 \frac{u' l_T}{s_L^0 l_F} \quad , \tag{3-4}$$

where s_L^0 is the laminar flame speed, l_T is the turbulence integral length scale, l_F is the laminar flame thickness, and a_4, b_1, and b_3 are model constants. The correlation of Metghalchi et al. [69] is used to calculate the laminar flame speed

$$s_L^0 = s_{L,ref}^0 \left(\frac{T_u}{T_{u,ref}}\right)^{\alpha} \left(\frac{P}{P_{ref}}\right)^{\beta} F_{dil} \quad . \tag{3-5}$$

The subscript ref corresponds to reference conditions taken as 298 K and 1 atm. A scaling factor, F_{dil} is used to consider the effects of inert species on the laminar flame speed. The exponents, α and β, used in this correlation are functions of equivalence ratio, ϕ, given by

$$\alpha = 2.18 - 0.8(\phi - 1) \tag{3-6}$$

$$\beta = -0.16 + 0.22(\phi - 1) \, . \tag{3-7}$$

The reference laminar flame speed is calculated using the approach suggested by Yang and Reitz [70] that considers the effect of PRF number (i.e., reactivity) on laminar flame speed.

$$S_{L,ref}^0 = 34.1\phi^{-0.134} \exp\left(-3.86(\phi - 1.146)^2\right) + \left(0.13482\phi - 0.09752\phi^2 + 0.01746\phi^3\right)(100 - PRF) \tag{3-8}$$

The laminar flame thickness, l_F, is found from the heat conductivity, λ, specific heat, C_p, density, and laminar flame speed.

$$L_F = \frac{\left(\lambda / C_p\right)_0}{\left(\rho S_L^0\right)_u} \quad \textbf{(3-9)}$$

3.1.2 Emissions Formation

Soot was predicted using a two-step phenomenological soot model [54] based on the approach of Hiroyasu [71]. The rate of change of soot mass within a computational cell, $\dot{M}_s$, is given by competition between formation, $\dot{M}_{sf}$, and oxidation, $\dot{M}_{so}$, processes

$$\dot{M}_s = \dot{M}_{sf} - \dot{M}_{so}, \quad \textbf{(3-10)}$$

where the soot formation rate is given by the Arrhenius expression

$$\dot{M}_{sf} = \frac{dM_s}{dt} = A_{sf} M_{C_2H_2} P^n \exp\left(-\frac{E_{sf}}{RT}\right) \quad \textbf{(3-11)}$$

and the oxidation rate, R_{Total}, is given by the carbon oxidation model of Nagle and Strickland-Constable [72]. The oxidation rate is discussed by Liu et al. [73], and given by

$$\dot{M}_{so} = \frac{dM_{so}}{dt} = \frac{6MW_c}{\rho_s D_s} M_s R_{Total}, \quad \textbf{(3-12)}$$

where M_s is the soot mass in the computational cell, The soot density, ρ_s, and soot particle diameter, D_s, were taken as 2 g/cm^3 and 0.025 micron, respectively.

The soot model used in the present study uses acetylene as an inception species, allowing coupling of the soot model and chemistry solver through the addition of 13 reactions involving acetylene.

Two model constants in Eqn. 3-11, the soot formation pre-exponential (A_{sf}) and activation energy (E_{sf}), are tuned to match measured soot levels. However, no single set was found that captured the soot levels of both RCCI and conventional diesel combustion. In order to match soot levels for both operating modes, two different values for the pre-exponential and activation energy were used. The values are shown in Table 3-1. The reason for the required difference in activation energy is unclear; however, the difference in soot composition may be responsible. Prikhodko et al. [74] performed detailed soot measurements of engines operating in conventional diesel, diesel PCCI (LTC), and dual-fuel RCCI. They suggested that soot formed during dual-fuel RCCI operation consists of more semi-volatile organic compounds than conventional diesel or diesel LTC combustion.

Table 3-1. Soot model constants used for conventional diesel and RCCI combustion.

	A_{sf}	E_{sf}
Conventional Diesel	1000	12,500
RCCI	700	1,250

NOx emissions are predicted using a reduced NO mechanism [75] consisting of 4 additional species and 12 reactions. The reduced NO mechanism is based on the Gas Research Institute (GRI) NO mechanism [76]. The reduced NO mechanism described by Sun [75] is given by reactions 3-13 through 3-24 below. Reactions 3-13 through 3-15 are the thermal or extended Zeldovich NO pathways that dominate at high temperatures [5].

$$\mathrm{N + NO <=> N_2 + O} \qquad \textbf{(3-13)}$$

$$\mathrm{N + O_2 <=> NO + O} \qquad \textbf{(3-14)}$$

$$\mathrm{N + OH <=> NO + H} \qquad \textbf{(3-15)}$$

$$\mathrm{N_2O + O <=> N_2 + O_2} \qquad \textbf{(3-16)}$$

$$\mathrm{N_2O + O <=> 2NO} \qquad \textbf{(3-17)}$$

$$\mathrm{N_2O + H <=> N_2 + OH} \qquad \textbf{(3-18)}$$

$$\mathrm{N_2O + OH <=> N_2 + HO_2} \qquad \textbf{(3-19)}$$

$$\mathrm{N_2O + M <=> N_2 + O + M} \qquad \textbf{(3-20)}$$

$$\mathrm{HO_2 + NO <=> NO_2 + OH} \qquad \textbf{(3-21)}$$

$$\mathrm{NO + O + M <=> NO_2 + M} \qquad \textbf{(3-22)}$$

$$\mathrm{NO_2 + O <=> NO + O_2} \qquad \textbf{(3-23)}$$

$$\mathrm{NO_2 + H <=> NO + OH} \qquad \textbf{(3-24)}$$

3.1.3 Spray Model

The spray model employed in this study uses the Lagrangian-Drop and Eulerian-Fluid (LDEF) approach. Because a detailed chemistry model is used, it is desirable to use a relatively coarse computational mesh; however, severe grid size dependency has been observed in LDEF spray models. This problem is most severe in the near nozzle region where the droplets are very close together and occupy only small portions of the Eulerian mesh. Abraham [77] showed that accurate modeling of the near nozzle region required grid resolution on the order of the orifice diameter. However, it is not feasible from a computational time standpoint to solve engine problems on such a fine mesh. Furthermore, a fundamental assumption of the LDEF approach is that the volume fraction of droplets in each cell is small, that is, the void fraction is near one. Thus, if the mesh size is overly refined (i.e., mesh size of the order of the droplet size) this assumption may be violated. In order to reduce the grid size dependency of the LDEF spray model and allow accurate spray simulation on a relatively coarse grid, the Gasjet model of Abani et al. [56, 57] is employed to model the relative velocity between the droplets and gas phase in the near nozzle region. Their approach assumes that the relative velocity of between a droplet and the gas phase is equal to that between the droplet and a turbulent gas jet with the same mass and momentum of that of the injected fuel. This approach imposes an axial component for the gas phase velocity as a function of distance from the nozzle, which is used in the droplet acceleration equation given by

$$\frac{dU}{dt}=\frac{3}{8}C_D\frac{\rho_g}{\rho_l r_d}\left|U-V_{gas}\right|\left(U-V_{gas}\right) \qquad \textbf{(3-25)}$$
,

where U is the droplet velocity vector, C_D is the droplet drag coefficient, which is a function of Reynolds number, ρ_g and ρ_l are the gas and liquid phase densities, respectively, r_d is the droplet radius, and V_{gas} is the gas phase velocity vector given as $V_{gas}=(V_x,V_y,V_z)$. The velocity components perpendicular to the spray axis (i.e., V_y and V_z) are obtained from the Eulerian gas phase solution and V_x, the axial component of the gas phase velocity, is found from gas-jet theory as

$$V_x = \min\left[U_{inj,} \; \frac{3U_{inj} d_{noz} \sqrt{\frac{\rho_l}{\rho_g}}}{K_{entr} x} \left(\frac{1}{\left(1 + \frac{12r^2}{K_{entr}^2 x^2} \right)^2} \right) \right], \tag{3-26}$$

where U_{inj} is the injection velocity, d_{noz} is the nozzle diameter, K_{entr} is a model constant taken to be 0.7 as suggested by Abani et al. [57], x is the position downstream of the nozzle on the spray axis, and r is the radial position.

Droplet breakup is modeled using the hybrid Kelvin Helmholtz (KH) – Rayleigh Taylor (RT) model described by Beale and Reitz [53]. The droplet collision model is based on O'Rourke's model; however, a radius of influence method is used to determine the possible collision partners to further reduce mesh dependency [78]. In addition, the collision model was expanded by Munnannur [78] to include a more comprehensive range of collision outcomes. The current implementation of the droplet collision model considers the effects of bounce, coalescence, and fragmenting and non-fragmenting separations. Droplet interactions with the wall are considered through a wall film submodel [79, 80], which includes the effects associated with splash, film spreading, and motion due to inertia.

3.1.4 Genetic Algorithm Optimization

A genetic algorithm (GA) is a search technique inspired by the Darwinian idea of "survival of the fittest" and mutation. Relying on Senecal [81], the GA technique is summarized as follows:

1. An initial population is generated by randomly assigned values for each optimization parameter to a specified number of optimization citizens.
2. The “fitness” of each citizen is evaluated by performing experiments or simulations.
3. Citizens with high “fitness” are allowed to reproduce resulting in a new generation of citizens. At this point, changes in a portion of the population may be introduced via mutations.
4. Successive generations are performed until the goals of the optimization are attained.

In this work parameter optimization was performed using a multi-objective genetic algorithm (MOGA). Shi [82] has shown that the Nondominated Sorting Genetic Algorithm (NSGAII) proposed by Deb et al. [83] performs well in engine optimizations; therefore, NSGAII was selected as the optimization tool for this study. A multi-objective approach was favored over the use of a merit function based single-objective optimization scheme in order to generate a set of Pareto solutions rather than a single “optimum” point. Of course, a single “optimum” point must be selected from the Pareto solutions after the optimization has completed; however, the power of the MOGA optimization is the generation of the tradeoff curves or surfaces.

3.2 Role of Turbulent-Chemistry Interactions in Conventional and Low Temperature Combustion

Prior to exploring any new combustion concept (e.g., RCCI) using CFD modeling, it is important to ensure that the combustion models used in this study are robust and capable of capturing the combustion characteristics over a range of conditions. In this section, model predictions are compared to the measurements of Singh et al. [63] over a range of conditions from conventional high-temperature diesel combustion to diesel LTC combustion and the need to consider turbulence-chemistry interactions in engine combustion modeling is discussed. The model predictions with and without the consideration of flame propagation are presented and the predictions are used to help explain and support observations from optical engine experiments. A detailed description of this study can be found in Kokjohn et al. [84].

3.2.1 Engine Specifications

The engine modeled in this study is an optically accessible, single-cylinder, direct-injection (DI), heavy-duty diesel engine based on a Cummins N-series production engine. The specifications are given in Table 3-2 and a schematic of the engine is presented in Figure 3-1. A more detailed description of the engine is presented with the RCCI optical engine experiments shown in Chapter 8 and a very detailed description of the engine can be found in Ref. [85]. In the present study, optical access is gained through an extended piston and a flat piston crown window. The fuel used in the engine experiments was Philips Petroleum 2007 emissions certification number 2 ultra-low sulfur diesel fuel (detailed specifications given in Ref.[86]). The injector is a high-pressure, solenoid actuated, common-rail type fuel injector with specifications given in Table 3-2. Model predictions of the ignition processes and flame structures are compared to Singh's [63] measurements of naturally occurring luminous emission and OH planar laser induced fluorescence, respectively. Details of the optical diagnostics can be found in Singh's [63] work.

Table 3-2. Engine and injector specifications

Base engine type	Cummins N-14 DI diesel
Number of cylinders	1
Bore x stroke	13.97 x 15.24 cm
Connecting rod length	30.48 cm
Displacement	2.34 L
Geometric compression ratio	10.75:1
Simulated compression ratio	16:1
Bowl width	9.78 cm
Bowl depth	1.55 cm
Fuel injector type	Common-rail
Cup (tip) type	mini-sac
Number of holes	8, equally spaced
Spray included angle	152°
Nozzle orifice diameter	0.196 mm
Nozzle orifice L/D	5

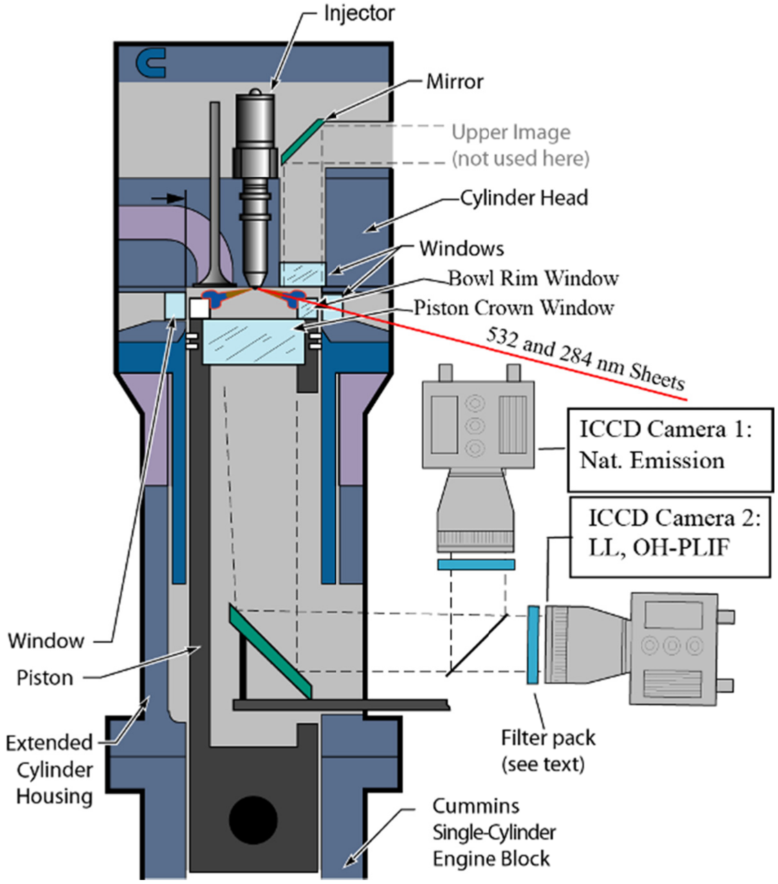

Figure 3-1. Schematic of the optically accessible DI research engine [63].

The operating conditions are given in Table 3-3. Singh et al. [63] adjusted the intake conditions to explore a range of combustion characteristics from conventional, mixing controlled combustion (i.e., HTC-short ignition delay) to low temperature combustion (i.e., LTC-long ignition delay). These conditions are discussed in detail with the presentation of the results.

Table 3-3. Engine operating conditions for model validation study.

	HTC-short ID	HTC-med. ID	LTC-Long ID
Inlet O_2 Conc. (Vol %)	21	21	12.7
Speed (rev/min)	1200	1200	1200
IMEP (bar)	4.5	4.5	3.9
Intake Temp (°C)	111	47	90
Intake Pressure (bar)	2.33	1.92	2.14
TDC Motored Temperature (K)	905	800	870
TDC Motored Density (kg/m^3)	24	22.3	22.9
Peak Adiabatic Flame Temp. [K]	2760	2700	2256
Rail Pressure (bar)	1200	1200	1600
Start of Injection (°ATDC)	-7	-5	-22
Duration of Injection (°CA)	10	10	7
Injection Quantity (mg)	61	61	56
Ignition Delay (°CA)	4	8.75	11
Ignition Dwell (°CA)	-6	-1.25	+4

3.2.2 CFD Grid

The computational domain represents a single hole of the eight hole injector used in the experiments of Singh et al. [63]. The 45 degree sector mesh, shown in Figure 3-2, is made up of 110,000 cells at BDC with a grid resolution of 1x1x1.5 mm at the piston bowl wall. The crevice region is represented as the elongated volume. Furthermore, the volumes associated with unresolved geometric features (e.g., the head gasket and pressure transducer crevices) were added to the crevice volume to ensure the correct compression ratio was retained.

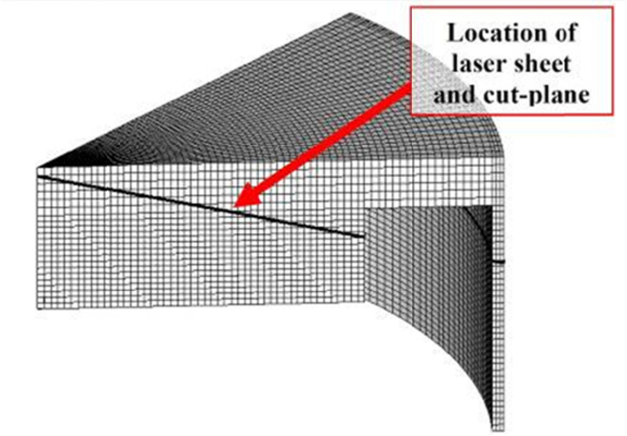

Figure 3-2. Computational grid showing the location of the laser sheet in the experiments and cut-plane in the simulations. The grid consists of 110,000 Cells at BDC (1 x 1 x 1.5 mm at the piston bowl wall) [84].

3.2.3 Results and Discussion

3.2.3.1 Cylinder Pressure and Apparent Heat Release Rate

Figure 3-3 shows comparisons between the measured [63] and predicted cylinder pressure and apparent heat release rate (AHRR). The cylinder pressure and AHRR for the three cases are plotted together to highlight the differences in combustion characteristics. The AHRR for both the experiments and simulations are calculated using the air standard cycle assuming no heat transfer to the walls [87].

In general, the simulations are able to capture the cylinder pressure and AHRR well. Additionally, notice that there is very little difference in the cylinder pressure or AHRR with and without consideration of flame propagation. This suggests that volumetric heat release and mixing control the rate of combustion at the conditions of interest for this study. The largest differences between the experiments and simulations are observed for the LTC-early case, where the simulations over-predict the rate of heat release. However, all model constants were held fixed and no changes were made to the reaction mechanism or spray model constants to try to 'tune' the predictions to match the experimental results as the combustion regimes changed. The acceptable agreement over a range of combustion regimes suggests that the physical models are accurately capturing the behavior of the dominant spray, mixing, and combustion processes. Furthermore, the similarity between the results with and without consideration of flame propagation suggests that the model predictions without consideration of flame propagation and without consideration of sub-grid scale chemistry-turbulence interactions are sufficient to capture the bulk combustion characteristics.

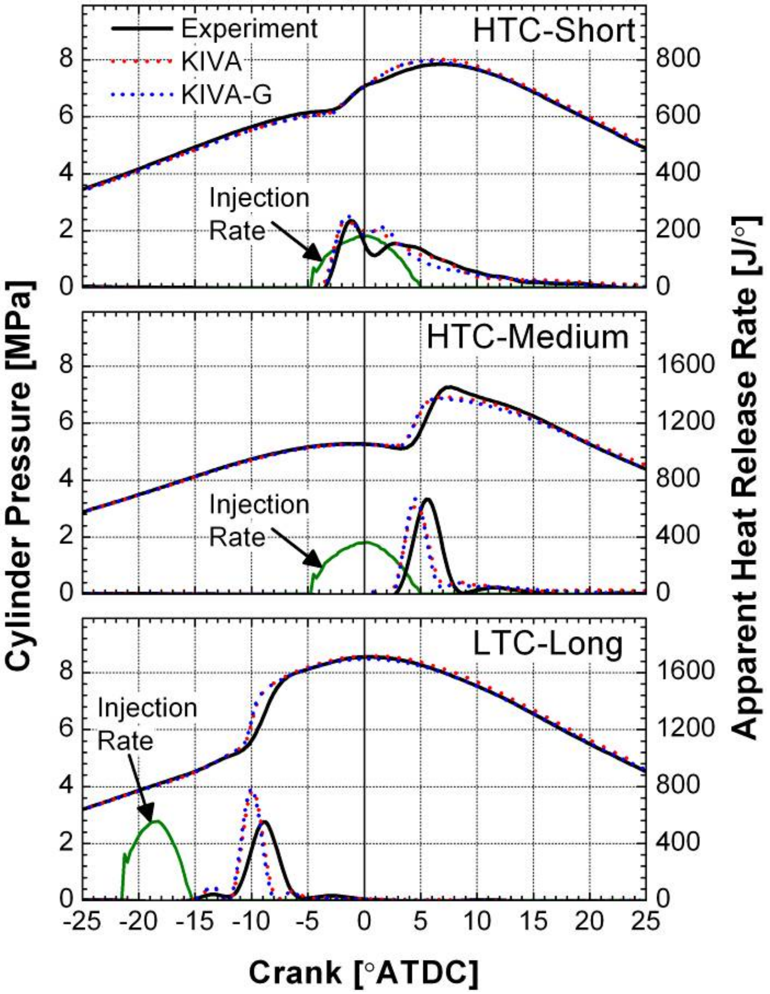

Figure 3-3. Comparison of measured [63] and predicted [84] cylinder pressure and AHRR for the different cases. The measured cylinder pressure and AHRR are shown in solid black lines, the calculated cylinder pressure and AHRR only considering volumetric heat release (i.e., KIVA-CHEMKIN) are shown with red dashes, and the calculated cylinder pressure and AHRR considering both flame propagation and volumetric heat release (i.e., KIVA-CHEMKIN-G) are shown with blue dots.

3.2.3.2 Comparison of First Stage Ignition Process with Naturally Occurring Luminous Emission

The previous section showed that the simulations are capable of capturing the bulk combustion characteristics (e.g., cylinder pressure). The validity of the present modeling approach is further assessed by comparison to in-cylinder images of the spray and combustion process. Singh et al. [63] simultaneously acquired single-shot images of liquid fuel and line-of-sight natural emission images for each operating condition. These images were used to validate model predicted spray penetration and early stage combustion. In the experiments, first stage ignition was identified by naturally occurring luminous emission. The relative change in emission intensity (i.e., the required camera gain) was used to differentiate first-stage ignition (relative camera gains on the order of 10e5), second-stage ignition (relative camera gains on the order of 10e3), and soot luminosity (relative camera gains on the order of 1).

Formaldehyde (CH_2O) tracks well with the "soup" of hydrocarbons formed during the early stage reactions [88]. Thus, formaldehyde was used to mark the location of first stage ignition in the simulations. As the charge transitions to second stage ignition, a buildup of OH radicals is observed. Thus, second stage ignition was marked by the location of OH radicals. As the combustion process continues, soot precursors are formed in fuel rich regions. In the current simulations acetylene (C_2H_2) is used as a soot precursor. Thus, acetylene was used as a marker for regions likely to form soot.

In both the experimental and computational images, the field of view focuses on a single fuel jet looking upward through the piston window. Note that only a single nozzle hole was modeled in this study; however, to facilitate comparisons with the experimental images, the modeling results were duplicated to show five of the eight fuel jets. The liquid fuel is shown in blue for both the experiments and simulations. The experimentally observed naturally occurring luminous emission is shown in green and the relative camera gain is shown in the upper right-hand corner of each image. In the simulations, formaldehyde is shown in light green, OH is shown in bright green, and acetylene is shown in red. The white dot on the left side of each image shows the location of the fuel injector nozzle and the white curve on the right side of each image shows the location of the piston bowl rim. The crank angle in degrees after the start-of-injection (ASOI) is shown in the lower left-hand corner of each image. Two sets of modeling images are presented. The top row of modeling images shows the results considering both volumetric heat release and flame propagation (i.e., KIVA-G see Eq. 3-2). In the KIVA-G results, the predicted flame surface is shown by a purple curve. The bottom row of results shows images without considering flame propagation.

Figure 3-4 shows the comparison for the HTC-short ignition delay condition. At 4 degrees after the start-of-injection, the experiments show weak chemiluminescence around the spray plume. Note that the camera gain at 4 degrees after the start-of-injection was 2.5e5. At this time in the simulations, formaldehyde is seen to form around the downstream portion of the spray jet. Additionally, it appears that the liquid penetration is captured well by the simulations. Only 1 crank angle degree later, strong luminosity was observed in the experiments (noted by the 4 order of magnitude reduction in the required camera gain). The simulations show that at this point the jet transitions to second stage ignition. Note that OH forms around the outer edge of the spray plume and the inner region of the jet fills with soot precursors. The remaining images show that the transition to second stage ignition is complete and a soot filled jet is observed. The simulations show that a thin diffusion flame is present on the outer edges of the jet while the inner region is filled with soot precursors. Notice that by 6° ASOI, Singh et al. [63] reduced the

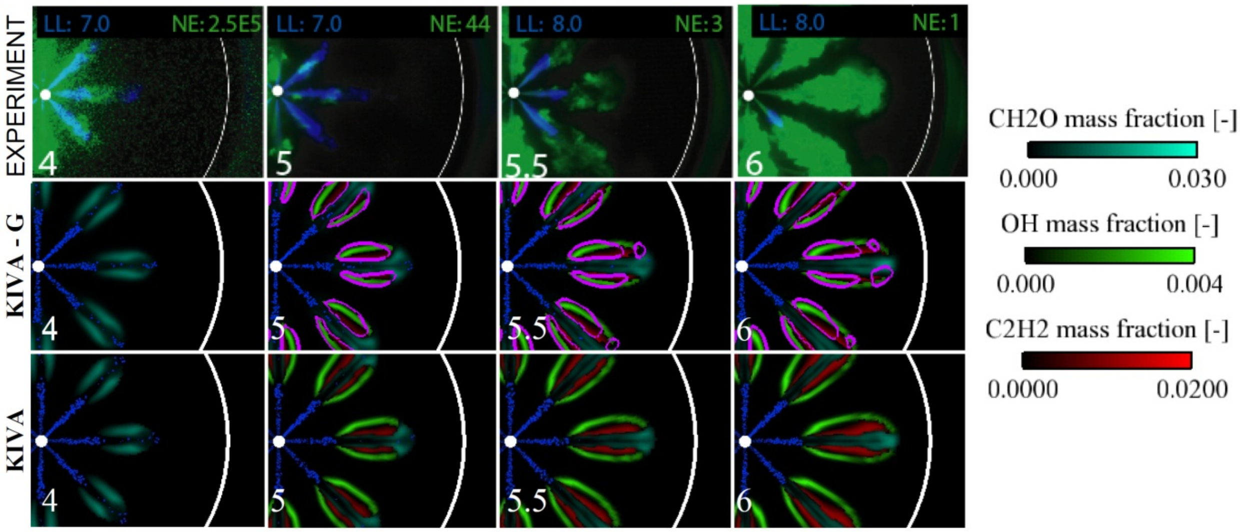

Figure 3-4. Comparison of single–shot broadband natural emission images [63] with computed contours of formaldehyde, OH, and acetylene [84] for the HTC-short ignition delay condition.

camera gain to unity to avoid saturation due to the high intensity soot luminosity throughout the jet cross section. Thus, it appears that the soot-filled jet predicted by the simulations is consistent with the experimental observations. The flame structure and locations of intermediate species are nearly identical with and without the consideration of flame propagation. However, notice that near the lift-off location, the flame propagation model predicts a flame surface with a nose-shaped structure along the thin band of OH (i.e., the diffusion flame). The flame exists in both the inner (rich) and outer (lean) portions of the jet and a diffusion flame exists behind the flame front. Thus, it appears the flame propagation model is able to capture the triple or edge flame structure at the diffusion flame lift-off location. This will be discussed in more detail in the discussion of the flame structure.

The comparison of the first stage combustion process and transition to thermal ignition for the HTC-medium ignition delay condition is shown in Figure 3-5. At the HTC-medium ignition delay operating condition, the intake temperature and pressure were reduced from those of the HTC-short condition to reduce the TDC temperature from 905 K to 800 K in order to extend the ignition delay [63]. Figure 3-3 shows that the start of combustion occurs only 2 crank angle degrees before the end-of-injection (EOI). Thus, it is expected that significantly more pre-combustion mixing is present in the HTC-medium ignition delay case compared to the HTC-short ignition delay case. In both the experiments and simulations, first stage ignition is seen to occur on the outer region of the spray jet near 6° ASOI. In contrast to the HTC-short ignition delay condition, the experiments at the HTC-medium ignition delay condition show that low intensity luminosity persists for several crank angle degrees after it first appears. The simulations show that formaldehyde exists in similar locations and for a similar duration as the low intensity luminosity observed in the experiments. Thus, it is likely that the low intensity luminosity is due the "soup" of hydrocarbons formed during fuel decomposition (i.e., low temperature reactions). It can be seen that the increased ignition delay allows mixing to occur and, in the experiments, luminosity nearly fills the jet. Consistent with the experiments, the simulations show that the jet is nearly filled with formaldehyde. At 9° ASOI, the experiments show a transition to second stage ignition (requiring a reduction in camera gain by over an order of magnitude from 8° to 9° ASOI). Similarly, the simulations show that OH and acetylene first appear at 9° ASOI; suggesting that the simulations capture the ignition process well. Furthermore, it is interesting to note that both the experiments and simulations show that the transition to second stage ignition occurs first on the outer edge of the jet. As expected, early in the combustion process, comparisons of the model predictions with and without the flame propagation model show very similar results.

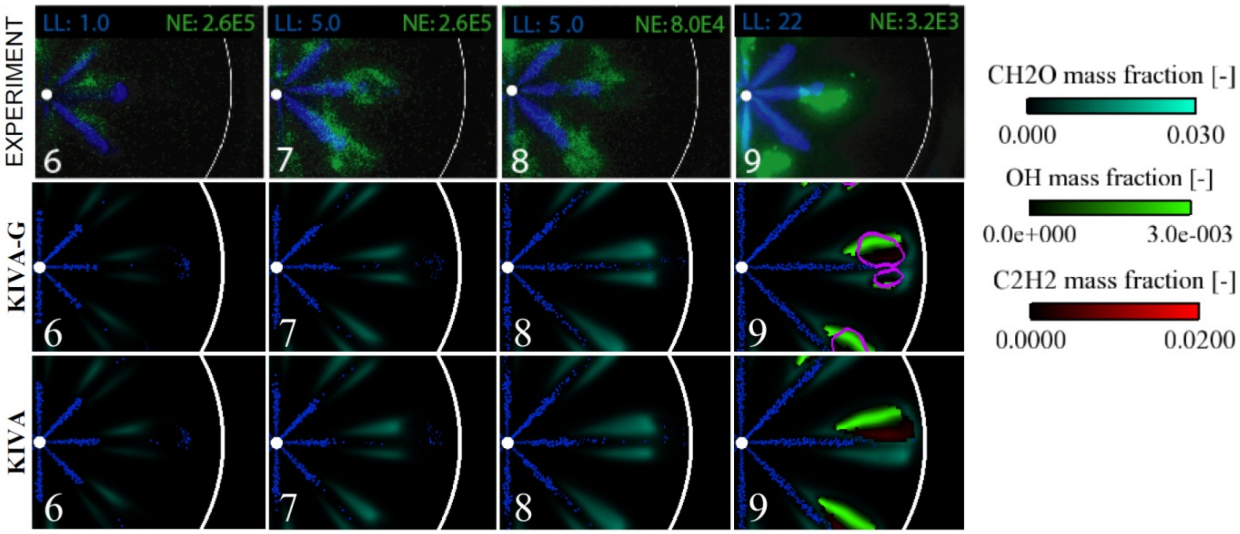

Figure 3-5. Comparison of single–shot broadband natural emission images [63] with computed contours of formaldehyde, OH, and acetylene [84] for the HTC-medium ignition delay condition.

By reducing the inlet oxygen concentration to 12.7% and advancing the injection timing, the ignition delay is extended past the end of injection and LTC is achieved. Figure 3-6 shows the comparison of the first stage ignition process for the LTC-long ignition delay condition. At 7° and 7.5° ASOI the experiments show weak chemiluminescence (camera gain on the order of 1e5) on the outer edge of the spray plume. Notice that, in the experiments, it is difficult to see the luminosity in the three o'clock jet in the 7° ASOI; however, the jets on both sides appear to show luminescence around the edges of the jet. In good agreement with the observed luminescence, the simulations show first stage ignition occurs first on the outer portions of the jet. At 10° ASOI it can be seen that first stage ignition occurs throughout the jet cross section. This is shown by the weak luminescence (camera gain on the order of 1e5) in the experiments and location of formaldehyde in the simulations. At 12° ASOI, the camera gain in the experiments was reduced by two orders of magnitude to avoid saturation. This increase in luminosity suggests a transition to second stage ignition. At this point luminosity was observed

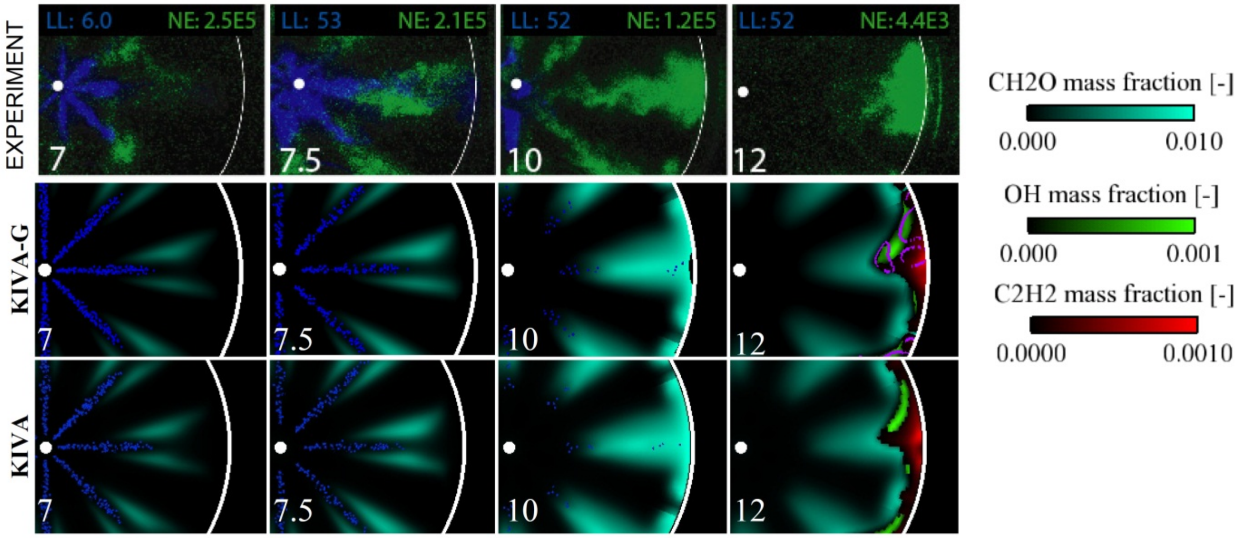

Figure 3-6. Comparison of single–shot broadband natural emission images [63] with computed contours of formaldehyde, OH, and acetylene [84] for the LTC-long ignition delay condition.

mainly at the location where the jet interacts with the piston bowl. The increase in luminosity likely signals a transition to second stage ignition and the presence of luminous soot. In good agreement with the observed results, the simulations show the presence of soot precursors in the jet-bowl interaction region. Additionally, the simulations show that the transition to second stage ignition (signaled by the buildup of OH radicals) occurs first near the location of jet-bowl interaction.

Singh et al. [63] point out that, in the experiments the location of ignition varied slightly cycle-to-cycle, but was always constrained to the downstream portion of the jet, near the location of impingement on the piston bowl surface. It is thought that the transition to second stage combustion occurs first in the downstream portion of the jet because a near stoichiometric region is created near the location of jet impingement (this is discussed in detail in the section discussing the flame thickness dependency on mixing time, see Figure 3-11).

3.2.3.3 Comparison of Computed Flame Structure with OH PLIF Images

Figure 3-7 shows the comparison between measured [63] OH PLIF and predicted OH mass fraction contours at several crank angles for the HTC-short ignition delay condition. The top row of images shows collected fluorescence with the laser tuned to the OH line near 284.01 nm. Because other species likely to be present in the combustion chamber (e.g., PAH and soot) may also fluoresce at 284.01 nm, Singh et al. [63] collected a second set of images (second row) with the laser tuned to 283.90 nm (i.e., slightly off of the OH line at 284.01 nm). By comparing the online (first row) and offline (second row) images, the amount of fluorescence due to OH and that due to other species can be deduced. The third row of images show the OH mass fraction contours computed by the KIVA-CHEMKIN code considering flame propagation. The predicted flame surfaces are shown by the purple curves. The fourth row of images show the OH mass fractions contours computed by the KIVA-CHEMKIN code without considering flame propagation. In each image, the blue spheres represent the liquid droplets.

At the HTC-short ID condition, both the simulations and experiments show a thin band of OH surrounding the spray plume. This thin band of OH indicates the presence of a diffusion flame at the periphery of the jet. Note that Singh et al. [63] point out that OH PLIF emission in the upstream portion of the 3 o'clock jet is attenuated by soot. However, they also point out that the jets on either side of the 3 o'clock jet show OH PLIF emission extending upstream. Thus, consistent with the model predictions, the measurements of OH PLIF emission suggest that the thin diffusion flame extends completely around the periphery of the jet. Additionally, both the simulations and experiments suggest the thickness of the OH producing regions (i.e., the diffusion flame) is ~1 mm.

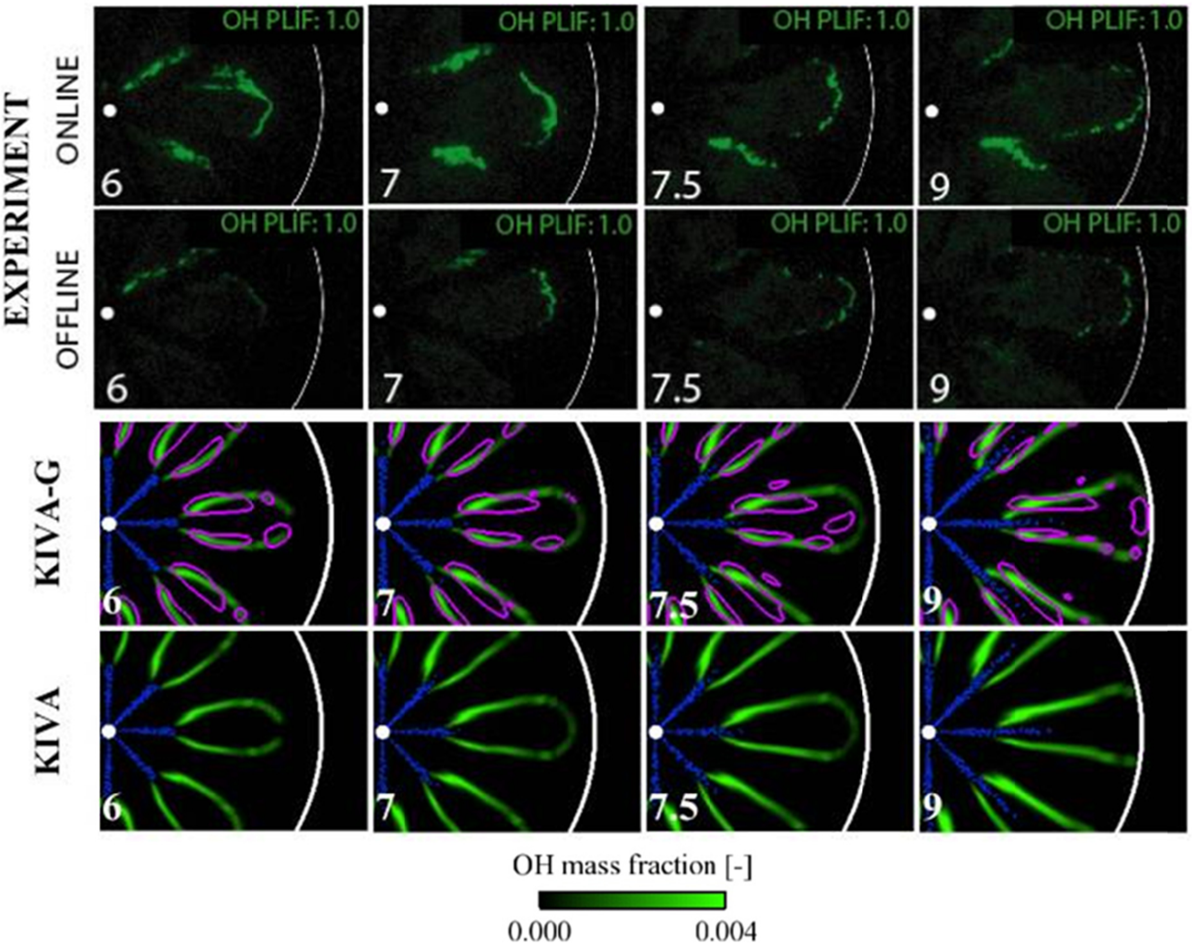

Figure 3-7. Comparison of measured [63] OH PLIF and computed OH mass fractions [84] for the HTC-short ignition delay condition. The computed OH mass fraction scale ranges from 0 to 0.004.

As was shown earlier, the overall results are very similar with and without the flame propagation model. However, the simulations using the flame propagation model show the presence of a triple or edge flame structure near the lift-off location. Figure 3-8 (a) shows contours of OH mass fraction at 6° ASOI with the flame surface colored by equivalence ratio. It can be seen that near the lift-off location, the flame has a nose-like structure with the stoichiometric region furthest towards the nozzle and the rich and lean branches downstream. Figure 3-8 (b) shows the same image, but with the flame surface now colored by turbulent flame speed. It can be seen that the only region where the flame speed is non-negligible is at the

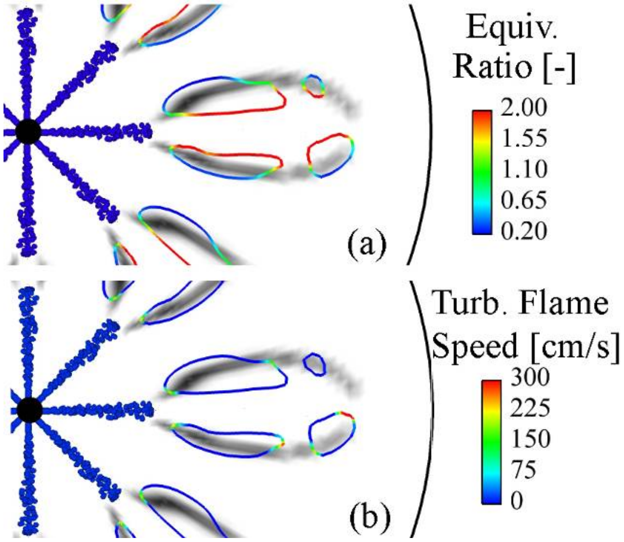

Figure 3-8. Contours of OH mass fraction (grey) at 6° ASOI with flame surfaces (colored lines) colored by (a) equivalence ratio and (b) turbulent flame speed. The computed OH mass fraction scale ranges from 0 (light) to 0.0039 (dark) [84].

location of the stoichiometric mixture. Thus, the flame surfaces at locations other than the stoichiometric mixture location do not contribute to the overall heat release. It appears that if flame propagation plays a role, it is only in the near stoichiometric region in the vicinity of the lift-off location.

Figure 3-9 shows the comparison of measured OH PLIF and predicted OH mass fraction contours at several crank angles for the HTC-medium ignition delay condition. Recall that for this condition the intake temperature and pressure were reduced to provide an extended ignition delay. Consistent with the HTC-short ignition delay condition, the inlet oxygen concentration is 21% by volume (i.e., no EGR). Similar to the HTC-short ignition delay condition, OH appears on the periphery of the jet. It can be seen that the location of OH and the structure of the reaction zone are captured well by the model. The structure is similar to the diffusion flame found for the HTC-short ignition delay condition; however, the thickness of the OH producing region has increased significantly. This increase in thickness is observed in both the simulations and OH

PLIF emission images. The simulations predict that OH exists in a band around the outside of the jet ~3.4 to 5 mm thick. The experiments show OH PLIF emission is present in a band ranging from 5 to 6 mm thick. Thus, it appears the simulations capture the increase in flame thickness as the ignition delay is extended, but may slightly under-predict the diffusion flame thickness in this regime. However, it must be noted that the diffusion flame thickness is not constant around the jet. The thickest portion exists in a clockwise direction from the spray axis approximately halfway between the nozzle and bowl rim. Similar to the HTC-short ID case, the results with and without the flame propagation model are nearly identical.

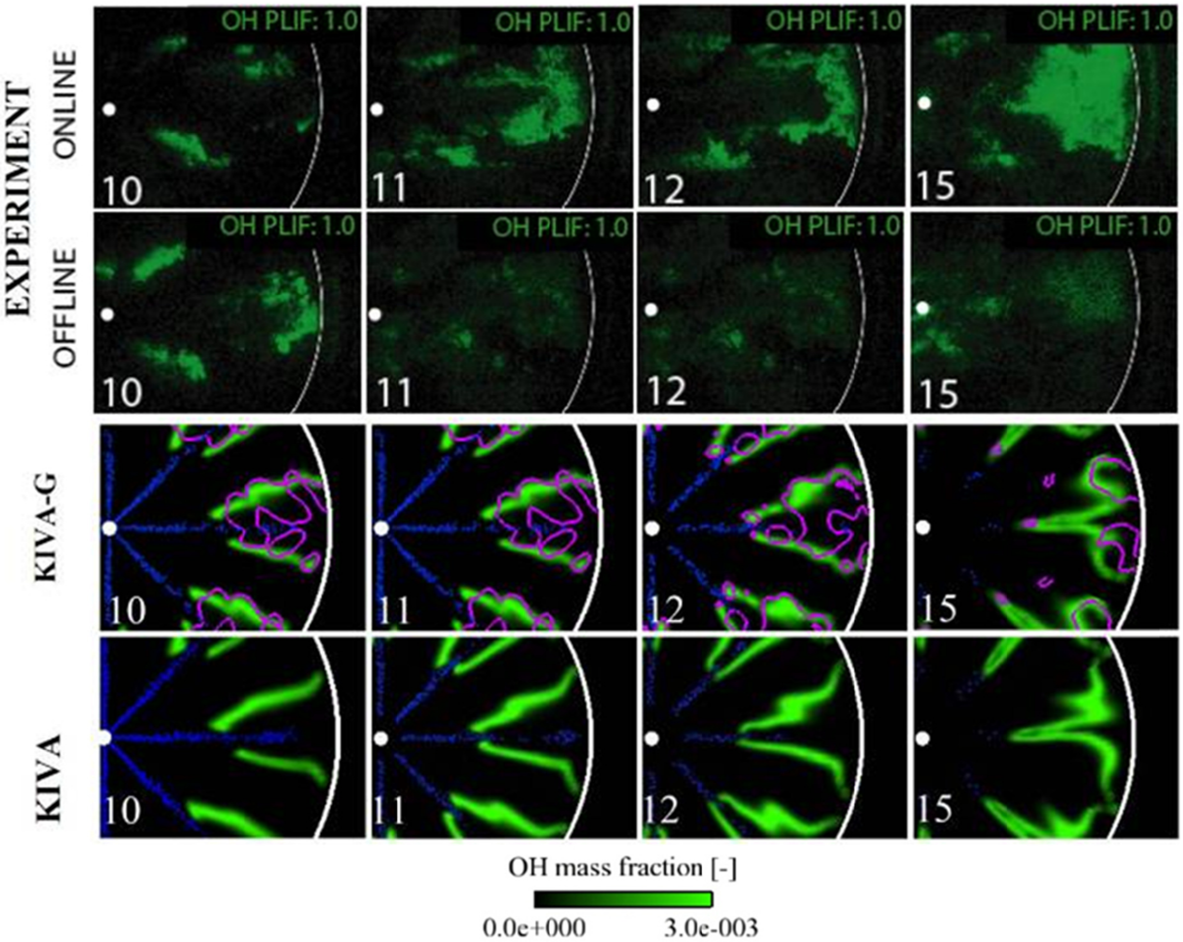

Figure 3-9. Comparison of measured [63] OH PLIF and computed OH mass fraction [84] for the HTC-medium ignition delay condition. The computed OH mass fraction scale ranges from 0 to 0.003.

Figure 3-10 shows the comparison of measured OH PLIF and predicted OH mass fraction contours at several crank angles for the LTC-long ignition delay condition. Recall that for this condition the inlet oxygen concentration was reduced to 12.7% by dilution with nitrogen gas to simulate reduced inlet oxygen concentration due dilution with recirculated exhaust gas (EGR). Additionally, the injection timing has been advanced to 22° BTDC to allow adequate time for mixing. At this condition, the ignition dwell is positive; that is, the end of injection occurs prior to the start of the high temperature heat release. In contrast to the HTC cases, no diffusion flame is observed and significant OH levels are observed across the entire jet cross section. Further

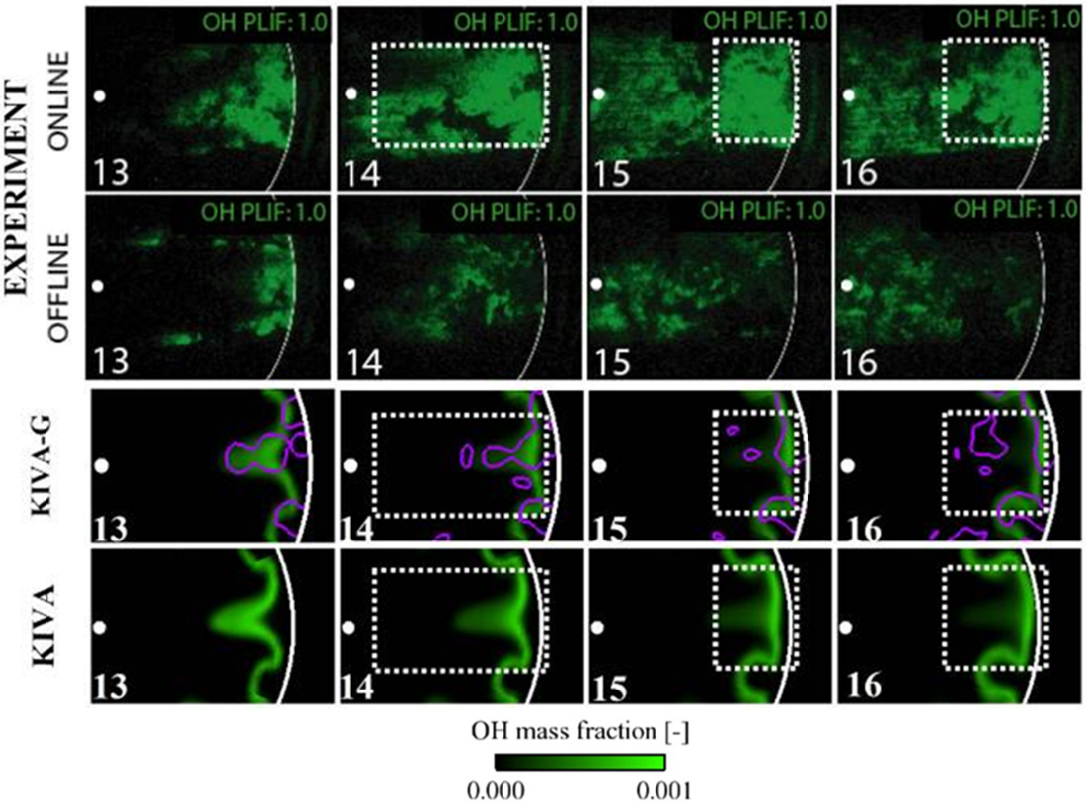

Figure 3-10. Comparison of measured [63] OH PLIF and computed OH mass fraction [84] for the LTC-long ignition delay condition. The computed OH mass fraction scale ranges from 0 to 0.001.

note that comparisons of the online and offline images show that OH fluorescence is dominated by the downstream region. To highlight this, Singh et al. [63] have included a dashed rectangular box showing the location of the highest OH fluorescence. Comparing the measured OH fluorescence and simulated OH mass fraction contours, it can be seen that the simulations capture the change in combustion characteristics very accurately. That is, significant OH concentration is observed across the entire jet cross section. Furthermore, consistent with the experiments, the predicted OH is confined to the downstream portion of the jet.

3.2.3.4 Flame Thickness Dependency on Mixing Time

It was found that the thickness of the reaction zone varied markedly across the range of combustion regimes explored by Singh et al. [63]. To summarize, the HTC-short ID condition showed a diffusion flame surrounding the spray jet with a thickness of ~1 mm. As the ignition delay was extended for the HTC-medium ID condition, the diffusion flame thickness grew to ~5 mm. Finally, the LTC-long ID condition showed no diffusion flame and it was found that the reaction zone completely filled the head of the jet.

Figure 3-11 shows cut-planes colored by OH mass fraction with contours of equivalence ratio overlaid. The contours of equivalence ratio were adjusted to match the inner (rich) and outer (lean) edges of the OH mass fraction images. Notice that the equivalence ratio contours line up nearly exactly with the OH mass fraction contours. The HTC – short ignition delay condition shows significant OH levels for $0.35 < \Phi < 1.65$, the HTC – medium ignition delay condition shows significant OH levels for $0.35 < \Phi < 1.50$, and the LTC – long ignition delay condition shows that the OH producing regions exits within $0.55 < \Phi < 1.20$. Figure 3-11 clearly highlights the dependence of flame structure on mixing time. For a fixed oxygen concentration, as the ignition delay is extended the time available to achieve an ignitable mixture increases and the thickness of the reaction zone increases. Further, when the LTC regime is entered (i.e., the ignition delay is extended beyond the end of injection), sufficient pre-combustion mixing occurs to allow the reaction zone to completely fill the jet.

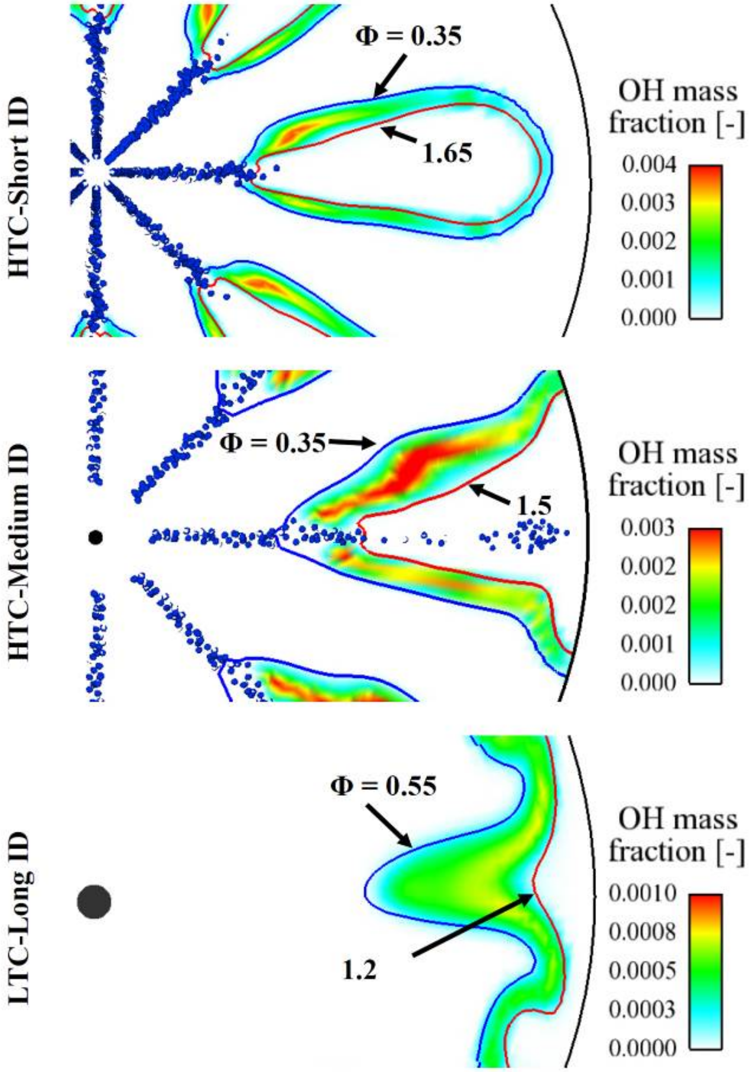

Figure 3-11. Overlaid contours of OH mass fraction and equivalence ratio for the three operating conditions [84].

However, it can also be seen that the reduced oxygen concentration conditions of the LTC-long ID case results in a narrower band of reactive mixture. This has implications on the levels of unburned hydrocarbons (UHC) resulting from incomplete combustion when the LTC regime is entered. That is, regions outside of the 0.55 to 1.2 equivalence ratio band are not likely to achieve complete combustion and will result in reduced combustion efficiency, higher emission of UHC, and potentially increased fuel consumption.

3.2.3.5 Discussion of the validity of KIVA-CHEMKIN without consideration of turbulence-chemistry interactions

The previous comparisons have shown that the models used in this study are capable of capturing both the bulk combustion characteristics (e.g., cylinder pressure) as well as details of the flame structure over a range of combustion regimes without considering sub-grid scale turbulence-chemistry interactions. This is not to say that turbulence is not important in the mixing processes that create and sustain the diffusion flame, but rather that it appears that small-scale interactions between turbulence and chemistry may not play a dominant role in the overall combustion process. To understand the roles of turbulent mixing and volumetric energy release, the turbulent mixing, fuel consumption, and energy release rates are compared. Figure 3-12 shows the inverse of the eddy turnover time (ε/tke), where ε is the dissipation rate and tke is the turbulent kinetic energy, the fuel consumption rate (FCR), heat release rate (HRR), and injection rate for each case. The fuel consumption rate is calculated as

$$FCR = \frac{dm_{fuel}}{dt} - \frac{dm_{fuel,inj}}{dt} , \qquad \textbf{(3-27)}$$

where m_{fuel} is the total fuel mass in the combustion chamber, and $m_{\mathrm{fuel,inj}}$ is the mass of fuel added due to the direct injection of diesel fuel. Note that the results with and without the flame propagation model were nearly identical; thus, only the results considering flame propagation are presented.

First, the discussion focuses on the HTC-short ID case. Comparing the turbulence mixing rate and the injection rate, it can be seen that the sharp increase in the turbulent mixing rate at 2° ASOI (~5° BTDC) is due to the injection event. A small delay exists between the ramp-up in the turbulent mixing rate and the ramp-up in the fuel consumption rate (i.e., pre-combustion mixing). This delay is due to a combination of finite fuel vaporization and chemical decomposition timescales. After the short delay, the fuel consumption rate spikes and a short time later the premixed burn portion of the energy release is observed. Following the premixed spike, the fuel consumption rate decreases and approaches zero as the injection event nears completion. Notice that the rate of heat release follows the mixing rate nearly identically during the later stages of combustion. Recall that turbulence-chemistry interactions at the sub-grid scale are not considered in this study; therefore, it appears that the turbulent combustion process of the HTC-short ID condition is controlled by the large-scale turbulent mixing processes, rather than small-scale interactions. That is, the energy release rate is controlled by the transport of reactive mixture to the thin reaction zone shown in the previous section (see Figure 3-7). As previously described, the thickness of the reaction zone is characterized by the pre-combustion mixing time. It appears that, early in the combustion process, the turbulence generation is primarily the result of the injection event; however, it can be seen that the turbulence mixing rate remains at elevated levels until the end-of-combustion. Thus, it appears that near the end-of-combustion, the mixing rate is enhanced by the reaction, which aids in the transport of reactive material to the reaction zone and sustains the combustion process.

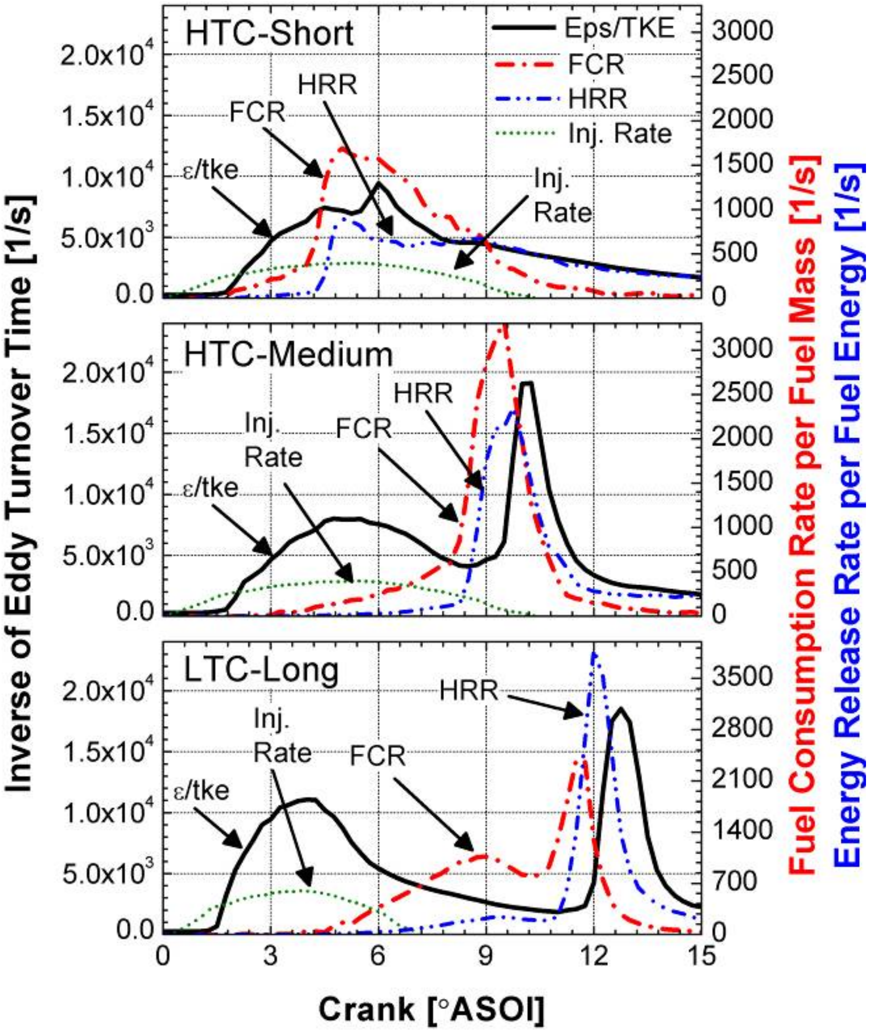

Figure 3-12. Inverse of eddy turnover time (ε/TkE), fuel consumption rate per fuel mass (FCR), energy release rate per fuel energy (HRR), and injection rate [84]. Note that the x-axis is given as degrees after start-of-injection (ASOI).

Similar to the HTC-short ID case, the HTC-medium ID case shows a sharp increase in the turbulent mixing rate due to the injection event. However, in contrast to the HTC-short ID case, the HTC-medium ID case shows that the injection event is nearly completed by the auto-ignition time. Furthermore, it can be seen that the turbulent mixing rate begins to decrease prior to the auto-ignition event. The mixing rate continues to decrease until ignition is achieved. As the rate of energy release increases, the mixing rate also increases. Thus, it appears that the second spike in the turbulent mixing rate is due to expansion of hot products. Notice that, by the time the second spike in the mixing rate is observed, the fuel consumption rate has already peaked and is beginning to decrease. It appears that, as the ignition delay is extended, the spray-induced mixing becomes less dominant in the shape of the energy release profile.

As the ignition delay is further extended to achieve the LTC-long ID condition, it can be seen that the injection generated turbulence is nearly dissipated at the time of significant fuel consumption and energy release. Additionally, it can be seen that by the time the mixing rate increases due to the expansion of hot products, the fuel consumption rate is approaching zero, suggesting nearly all of the fuel has been converted to intermediates. It appears that for the LTC-long ignition delay case, injection generated turbulent mixing plays only an indirect role in the rate of energy release. That is, turbulent mixing is very important for the early stage mixing processes and fuel distribution; however, since the injection generated turbulence has dissipated significantly prior to auto-ignition, it appears that the rate of energy release is dominated by chemistry effects, rather than turbulent transport. Furthermore, in contrast to the HTC-short ignition delay case, it appears that the mixing rate during combustion plays a minor role in sustaining the reaction.

3.2.4 Discussion

This section used a multi-mode combustion model to provide model validation over a range of combustion regimes. Comparisons were made between model predictions and optical diagnostic imaging from the literature [63]. It was found that the model was able to capture both the bulk combustion characteristics (e.g., AHRR) as well as details of the spray penetration, early stage reactions, and flame structure.

Comparisons of early stage combustion images showed that even for a diffusion flame combustion regime, ignition occurs in a region where the fuel and oxidizer are well-mixed. The level of pre-combustion mixing determines the flame lift off length and thickness of the diffusion flame. Even in conventional (HTC-short ignition delay) diesel combustion the ignition processes occurred in regions where the fuel and air were premixed. The following combustion process was then controlled by the large scale mixing and diffusion processes. In the limit of mixing controlled combustion (i.e., HTC-short ID), the reaction rate was controlled by the large scale transport of reactive mixture to the reaction zone. This gave the appearance of a thin diffusion flame on the outer edge of the spray plume.

As the pre-combustion mixing time increased, it was found that the diffusion flame became thicker. Once the ignition delay was increased past the end of injection, a diffusion flame was no longer observed and reaction was seen to occur completely across the jet cross section. In the limit of premixed combustion, it was found that the injection generated turbulence was dissipated significantly prior to auto-ignition; thus, the rate of energy release is dominated by chemistry effects, rather than turbulent transport.

It was found that the results were very similar with and without use of the flame propagation model. However, the simulations using the flame propagation model revealed details of the edge or triple-flame structure in the region surrounding the diffusion flame at the lift off location. These details were not captured by the purely kinetics based combustion model. However, they do not appear to significantly influence the bulk energy release rate.

The major conclusion of the model validation study is that flame structure is well predicted over the entire range from non-premixed to premixed combustion without the need to consider sub-grid scale turbulence chemistry interactions. Further, the similarity between results with and without consideration of flame propagation suggest that the chemistry-only model is sufficient to capture the bulk combustion characteristics. Thus, the preliminary CFD modeling will consider only the kinetics solution. Evaluation of the role of flame propagation in RCCI combustion will be discussed in Chapter 9.

Chapter 4

Preliminary RCCI Development using CFD Modeling

This chapter describes preliminary development of the RCCI combustion concept. It is split into three parts. In the first part, HCCI (kinetics) simulations are performed to select the optimal EGR and fuel blend at three operating conditions: 6, 9 and 11 bar IMEP. Although the exact operating conditions will be dependent on many parameters (e.g., intake temperature), the methods presented in this section have been shown to provide robust starting points for further optimization through CFD modeling and engine experiments. In the second section, a charge preparation study is performed to select an optimal injection strategy to create a well-mixed charge at the desired fuel reactivity for dual-fuel RCCI operation. In the third section, the results of the HCCI simulations and charge preparation optimization are combined to demonstrate RCCI operation using in-cylinder fuel blending.

4.1 Engine Specifications

A heavy-duty 2.44 L Caterpillar 3401 Single Cylinder Oil Test Engine (SCOTE) was used for all engine modeling and experiments in this chapter and Chapter 5. The engine geometry is given in Table 4-1 and the computational grid is shown in Figure 4-1.

Table 4-1. Specifications for the Caterpillar Single Cylinder Oil Test Engine (SCOTE) and specifications for the common-rail injector and port-fuel-injector (used in the engine experiments of Chapter 5) are also shown.

Base engine type	Caterpillar SCOTE
Bore x stroke	13.72 x 16.51cm
Connecting Rod Length	21.16 cm
Squish height	0.157 cm
Displacement	2.44 L
Geometric compression ratio	16.1:1
Effective compression ratio	9.1:1
Swirl ratio	0.7
Bowl type	"Mexican Hat"
Number of valves	4
Intake valve opening	-335° ATDC Firing
Intake valve closing	-85° and -143 ATDC Firing
Exhaust valve opening	130° ATDC Firing
Exhaust valve closing	-355° ATDC Firing
Common-Rail Injector Specifications	
Number of holes	6
Steady flow rate @100 bar	33.3 cc/sec
Hole diameter	250 µm
Included spray angle	145°
Port-Fuel-Injector Specifications	
Steady flow rate @ 3 bar	12.5 cc/sec
Included spray angle	15°
Fuel pressure	5.17 bar

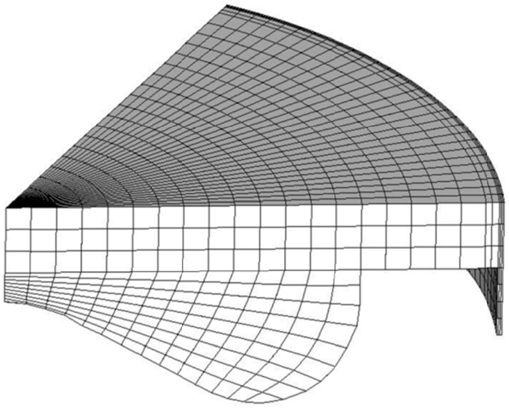

Figure 4-1. Computational grid showing the piston-bowl geometry of the Caterpillar SCOTE engine used in this study.

4.2 Preliminary Study to Select Baseline PRF and EGR as a Function of Load

In this section the KIVA-CHEMKIN code with the reduced primary reference fuel (PRF) mechanism was used to choose an optimized[2] fuel blend and EGR combination for PCI operation at three engine loads (6, 9, and 11 bar IMEP). The operating conditions for each load point are given in Table 4-2. A homogeneous mixture of the specified PRF blend, EGR (complete stoichiometric products (CSP) only), and air was assumed at intake valve closure and simulations were run from IVC to EVO. The design space was populated by varying EGR from 0% to 60% and the PRF number from 0 (neat n-heptane) to 100 (neat iso-octane).

Table 4-2. Engine operating conditions used to select baseline PRF and EGR at each load

Nominal IMEP (bar)	6	9	11
Engine speed (rev/min)	1300		
Intake temperature (°C)	32		
Intake pressure (bar)	1.38	1.74	2.0
Total fuel (mg/cycle)	67	94	128

Figure 4-2 shows the net indicated specific fuel consumption (ISFC)[3] and CA50 predictions at 6 bar IMEP. Several observations can be made from the results. At the 6 bar IMEP operating point, the minimum ISFC can be achieved for a range of PRF numbers from neat diesel to PRF 70. However, in order to phase combustion appropriately to retain a reasonable rate of pressure rise (shown by the points indicated with stars in Figure 4-2), the operating range is limited to fuels with PRF numbers ranging from 20 to 70. Further note the tradeoff between the fuel reactivity (i.e., PRF) and EGR levels required to achieve high-efficiency, low-pressure rise rate operation. The results suggest that, while highly efficient

---

[2] The presented fuel blends and EGR combinations will be dependent on the specific operating conditions (e.g., intake temperature); however, the methodology presented in this section has proven useful in selecting a baseline fuel distribution.

[3] Note that only the closed portion of the cycle was modeled. However, the pumping loop was taken from experiments at a similar operating condition such that the ISFC numbers can be compared to results from the literature.

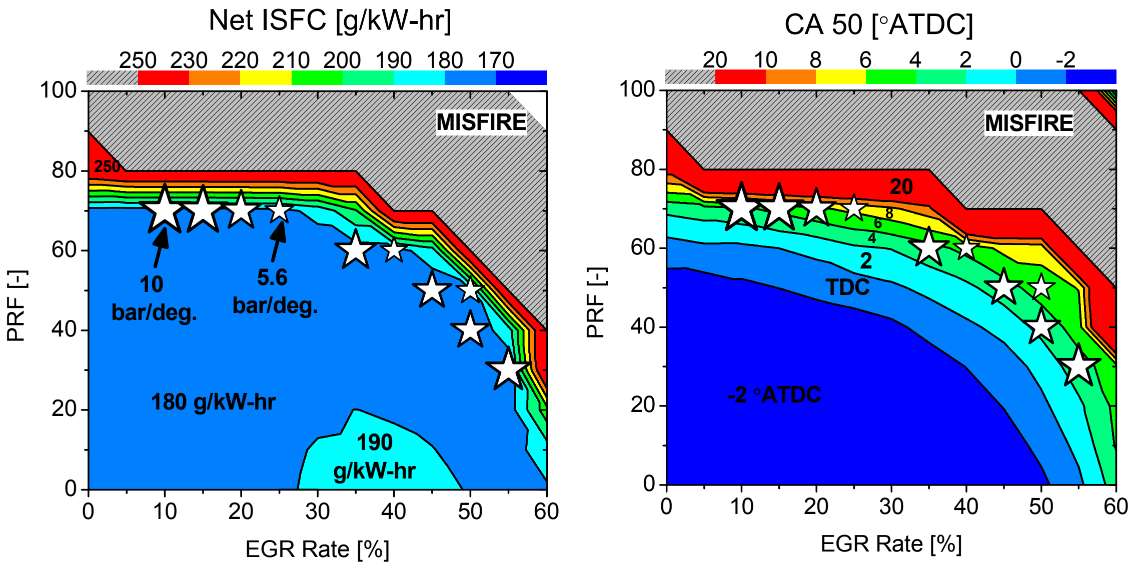

Figure 4-2. Predicted ISFC and CA50 contours as a function of fuel reactivity (PRF) and EGR level for operation at 6 bar IMEP and 1300 rev/min. Note the EGR considers only stoichiometric products and the ~4.4% residual are included in the presented EGR level [17].

HCCI operation at 6 bar IMEP is possible with neat diesel fuel, the EGR level must be near 50% to maintain acceptable combustion phasing such that the rate of pressure rise is reasonable. Of course, considering the work of Dec et al. [10], it may be possible to maintain acceptable pressure rise rate using partial fuel stratification (the effect of stratification is discussed in detail in Chapter 10). However, as the fuel reactivity is decreased, a reasonable pressure rise rate and optimal combustion phasing can be achieved with significantly less EGR. Thus, control over the fuel reactivity may significantly reduce the burden on the air handling system by allowing operation at lower EGR rates. Furthermore, the ability to operate at low EGR rates may be beneficial for combustion phasing control during transient LTC operation.

Figure 4-3 shows the fuel consumption and CA50 predictions at 9 bar IMEP. As the load is increased to 9 bar IMEP the minimum fuel consumption point moves to higher PRF blends (i.e., less reactive fuel). While the results suggest that the minimum fuel consumption can still

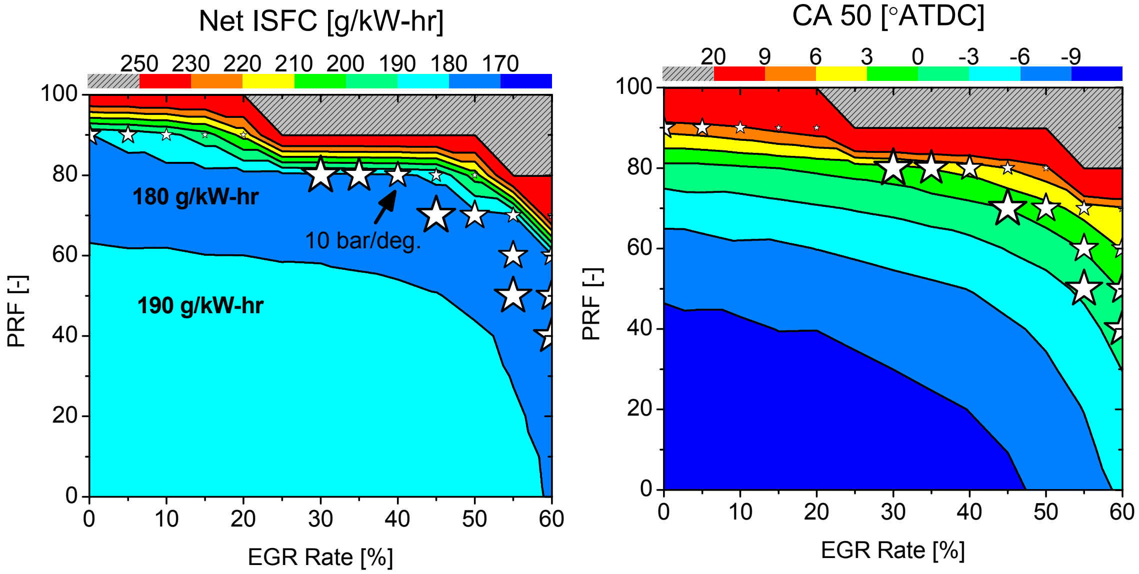

Figure 4-3. Predicted ISFC and CA50 contours as a function of fuel reactivity (PRF) and EGR level for operation at 9 bar IMEP and 1300 rev/min.

be achieved with neat diesel fuel (n-heptane in the simulations), the EGR level must be near 60%. As the load is increased to 9 bar IMEP, the contours shift toward higher PRF numbers in order to phase combustion after TDC. The contours of Figure 4-3 show that low ISFC can be achieved using PRF blends ranging from 60 to 90, depending on the EGR level.

Since the combustion process is kinetically controlled, the combustion phasing and fuel consumption are strongly influenced by intake temperature. To demonstrate this, the intake temperature was increased by 20 K and the simulations were repeated. Figure 4-4 shows the predicted ISFC and CA50 contours at 9 bar IMEP with the intake temperature increased by 20 K. Comparison of Figure 4-3 and Figure 4-4 shows that the optimal fuel blend shifts to higher PRF numbers or higher EGR rates. The band of minimum fuel consumption narrows slightly as the intake temperature is increased. However, the key observation from Figure 4-4 is that the minimum fuel consumption range is dominated by the combustion phasing. That is, the

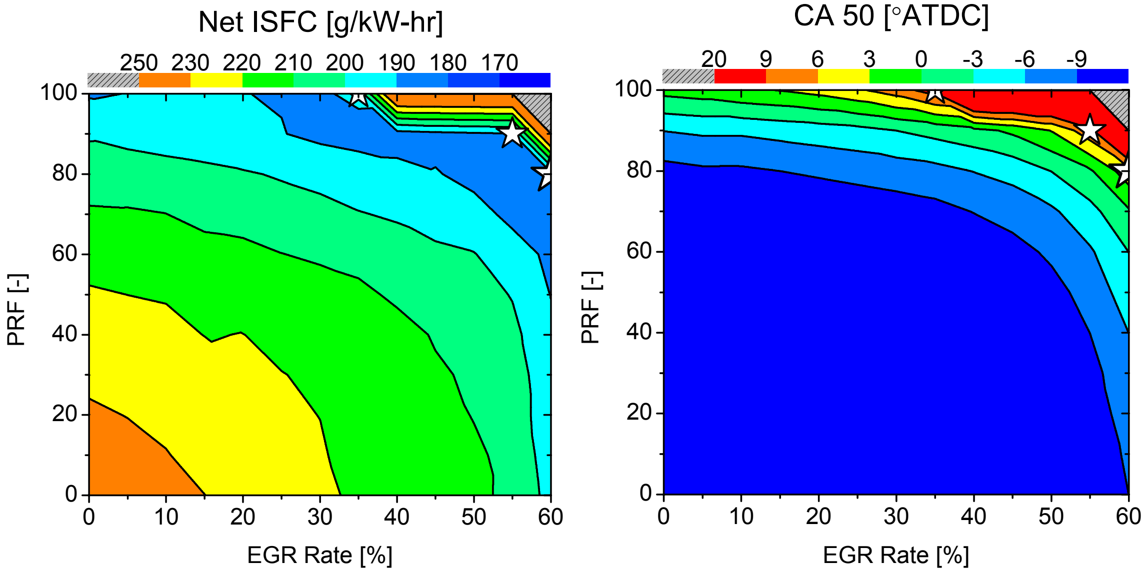

Figure 4-4. Predicted ISFC and CA50 contours as a function of fuel reactivity (PRF) and EGR level for operation at 9 bar IMEP and 1300 rev/min with the intake temperature set 20 K higher than the contours presented in Figure 4-3.

minimum fuel consumption for fully premixed operation at this speed-load point occurs near a CA50 of ~4° ATDC in both Figure 4-3 and Figure 4-4. The key benefit of the dual-fuel RCCI combustion process over a single-fuel HCCI process is the ability to control combustion phasing when the operating conditions change. In the present example, where intake temperature was changed by 20 K, the PRF number would need to be increased by ~20 PRF units to maintain constant combustion phasing. Of course this same control over combustion phasing could be achieved by adjusting the EGR level; however, in a production engine the response to a commanded increase in EGR level is slow (on the order of 20 cycles [89]). Conversely, the fuel blend can be changed on a cycle-to-cycle basis. It is this ability to control combustion phasing as the operating conditions change that makes the dual-fuel RCCI process attractive.

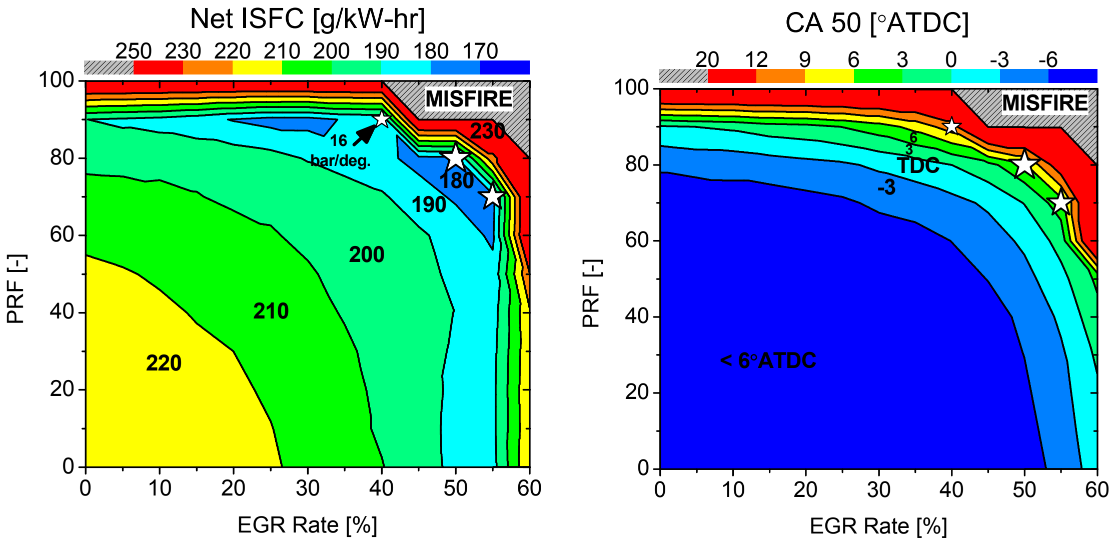

Figure 4-5. Predicted ISFC and CA50 contours as a function of fuel reactivity (PRF) and EGR level for operation at 11 bar IMEP and 1300 rev/min. [17].

Figure 4-5 shows the fuel consumption and CA50 predictions at 11 bar IMEP. At 11 bar IMEP, the minimum ISFC (corresponding to a CA50 of 6° ATDC) cannot be achieved with either neat diesel fuel or neat gasoline. Furthermore, as the load is increased, operation must be shifted to higher EGR levels in order to reduce the rate of heat release and meet the peak pressure rise rate constraint. Note that even with combustion phasing after TDC, the peak pressure rise rate was excessive (~20 to 30 bar/deg.) due to the volumetric heat release. This suggests that stratification is needed to control the rate of heat release.

4.3 Charge Preparation Optimization

The HCCI combustion study indicated that it is possible to improve fuel economy by optimizing the fuel blend for a specific operating condition. Accordingly, the next phase of the work focused on achieving a desired fuel blend by port-fuel-injection of gasoline and direct injection of diesel fuel. The 11 bar IMEP operating point was selected for the charge preparation study and a PRF number of 65 was used (i.e., 88 mg of gasoline was premixed and 47 mg of diesel fuel was direct-injected using the injector of Table 4-1). The KIVA-3v release 2 code was used for the spray simulations and was coupled with a multi-objective genetic algorithm (MOGA) for parameter optimization.

4.3.1 Charge Preparation Optimization Results

The charge preparation optimization considers only spray and mixing, that is, chemistry is not solved. Calculations were run from IVC to 10° BTDC (near ignition). To evaluate the effectiveness of each design, wall film levels and PRF number inhomogeneity were compared. The PRF number inhomogeneity is a mass weighted sum of the squared difference between the local (cell) and global PRF number and is defined as

$$NSD_{PRF} = \sqrt{\frac{\sum_{i=1}^{ncells}\left(m_i\left(PRF_i - PRF_{GLOBAL}\right)^2\right)}{PRF_{GLOBAL}\sum_{i=1}^{ncells} m_i}} \qquad \textbf{(4-1)}$$

,

where PRF_i and m_i are the fuel PRF number and mass in each computational cell, respectively. PRF_{GLOBAL} is the overall PRF number for the entire combustion chamber. Note that future sections will show that fuel reactivity stratification (i.e., PRF stratification) is an effective method of controlling the rate of heat release; however, the present optimization is an effective method to understand the factors controlling fuel reactivity stratification. Further, once an injection strategy is found that yields the most homogeneous charge, small parameter variations can be added that will increase the level of reactivity stratification. The optimal level of reactivity stratification will depend on operating conditions (e.g., load) and engine constraints (e.g., maximum allowable pressure rise rate). For example, light-load conditions may benefit from a nearly homogenous charge since the energy release rate is often low. However, as load is increased, additional fuel reactivity stratification is expected to broaden the combustion duration (i.e., reduce the pressure rise rate) and allow an expansion of the PCI combustion regime.

Table 4-3 shows the parameters and ranges of the charge preparation optimization study. This study considers the use of a variable pressure pulse (VPP) fuel system [16, 90] capable of switching between high and low injection pressures in a single cycle. With the use of this system, the optimization parameters are first and second pulse injection timing and pressure and the relative quantities of fuel in each pulse. The results of the optimization are shown in Figure 4-6. A case with minimum PRF inhomogeneity and very low wall film was selected for further analysis. The parameters of the selected case are representative of the Pareto solutions (see the box plot of Figure 4-7). Generally, the Pareto solutions used a low-pressure (100 to 200 bar) first injection between 57° and 70° BTDC with ~60% of the diesel fuel followed by a higher pressure (350 to 600 bar) second injection near 33° BTDC.

Table 4-3. Charge preparation optimization parameters and ranges.

SOI 1	-85 to (SOI2 – 20°)
SOI 2	-50 to -30 °ATDC
First pulse injection pressure	100 to 1500 bar
Second pulse injection pressure	100 to 1500 bar
Fraction of fuel in the first pulse	0 to 1

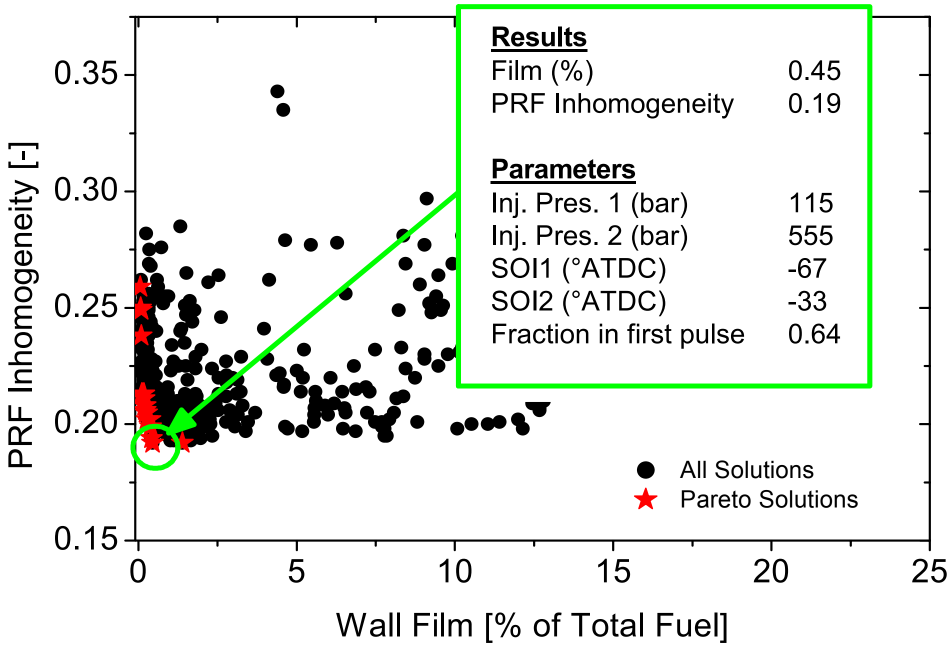

Figure 4-6. Charge preparation optimization results. The stars indicate Pareto solutions and the case selected for further analysis is designated with a circle. The results and parameters of the selected Pareto solution are also shown.

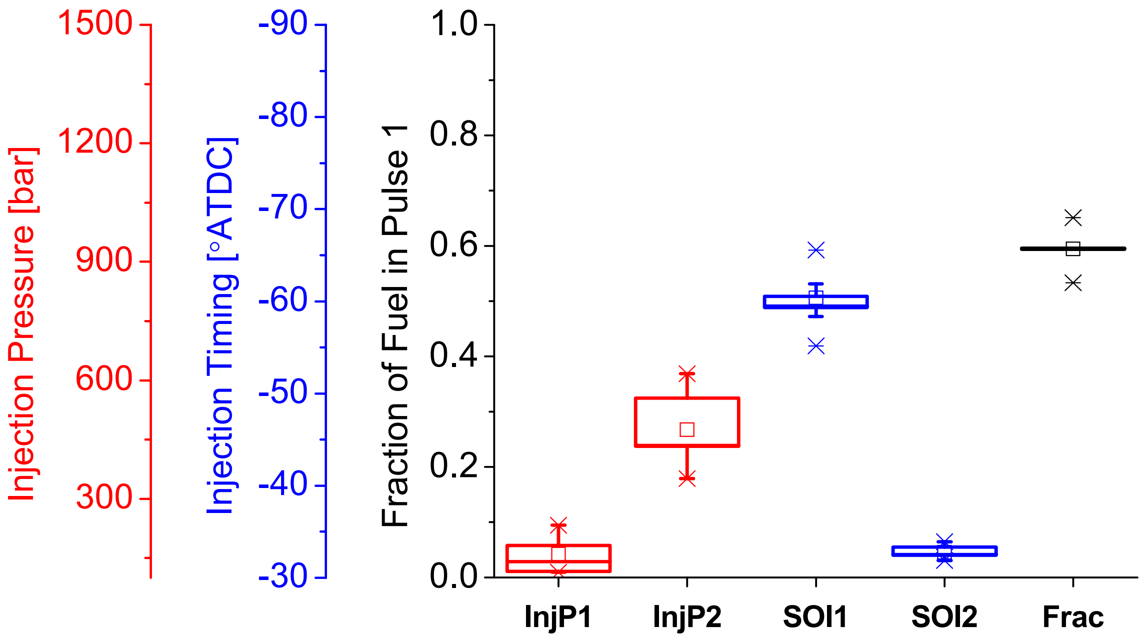

Figure 4-7. Box plot showing the distribution of parameters for the Pareto solutions.

The COmponent Selection and Smoothing Operator (COSSO) [91-95] technique was used to provide a quantitative interpretation of the effect of each design parameter. Using the COSSO technique with the selected design of Figure 4-6 as the center point, it was found that PRF inhomogeneity is mainly influenced by the fuel split and first pulse injection timing. Figure 4-8 shows the response surface of PRF inhomogeneity and wall film as a function of fuel split and first injection timing. These two parameters influence the distribution of the injected fuel (i.e., the split of fuel between the piston bowl and squish regions). To create a homogeneous charge the fuel must be optimally distributed between these two regions of the combustion chamber; thus, it is reasonable that fuel split and first pulse injection timing are key factors to minimize PRF inhomogeneity. Furthermore, it can be concluded that the choice of the range of second injection timing is responsible for the small impact of second injection timing on PRF inhomogeneity. Specifically, for the allowed second injection timings, the spray targeting is such that the majority of the fuel is directed into the piston bowl.

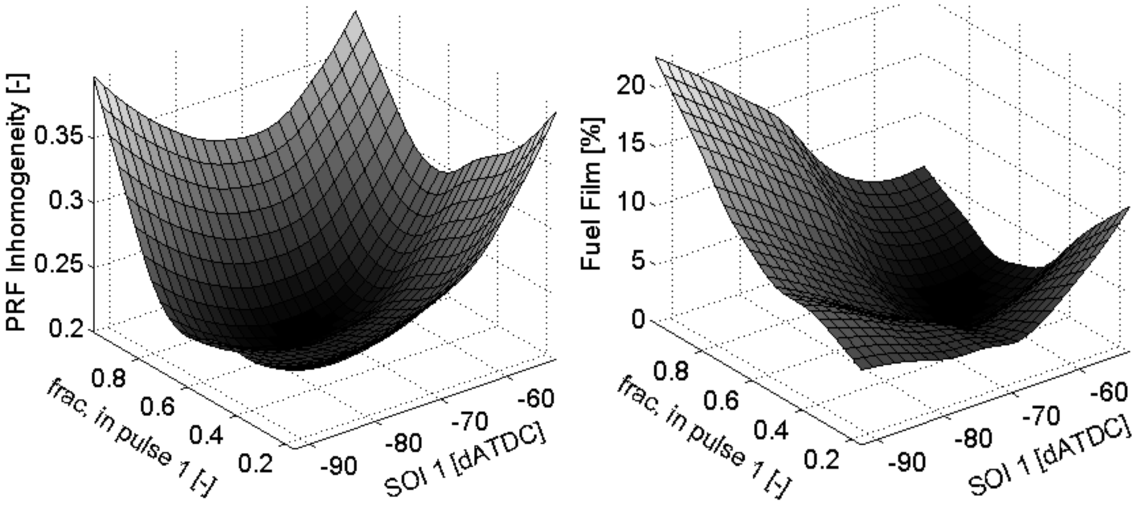

Figure 4-8. Response surfaces for PRF inhomogeneity and fuel film generated using the COSSO [91-95] **technique**

The response surfaces for fuel film suggest there are three controlling factors for wall film levels: first pulse injection pressure (not shown), first pulse injection timing, and fuel split. Because early cycle charge densities are low, long liquid lengths are observed and controlling the targeting and spray penetration becomes important. Consequently, the parameters of the first injection have the largest influence on fuel film levels. In this work, it is shown that appropriately combining, fuel split, injection pressure, and injection timing is essential to minimize wall film levels and create a well-mixed charge.

4.4 Combusting Case

To complete the preliminary RCCI development in the heavy-duty engine, the results of the HCCI simulations and spray optimization were extended to a closed cycle combustion analysis. Table 4-4 shows the parameters and results of the selected case of Figure 4-6. As can be seen, RCCI operation at an IMEP of 11 bar is achieved with near zero NOx emissions, the GIE is greater than 50% (gross ISFC ~160 g/kW-hr), and the pressure rise rate is at an acceptable value. The very low fuel consumption will be discussed after validation from engine experiments in the next chapter.

Table 4-4. Parameters and results of spray and combustion study at 11 bar IMEP and 1300 rev/min. The GIE was calculated using the simulated pressure trace combined with the open portion of the cycle obtained from experimental data at a similar condition.

Parameters							Results			
PRF (-)	EGR (%)	Inj. P1 (bar)	Inj. P2 (bar)	SOI 1 (°ATDC)	SOI 2 (°ATDC)	Fract. (-)	NOx (g/kW-hr)	Soot (g/kW-hr)	PRR (bar/deg.)	GIE (%)
65	50	115	555	-67	-33	0.64	0.02	0.36	7.7	51.3

4.5 Discussion

This chapter has highlighted the development of a dual-fuel premixed compression ignition concept and proposed a simple method to select a fuel blend, EGR rate, and injection strategy. Although the specific fuel blends and EGR requirements will change with operating condition, the methods presented in this chapter have proven to be a robust starting point for further optimization. The next three chapters discuss application of RCCI combustion to a range of conditions in two different engines. In all cases, the knowledge gained in this preliminary development is used as a starting point.

Chapter 5

Experimental Validation of RCCI Operation and Analysis Using CFD Modeling

Chapter 4 highlighted the development of the RCCI combustion process using CFD modeling. It was found that the improved control over the combustion phasing resulted in very low fuel consumption and near zero NOx emissions. In this chapter, the model predictions are validated by heavy-duty metal engine experiments performed by Hanson et al. [96] and Splitter et al. [97].

First, the CFD predictions are validated by comparisons to the measured cylinder pressure and AHRR over a range of conditions. The CFD predictions are then used to offer a hypothesis of the in-cylinder processes controlling RCCI combustion (this hypothesis will be validated using optical engine experiments in Chapter 9). Next, the measured and predicted emissions and performance are compared and the CFD modeling is used explain the trends in the measurements. After that, a selected RCCI case is compared to conventional diesel operation and the performance benefits and drawbacks of RCCI combustion are discussed. Finally, the KIVA-code is used to highlight the parameters controlling RCCI combustion.

5.1 Operating Conditions

The results presented here are a combination of the highest efficiency cases from a number of different experiments; thus, the engine parameters and operating variables are not fixed over the load sweep. Further, note that to accommodate concurrent research projects, the 4.6 bar IMEP case uses a slightly modified piston from that shown in Figure 4-1 with a compression ratio of 15.5:1. This slight change in compression ratio is not expected to significantly influence the results. Table 5-1 shows the operating conditions over the range of loads considered in this work. Gasoline was delivered through an automotive-type port-fuel-injector (PFI) with specifications given in Table 4-1. The diesel was delivered through a centrally mounted common-rail injector discussed in Table 4-1. Although, the computational charge preparation study used a variable pressure pulse injection system, capable of delivering

Table 5-1. Operating conditions for dual-fuel RCCI load sweep from 4.6 to 14.6 bar IMEPg. The engine experiments were performed by Hanson et al. [96] and Splitter et al. [97]. The load sweep was compiled by the author to show the peak efficiency operating conditions over a range of loads. The Fuel/Air ϕ is defined as the stoichiometric air-fuel ratio divided by the air-fuel ratio based on fresh air and the Fuel/Charge ϕ is defined as the stoichiometric air-fuel ratio divided by the air-fuel ratio based on total intake charge (i.e., air + EGR).

IMEP gross (bar)	4.6	5.9	9.3	11.6	14.6
Engine speed (rev/min)	1300				
Fuel flowrate (g/s)	0.57	0.71	1.02	1.36	1.74
Percent gasoline (% by mass)	48	69	89	85	90
Diesel SOI 1 (°ATDC)	-62	-63	-58	-67	-58
Diesel SOI 2 (°ATDC)	-37	-34	-37	-36	-37
DI fuel in pulse 1 (% by mass)	65	32	67	68	37
DI injection Pressure (bar)	400	600	800	800	800
Intake surge tank pressure (bar abs.)	1.03	1.38	1.74	2.00	2.34
Exhaust surge tank pressure (bar abs.)	1.10	1.45	1.84	2.13	2.52
Intake surge tank temperature (deg. C)	32	36	32	32	32
Air fuel ratio (-)	45.4	40.9	29.0	19.1	15.1
Fuel/Air ϕ	0.33	0.36	0.51	0.77	0.98
Fuel/Charge ϕ	0.33	0.31	0.36	0.53	0.62
EGR rate (%)	0	17	41	46	57

multiple pulses in a single engine cycle (which was not available at the time of the experiments), the resulting injection scheme was used as the baseline for the present study – that is, a split injection strategy with a first injection near 60° BTDC with ~60% of the diesel fuel followed by a second injection near 33° BTDC. Because a single injection pressure was used (rather than the VPP system), slight modifications were made to the injection parameters. The fuel reactivities (i.e., the fraction of gasoline) were chosen based on the previous investigation, but were fine-tuned to minimize fuel consumption.

5.2 Validation of Model Predictions and Description of RCCI Combustion Process using CFD Modeling

Figure 5-1 shows the measured and predicted cylinder pressure and AHRR over the load sweep. It can be seen that the simulations are able to accurately capture the combustion characteristics over the range of loads considered in this work without considering flame propagation. Additional model validation can be found in the author's work (e.g., Refs. [16-18, 20, 21, 61, 62, 98-100]). The experiments show that dual-fuel RCCI operation is possible over a range of conditions. Further, notice that even at the 14.6 bar IMEP operating point, the pressure rise rate is maintained at an acceptable level and the combustion duration is much longer than would be expected for typical highly premixed operation.

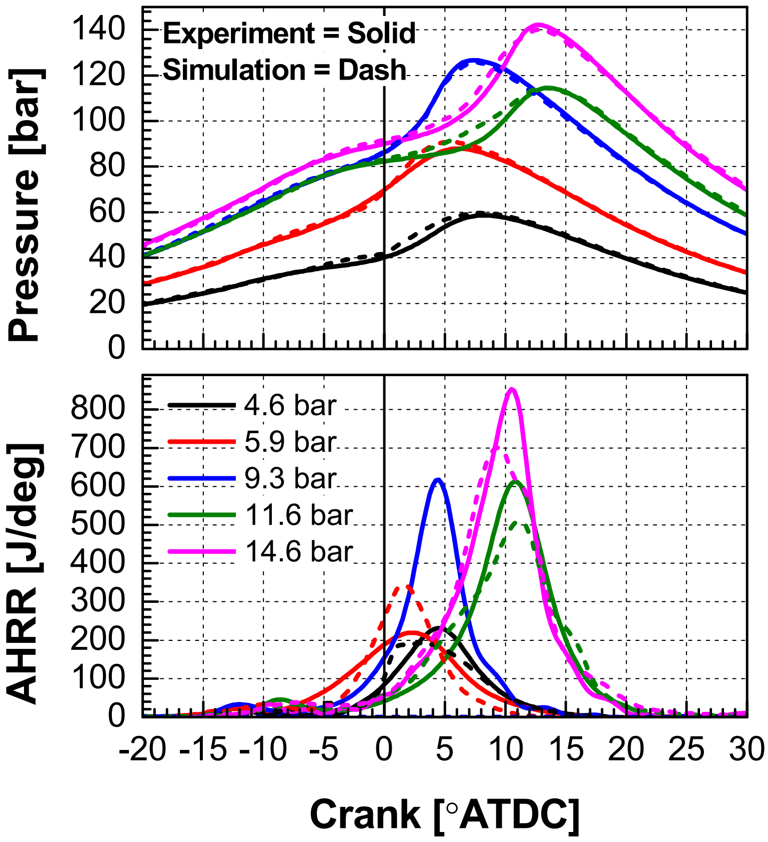

Figure 5-1. Comparison of measured and predicted cylinder pressure and AHRR over the load range from 4.6 to 14.6 bar IMEP. The experimental pressure and AHRR traces are shown in solid lines and the simulation results are shown in the dashed curves [61].

5.2.1 Description of RCCI Combustion Process Based on CFD Modeling Results

The modeling results are used to help explain the observed extended heat release. Figure 5-2 shows the evolution of several key species as predicted by the models. The first observation that can be made from Figure 5-2 is that n-heptane is consumed significantly earlier in the cycle than iso-octane (notice that by 5 °BTDC n-heptane has been reduced by nearly an order of magnitude, but iso-octane remains near its IVC concentration). The consumption of n-heptane also appears to coincide with the appearance of formaldehyde (CH_2O). Formaldehyde consumption and OH accumulation (i.e., a transition from thermal preparation to thermal ignition of the n-heptane) appears to track with iso-octane consumption. This suggests that significant

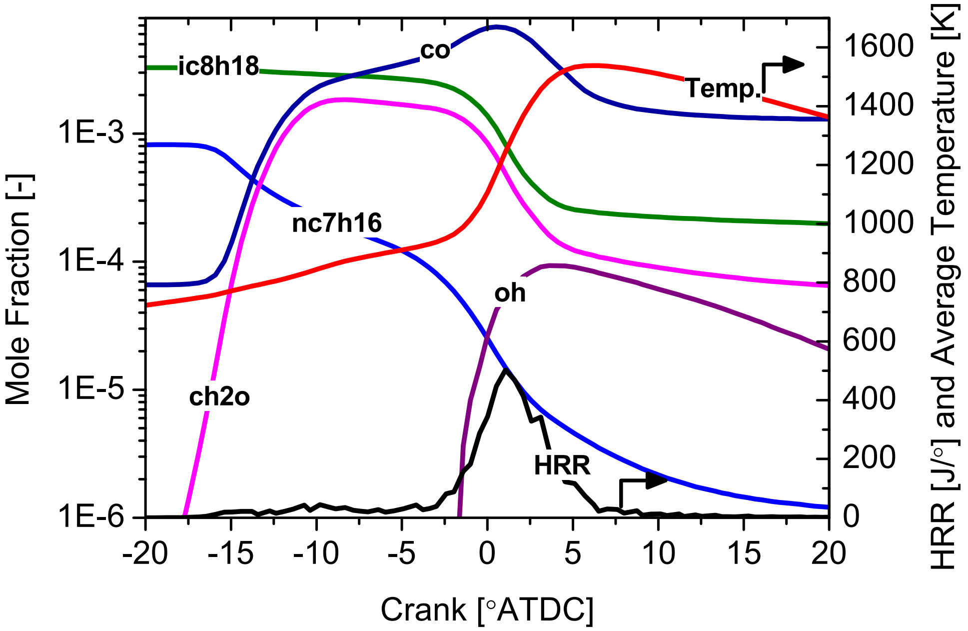

Figure 5-2. In-cylinder evolution of several key species for dual-fuel PCCI operation at 6 bar IMEP. Note that the mole fraction data are presented on a log scale to show minor species. Also shown are the heat release rate and the average temperature [17].

iso-octane consumption does not occur until thermal ignition of the n-heptane is reached. Once thermal ignition of the n-heptane is reached, CO oxidation begins, energy is released, cylinder temperatures rise, and fuel series reactions of iso-octane accelerate. The results of Figure 5-2 suggest the extended heat release is due to a staged consumption of the more reactive diesel fuel followed by the less reactive gasoline.

To further understand the staged consumption of the less reactive iso-octane (gasoline) and more reactive n-heptane (diesel fuel), in cylinder images from the modeling work are presented. Figure 5-3 shows cut planes coincident with the spray axis colored by temperature, mass fraction of n-heptane, mass fraction of iso-octane, mass fraction of formaldehyde, and mass fraction of OH. At -14° ATDC n-heptane begins to be consumed and lower carbon number species are formed. The temperature is ~770 K. By -10° ATDC a significant amount of the n-

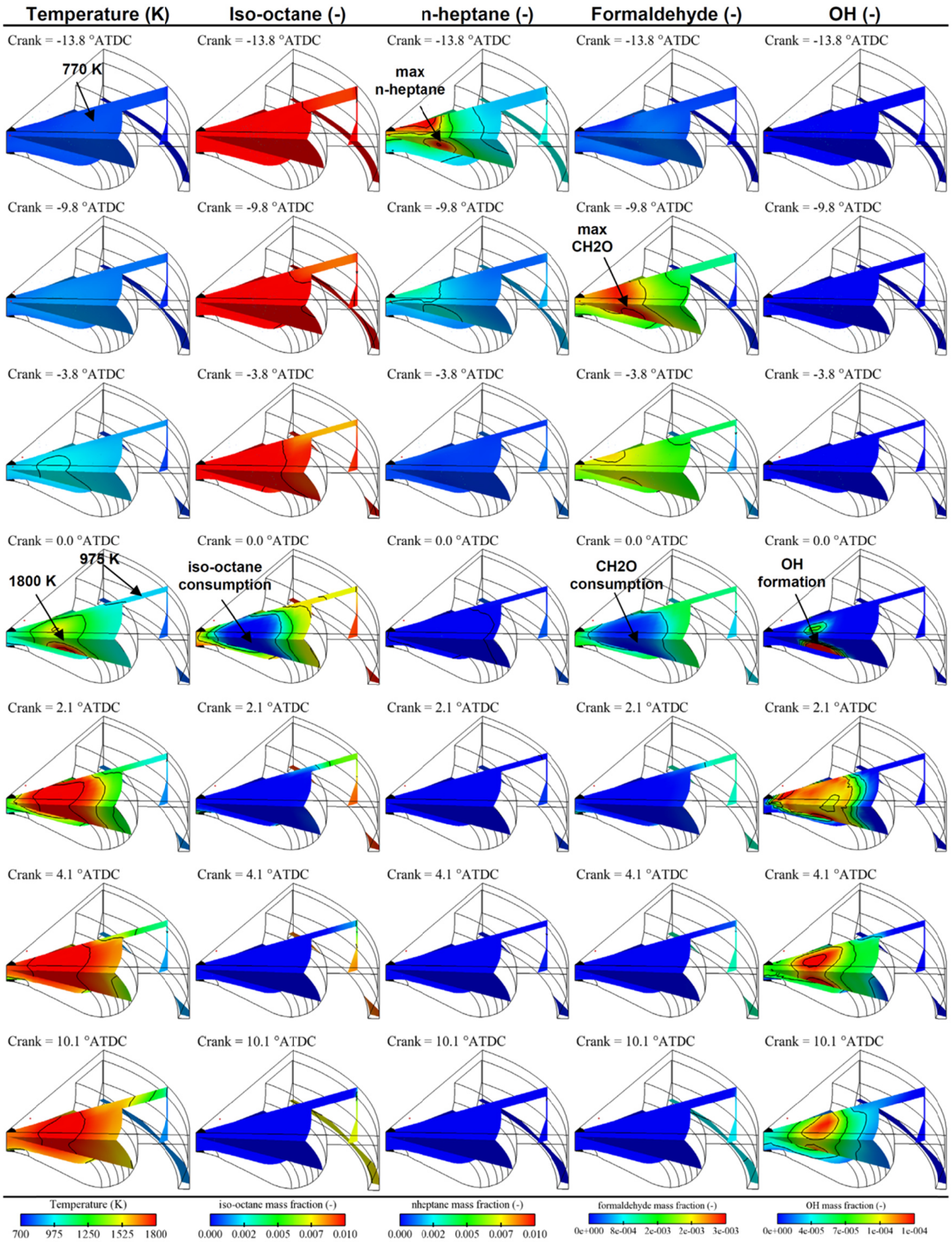

Figure 5-3. Cut planes coincident with the spray axis colored by temperature, mass fraction of n-heptane, mass fraction of iso-octane, mass fraction of formaldehyde, and mass fraction of OH for dual-fuel RCCI operation at 6 bar IMEP [17].

heptane has been consumed and formaldehyde has been formed through fuel fragmenting reactions. At this point, the temperature is ~800 K. Notice the similarity in locations of the highest concentration of formaldehyde at -10° ATDC and n-heptane at -14° ATDC. By -4° ATDC the temperature is ~920 K, formaldehyde consumption is taking place. Note that very little iso-octane has been consumed by this point. Thus, it is thought that most of the intermediates are the result of n-heptane decomposition. At TDC, OH appears near the locations of the highest n-heptane concentration in earlier images (e.g., -14° ATDC) and high temperature reactions begin. At this point, consumption of iso-octane begins and by 4° ATDC nearly all of the iso-octane has been consumed. Figure 5-3 suggests that spatial stratification in the fuel reactivity is a dominant factor controlling the energy release of dual-fuel RCCI. That is, ignition occurs in the most reactive region of the chamber and the charge is sequentially consumed from more-to-less reactive regions.

5.2.2 RCCI Emissions and Performance

Figure 5-4 shows the measured and predicted emissions and performance over the range of loads. In Figure 5-4 NOx and soot are shown on a gross indicated basis. The gross indicated efficiency is defined as the (gross-indicated-work)/(fuel energy). Because the engine operates under boosted condition for all but the lightest load, the peak pressure rise rate (PRR) is not representative of knock [101]; therefore, the ringing intensity (RI) correlation of Eng [102] is used

$$RI = \frac{1}{2\gamma}\frac{\left(0.05\left(dP/dt\right)_{\max}\right)^2}{P_{\max}}\sqrt{\gamma R T_{\max}} \qquad \textbf{(5-1)}$$

,

where γ is the ratio of specific heats, $(dP/dt)_{max}$ is the peak pressure rise rate, P_{max} is the peak pressure, R is the ideal gas constant, and T_{max} is the peak temperature. In a similar engine, Dec

[101] stated that ringing intensities below 5 MW/m^2 resulted in acceptable combustion noise and knock free operation; thus, in this work 5 MW/m^2 is used as an upper limit for acceptable combustion noise. Also shown in Figure 5-4 are the United States (US) 2010 Environmental Protection Agency's (EPA) heavy-duty (HD) on-highway truck limits [103] for NOx and soot emissions (i.e., 0.268 g/kW-hr and 0.0134 g/kW-hr for NOx and soot, respectively).

Consistent with the simulation results presented in Chapter 4, the measured NOx is near

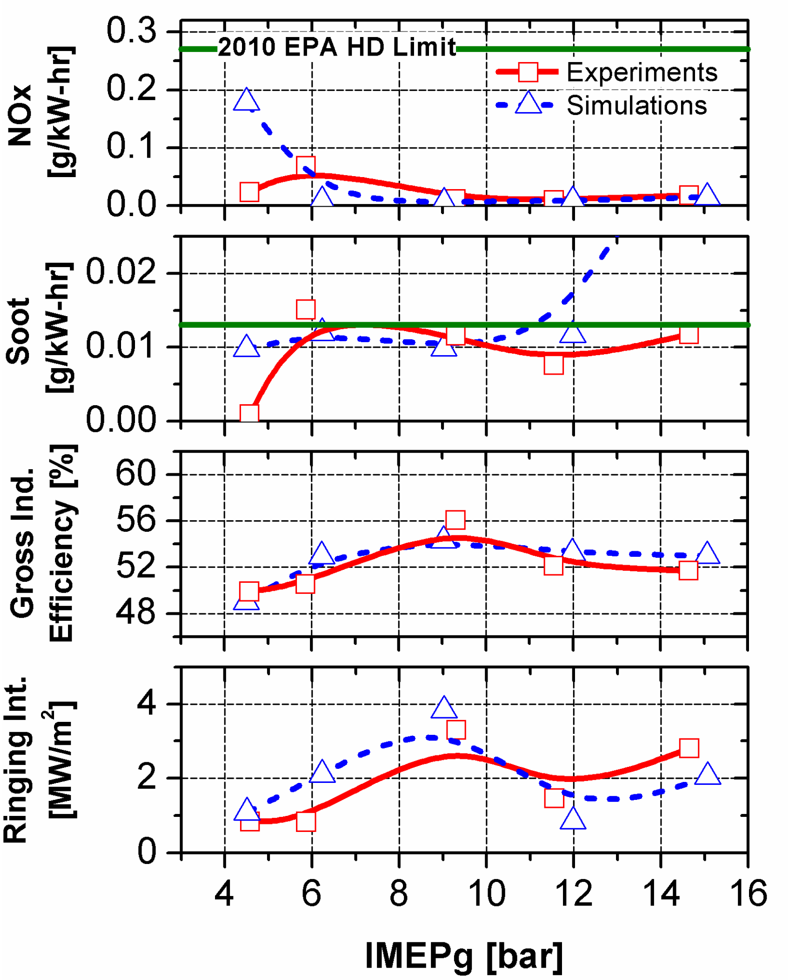

Figure 5-4. Emissions and performance of dual-fuel RCCI over a range of loads from 4.6 to 14.6 bar IMEP. The solid green horizontal lines show the US 2010 environmental protection agency's (EPA) on-highway truck emissions limits for NOx and soot [61].

zero and significantly below the 2010 EPA HD limits. Furthermore, it can be seen that soot is extremely low and below the 2010 EPA HD limits for all but the 6 bar IMEP point, which is very near the limit. It is possible that slight modifications to the operating parameters could be explored that would result in passing soot over the load sweep; however, even with the current soot levels, it can be seen that dual-fuel RCCI combustion is a promising technique to meet the stringent emissions regulations without the need for NOx aftertreatment. Further, since soot is extremely low, if a DPF were required, the time between regenerations could be significantly extended compared to higher sooting operation.

It can be seen that the gross indicated efficiency is ~49% at the low load condition, peaks at ~56% at 9.3 bar IMEP, and levels out near 52% for the higher loads. It should be noted that the most optimization has been conducted at the 9.3 bar IMEP operating point, which is likely part of the reason for the peak in the fuel efficiency at this point. However, it is still informative to investigate the fuel efficiency trends over the load sweep. Figure 5-5 shows the energy balances for each case. The gross indicated efficiency is calculated as the (gross work)/(fuel energy). The combustion losses are calculated as

$$\eta_{\substack{\text{comb}\\\text{loss}}} = \frac{\dot{m}_{CO} LHV_{CO} + \dot{m}_{HC} LHV_{fuel}}{\dot{m}_{fuel} LHV_{fuel}}, \qquad \textbf{(5-2)}$$

where $\dot{m}_{CO}$ and $\dot{m}_{HC}$ are the measured exhaust mass flowrates of CO and UHC, respectively. LHV_{CO} and LHV_{fuel} are the lower heating values of the CO and fuel, respectively. Here it is assumed that the unburned hydrocarbons have the same heating value as the fuel blend. The exhaust energy is calculated from the measured exhaust temperature as

$$\eta_{exhaust} = \frac{\dot{m}_{exh}\left(h_{exh}\left(T_{exh}\right) - h_{\text{int}}\left(T_{\text{int}}\right)\right)}{\dot{m}_{fuel} LHV_{fuel}}, \qquad \textbf{(5-3)}$$

where $\dot{m}_{exh}$ is the mass flowrate of the exhaust, h_{exh} and h_{int} are the exhaust and intake enthalpies evaluated using the NASA database [104] assuming the exhaust contains only O_2, N_2, CO_2, H_2O, CO, UHC, and NO. Note that all species except UHC were measured on a dry basis; thus, the water concentration in the exhaust stream was solved for using atom balances. The heat loss contains the contributions of losses to the coolant, oil, and ambient and was solved for using an energy balance with the EGR loop located outside of the control volume; thus, the exhaust energy contribution contains heat rejected in the EGR heat exchanger.

Starting with the peak efficiency point (i.e., 9.3 bar IMEP), it can be seen that as the load is decreased, the heat transfer and combustion losses increase; however, the exhaust losses decrease, nearly cancelling out the increase in heat transfer losses. Thus, it can be seen that the

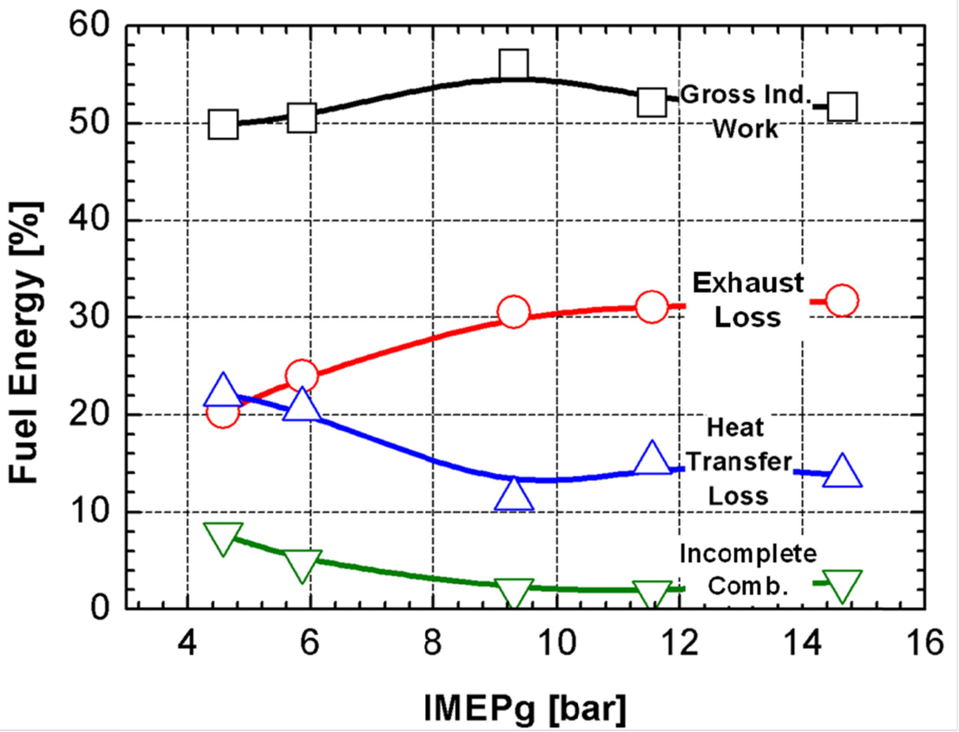

Figure 5-5. Flow of fuel energy over the load sweep for heavy-duty RCCI combustion [61].

main cause of the reduced efficiency at the lightest loads is the reduced combustion efficiency. Further, as the load is increased past the peak efficiency point, the engine begins to approach stoichiometric operation (see Table 5-1); and thus it appears that the slight reduction in fuel consumption is also due to increased incomplete combustion losses.

Comparing the model predicted and measured values in Figure 5-4, it can be seen that, similar to the combustion characteristics, the models do a reasonable job capturing the emissions and engine performance over the load sweep. Notice that, at the 4.6 bar IMEP condition NOx is over predicted by the model, but for the remainder of the load sweep NOx is predicted reasonably well. It should also be noted that for these cases both the measured and predicted NOx levels are very low; thus slight differences are not of significant concern. Comparing the measured and predicted soot emissions it can be seen that the models do a reasonable job capturing the soot trends; however, soot is significantly over predicted at the 14.6 bar IMEP operating point. It should be noted that the soot model constants were held fixed over the load sweep (i.e., no attempts were made to "tune" the soot model to each specific operating condition). Recall that the 14.6 bar IMEP operation point is near stoichiometric (see Table 5-1) and some portions of the combustion chamber undergo slightly rich combustion. The over prediction of soot as rich combustion is encountered may suggest that different soot model constants are required for rich and lean combustion. However, since the primary focus of this work is fuel consumption, adjustments to the soot model parameters were not explored during this study (i.e., the soot model constants shown in Table 3-1 were used). More importantly in the scope of this work, it can be seen that both the trends and magnitudes of the gross indicated efficiencies are captured well by the models. Furthermore, because pressure rise rate and combustion noise are a major limiting factor for premixed operation, it is important to note that the simulations do an excellent job capturing both the trends and magnitudes of the ringing intensity.

Because the simulations reproduce the experimental results well and it appears that combustion efficiency dominates the gross indicated efficiency trend, the simulations are used to understand the combustion efficiency trends observed in Figure 5-5. Figure 5-6 shows iso-volumes of UHC and CO for the 4.6, 9.3, and 14.6 bar IMEP cases at a crank angle of 40° ATDC. It can be seen that at the light load condition UHC is found in both the centerline (i.e., cylinder symmetry axis) and crevice regions. For this case CO is primarily found in the centerline region. The centerline UHC and CO is due to an overly lean region which does not release enough energy to completely oxidize the CO and UHC. Moving to the 9.3 bar IMEP case it can be seen that UHC is only located in the crevice region and CO is only located in the region near the cylinder liner. The UHC in the crevice region is primarily unreacted iso-octane (gasoline) resulting from the premixed charge. The CO in the near liner region is due to relatively low temperatures due to heat transfer from the gas to the cylinder liner. Additionally, as the crevice region outgasses late in the cycle, some UHC is converted to CO; however, temperatures fall rapidly and the CO in this region is not oxidized to CO_2. Finally moving to the 14.6 bar IMEP case it can be seen that, similar to the 9.3 bar IMEP case, UHC is found only in the crevice region. However, in this case it can be seen that CO is present both in the near liner region and the centerline. Similar to the 9.3 bar IMEP case, the CO near the liner is likely due to a combination of crevice out gassing and heat transfer from the fluid resulting in low reaction rates. In this case, the centerline CO is not the result of overly lean regions, but rather locally

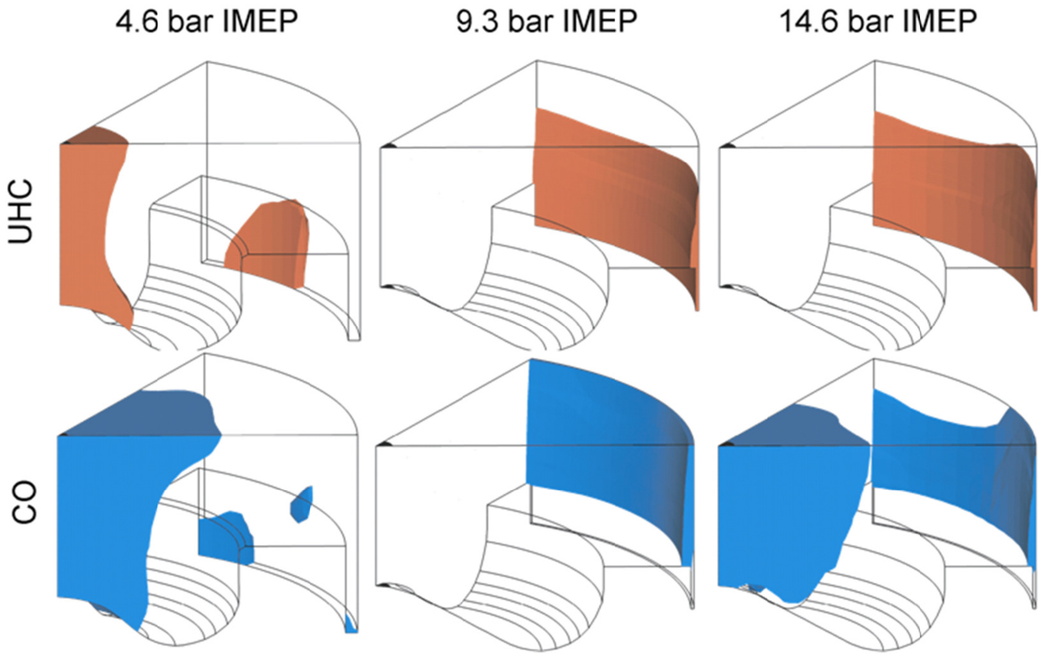

Figure 5-6. Iso-volumes showing regions with mass fractions of UHC (top) and CO (bottom) greater than 4000 ppm [61].

rich regions created by the direct injection event. Recall that for this case operation occurs only slightly lean of stoichiometric (equivalence ratio of ~0.98), thus due to the direct injection event, some regions of the combustion chamber undergo rich combustion and insufficient oxygen is available to completely oxidize the CO.

Considering Figure 5-6, the trend in combustion efficiency and gross indicated efficiency is clear. At the lightest loads operation borders on the lean limit for the premixed gasoline and complete oxidation of UHC and CO is difficult. At higher engine loads, as stoichiometric operation is approached, the direct injection event must be carefully controlled to avoid rich regions and incomplete combustion due to insufficient oxygen. Note that it is likely that at the highest engine loads the UHC and CO emissions could be reduced by increasing the boost pressure to eliminate the regions undergoing rich combustion. However, this has not been explored at this time. Finally, the peak in gross indicated efficiency and combustion efficiency at 9.3 bar IMEP is the result of operation avoiding both the lean and rich oxidation limits.

5.3 Comparison of Conventional Diesel and RCCI Combustion in a Heavy-duty Engine

5.3.1 Model validation for conventional diesel and RCCI operation

The previous sections demonstrated the RCCI combustion strategy over a range conditions and suggested that in-cylinder fuel blending offers efficiency advantages. To gauge the emissions and performance benefits of RCCI, comparisons are made to conventional diesel combustion (CDC). First, to ensure the CFD models accurately capture the emissions and performance of CDC operation, model predicted emissions and performance are compared to engine experiments from the literature. The conventional diesel case was taken from the experiments of Tess [105] and were performed in the same engine used for the RCCI experiments. The CFD modeling is used to explain the differences in emissions and performance of RCCI and CDC combustion. Finally, to ensure the initial conditions do not influence the results of the study, RCCI and CDC are compared (using CFD modeling only) at identical initial conditions.

5.3.1.1 Operating Conditions

The operating conditions for both cases are shown in Table 5-2. Note that the RCCI case is the same as the 9.3 bar IMEP case presented in Table 5-1; however, it is repeated here to facilitate comparisons with the CDC case. Tess' [105] CDC experiments were performed using the same engine discussed in the previous section (engine specifications are given in Table 4-1). However, the conventional diesel case was operated at a slightly lower speed than the RCCI case. The conventional diesel case uses a single direct-injection at -10° ATDC with an injection

Table 5-2. Operating conditions for model validation experiments.

	RCCI	Conv. Diesel
IMEP gross (bar)	9.3	9.9
Engine speed (rev/min)	1300	1208
Fuel flowrate (g/s)	1.02	1.19
Percent gasoline (% by mass)	89	0
Air flowrate (kg/s)	0.03	0.042
DI SOI 1 (°ATDC)	-58	-10
DI SOI 2 (°ATDC)	-37	NA
DI duration 1 (CA°)	3.9	22
DI duration 2 (CA°)	1.95	NA
DI fuel in pulse 1 (% by mass)	67	1
DI injection Pressure (bar)	800	755
Intake surge tank pressure (bar)	1.74	1.72
Exhaust surge tank pressure (bar)	1.84	1.83
Intake surge tank temp. (deg C)	32	36
Air fuel ratio (-)	29	36
Fuel/Air ϕ	0.51	0.41
Fuel/Charge ϕ	0.36	0.41
EGR rate (%)	41	0
Fuel MEP[4] (bar)	16.6	20.5
IVC (°ATDC)	-143	-143
EVO (°ATDC)	130	130

pressure of 755 bar. The conventional diesel case did not use EGR and, similar to the RCCI case, the intake pressure was near 1.7 bar absolute.

5.3.1.2 Results

Figure 5-7 shows a comparison of the measured and predicted cylinder pressure and apparent heat release rate (AHRR) for conventional and RCCI combustion. The comparison of measured and predicted emissions and performance is shown in Table 5-3. The same spray model constants and chemical kinetics mechanism were used to model both the conventional

---

[4] The fuel mean effective pressure (MEP) is defined as the fuel energy divided by the displacement (i.e., $\text{Fuel MEP} = m_{fuel} LHV_{fuel} / V_D$). This normalization facilitates comparisons of the fuel flowrates from engines of different displacements.

diesel and RCCI combustion cases. However, as discussed in the model description section, different soot model constants are required for RCCI and CDC combustion. Aside from the soot prediction, the models used in this study are capable of capturing the combustion characteristics over a wide range of operating conditions from the low-temperature combustion, dual-fuel RCCI mode to the high-temperature, mixing controlled conventional diesel mode without tuning model constants. The ability to capture the combustion characteristics over this range of conditions suggests that the physical models implemented in the KIVA-CHEMKIN code are adequately capturing the most dominant physical processes.

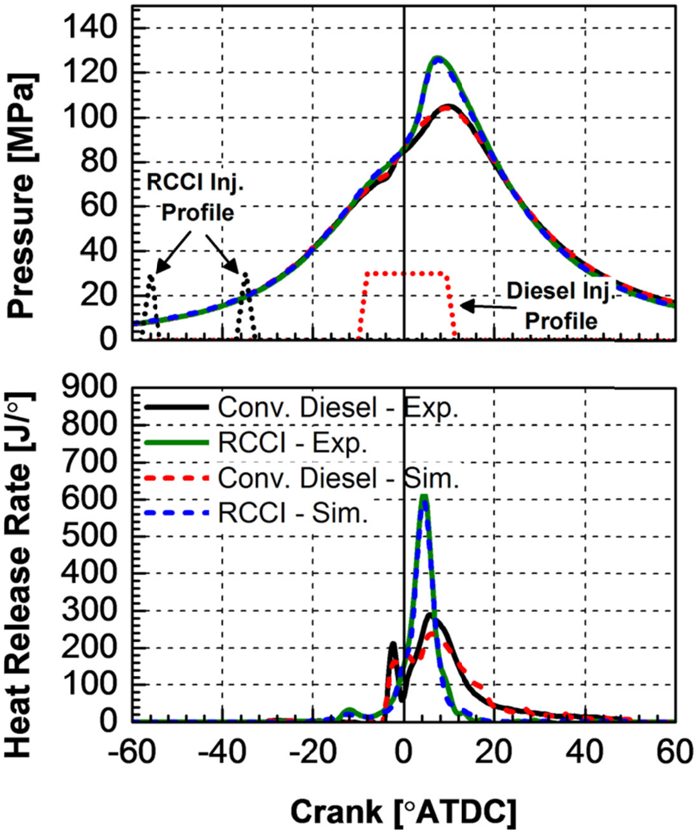

Figure 5-7. Measured and predicted cylinder pressure and apparent heat release rates for conventional diesel and RCCI [61].

As seen in Table 5-3, compared to conventional diesel combustion, RCCI demonstrates 3 orders of magnitude lower NOx emissions, a factor of 6 lower soot emissions, and 16.4 percent higher gross indicated efficiency (i.e., the RCCI case converts 7.9 percent more of the fuel energy to work). However, RCCI combustion shows increased rates of pressure rise, ringing intensity, and incomplete combustion losses (i.e., increased UHC and CO). However, it can be seen that the ringing intensity is well below the value of 5 MW/m^2 suggested as an upper limit by Dec et al. [101]. Additionally, model results show that, at this condition, nearly all of the UHC emissions result from the relatively large ring-pack crevice volume and UHC reductions may be possible through improved ring pack design. More discussion of the effect of ring-pack crevice volume size can be found in Splitter et al. [106].

Table 5-3. Emissions and performance of RCCI and conventional diesel combustion.

	RCCI		Conv. Diesel	
	Exp.	Sim.	Exp.	Sim.
ISNOx (g/kW-hr)	0.011	0.006	10	9.2
ISsoot (g/kW-hr)	0.012	0.019	0.076	0.133
Ringing Int. (MW/m^2)	3.3	3.8	0.9	1
Max PRR (bar/deg)	9.7	10.3	4.9	5.2
GIE (%)	56.1	54.3	48.2	47.6
Incomplete Comb. (%)	2	1.3	0.1	0.3

5.3.2 Comparison of High-EGR Diesel and RCCI Combustion

Although the model validation experiments show that, compared to conventional diesel operation without EGR, RCCI operation offers significant reductions in NOx and soot emissions and improved gross indicated efficiency, the experiments were conducted at slightly different conditions. Further, mid-load operation without EGR is not representative of current engine configurations. To ensure that the comparison of RCCI combustion and conventional diesel combustion was not biased due to differences in initial conditions, CFD modeling was used to compare RCCI combustion and conventional diesel combustion at the same operating conditions. The operating conditions for the modeling study are provided in Table 5-4.

Table 5-4. Operating conditions for the comparison between high-EGR diesel and RCCI combustion.

	RCCI	High-EGR Diesel
IMEP gross (bar)	9.3	8
Engine speed (rev/min)	1300	
Fuel flowrate (g/s)	1.02	
Gasoline mass (%)	89	0
Air flowrate (kg/s)	0.03	
DI SOI 1 (°ATDC)	-58	-20 to +4
DI SOI 2 (°ATDC)	-37	NA
DI duration 1 (CA°)	3.9	21
DI duration 2 (CA°)	1.95	NA
DI fuel in pulse 1 (% by mass)	67	100
DI injection Pressure (bar)	800	800&1800
Intake pressure (bar)	1.74	
Exhaust pressure (bar)	1.84	
Intake Temperature (deg C)	32	
Air fuel ratio (-)	29	
Fuel/Air ϕ	0.51	
Fuel/Charge ϕ	0.36	
EGR rate (%)	41	
Fuel MEP (bar)	16.6	
IVC (°ATDC)	-143	
EVO (°ATDC)	130	

For the high-EGR diesel combustion case the injection timing was varied from -20° to +4° ATDC. Further, two injection pressures were evaluated (800 and 1800 bar). The lower injection pressure was chosen to be consistent with the dual-fuel RCCI case and the higher injection pressure was chosen to be representative of current injection system capabilities. Notice that the fueling was held constant, thus the reduced efficiency of the high-EGR diesel case results in a lower IMEP.

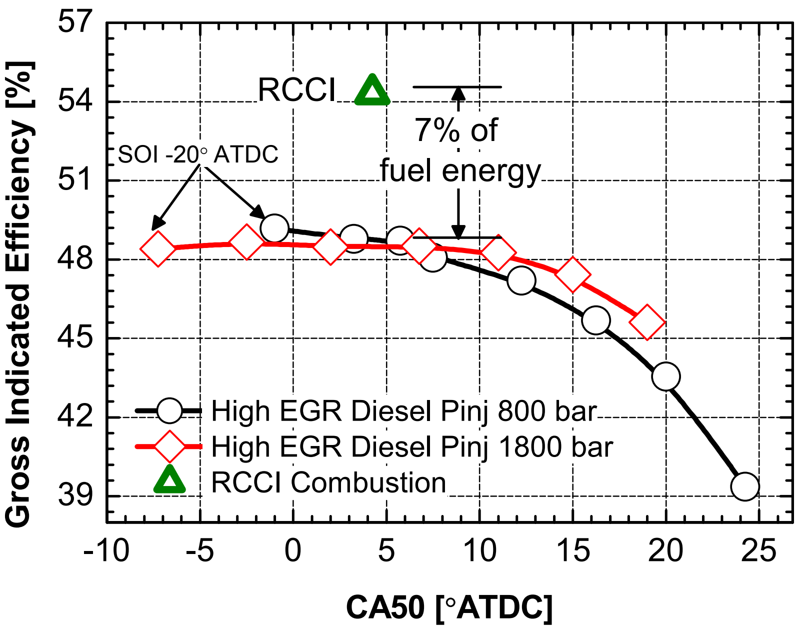

Figure 5-8. Model predicted gross indicated efficiency for RCCI and high-EGR diesel combustion.

The primary focus of this study is fuel efficiency. Accordingly, Figure 5-8 shows the gross indicated efficiency as a function of combustion phasing (CA50) for both operating modes. It can be seen that at a similar CA50, RCCI combustion converts about 7 percent more of the fuel energy to work than high-EGR diesel combustion.

To understand the differences in gross indicated efficiency, energy balances for each case were evaluated. Figure 5-9 shows the model predicted heat transfer losses for RCCI and high-EGR diesel combustion. For a similar combustion phasing, RCCI shows around 8 percent lower heat transfer losses. That is, the level of reduction in heat transfer loss is similar to the observed increase in gross indicated efficiency.

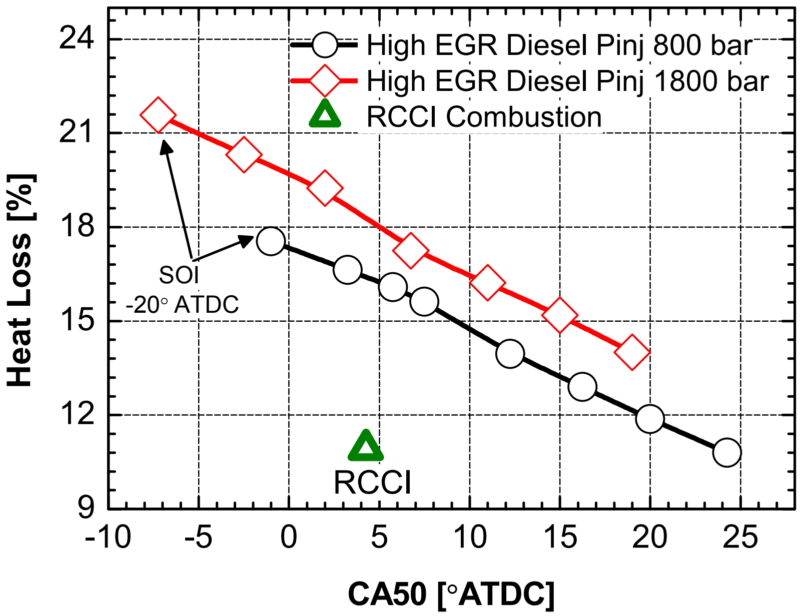

Figure 5-9. Model predicted heat transfer losses for RCCI and high-EGR diesel combustion.

Figure 5-9 suggests that the primary mechanism for the increased efficiency of RCCI combustion is a reduction in heat transfer losses. To investigate the differences in heat transfer losses, Figure 5-10 shows contours of predicted temperatures for the RCCI and a high-EGR diesel case (SOI = -12°ATDC and 1800 bar injection pressure). Recall that the high-EGR diesel and RCCI cases have identical initial conditions; thus for a given equivalence ratio the global adiabatic flame temperatures are identical. However, since the RCCI injection strategy allows sufficient time for mixing prior to ignition, the peak local equivalence ratio during the combustion process is only 0.6. The lean operation results in a peak temperature near 1800 K. Further, these highest temperature regions are located in the center of the combustion chamber, away from heat transfer surfaces. Conversely, combustion in the high-EGR diesel case is mixing controlled and reactions occur in a near stoichiometric band on the outer edge of the spray plume (see Figure 3-11). Because combustion occurs in a stoichiometric region, the peak temperature of the high-EGR diesel case is over 2500 K. Further, the fuel jet penetrates to the piston bowl and combustion occurs at the bowl surface (as well as upstream in the fuel jet). Combustion near the piston bowl surface results in a high-temperature region in-close proximity to a heat transfer surface. Thus, it appears that RCCI combustion reduces heat transfer losses by lowering combustion temperatures – by increasing the pre-combustion mixing – and by keeping high-temperature regions away from surfaces.

Although somewhat outside of the scope of this study, it is interesting to examine the heat transfer losses in high-EGR diesel operation. The heat transfer losses for high-EGR diesel combustion are a strong function of combustion phasing and injection pressure. The influence of combustion phasing on heat transfer losses is expected. That is, as CA50 is advanced, the charge temperature increases and heat transfer losses also increase. The effect of the injection pressure is less intuitive. Figure 5-9 shows that, at a similar combustion phasing, increasing the injection pressure from 800 to 1800 bar increases heat transfer by an amount of energy equivalent to 2 percent of the fuel energy. Of course, heat transfer is a strong function of turbulence levels and for conventional diesel-like combustion (i.e., negative ignition dwell), in-cylinder turbulence is dominated by the injection process. Thus, one is tempted to conclude that the predicted increase in heat loss with increased injection pressure is correlated to enhancements in turbulent mixing. However, heat transfer is also a function of the temperature distribution near the heat transfer surface. Thus, the predicted dependence of heat transfer losses on injection pressure may be partially due to enhancements in convection due to turbulent mixing (i.e., small scale mixing) and partially due to differences in the spatial distribution of the temperature field that results from differences in pre-combustion mixing (i.e., large scale mixing).

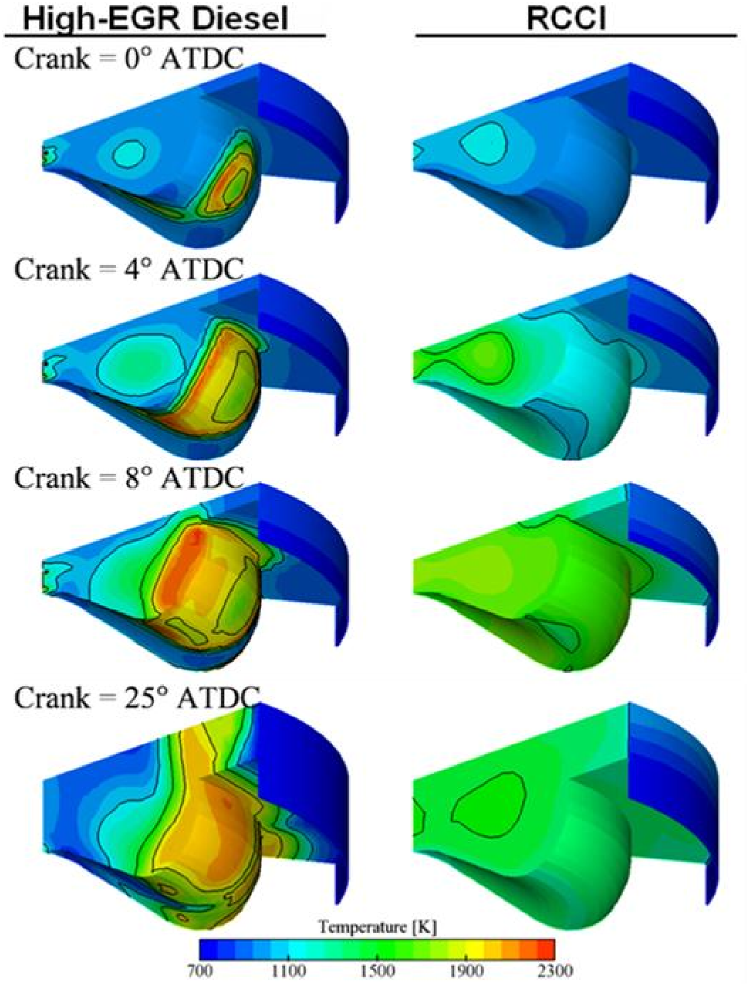

Figure 5-10. Contours of temperature at several times during the combustion process for high-EGR diesel (SOI = -12°ATDC and 1800 bar injection pressure) and RCCI combustion.

The high-EGR diesel cases show that, although heat transfer losses decrease as combustion phasing is retarded, this decrease in heat transfer does not result in an increase in efficiency. Figure 5-11 shows the predicted exhaust energy. Notice that, for the high-EGR diesel cases, the exhaust losses are inversely related to the heat transfer losses. That is, as combustion is phased later in the cycle, the reduced heat transfer losses do not contribute to increased work, rather the energy simply contributes to increased exhaust temperature. Further,

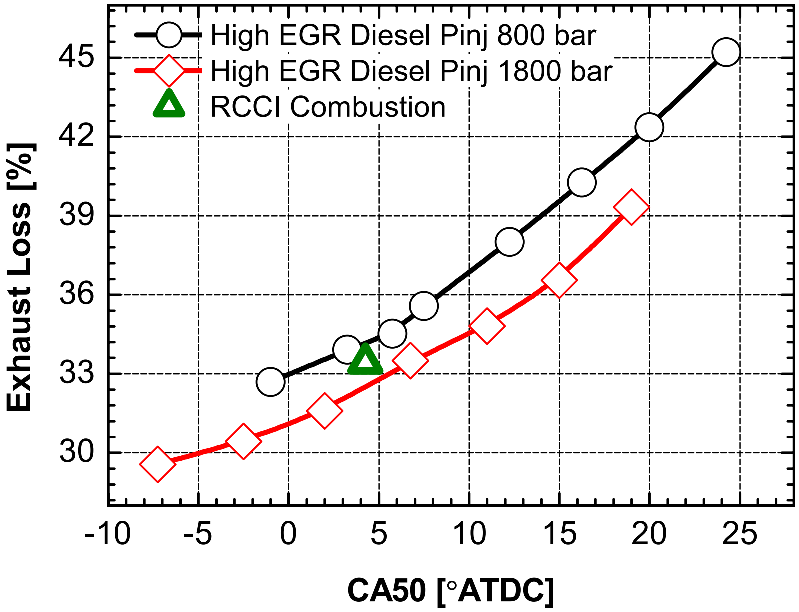

Figure 5-11. Exhaust loss as a function of CA50 for high-EGR diesel and RCCI combustion.

notice that the heat transfer reduction observed through the injection pressure decrease appears primarily in the form of increased exhaust energy. That is, for a fixed CA50, the efficiencies of the low- and high-injection pressure cases are nearly the same. Note also, that the steep decline in gross indicated efficiency at CA50s later than 15° ATDC seen in Figure 5-8 is not only due to increased exhaust temperature, but also significantly reduced combustion efficiency due to the retarded combustion phasing.

Figure 5-9 suggests that a majority of the increased efficiency of RCCI combustion is the result of reduced heat transfer loss. If heat transfer were the only difference between high-EGR diesel and RCCI combustion, adiabatic operation should show equal efficiency. Figure 5-12 shows the energy balance of high-EGR diesel and RCCI operation with and without heat transfer losses. As expected, both the high-EGR diesel and RCCI cases show increases in indicated efficiency when the heat transfer is removed. However, the adiabatic RCCI case still converts 4 percent more of the fuel energy to work than the adiabatic high-EGR diesel case. To investigate the work extraction efficiency, the amount of recovered heat loss converted to work is compared. The RCCI combustion process converts 58 percent of the recovered heat loss to work, while the high-EGR diesel case converts 44 percent of the recovered heat loss to work. This finding has several implications. First, the improved control over the combustion event gained through RCCI operation results in more efficient work extraction by tailoring the energy release to the specific operating condition (e.g., shorter combustion duration). Next, reductions in heat transfer losses have the potential to increase efficiency from both conventional and advanced combustion strategies[5]. Finally, the improvements in efficiency for highly-premixed combustion strategies (e.g., RCCI) will likely be greater than those for mixing controlled combustion strategies.

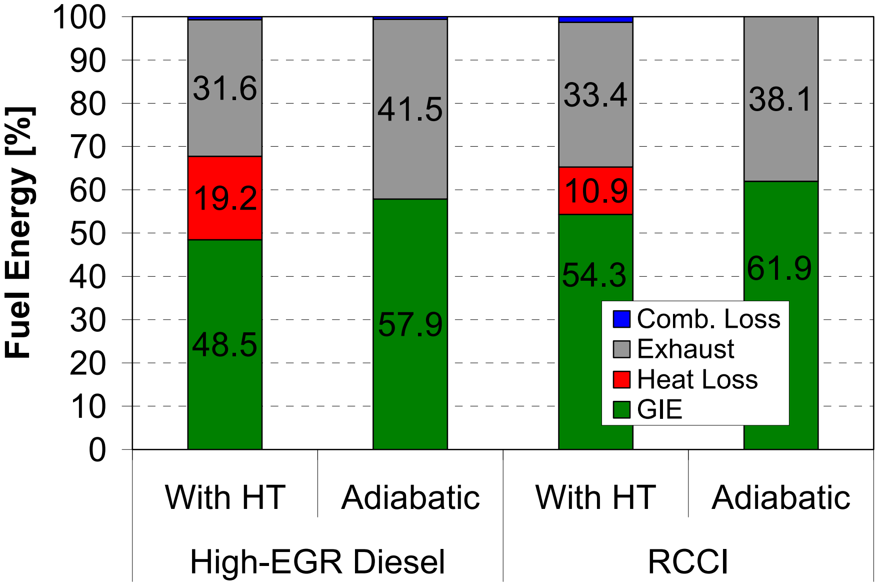

Figure 5-12. Comparison of a high-EGR diesel case and RCCI combustion with and without heat transfer losses. Note that the high-EGR diesel case has an SOI timing of -12° ATDC and an injection pressure of 1800 bar.

---

[5] It should be noted that NOx increased by a factor of 1.5 for the adiabatic conventional diesel case, while NOx remained nearly constant for the RCCI combustion case.

Although the primary focus of this study is thermal efficiency, it is worthwhile to mention the emissions characteristics of RCCI and high-EGR diesel combustion. Table 5-5 shows a comparison of the emissions and performance of RCCI combustion and high-EGR diesel operation at a CA50 near 4° ATDC. Although, significant improvements in indicated efficiency are achieved, similar to the comparisons in the model validation section, RCCI combustion does show a slightly higher pressure rise rate than high-EGR diesel operation. However, as previously discussed, the ringing intensity shows that the combustion rate of the present RCCI case is well within the acceptable limits.

Table 5-5. Emissions and performance of RCCI and high-EGR diesel combustion. All cases have a CA50 near 4.5° ATDC. The high-EGR diesel case with an injection pressure of 1800 bar has an SOI timing of -12° ATDC and the high-EGR diesel case with an injection pressure of 800 bar has an SOI timing of -16° ATDC.

	RCCI	High-EGR Diesel (Pinj 1800 bar)	High-EGR Diesel (Pinj 800 bar)
Ringing Intensity (MW/m^2)	3.8	2.8	2.4
Max PRR (bar/deg)	10.3	8.9	8.0
Gross Indicated Efficiency (%)	54.3	48.7	49.0
Incomplete Combustion (%)	1.3	0.7	0.6
ISNOx (g/kW-hr)	0.006	0.97	1.0
ISsoot (g/kW-hr)	0.019	0.097	0.11

RCCI combustion shows two orders of magnitude lower NOx than the high-EGR conventional diesel combustion case at the peak efficiency point. The lower NOx emissions are attributed to avoidance of regions near stoichiometric equivalence ratios. Recall that the RCCI case has a peak temperature near 1700 K, while the high-EGR diesel case has a peak temperature near 2500 K due to reactions occurring in a near stoichiometric equivalence ratio range. Of course, it would be possible to reduce the flame temperatures of the high-EGR diesel case to

1700 K by further reducing the inlet oxygen concentration (i.e., increasing the EGR rate). Since it is expected that combustion would occur in a stoichiometric region for this case, the required level of EGR can be computed using homogenous reactor simulations. Assuming constant pressure combustion, it is found that the inlet oxygen concentration must be reduced to 8.5 per cent by volume to achieve a stoichiometric flame temperature of 1700 K. To realize this reduction in inlet oxygen concentration at the present operating condition, the EGR must be increased to approximately 70 percent. In addition to lower NOx emissions, RCCI combustion shows 5 times lower soot emissions. The lower soot emissions are attributed to the avoidance of rich regions.

5.4 Discussion of Parameters Controlling RCCI Combustion

The results show that RCCI can achieve very high GIE and near zero NOx and soot emissions. In the laboratory, conditions (e.g., intake temperature) can be precisely controlled; however, in practice, conditions will be more difficult to control. A primary limiting factor for the widespread implementation of HCCI-like combustion strategies is difficulty controlling combustion phasing. Additionally, a genetic algorithm optimization performed at the 9.3 bar operating point (896 KIVA runs considering the effects of gasoline percentage, EGR, SOI1, SOI2, fuel split, and injection pressure) showed that the primary factor controlling the fuel efficiency of RCCI is combustion phasing. That is, for highly-premixed combustion, the resulting increase or decrease in GIE that results from tuning injection parameters and EGR is primarily related to changes in combustion phasing. To illustrate this, Figure 5-13 shows the closed cycle indicated efficiency (IVC to EVO) as a function of combustion phasing (CA50) for the optimization cases with NOx less than 1 g/kgf (approximately the 2010 HD target levels) and the baseline case. Since the optimization showed that the 9.3 bar IMEP condition discussed in Table 5-2 is highly optimized and only marginal improvements in fuel efficiency are possible, no additional discussion of the optimization results will be presented here.

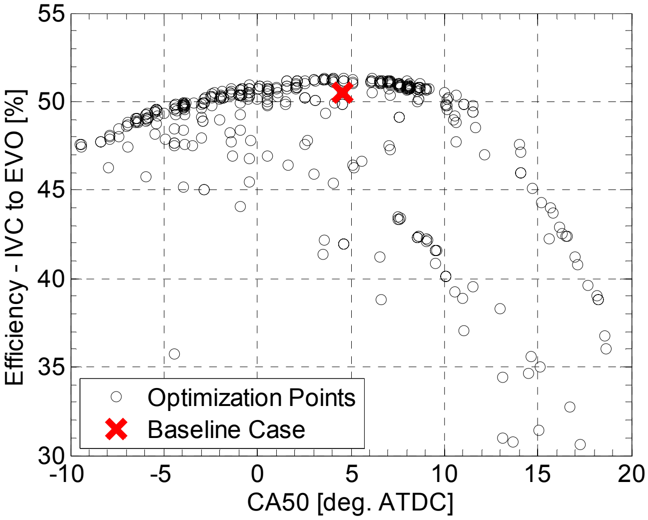

	Lower range	Upper range	Baseline
Gasoline Percentage (%)	0	100	89
SOI1 (deg. ATDC)	-142	-50	-58
SOI2 (deg. ATDC)	-40	0	-37
Injection Pressure (bar)	400	2000	800
Fraction of diesel in pulse 1 (-)	0	1	0.62
EGR (%)	0	60	43

Figure 5-13. Closed cycle efficiency (IVC to EVO) as a function of (a) peak pressure rise rate (PRR) and (b) CA50 for the optimization cases with NOx less than 1 g/kgf (open circles) and the baseline case (x). The inset table shows the parameters and ranges used in the optimization.

Although the optimization resulted in only a marginal improvement in fuel efficiency, it does show that the efficiency of PCI combustion strategies is strongly influenced by combustion phasing. Thus, to maintain high-efficiency, a combustion strategy must be able to control combustion phasing as conditions change. At a fixed operating point, it is expected that environmental factors may cause variations in the intake conditions (i.e., air system) that cannot be controlled on a cycle-to-cycle basis. In this study, the effects of intake pressure, intake temperature, and EGR are considered. It is desirable to have control over combustion phasing on a cycle-to-cycle basis; thus, the fuel system parameters are used as control variables. The control variables are: SOI1, SOI2, gasoline percentage, and percent of fuel in the first injection (CR Split

1). A 2^7 full factorial design of experiments (DOE) (i.e., 128 KIVA runs) was used to determine the effects of these variables on combustion phasing. The variations were performed about the baseline case from the optimization discussed above. The high- and low-levels of the DOE are shown in Table 5-6. The main effects of the air and fuel system parameters on combustion phasing are shown in Figure 5-14. The results show that, of the air system parameters, the intake temperature has the largest effect on combustion phasing. Of the fuel system parameters, the gasoline percentage has the largest main effect. Thus, the gasoline percentage should be considered the main control parameter at this condition.

Table 5-6. High- and Low-Levels used for parametric variations.

	High	Low	Baseline (variation)
SOI1 (deg. ATDC)	-52.2	-63.8	-58 (±10%)
SOI2 (deg. ATDC)	-33.3	-40.7	-37 (±10%)
CR Split 1 (%)	60	73.3	66.7 (±10%)
Gasoline Quantity (%)	93.5	84.6	89 (±5%)
IVC Temperature (K)	360	342	351 (±2.5%)
IVC Pressure (bar)	2.1	1.9	2 (±5%)
EGR (%)	45.1	36.9	41 (±10%)

The ability to control combustion phasing by changes in the gasoline-to-diesel ratio is a key advantage of RCCI over single-fuel HCCI strategies. To illustrate this control Figure 5-15 shows the changes in gasoline percentage required to maintain a fixed combustion phasing as the IVC temperature changes.

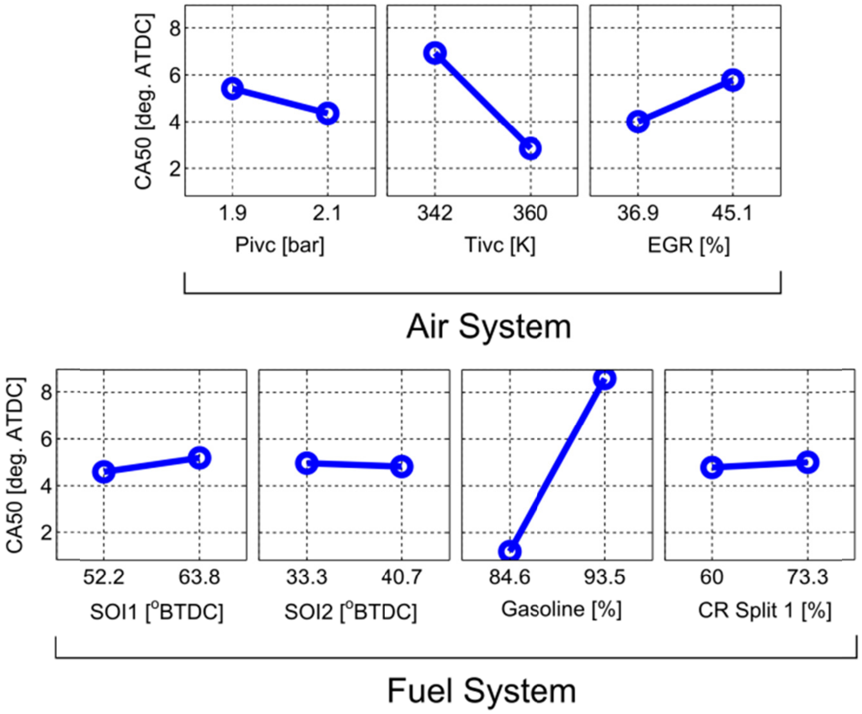

Figure 5-14. Main effects of air and fuel system parameters on combustion phasing.

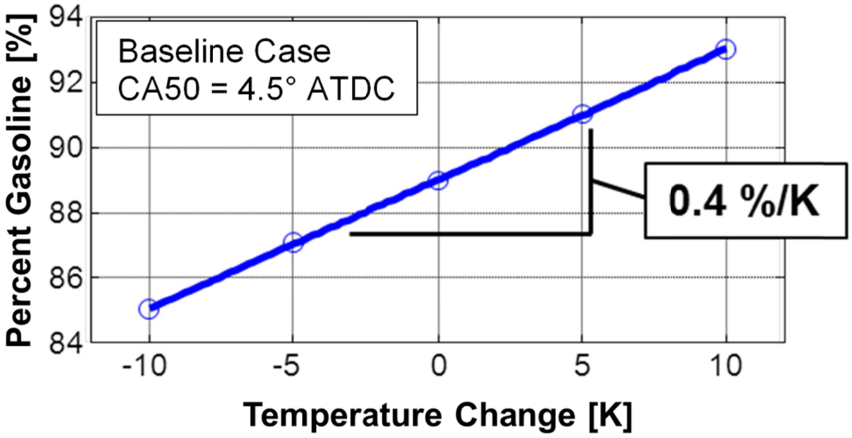

Figure 5-15. Required change in gasoline percentage to maintain a constant combustion phasing as the intake temperature changes.

5.5 Discussion

The results of the combined modeling and experimental work showed that RCCI combustion is capable of achieving high-efficiency combustion with low NOx and soot emissions over a range of conditions. The modeling results were further used to explain the RCCI combustion process. The simulations suggest that ignition is controlled by the location of the highest fuel reactivity and the combustion process proceeds in a staged event from regions of high-to low-fuel reactivity. This staged combustion event extends the combustion duration, which can be beneficial to increase the load limit of PCI strategies. The comparisons between RCCI and conventional diesel combustion show that, at the conditions of the present study, RCCI offers an 11.5% increase in GIE (i.e., 5.6% more of the fuel energy is converted to work). Further, RCCI shows the potential to meet NOx and soot emissions in-cylinder.

Further, optimization was explored by coupling a genetic algorithm to the KIVA-CHEMKIN code. The primary result of the optimization is that the fuel consumption of PCI strategies is most strongly influence by combustion phasing. In practice, conditions are not constant; thus, for a combustion strategy to achieve high-efficiency, the strategy must be able to control combustion phasing as conditions change. A 2^7 DOE was used to determine the most influential air and fuel system parameters. The DOE showed that combustion phasing is most strongly influenced by intake temperature and gasoline percentage. Since intake temperature is not controllable on a cycle-to-cycle basis, it should not be considered a control parameter. The gasoline percentage can be controlled on a cycle-to-cycle basis; thus, gasoline percentage should be considered the primary control parameter.

Chapter 6

A comparison of light- and heavy-duty RCCI combustion

Chapter 4 and Chapter 5 demonstrated RCCI operation in a heavy-duty engine. In this chapter, metal engine experiments are performed to adapt the heavy-duty operating conditions to the light-duty engine and emissions comparisons are made between the light- and heavy-duty engine platforms. In the final section of this chapter, CFD modeling is used to suggest methods to reduce the heat transfer and combustion losses in the light-duty engine.

6.1 Engine Specifications

The specifications for the heavy-duty engine were presented in Chapter 4; however, they are repeated in Table 6-1 to facilitate comparisons with the light-duty engine. Figure 6-1 shows a comparison of the piston bowl geometries. The light-duty engine is a single cylinder version of a GM 1.9 L and is typical of an automotive application. The displacement of the light-duty engine is ~5 times smaller than the heavy-duty engine and it has an 8.2 cm bore, a bore-to-stroke ratio of 0.91, and a displacement of 0.48 L per cylinder. The engine has an open crater-type piston bowl and a geometric compression ratio of 15.24:1. In contrast to the quiescent chamber of the heavy-duty engine, in the stock configuration, the light-duty engine has a much higher level of charge motion with a swirl ratio of 2.2. The IVC and EVO events occur at -132° and 112° ATDC, respectively. Notice that the TDC surface area-to-volume ratio of the light-duty engine is more than two times that of the heavy-duty engine.

Table 6-1. Engine specifications for the light- and heavy-duty engines.

	Heavy Duty	Light Duty
Engine	CAT SCOTE	GM 1.9 L
Displacement (L/cyl)	2.44	0.48
Bore (cm)	13.72	8.2
Stroke (cm)	16.51	9.04
Squish (cm)	0.157	0.133
CR	16.1:1	15.24:1
Swirl ratio	0.7	2.2
IVO (°ATDC)	335	344
IVC (°ATDC)	-143	-132
EVO (°ATDC)	130	112
EVC (°ATDC)	-355	-332
Number of valves	4	
Piston bowl geometry	open crater	
TDC surface area-to-volume ratio (1/cm)	2.7	5.6

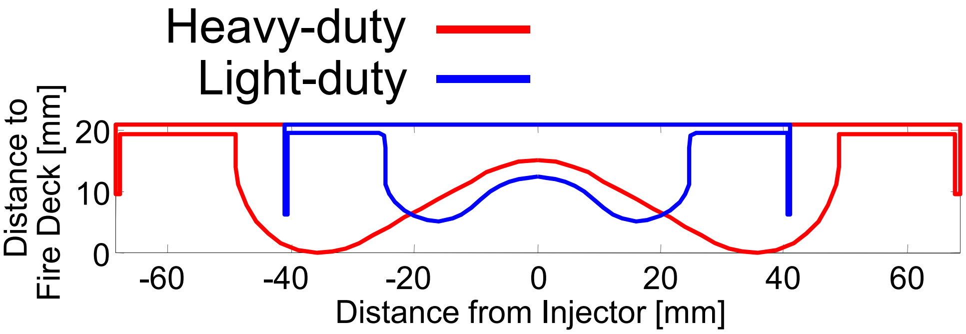

Figure 6-1. Comparison of the light duty (blue) and heavy-duty (red) combustion piston bowl profiles.

6.1.1 Injection Systems

In both engines, the gasoline was delivered using automotive type port-fuel-injection (PFI) systems and the diesel fuel was delivered using common-rail type direct-injection (DI) systems. Table 6-2 gives the specifications for the common-rail systems. The same PFI system used for the HD experiments was used in the light-duty engine. The PFI specifications were presented in Table 4-1.

Table 6-2. Comparison of common-rail fuel injectors used in the heavy-duty and light-duty engine

Engine	Heavy-duty	Light-duty
Manufacturer	Bosch	Denso
Number of holes	6	8
Steady flow rate @ 100 bar [cc/30 sec]	1000	440
Hole diameter [µm]	250	128
Included spray angle [°]	145	130
Injection pressure [bar]	800	500

6.1.2 Data Acquisition and Laboratory Setup

The light- and heavy-duty engine laboratories are described in detail in Refs. [90] and [17], respectively. The engine laboratories are similar; thus, only the light-duty laboratory is discussed here. In the light-duty laboratory, cylinder pressure was measured with a Kistler model 6125A piezo-electric cylinder pressure transducer and in the heavy-duty laboratory a Kistler model 6043 was used. Both laboratories used Kistler model 510 charge amplifiers and acquired cylinder pressure traces were averaged for 500 cycles.

PM measurements were performed with an AVL model 415s smoke meter. PM measurements of filter smoke number (FSN), mass per volume (mg/m^3) and specific emissions (g/kW-hr) were related with the factory AVL calibration and averaged between 5 2 L samples with paper saving mode off. All gaseous emissions measurements were performed with a 5 gas emissions bench. The EGR rate was determined through the ratio of intake CO_2 to exhaust CO_2 levels.

6.1.3 Fuels

Commercially available 91.6 antiknock index ((RON+MON)/2) gasoline and ultra-low sulfur diesel fuel (ULSD) with a cetane number of 46 were used for all engine tests. Table 6-3 and Table 6-4 show an independent lab analysis of the fuel properties.

Table 6-3. Gasoline fuel properties

Distillation curve method	ASTM D86
Initial boiling point	38.9 °C
Temperature 10% evaporated	69.4 °C
Temperature 50% evaporated	105.0 °C
Temperature 90% evaporated	160.6 °C
Final boiling point	215.6 °C
Lower heating value	43.2 MJ/kg
MON	87.8
RON	95.6
(R+M)/2	91.6
Ethanol	0 %
H/C ratio	1.88
Density	756 kg/m^3

Table 6-4. Diesel fuel properties

Viscosity (@ 40 °C)	2.71 cSt
Surface tension (@ 25 °C)	30.0 dyne/cm
Lower heating value	42.5 MJ/kg
Cetane number	46.1
H/C ratio	1.74
Density	856 kg/m^3

6.1.4 CFD Model Setup

Computations were performed using the KIVA-3v release 2 code [52] discussed in Chapter 3. Simulations were performed on the computational grids shown in Figure 6-2. Each grid represents a single hole of the direct injectors described in Table 6-2.

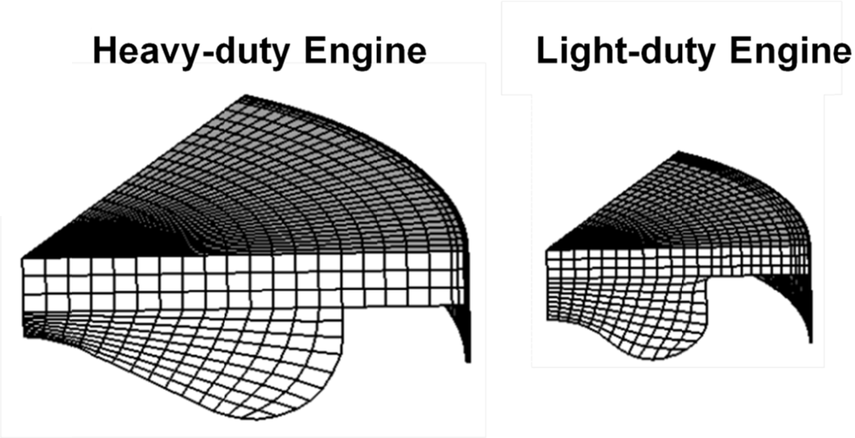

Figure 6-2. Computational grids used for the CFD modeling studies [21].

6.2 Results and Discussion

6.2.1 Extension of RCCI combustion to the light-duty engine

The most optimization work in the heavy-duty engine has been performed at the 9.3 bar IMEP operating point (see Chapter 5) in the heavy-duty engine; thus, the 9.3 bar IMEP operating point is the focus of the comparisons between the light- and heavy-duty engines. The operating conditions for the light-duty experiments of the current study and the heavy-duty experiments of Hanson et al. [18] are shown in in Table 6-5. The heavy-duty engine was operated at 1300 rev/min. Engine size scaling laws (e.g., Shi et al. [107]) do not provide a scaling parameter for engine speed; however, two arguments can be made regarding the engine speed at which to operate the light-duty engine in order to make a direct comparison to the heavy-duty engine. First, relying on chemical kinetics it is expected that the two engines should have the same ignition delay; thus, from a chemical kinetics perspective the engines should operate at identical engine speeds. However, if heat transfer is considered a very different result is achieved. Considering convective heat transfer only (i.e., $\dot{Q} = hA\Delta T$), representing the heat transfer coefficient, h, as a function of the Reynolds number (i.e., $Nu = \alpha \mathrm{Re}^m$, where α and m are empirical constants), and normalizing the heat loss by the fuel energy, the following relation can be found for the fuel energy lost due to heat transfer.

$$\frac{\dot{Q}}{\dot{m}_{fuel} LHV_{fuel}} = \alpha \frac{rpm^{m-1} stroke^{m} bore^{m+1}}{m_{fuel}}, \qquad \textbf{(6-1)}$$

Taking a scaling factor, L, as the cube root of the ratio of the light-duty to heavy-duty TDC volumes [107], assuming that the bore and stroke scale as L, and the fuel mass scales with the displacement (i.e., L^3), it is found that in order to scale the heat transfer losses, the engine speed scales as

$$rpm_{LD} = \frac{rpm_{HD}}{L^2}, \quad \textbf{(6-2)}$$

where rpm_{LD} and rpm_{HD} are the engine speeds of the light- and heavy-duty engines, respectively. Therefore, if the engines were perfectly scaled, the light-duty engine would need to be operated at around 3800 rev/min to scale the heat transfer losses. Recall that kinetics suggests that the two engines should operate at the same speed. Additionally, laboratory limitations restrict high-speed operation. Thus, to make a compromise between kinetics and heat transfer timescales, an intermediate speed of 1900 rev/min was selected.

Both engines were operated with 41 percent external EGR and the inlet temperature and pressure of the light-duty engine was adjusted to match the compression stroke pressure and temperature of the heavy-duty engine. The injection parameters were similar between the two engines; however, the injection pressure of the light-duty engine was reduced to 500 bar to allow an increase in the injection duration in order to achieve more stable fuel delivery. However, it is thought that, due to the early injection timings and short injection durations, the differences in the injection characteristics will have a minimal effect on the results of this study. As suggested by the modeling work of Chapter 4 and Chapter 5, the premixed gasoline fraction (i.e., $\dot{m}_{gasoline} / \dot{m}_{fuel}$) was used to control the combustion phasing and account for the differences in the engine speeds for the two engines. The quantity of the premixed gasoline in the heavy-duty engine was swept from 82 to 89 percent by mass and the quantity of the premixed gasoline in the light-duty engine was swept from 81 to 84 percent by mass. Note that the range of the premixed gasoline fraction sweeps for the light- and heavy-duty are different due to the several factors. First, since the engine speed of the light-duty engine is higher than that of the heavy-duty engine, the light-duty engine has less time available for ignition; thus, for a given fuel blend, the light-duty engine will ignite later than that of the heavy-duty engine. Further, the heat transfer differences in the two engines may result in slight differences in the TDC conditions.

Table 6-5. Operating conditions for the comparison between light- and heavy-duty RCCI combustion at 9.3 bar IMEP.

	Heavy	Light
Engine	CAT	GM 1.9 L
IMEP (bar)	9.3	
Engine speed (rev/min)	1300	1900
Mean piston speed (m/s)	7.2	5.7
Total fuel mass (mg)	94	20.2
EGR (%)	41	
Premixed gasoline (%)	82 to 89	81 to 84
Diesel SOI 1 (°ATDC)	-58	-56
Diesel SOI 2 (°ATDC)	-37	-35
Diesel inj. pressure (bar)	800	500
Intake pressure (bar)	1.74	1.86
Intake runner temp. (°C)	32	39
Air flow rate (kg/min)	1.75	0.46
Abs. Exhaust back pressure (bar)	1.84	1.98
Ave. Exhaust temperature (°C)	271	319
Fuel/Air ϕ	0.51	0.61
Fuel/Charge ϕ	0.36	0.43
Port-injected fuel	Gasoline	
Direct-injected fuel	Diesel Fuel	

Figure 6-3 shows the cylinder pressure and apparent heat release rates for the light-and heavy-duty engines over the premixed gasoline percentage sweeps. Note that to facilitate comparisons between the two engines operating at different speeds, the heat release rates are normalized by the fuel energy and shown as time derivatives (i.e., 1/ms), rather than crank angle derivatives. It can be seen that in both engines, the combustion phasing is easily controlled by adjustments in the premixed gasoline percentage.

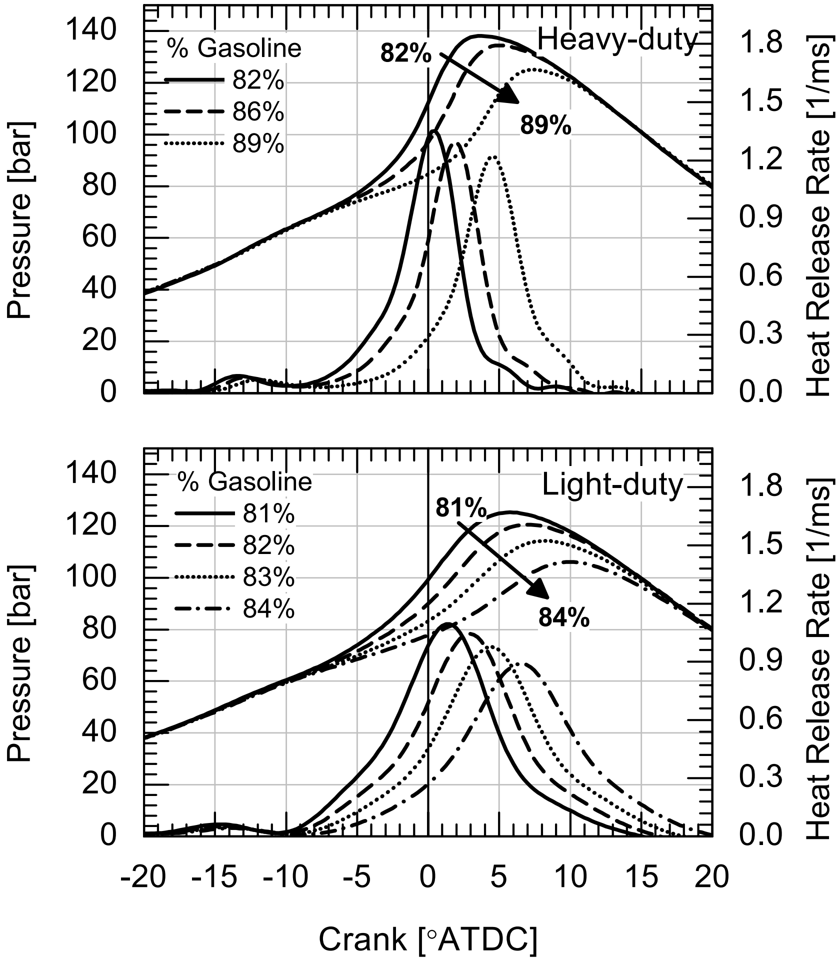

Figure 6-3. Cylinder pressure and apparent heat release rates for the heavy- and light-duty engines over the gasoline quantity sweeps at a fixed load of 9 bar IMEP. Note that gasoline quantity refers to the mass fraction or per cent of gasoline in the charge [21].

Figure 6-4 highlights the control in combustion phasing (CA50) introduced by changes in the premixed gasoline percentage, as demonstrated using CFD modeling in Chapter 5. That is, increasing the gasoline mass percentage in the fuel results in a very predictable delay in the combustion phasing. The predictable dependence of combustion phasing on the premixed gasoline percentage has several implications for the practical application of the RCCI combustion concept. First, an engine operating in the RCCI combustion mode must have accurate control over the fuel quantity delivered from each of the two fuel streams. Second, the

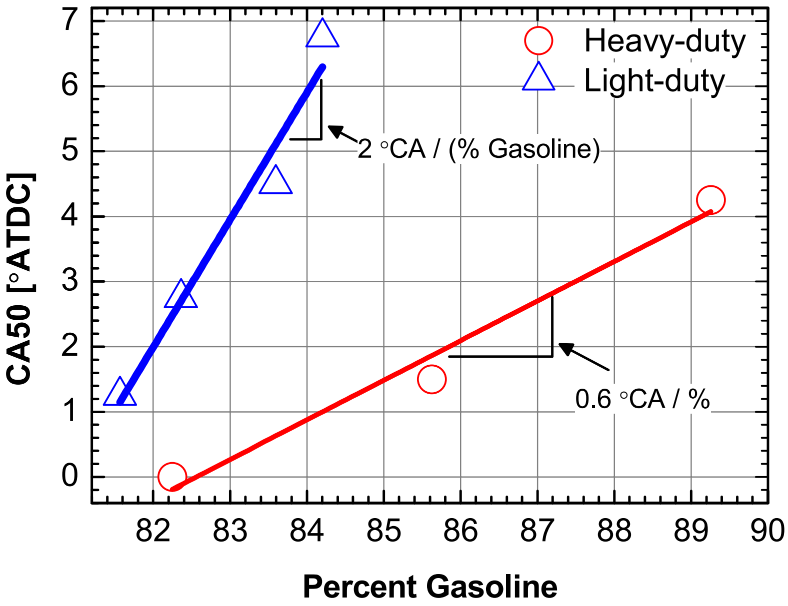

Figure 6-4. Effect of premixed gasoline percent on combustion phasing (CA50) [21].

RCCI combustion process regains the coupling between the injection and combustion events that is lost with traditional HCCI or early injection PCCI combustion.

Notice that the dependence of combustion phasing on premixed gasoline percentage is different for the two engines; however, recall that the two engines were operated at different speeds. The light-duty engine was operated at 1900 rev/min and the heavy-duty engine was operated at 1300 rev/min. For the light-duty engine a percent increase in the premixed gasoline and corresponding decrease in the direct-injected diesel quantity results in a retard in combustion phasing of 2° CA at 1900 rev/min or 175 μs and for the heavy-duty engine a percent increase in the premixed gasoline percentage results in a retard in combustion phasing of 0.6° CA at 1300 rev/min or 78 μs. The increase in the slope for the light-duty engine is likely due to the increased expansion rate due to the higher engine speed. Thus, it appears that at higher engine speeds the combustion phasing becomes more sensitive to changes in the premixed gasoline percentage.

Figure 6-5 shows the coefficient of variation (COV) in IMEP as a function of combustion phasing for the light- and heavy-duty engines. It can be seen that with appropriate combustion phasing (i.e., CA50 < ~5° ATDC), the engine operation is stable. As expected, the COV of IMEP increases significantly as combustion phasing is retarded. This effect appears to be stronger for the light-duty engine, possibly due to the higher engine speed. Note that the gasoline percent for the light-duty engine was not increased past 84 per cent due to the unacceptably high COV that results from very retarded combustion phasing. Obviously, the operating parameters could be changed such that higher gasoline percentages could be explored; however, this is beyond the scope of the present study.

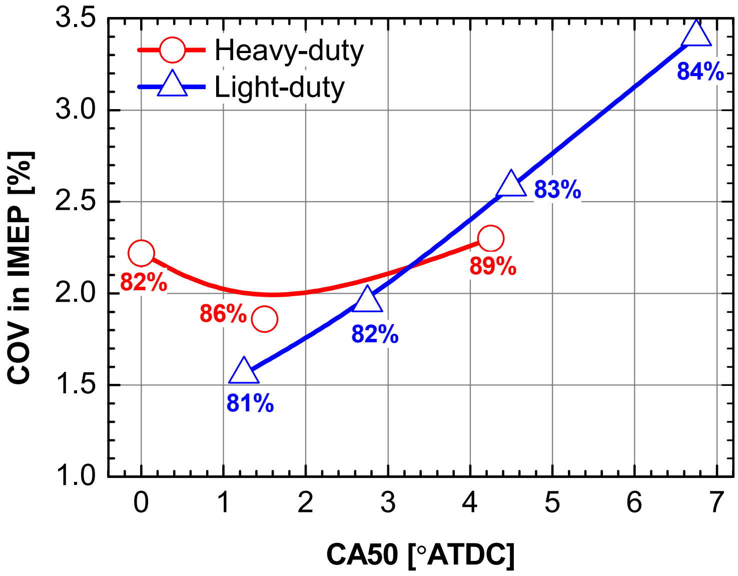

Figure 6-5. COV in IMEP as a function of combustion phasing (CA50) for the light- and heavy-duty engines. The numbers on the plot show the corresponding per cent gasoline for each case [21].

Figure 6-6 shows comparisons between light- and heavy-duty engine emissions and performance over the premixed gasoline percentage sweep. Note that the results are presented as functions of combustion phasing (CA50) to facilitate comparisons between the two engines at similar combustion phasing. NOx and soot emissions are shown on a gross indicated basis. Also shown in Figure 6-6 are the United States (US) 2010 Environmental Protection Agency's (EPA) heavy-duty (HD) on-highway truck limits for NOx and soot emissions (i.e., 0.268 g/kW-hr and 0.0134 g/kW-hr for NOx and soot, respectively).

Both engines achieve NOx levels significantly below the 2010 heavy-duty limits;

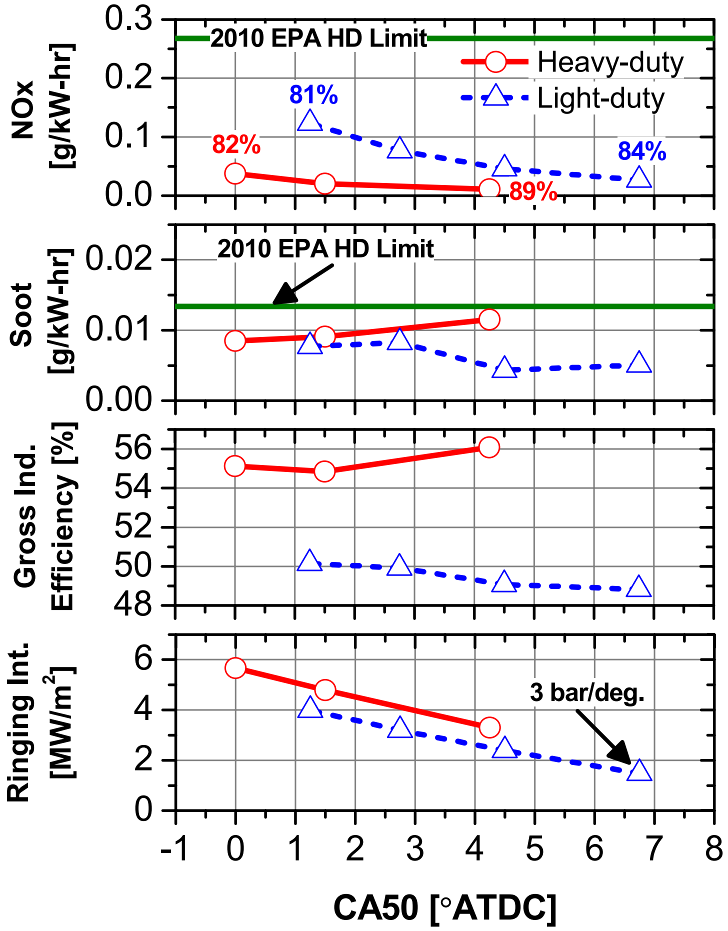

Figure 6-6. Measured emissions and performance of the light- and heavy-duty engines over a gasoline percentage sweep. The data are shown as a function of combustion phasing (CA50) [21].

however, it can be seen that, for similar combustion phasing, the light-duty engine has slightly higher NOx emissions. NOx decreases significantly as the combustion phasing is retarded. Soot emissions are nearly identical for the two engines and, similar to the NOx emissions, both engines have soot levels below the 2010 heavy-duty limit. Further, it can be seen that soot is relatively insensitive to combustion phasing. In addition to very low NOx and soot levels, both engines show acceptable ringing intensities. More importantly, the engines show significant control over the ringing intensity via changes in the premixed gasoline percentage. Comparing the gross indicated efficiencies it can be seen that the heavy-duty engine shows 5 to 7 percent higher indicated efficiency than the light-duty engine.

6.2.2 Analysis of the Efficiency Difference between LD and HD RCCI

To understand the differences in indicated efficiencies, the energy flows are analyzed using a combination of experiments and CFD modeling. Figure 6-7 shows the measured and model predicted cylinder pressures and the apparent heat release rates for cases with CA50s near 1.5° ATDC. In general, the simulations capture the combustion characteristics of both engines well.

Figure 6-8 shows the measured and calculated GIE and incomplete combustion and the calculated heat transfer losses. The simulations slightly under-predict the GIE for both engines; however, the difference in GIE between the engines is captured well by the simulations. Since the difference in GIE and combustion efficiency are accurately reproduced by the simulations, it is expected that the model predicted heat loss is at least trend wise accurate. Figure 6-8 shows that the differences in GIE between the two engines are due to the differences in combustion efficiency (i.e., higher UHC and CO) and heat transfer losses.

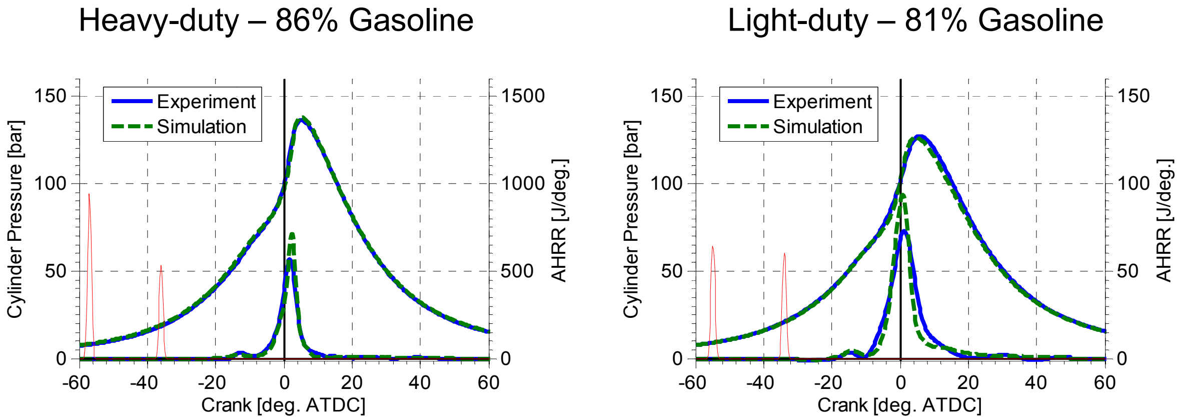

Figure 6-7. Comparison of measured and predicted cylinder pressures and heat release rates for the light- and heavy-duty engines operating at 9 bar IMEP with a fixed combustion phasing of 1.5° ATDC. The light-duty engine is fueled with 81 percent gasoline and the heavy-duty engine is fueled with 86 percent gasoline.

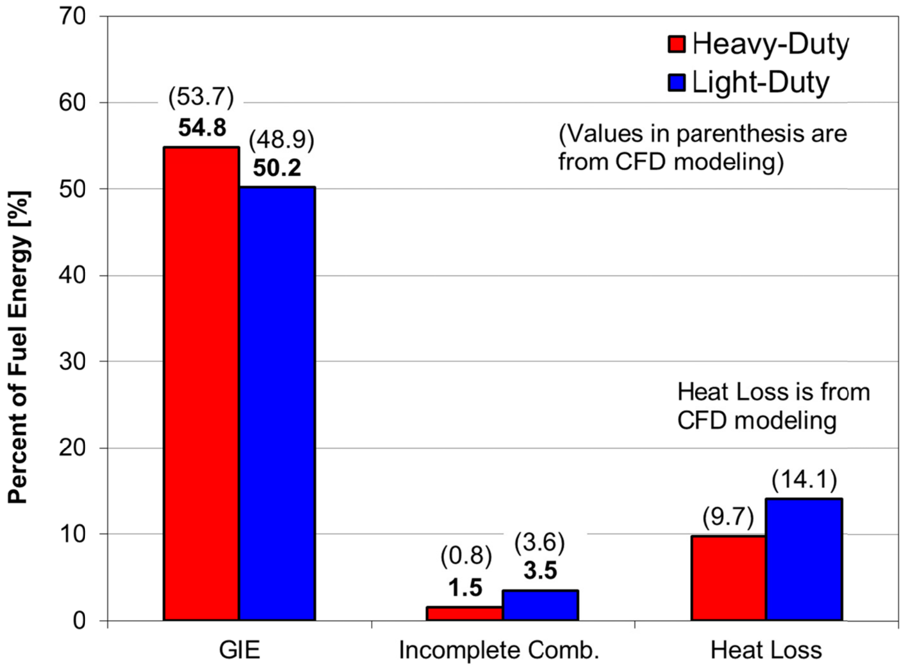

Figure 6-8. Energy balances[6] for the light- and heavy-duty engines for the cases operating at 9 bar IMEP with combustion phasing at 1.5° ATDC. Values without parenthesis are measured and values with parenthesis are from CFD modeling.

---

[6] In Chapter 5 energy balances were computed from the measured work, incomplete combustion, and exhaust temperature. The heat loss term was then solved for by closing the energy balance. When results in a single engine/lab are compared, this method should provide good estimate of the energy flows; however, the relative contributions of the exhaust energy and heat loss terms are estimates. Using this method to compare across labs may introduce errors due to differences in the thermocouple placements. To avoid this uncertainty, the heat loss from the models is considered.

6.2.2.1 Investigation of Methods to Reduce Heat Transfer Losses in the Light-duty Engine

The comparison of the light- and heavy-duty RCCI engine experiments suggested that heat transfer is one of the primary limiting factors on the indicated efficiency of the light-duty engine. It is expected that the light-duty engine has higher heat transfer losses for several reasons:

1) As previously discussed, Eq. 6-2 shows that heat transfer scales with mean piston speed and in this study the light-duty engine operates at a lower mean piston speed than the heavy-duty engine (see Table 6-5).
2) The two engines have different combustion chamber and injector geometries. The combustion chamber geometry affects heat transfer losses directly through the amount of surface area. In this case, the surface-to-volume ratio of the light-duty engine is more than two-times higher than that of the heavy-duty engine. Furthermore, the combination of combustion chamber and injector geometry can also play a role in heat transfer losses via the fuel distribution. The comparison between heat transfer losses of RCCI and conventional diesel combustion presented in Section 5.3 showed that heat transfer losses were reduced for RCCI combustion not only through reductions the peak temperature, but also by keeping high temperature regions away from the piston surface.
3) In the stock configuration, the swirl ratio of the light-duty engine is more than three times higher than that of the heavy-duty engine.
4) The light-duty engine uses an aluminum piston and the heavy-duty engine uses a steel piston. The higher thermal conductivity of the aluminum piston results in higher heat transfer losses.

Accordingly, CFD modeling is used to investigate methods to reduce the heat transfer losses in the light-duty engine. The present study will focus on the effect of swirl ratio and piston material. To isolate the effects of these two factors, the combustion chamber and injector geometry of the heavy-duty engine were scaled down to the light-duty displacement by applying a scaling factor defined as the cube root of the ratio of the light-duty to heavy-duty TDC volumes. The engine speed of the scaled light-duty engine was set to give the same mean piston speed as the heavy-duty engine. Note that this is a relatively small increase in engine speed and was found to have a minimal effect on the results, a detailed discussion of effect of engine speed is shown in Kokjohn et al. [21]. The specifications of the heavy-duty engine, baseline light-duty engine, and scaled geometry light-duty engine are compared in Table 6-6 and a comparison of the three combustion chamber geometries is shown in Figure 6-9.

Table 6-6. Engine parameters comparing the heavy-duty engine, baseline light-duty engine, and scaled light-duty engine. Note that the parameters for the heavy-duty engine and baseline light-duty engine are the same as those presented in Table 6-1, but are repeated here for completeness.

Engine	Heavy -duty	Light -duty	Scaled light-duty
Displacement (L)	2.44	0.48	0.48
Bore (cm)	13.72	8.2	8.0
Stroke (cm)	16.51	9.04	9.64
CR	16.1:1	15.24:1	16.1:1
IVC (°ATDC)	-143	-132	-132
EVO (°ATDC)	130	112	112
Injector type		Common rail	
Nozzle holes	6	8	6
Hole size (μm)	250	128	146
Included angle (°)	145	130	145
TDC surface area-to-volume ratio (1/cm)	2.7	5.6	4.7
Engine speed (rev/min)	1300	1900	2239

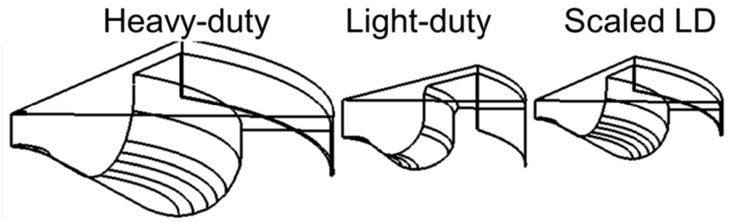

Figure 6-9. Comparison of the combustion chamber geometries for the heavy-duty, baseline light-duty, and scaled light-duty engines [21].

The CFD modeling approach used in this study does not include a conjugate heat transfer model (CHT); thus, the effect of material properties cannot be directly investigated. However, the effect of material properties can be indirectly investigated by studying the effect of surface temperature. The wall temperature used to model the light-duty engine (aluminum piston) is 450 K and the heavy-duty engine (steel piston) is 500 K. The scaled light-duty engine is modeled with these two surface temperatures at the swirl ratios of 2.2 and 0.7 (i.e., the baseline LD and HD values).

The results are shown in Table 6-7. Since GIE is strongly influenced by combustion phasing (as discussed in Chapter 5), the IVC temperature was adjusted at each surface temperature-swirl ratio combination to allow comparisons to be made at similar combustion phasing. In practice, the gasoline percentage is the preferable control parameter since it can be adjusted on a cycle-to-cycle basis; however, to avoid changing the fuel distribution the IVC temperature was used to control CA50. All of the presented cases have CA50's within 0.5° of 2° ATDC.

Beginning with the baseline LD engine and scaling the geometry to the HD engine geometry (case 1) increases the GIE from 48.9% to 50.8%. Notice that the heat transfer loss is nearly constant; however, the incomplete combustion losses drop from 3.7% to 1.6% due to the difference in ring-pack geometry. Increasing the surface temperatures by 50 K at a constant swirl ratio (Case 1 to Case 2) reduces the heat transfer losses from 14.3% to 12.3%. The reduced heat transfer increases the GIE from 50.8% to 51.7%. Similarly, reducing the swirl ratio from 2.2 to 0.7 at a constant surface temperature (Case 1 to Case 3) results in an increase in GIE from 50.8% to 51.7% due to reduced heat transfer losses. It is interesting that increasing the surface temperature by 50 K and reducing the swirl ratio by a factor of three have nearly identical effects on GIE. Finally, combining the increased surface temperature and reduced swirl ratio (Case 4) lowers the heat transfer losses to 11.3% and increases the GIE to 52.6%. Notice the decreased heat transfer of Case 4 lowers the combustion losses to 1.1% of the fuel energy due to the higher in-cylinder temperatures. This finding suggests that, with a fixed geometry, methods that lower the heat transfer losses will also result in improved combustion efficiency. Recall that this was also shown in the heavy-duty engine in Chapter 5 (see Figure 5-12) when adiabatic operation was considered. Comparing Case 4 to the heavy-duty engine, it can be seen that when the geometry is scaled and the same surface temperatures (i.e., materials) are used, the light-duty engine efficiency approaches that of the heavy-duty engine. The slightly lower GIE of the improved LD RCCI engine is due to the higher surface area-to-volume ratio of the small bore engine. The NOx and soot emissions of all cases are very similar (and low) due to the constant combustion phasing.

Table 6-7. Results of heat transfer reduction investigation at a constant CA50 of 2° ATDC.

	Geometry	SR	Surface Temp. (K)	GIE (%)	Heat Loss (%)	Incomplete Comb. (%)	ISNOx (g/kW-hr)	ISSoot (g/kW-hr)	IVC Temp. (K)
Base HD	HD	0.7	500	53.7	9.7	0.7	0.02	<0.01	347
Base LD	LD	2.2	450	48.9	14.1	3.7	0.03	<0.01	368
Case 1	Scaled LD	2.2	450	50.8	14.3	1.6	0.05	<0.01	365
Case 2	Scaled LD	2.2	500	51.7	12.3	1.4	0.03	<0.01	365
Case 3	Scaled LD	0.7	450	51.7	12.6	1.5	0.03	<0.01	370
Case 4	Scaled LD	0.7	500	52.6	11.3	1.1	0.03	<0.01	370

6.3 Discussion

The experiments of this study show that similar combustion characteristics can be found in both the light- and heavy-duty engines with appropriate selection of operating parameters. Thus, the heavy-duty optical engine results that will be presented in Chapter 9 and Chapter 10 should be applicable to both engine platforms. Further, this investigation shows that GIE's approaching 53% are achievable in an automotive-sized engine using RCCI combustion.

Chapter 7

Comparison of Conventional Diesel Combustion and RCCI Combustion in a Light-Duty Engine

To finalize the performance evaluation of RCCI combustion, this chapter presents a high-level comparison of RCCI combustion and conventional diesel combustion (CDC) at conditions used to estimate the light-duty drive cycle. This is a modeling study performed using the KIVA-CHEMKIN code [52].

7.1 Engine Setup

The light-duty engine modeled in this study is the GM 1.9 L. Specifications are given in Chapter 6; however, the engine modeled in this study uses the stock GM 1.9 L bowl geometry, resulting in a compression ratio of 16.7:1. Figure 7-1 shows the CFD grid used for the light-duty engine simulations. The CFD grid represents a single hole of the 7-hole Bosch injector used in this study. The common-rail injector specifications are shown in Table 7-1.

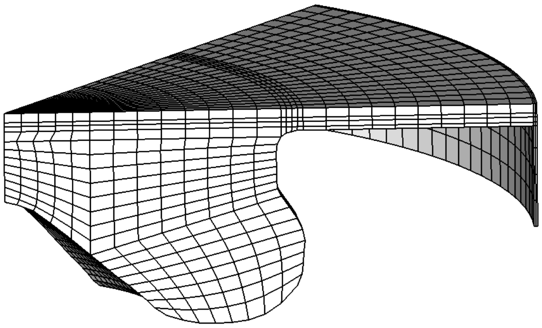

Figure 7-1. Computational grid shown at TDC. The grid is a 51.4 degree sector consisting of 25,500 cells at BDC.

Table 7-1. Common-rail injector specifications used to model the stock GM 1.9 L engine

Manufacturer	Bosch
Number of holes	7
Hole diameter [μm]	141
Included spray angle [°]	155

7.2 Objective and Approach

The objective of this study is to compare conventional diesel combustion (CDC) and RCCI combustion at NOx levels equivalent to US Tier 2 Bin 5 and propose a simple method to account for the added fluid consumption required to meet NOx constraints using aftertreatment. The baseline cases are taken from a Euro 4 calibrated GM 1.9 L. The purpose of this study is to make a direct comparison to conditions achievable in an unmodified GM 1.9 L. Thus, the stock piston and material are used. Further, the minimum swirl ratio in the production engine is 1.5; thus, all RCCI cases use a swirl ratio of 1.5. This should be kept in mind when comparing the result of this study to the "improved" LD RCCI engine results presented in Chapter 6.

The combustion strategies are compared assuming that the CDC mode uses selective catalytic reduction (SCR) to meet NOx constraints. The diesel exhaust fluid (DEF) consumption is assumed to be 1% of the fuel consumption per 1 g/kW-hr NOx reduction [4]. In this comparison it is assumed that the RCCI engine operates without NOx aftertreatment. In all cases, it is assumed that the engine is equipped with soot aftertreatment (i.e., a DPF). The fuel consumed to regenerate the DPF is not included in the analysis. Note that, since RCCI has significantly lower soot emissions than CDC, this assumption biases the results toward the CDC strategy. Finally, it is assumed that the engine is equipped with a diesel oxidation catalyst (DOC) and the catalyst is capable of reducing CO and UHC in the exhaust stream such that the penalty of the incomplete combustion products is only included in the fuel consumption (i.e., through the reduced work).

7.3 Operating Conditions

The five operating points used by the Ad-hoc fuels working group [108] to evaluate fuel effects were used to compare RCCI combustion, CDC, and diesel LTC. The operating modes and relative weighting factors are shown in Table 7-2. Cycle averaged emissions and fluid consumption were calculated using a weighted average given by

$$E_{cycle} = \frac{\sum_{\text{imode}=1}^{5} E_{\text{imode}} Weight_{\text{imode}}}{\sum_{\text{imode}=1}^{5} Weight_{\text{imode}}} \quad , \tag{7-1}$$

where E_{cycle} is the cycle averaged value of emissions or performance, E_{imode} is the value of emissions or performance at each operating mode, and $Weight_{imode}$ is the Mode Weight given in Table 7-2.

Table 7-2. Operating modes and relative weights used for light-duty emissions and performance comparisons.

Mode	IMEP (bar)	Speed (rev/min)	Mode Weight (-)
1	2.3	1500	400
2	3.9	1500	600
3	3.3	2000	200
4	5.5	2300	200
5	9	2600	75

7.4 CDC-Model Validation

Hanson [109] performed engine experiments on the production, four-cylinder version of the GM 1.9 L engine at each test mode considered in this study. The engine is a stock 2007 version of the GM 1.9 L; however, the factory engine control module was replaced with a Drivven® control unit to allow flexibility. The engine control module was calibrated by

Drivven® to be representative of a Euro 4 production engine. The operating conditions are shown in Table 7-3. All CDC points use a small pilot injection containing between 5% and 30% of the total fuel. Operating modes 1-3 use moderately high EGR rates from 38 to 47%. The EGR rate decreases with load to 15% at the 9 bar IMEP – 2600 rev/min operating point.

Table 7-3. Operating conditions for CDC experiments of Hanson [109] **used to validate the model predictions.**

Mode	1	2	3	4	5
IMEPg (bar)	2.3	3.9	3.3	5.5	9
Speed (rev/min)	1500	1500	2000	2300	2600
Total Fuel (mg/inj.)	5.6	9.5	8	13.3	20.9
Intake Temp. (deg. C)	60	60	70	67	64
Intake Press. (bar abs.)	1	1	1	1.3	1.6
EGR Rate (%)	47	38	42	25	15
CR Inj. Pressure (bar)	330	400	500	780	1100
Pilot SOI (°CA) (actual)	-5.8	-7.2	-8.2	-11.7	-15.4
Main SOI (° ATDC) (actual)	1.6	0	1.6	-0.1	-2.6
Percent of DI fuel in Pilot (%)	34	16	15	10	5

Figure 7-2 shows comparisons of measured and predicted cylinder pressure and AHRR at each operating condition. The simulations do an adequate job capturing the combustion characteristics for modes 1-4. The agreement at mode 5 is not as good as the lighter load points. At the mode 5 point, the simulations tend to predict more rapid energy release than the experiments, which is likely due to inaccuracies in the pre-combustion mixing prediction. It is likely that this is due to a combination of modeling errors and uncertainty in the conditions from the measurements. No injection-bench work was performed for these conditions; therefore, the quantities of fuel in the pilot and main injections were estimated. Further, the injection rate-shapes were estimated using a simple injector model. However, the mode 5 point has a very small weighting factor in the drive cycle calculations (see Table 7-2); thus, uncertainties at the mode 5 point have little influence on the drive cycle average. Although some differences in the model predicted and measured cylinder pressure and AHRR are present, the primary purpose of this study is to provide a high-level comparison of CDC and RCCI combustion and demonstrate a methodology to compare the combustion modes. Thus, the agreement was deemed acceptable.

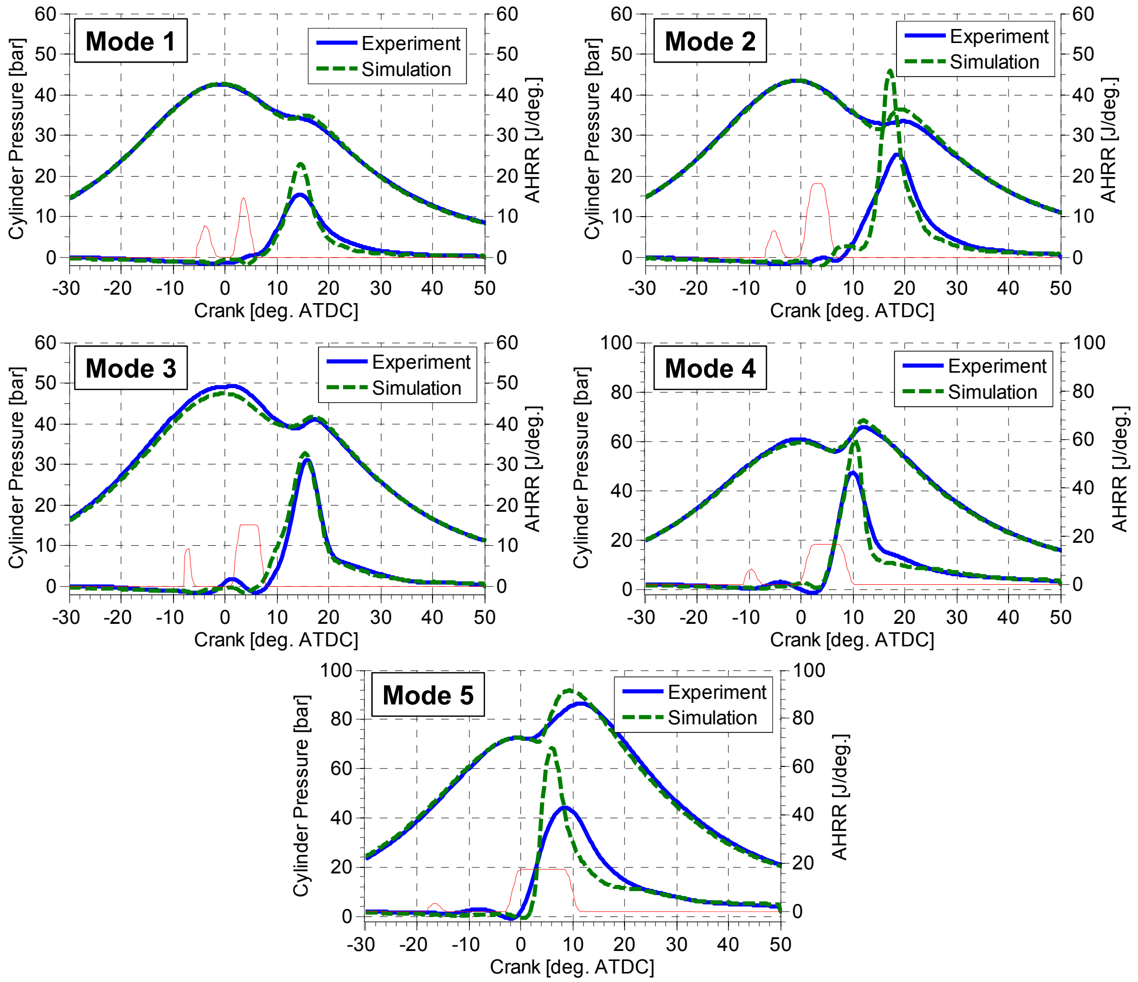

Figure 7-2. Comparison of measured and predicted cylinder pressure and AHRR for CDC operation with a Euro 4 calibration. The solid blue lines show the measurements, the dashed green lines show the simulation results and the red lines show the injection rate-shape used in the simulations.

Figure 7-3 shows a comparison of the measured and predicted NOx, soot, and GIE for the Euro 4 CDC operating conditions. The simulations capture the NOx trends and magnitudes well. The soot levels are captured acceptably; however, notice that soot at the mode 2 operating point is significantly over-predicted. The two-step soot model is generally not predictive and might need tuning to capture the soot levels as conditions change. The soot model constants discussed in Chapter 3 were used for the simulations presented in this study. However, the results of this study will focus on the NOx-efficiency tradeoffs for conventional diesel and RCCI; thus, predicted soot levels do not influence the conclusions of the present work. The trend in GIE is

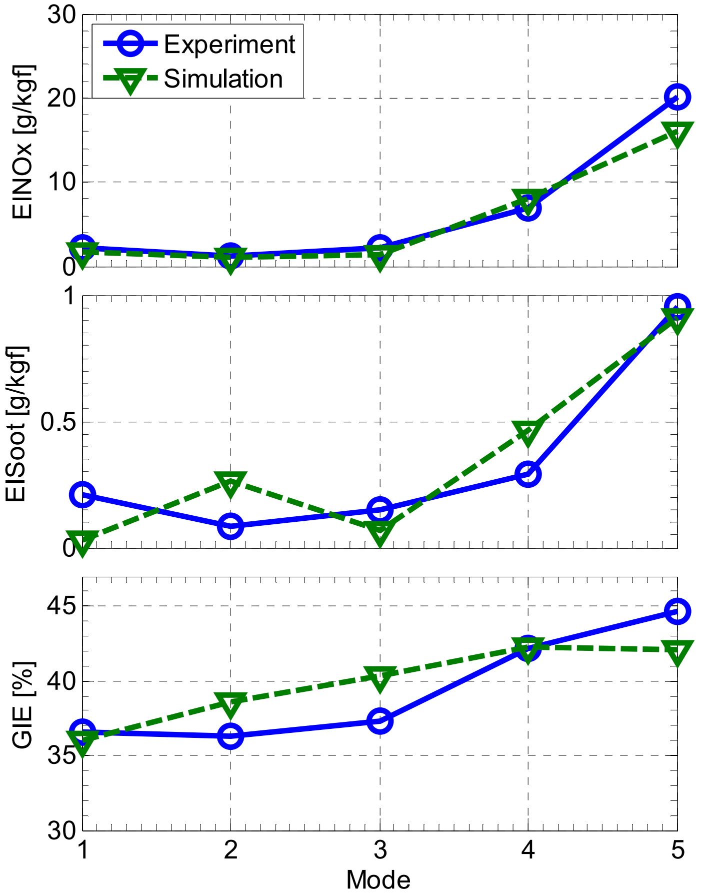

Figure 7-3. Comparison of measured and predicted NOx, soot, and GIE at each operating point.

captured reasonably well; however, it can be seen that the simulations under-predict the GIE at mode 5 and over-predict the GIE at modes 2 and 3. Since parameter sweeps were performed at each condition to maximize the GIE, the agreement is deemed acceptable.

Figure 7-4 shows the cycle averaged NOx, soot, and GIE calculated using Eqn. 7-1. The simulations capture the cycle averaged emissions and performance well. NOx emissions are slightly under-predicted and efficiency is slightly over-predicted by the simulations. Thus, it appears that the simulations will provide “best-case” estimates of CDC emissions and performance.

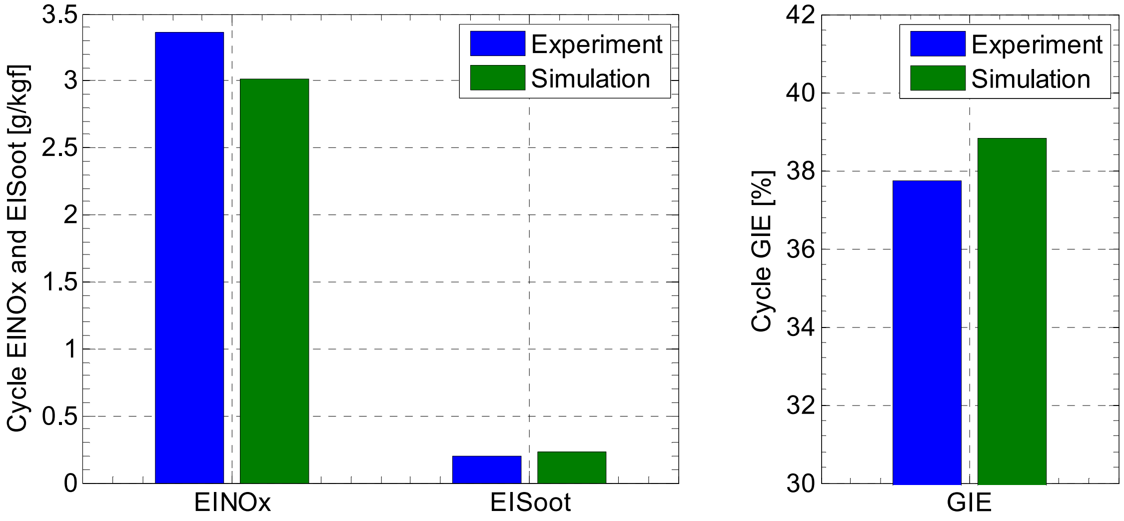

Figure 7-4. Comparison of measured and predicted cycle averaged NOx, soot, and GIE.

7.5 Selection of NOx Targets to Meet US Tier 2 – Bin 5 Regulations

The NOx targets were selected based on the work of Cooper et al. [110] and are based on a 3500 lb vehicle powered by a 2.0 L engine. Cooper presented targets at 4 loads: 3 bar, 6.6 bar, 10.8 bar, and 17.2 bar gross IMEP. The NOx targets used in the present study were selected by interpolating between the NOx targets of Cooper et al. [110], see Figure 7-5. Note that the 2.3

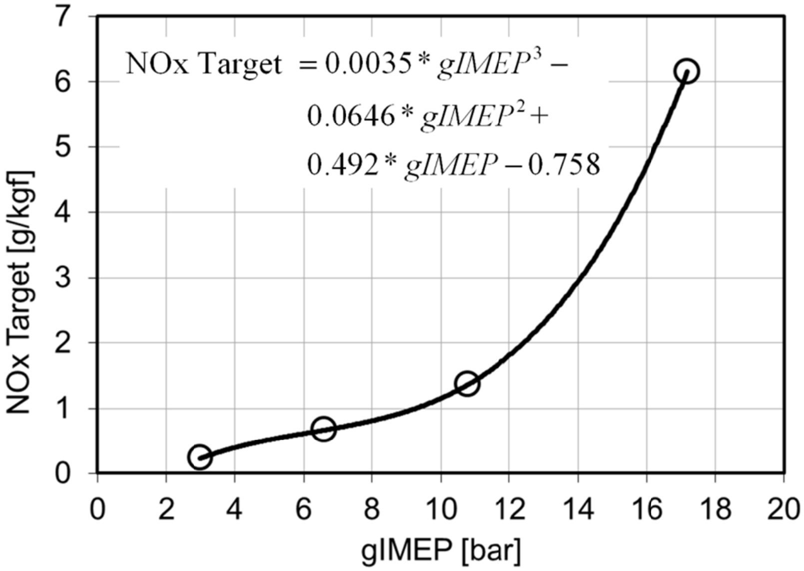

Figure 7-5. Curve fit used to calculate the NOx targets at each load point. The points on the curve are taken from Cooper et al. [110].

bar IMEP point is outside of the range covered by Cooper's work. By extrapolation, the NOx target for the 2.3 bar IMEP point was estimated at 0.2 g/kgf. The specific targets at each operating condition are shown in Table 7-4.

Table 7-4. NOx targets based on Cooper et al. [110].

Mode	1	2	3	4	5
Speed (rpm)	1500	1500	2000	2300	2600
IMEPg (bar)	2	3.9	3.3	5.5	9
NOx Target (g/kgf)	0.2	0.4	0.3	0.6	1.0

7.6 Operating Conditions

Parametric studies were performed to maximize the GIE for each investigation; however, the primary purpose of this study is to provide a high-level comparison of CDC and RCCI combustion and demonstrate a methodology to compare the combustion modes rather than fully optimize each individual combustion strategy. Although every attempt was made to present optimum fuel economy points, the design space is very large and thus it is expected that minor improvements in the GIE-NOx tradeoff may be possible. Further, this study focuses on fuel economy and NOx emissions and no attempt was made to minimize soot emissions.

RCCI is compared to five CDC operating points at each test mode. The operating conditions common between all cases are shown in Table 7-5 and the operating point specific conditions are shown in Table 7-6. The five CDC operating points are discussed below.

1) **Euro 4 Baseline**: EGR rates and SOI timings are set to the model validation points shown in Table 7-3. NOx constraints are not imposed for this case.

2) **CDC - Peak GIE – Euro 4 EGR**: EGR rates are set to the same as the Euro 4 Baseline cases. The pilot and main SOI timings are set to give maximum GIE. NOx constraints are not imposed for this case.

3) **CDC – Bin 5 NOx – Euro 4 EGR + SCR**: EGR rates are set to the same as the Euro 4 Baseline cases. The pilot and main SOI timings are set to give maximum GIE considering the DEF required to reduce NOx to Tier 2-Bin 5 levels.

4) **CDC - Peak GIE – Half of Euro 4 EGR**: EGR rates are set to half of the Euro 4 Baseline cases. The pilot and main SOI timings are set to give maximum GIE. NOx constraints are not imposed for this case.

5) **CDC - Bin 5 NOx – Half of Euro 4 EGR + SCR**: EGR rates are set to half of the Euro 4 Baseline cases. The pilot and main SOI timings are set to give maximum GIE considering the DEF required to reduce NOx to Tier 2-Bin 5 levels.

Table 7-5. Operating conditions common for all comparisons.

Mode	1	2	3	4	5
IMEPg (bar)	2.3	3.9	3.3	5.5	9
Speed (rev/min)	1500	1500	2000	2300	2600
Total Fuel (mg/inj.)	5.6	9.5	8	13.3	20.9
Intake Temp. (deg. C)	60	60	70	67	64
Intake Press. (bar abs.)	1	1	1	1.3	1.6

Table 7-6. Detailed operating conditions for the RCCI cases and each CDC case at the five operating modes.

			CDC Case 1	CDC Case 2	CDC Case 3	CDC Case 4	CDC Case 5
		RCCI	Euro 4 Baseline	Peak GIE Euro 4 EGR	Bin 5 Nox Euro 4 EGR + SCR	Peak GIE Half of Euro 4 EGR	Bin 5 NOx Half of Euro 4 EGR + SCR
Mode 1	EGR Rate (%)	61	47	47	47	23.5	23.5
	Percent Gasoline (%)	0	0				
	CR Inj. Pressure (bar)	500	330				
	Pilot SOI (°ATDC)	-33	-5.8	-14.4			
	Main SOI (°ATDC)	-8	1.6	-6	-6	-6	-3
	Diesel fuel in pilot (%)	42	34				
	DEF (%)	0	0	0	0.9	0	4.2
Mode 2	EGR Rate (%)	0	38	38	38	19	19
	Percent Gasoline (%)	80	0				
	CR Inj. Pressure (bar)	500	400				
	Pilot SOI (°ATDC)	-58	-7.2	-20.2			
	Main SOI (°ATDC)	-37	0	-5	-5	-14	-4
	Diesel fuel in pilot (%)	60	16				
	DEF (%)	0	0	0	0.8	0	4.8
Mode 3	EGR Rate (%)	0	42	42	42	21	21
	Percent Gasoline (%)	55	0				
	CR Inj. Pressure (bar)	500	500				
	Pilot SOI (°ATDC)	-58	-8.2	-15.8			
	Main SOI (°ATDC)	-37	1.6	-6	-6	-4	-2
	Diesel fuel in pilot (%)	60	15				
	DEF (%)	0	0	0	0.7	0	3.9
Mode 4	EGR Rate (%)	0	25	25	25	12.5	12.5
	Percent Gasoline (%)	80	0				
	CR Inj. Pressure (bar)	500	780				
	Pilot SOI (°ATDC)	-58	-11.68	-17.6			
	Main SOI (°ATDC)	-37	-0.08	-6	-6	-5	-3
	Diesel fuel in pilot (%)	60	10				
	DEF (%)	0	0	0	3.0	0	5.0
Mode 5	EGR Rate (%)	36	15	15	15	7.5	7.5
	Percent Gasoline (%)	88.5	0				
	CR Inj. Pressure (bar)	500	1100				
	Pilot SOI (°ATDC)	-58	-18.6	-23			
	Main SOI (°ATDC)	-37	-2.6	-7	-7	-8	-7
	Diesel fuel in pilot (%)	60	5				
	DEF (%)	0	0	0	4.6	0	6.9

7.6.1 Selection of RCCI Cases

The RCCI cases at modes 2-5 all used the same injection strategy developed in Chapter 4 and fine-tuned in Chapter 6: a split injection with a first pulse at -58° ATDC and a second pulse at -37° ATDC with 60% of the injected diesel fuel delivered in the first pulse. As demonstrated in the metal engine experiments of Chapter 6, the combustion phasing (i.e., the GIE-PRR tradeoff), was controlled by adjusting the gasoline percentage at each condition. Modes 2-4 did not require EGR to control combustion phasing; however, at mode 5 (9 bar IMEP – 2600 rev/min), combustion phasing could not be retarded enough using the gasoline percentage alone; therefore EGR was added to aid in combustion phasing control. The EGR rate at mode 5 is 36%.

At mode 1 (2 bar IMEP – 1500 rev/min), HCCI calculations showed that the optimum combustion phasing is achieved without using gasoline. Therefore, the RCCI strategy reverts to a diesel LTC strategy at the mode 1. To control NOx in the diesel LTC strategy, the inlet oxygen concentration must be significantly reduced; thus, the mode 1 RCCI point (diesel LTC point) uses 61% EGR. Recall that the RCCI engine is assumed to operate without NOx aftertreatment; therefore, all of the presented RCCI cases are selected to meet NOx targets in-cylinder.

7.6.2 Selection of CDC Cases

The baseline CDC cases are the Euro 4 operating conditions used for model validation (see Table 7-3). Two sets of SOI timing sweeps were used to control the GIE-NOx tradeoff of the CDC cases. First, main SOI timing sweeps were performed where the pilot and main SOI timings were moved together (i.e., the dwell time between the pilot and main was held constant). It was necessary to move the pilot and main SOI timings together because the baseline operating point has a close-coupled pilot injection and the SOI timing needed to be significantly advanced beyond the Euro 4 calibration presented in Table 7-3 to maximize efficiency. The pilot-SOI timing providing peak efficiency was selected as the pilot SOI timing used for the final set of main SOI timing sweeps. The CDC engine is assumed to be equipped with NOx aftertreatment; therefore, it may be possible to improve the efficiency by operating at a lower EGR rate. Two levels of EGR were evaluated for the CDC case: the baseline Euro 4 EGR (see Table 7-3) and half of the Euro 4 EGR level. The results will show that these two EGR levels are sufficient to extract the necessary trends. Figure 7-6 shows the GIE-NOx tradeoff for CDC combustion at each operating mode over the main SOI timing sweeps.

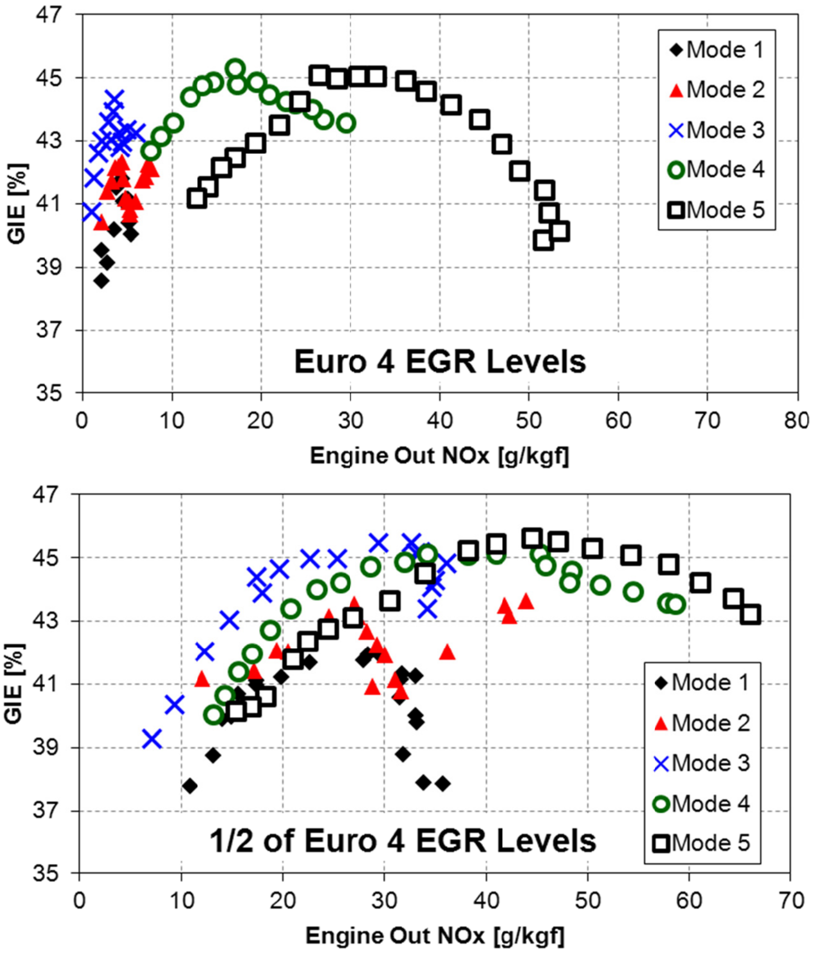

Figure 7-6. GIE-NOx tradeoff for the CDC cases.

The purpose of the present study is to compare CDC and RCCI combustion as methods to meet Tier 2 – Bin 5 NOx targets. Since RCCI is able to meet NOx targets in-cylinder, a fair comparison between CDC and RCCI combustion should consider the cost (i.e., fluid consumption) required to meet NOx emissions targets. Two options were considered for NOx reduction for the CDC strategy:

1) Retard the injection timing to comply with emissions targets.
2) Add SCR[7] and consider the diesel exhaust fluid (DEF) consumed in the SCR in the efficiency calculations.

A preliminary study considering only injection timing retard as a NOx control strategy showed very poor performance (cycle-averaged GIE was reduced to less than 35%). Thus, a combination of SCR and injection timing retard was used as a method to meet NOx targets. The cases were selected using the following procedure: First, main SOI timing sweeps were performed at each mode and each EGR level. Second, the quantity of DEF required to meet NOx targets was calculated as

$$\%DEF = \left(NOx_{EngineOut} - NOx_{\text{Target}}\right)*1\left[\frac{\%DEF}{g_{NOx}/kW-hr}\right], \tag{7-2}$$

where $NOx_{EngineOut}$ is the indicated specific engine out NOx, NOx_{Target} is the indicated specific NOx target, and the multiplier is 1 %DEF per g/kW-hr NOx reduction [4]. Third, the total GIE (considering the DEF consumption) is calculated as

$$GIE_{Total} = \frac{Work_{-180\text{ to }180}}{\left(m_{DEF} + m_{Fuel}\right)*LHV_{Fuel}}\times 100, \tag{7-3}$$

---

[7] Lean NOx traps (LNT) are also promising methods to reduce NOx emissions without the requirement of an additional fluid. However, LNT's require periodic rich operation for regeneration; thus, the analysis of an LNT equipped engine must include the fuel economy penalty resulting from the regeneration. To simplify the analysis in this study, only the SCR option, where it is straightforward to include the additional fluid consumption, is considered.

where m_{DEF} is the mass of the diesel exhaust fluid, m_{Fuel} is the mass of the fuel, LHV_{Fuel} is the lower heating value of the fuel[8], and $Work_{-180\ to\ 180}$ is the indicated work from bottom-dead-center (BDC) of the compression stroke to BDC of the expansion stroke. The work during the open portion of the cycle (i.e., BDC to IVC and EVO to BDC) was taken from the measured pressure traces of the model validation experiments.

As an example, Figure 7-7 shows NOx emissions, DEF consumption, and GIE as a function of main injection timing at the Mode 5 operating point in the conventional diesel combustion mode at the two EGR levels considered. At the Euro 4 EGR level, the peak efficiency point with and without consideration of the DEF consumption occurs at the same main SOI timing. When the EGR level is reduced, the peak efficiency point (without a NOx constraint) uses a main SOI timing of -8° ATDC giving a GIE of 45.6% and an engine out NOx level of 45 g/kgf. At this point the DEF quantity is 7.5% of the total fluid mass; however, the GIE curve considering DEF consumption shows that the DEF consumption can be reduced, resulting in a slight-improvement in total fluid consumption, by retarding the injection timing to -7° ATDC. This tradeoff for the lower EGR case shows the importance of considering total fluid consumption in the analysis.

---

[8] This analysis assumes that the “value” of DEF and diesel fuel are equal. The methodology is still valid when DEF and diesel fuel are at different prices; however, the total GIE should be recalculated based on the weighted masses of DEF and diesel fuel.

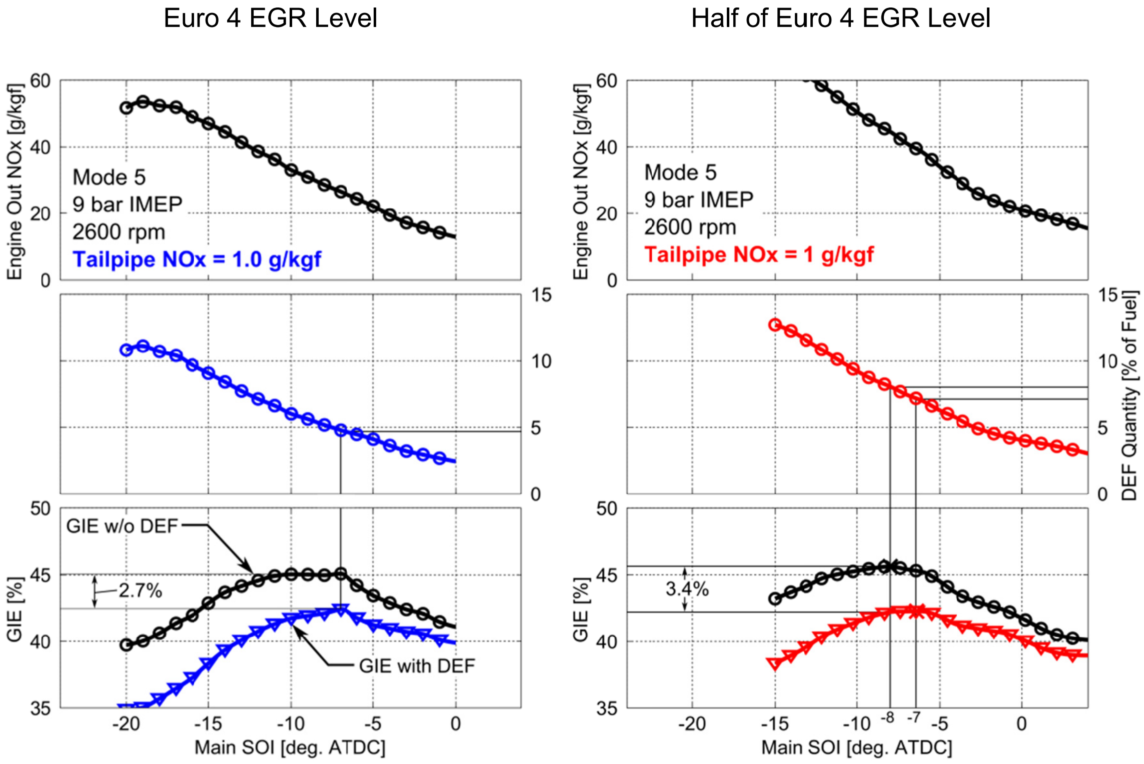

Figure 7-7. Engine out NOx (i.e., before SCR), quantity of DEF required to meet NOx target, and GIE with and without consideration of DEF at the Mode 5 operating point for the two EGR levels considered.

7.7 Results

Figure 7-8 shows the GIE and NOx emissions for each case. Compared to the baseline Euro 4 case (CDC Case 1), the RCCI strategy shows higher GIE and lower NOx emissions over the entire operating range. At the lightest load condition (mode 1), the improved CDC cases (CDC Cases 2-5) are capable of achieving higher GIE than RCCI. However, recall that the RCCI case at mode 1 is a diesel LTC case with 61% EGR. At modes 2-5, the RCCI cases show higher GIE than any of the CDC cases. Further, RCCI meets the Tier 2 – Bin 5 NOx targets in-cylinder. Conversely, the CDC cases require NOx aftertreatment to meet the Tier 2 – Bin 5

NOx targets. CDC Case 2 shows the peak GIE achievable at the Euro 4 EGR levels without imposing NOx constraints. CDC Case 3 shows the GIE penalty (i.e., DEF penalty) associated with meeting Tier 2 – Bin 5 NOx targets. Notice that, since the EGR levels of the Euro 4 baseline CDC case are relatively high at modes 1-3 (38% to 47%), the DEF penalty is very small. At modes 4 and 5, the DEF penalty increases due to the lower EGR rates and higher engine out NOx.

CDC Case 4 shows that removing EGR from the conventional diesel cases improves the GIE. However, notice the GIE of CDC Case 4 (which does not meet NOx targets) is significantly below the RCCI points for modes 2-4. Although, removing EGR from the CDC case results in an increase in the GIE, when the DEF required to reduce NOx to Tier 2-Bin 5 levels is considered, the improvement in GIE is removed. In fact, the higher EGR diesel case with SCR (CDC Case 3) shows higher efficiency than CDC Case 5 over the entire range of conditions.

Figure 7-9 shows the cycle averaged GIE, NOx, and soot emissions. At the peak GIE points (CDC Cases 2-5), the engine out, cycle-averaged NOx emissions of the CDC cases are an order of magnitude above the target value. All cases achieve acceptable cycle-averaged soot levels (less than 0.3 g/kgf).

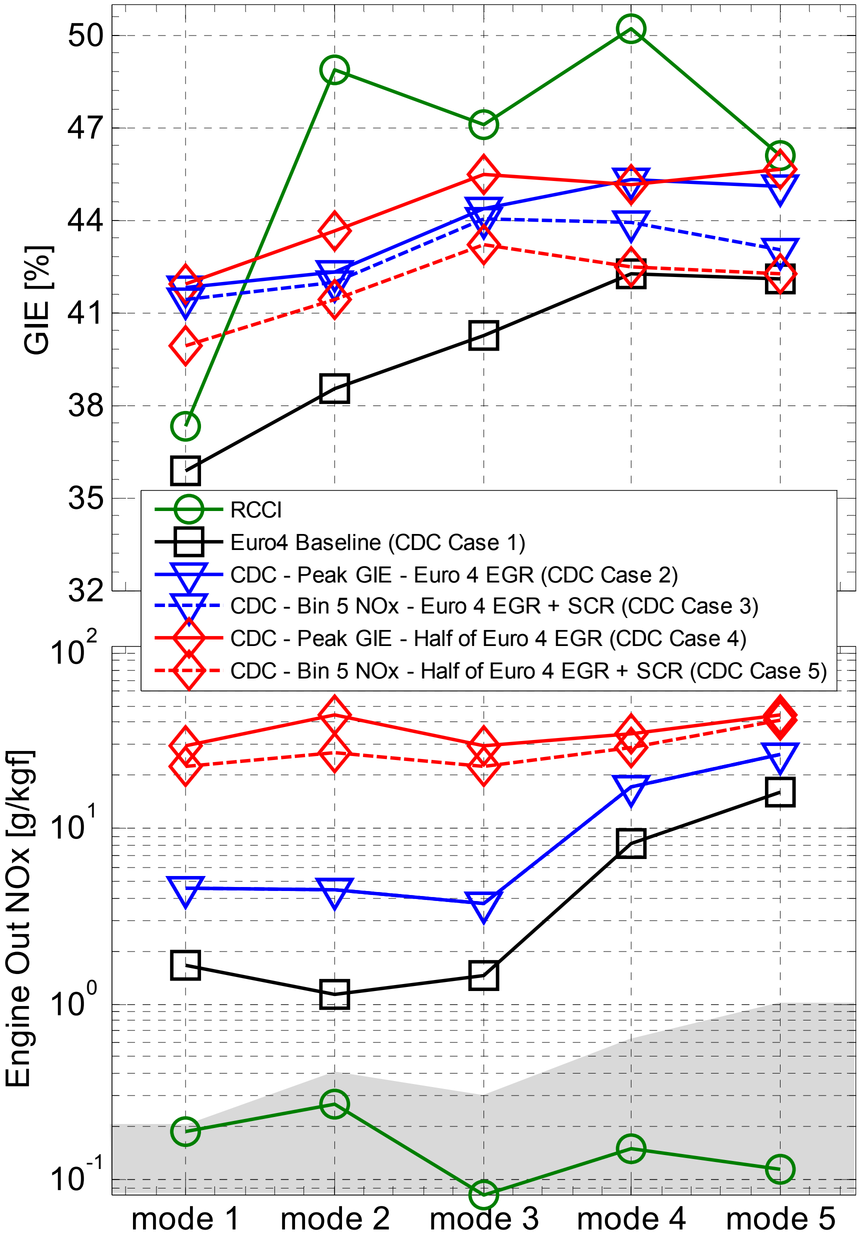

Figure 7-8. GIE and engine out NOx emissions at each operating mode. Engine out NOx is defined as the NOx level before the aftertreatment. Note the log scale on the y-axis of the NOx plot. The shaded area on the NOx plot indicates the Tier 2-Bin 5 target NOx levels. Also, the engine out NOx of CDC Cases 2 and 3 are on top of each other. The operating conditions are shown in Table 7-6.

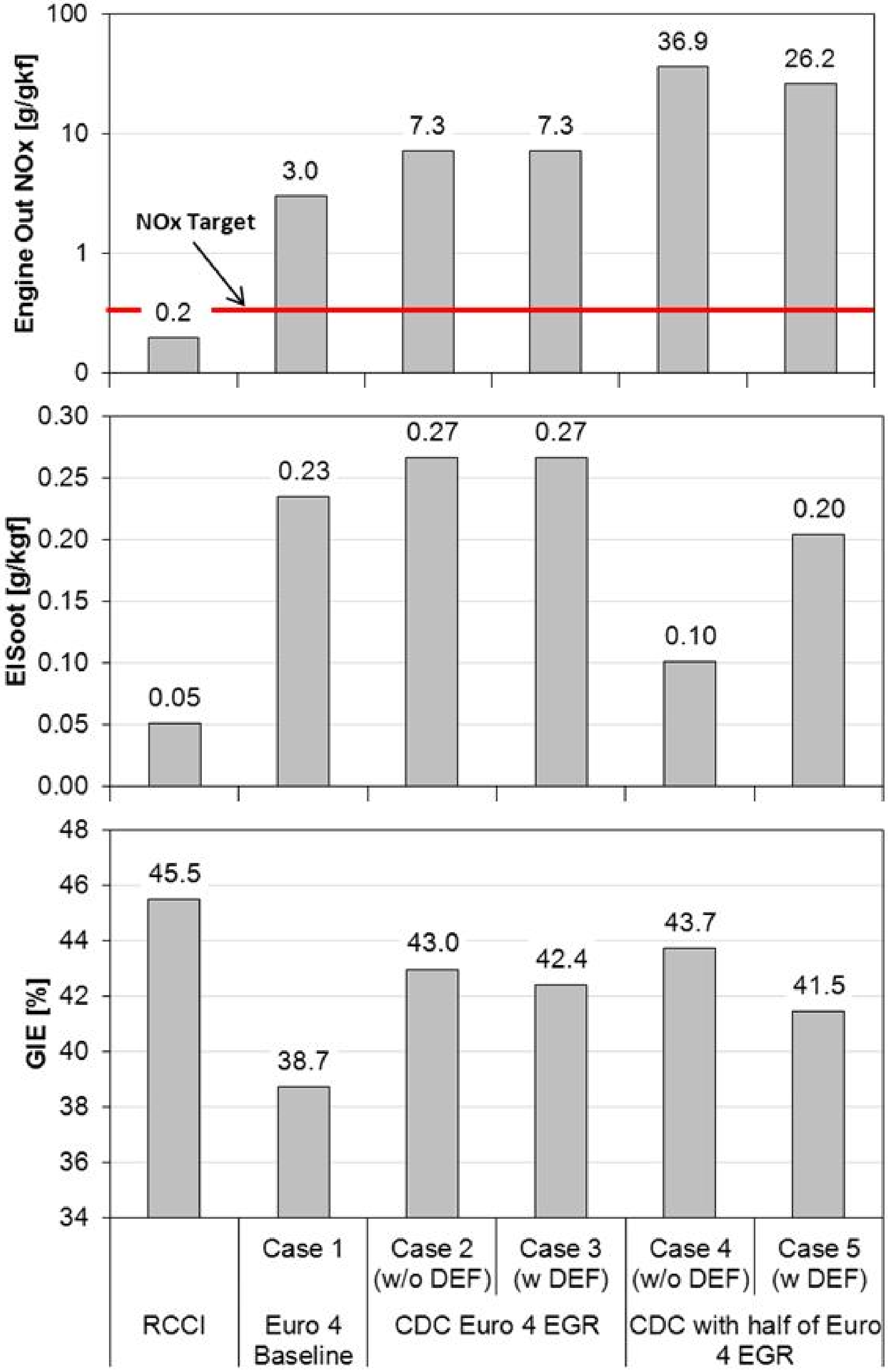

Figure 7-9. Cycle-averaged NOx, soot, and GIE for CDC, diesel LTC, and RCCI combustion with no NOx constraints. Note the log scale on the y-axis of the NOx plot. The solid red line on the NOx plot shows the cycle-averaged NOx target, 0.4 g/kgf.

The RCCI mode shows the highest cycle averaged GIE, 45.5%. The late injection timing of the Euro 4 calibration (CDC Case 1) results in a rather low cycle averaged GIE of only 38.7%. Advancing the injection timing (CDC Case 2) improves the cycle averaged GIE to 43%; however, when the fluid consumption penalty to meet Tier 2 – Bin 5 NOx levels is considered (CDC Case 3), the GIE is reduced to 42.4%. Reducing the EGR to half of the Euro 4 calibration level (CDC Case 4) improves the GIE to 43.7%; however, when the DEF penalty is considered (CDC Case 5), the GIE is reduced to 41.5%. Figure 7-10 shows the cycle averaged DEF consumption for each case. The lower EGR of Case 5 results in ~4 times higher NOx emissions than Case 3, causing the factor of 4 increase in DEF consumption.

To explain the improved thermal efficiency of RCCI combustion, Figure 7-11 shows the cycle averaged heat transfer losses. The Euro 4 Baseline (CDC Case 1) has the lowest heat transfer losses. However, the low heat transfer losses are due the very late combustion phasing,

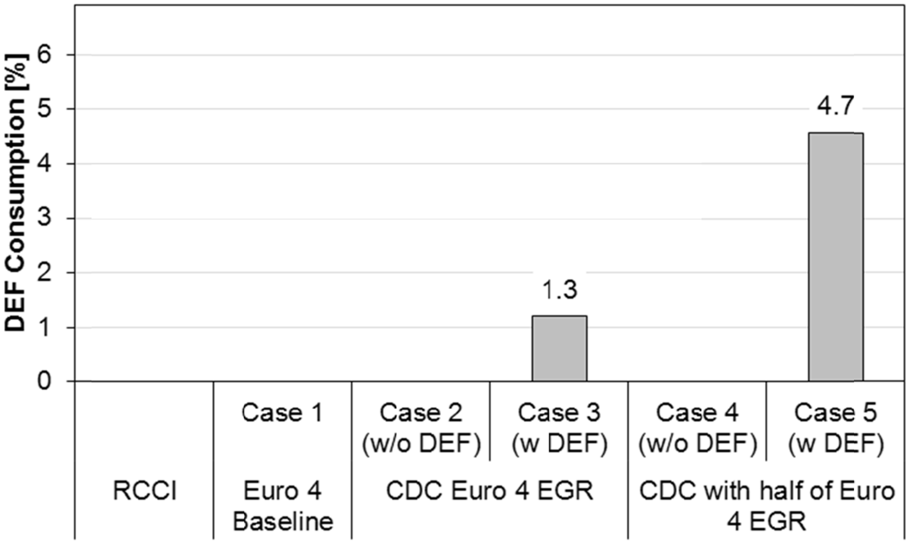

Figure 7-10. Cycle averaged DEF consumption.

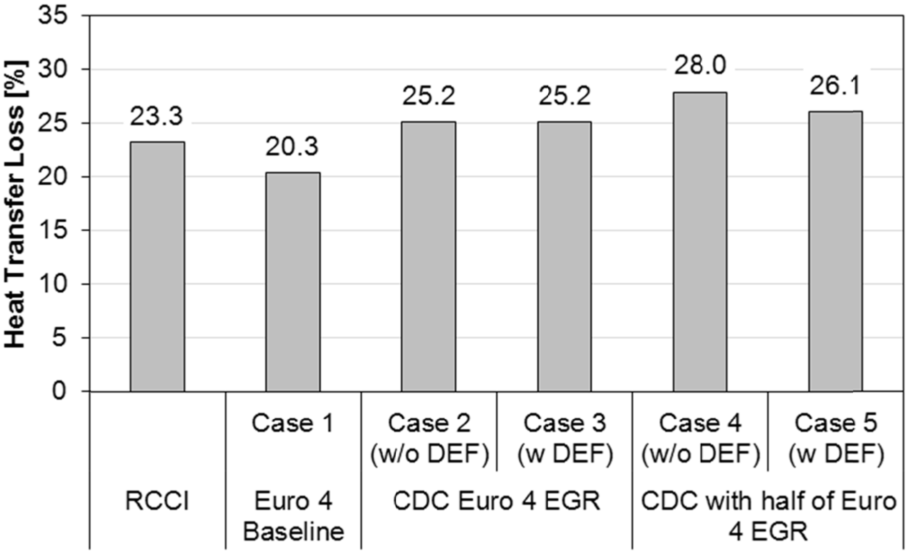

Figure 7-11. Cycle-averaged heat transfer losses as a percent of fuel energy.

which reduces the GIE significantly. The RCCI case shows the second lowest heat transfer losses (23.3% of the fuel energy). CDC Cases 2 and 3 have heat transfer losses of 25.2% of the fuel energy. The lower EGR of CDC case 4 increases the heat transfer losses to 28% of the fuel energy. Case 5 has slightly later injection timings than CDC Case 4, resulting in lower heat transfer losses. As was shown in the comparisons of CDC and RCCI in the heavy-duty engine, Figure 7-11 shows that the primary reason for the higher efficiency of RCCI combustion is the reduced heat transfer losses that results from lower flame temperatures and avoidance of high temperature regions near surfaces.

7.8 Discussion

Detailed CFD modeling was used to compare conventional diesel combustion and RCCI combustion in a light-duty engine at five operating modes representative of the light-duty drive cycle. The results showed RCCI is capable of meeting cycle-average NOx targets (equivalent to Tier 2-Bin 5) without NOx aftertreatment. Even without considering the fuel consumption penalty associated with NOx aftertreatment, RCCI shows at least a 4% improvement in fuel consumption over conventional diesel combustion. When the DEF penalty is considered, RCCI shows a 7.3% improvement in fuel consumption. The fuel consumption improvement is due primarily to lower heat transfer losses.

There are benefits and difficulties associated with both combustion modes. The CDC case is the most developed and control is likely the most robust. However, the addition of SCR adds significant cost to the engine system and adds the requirement of an additional fluid that perform no useful work. In the stock configuration, the RCCI case achieves the highest efficiency and has the potential for further efficiency improvements by lowering the swirl ratio and replacing the stock aluminum piston with a steel piston as discussed in Chapter 7; however, similar to the CDC+SCR strategy, RCCI requires a secondary fluid. Additionally, control of an RCCI combustion will likely be more challenging than conventional diesel combustion.

Chapter 8

Experimental Setup for the Optical Investigation of RCCI Combustion

Chapter 4 to Chapter 7 highlighted the development of the RCCI combustion process using a combination of CFD modeling and metal engine experiments. The focus of the previous chapters was to explain the performance benefits of RCCI combustion and demonstrate the application of RCCI combustion over a range of conditions and engine platforms. The model predictions were shown to accurately reproduce the combustion characteristics and engine out emissions. The simulations were used to explain the processes controlling RCCI combustion (see Chapter 5); however, without validation from optical engine experiments, it is difficult to know if the simulation predictions of the in-cylinder combustion processes are accurate. Accordingly, Chapter 9 and Chapter 10 will use a range of optical diagnostics to validate the model prediction and improve the understanding of the details of the RCCI process. This chapter discusses the experimental setup, operating conditions, optical diagnostics applied to the engine operating in the RCCI combustion mode.

8.1 Engine Specifications

The same optical engine discussed in model validation of Section 3.2 was used for this study. The engine specifications are given in Table 8-1 and a schematic of the combustion chamber is given in Figure 8-1. The research engine is typical of a heavy-duty diesel engine with a 13.97 cm bore and 15.24 cm stroke giving a displacement of 2.34 L per cylinder. The intake port geometry of the production engine, which has a steady-state (i.e., measured on a flow-bench) swirl ratio of 0.5 [111], is preserved in the research engine. To allow optical access, the engine is equipped with an extended piston and the stock metal piston bowl has been replaced with a flat fused silica piston crown window. Further, one of the two exhaust valves has been replaced with a window, and a periscope mirror in the rocker box gives a view of the squish region (i.e., the region above the piston bowl-rim). Four windows are also located around the upper portion of the cylinder wall to allow cross-optical access for laser based diagnostics. A complete description of the engine development is available in Refs. [85, 112].

Table 8-1. Sandia heavy-duty optical engine specifications.

Engine base type	Cummins N-14, DI diesel
Number of cylinders	1
Cycle	4-stroke
Number of intake valves	2
Number of exhaust valves	1[1]
Combustion chamber	Quiescent, flat bowl
Swirl Ratio	0.5 (approximate)
Bore	13.97 cm [5.5 in]
Stroke	15.24 cm [6.0 in]
Bowl width	9.78 cm [3.58 in]
Displacement	2.34 liters [142 in^3]
Connecting rod length	30.48 cm [12.0 in]
Piston pin offset	None
Geometric compression ratio	10.75:1

[1] One of the two exhaust valves of the production cylinder head has been replaced by a window and periscope

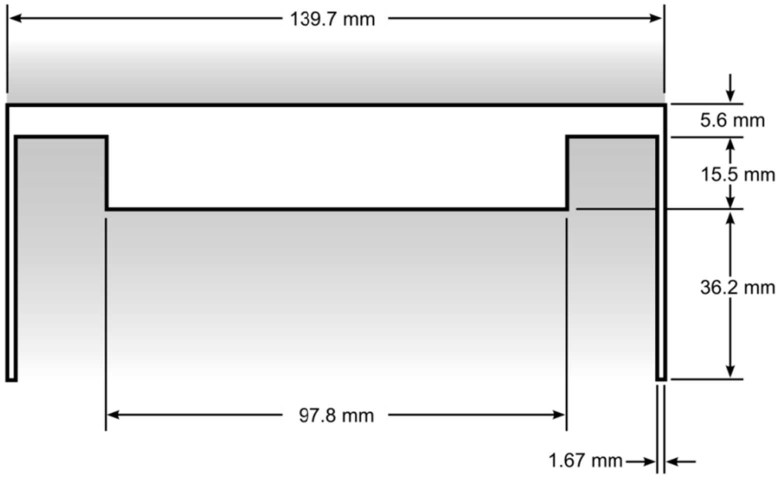

Figure 8-1. Layout of combustion chamber at TDC.

8.1.1 Fuel Injection Systems

RCCI combustion is achieved using in-cylinder blending of two fuels with different auto-ignition characteristics. In the metal engine experiments presented in Chapter 5 and Chapter 6, port-fuel-injection of gasoline and direct-injection of diesel fuel was used; however, multi-component gasoline and diesel fuels contain molecules that fluorescence when illuminated by ultraviolet light, which would interfere with the toluene fuel-tracer fluorescence diagnostic (described later). Hence, to facilitate the fuel-tracer measurements, purified gasoline primary reference fuel (PRF) components (i.e., n-heptane and iso-octane) were used because they display insignificant fluorescence interference. A charge of high-purity (99% or better) iso-octane was created using a gasoline direct injection (GDI) system. The GDI injector is mounted in a metal blank in place of one of the optical access windows formerly located in the cylinder liner (see e.g., Figure 8-2). The specifications of the GDI injector are provided in Table 8-2. The GDI has a 7-hole, asymmetric tip, with all seven holes located on one hemisphere of the injector. This hole layout prevented fuel impingement on the cylinder head when mounted in the cylinder wall window (i.e., perpendicular to the axis of the piston). HPLC-grade n-heptane was pressurized to 600 bar by a Newport Scientific high-pressure diaphragm pump and delivered through a Cummins XPI high-pressure, electronically-controlled, common-rail (CR) fuel injector with specifications given in Table 8-3. The injector is capable of multiple injections at up to 2000 bar injection pressure. For the present study, an 8-hole mini-sac tip was installed. Each hole of this tip, has a nominal orifice diameter of 140 microns with no hydrogrounding (i.e., the edges are sharp). The nozzle has an included angle of 152° (14° downward from the fire deck, i.e., the bottom surface of the cylinder head exposed to the combustion chamber). Finally, to minimize thermal loading, the engine was only fired 1 out of 10 cycles.

Table 8-2. Gasoline direct injector (GDI) specifications.

Injector type	Bosch GDI
Fuel	high-purity (99%+) iso-octane
Number of holes	7, asymmetric
Supply pressure	100 bar
Nominal orifice diameter	150 micron

Table 8-3. XPI common-rail (CR) fuel injector specs.

Injector type	common-rail, solenoid actuated
Fuel	HPLC-grade n-heptane
Cup (tip) type	mini-sac
Number of holes	8, equally spaced
Included angle	152°
Rail pressure	600 bar
Orifice treatment	none (square-edged)
Nominal orifice diameter	140 micron

8.1.2 Operating condition

The baseline engine operating conditions are shown in Table 8-4. These conditions were selected to be similar to the metal engine experiments presented in Chapter 4. The engine was operated at a speed of 1200 rev/min and a gross indicated mean effective pressure (IMEP) of 4.2 bar. This light-load condition was chosen to avoid damaging the large piston crown window. Under the baseline operating conditions, the peak heat-release rate for the 4.2 bar load is well below the allowable threshold for the optical engine. However, some conditions in a parametric variation of injection timing in part of a larger study (see Chapter 10) have much higher peak heat-release rates, so the engine load was restricted to 4.2 bar IMEP.

With the intent of creating a well-mixed charge of iso-octane, 41 mg of iso-octane was delivered through the GDI injector at -240° ATDC (during the intake stroke) at an injection pressure of 100 bar. The n-heptane was delivered through the common-rail injector at a pressure of 600 bar using a split-injection with a first pulse beginning at -57° ATDC and a second pulse beginning at -37° ATDC. These injection timings were selected to be similar to the CFD modeling and metal engine experiments presented in Chapter 4. The total injected mass of n-heptane was 21 mg and approximately 60% of the n-heptane was delivered in the first injection (i.e., at -57° ATDC). The engine was operated without dilution (i.e., the inlet oxygen concentration was 21% by volume) and the intake pressure was set to slightly above atmospheric at 1.1 bar absolute. The intake temperature was set to 90° C and the resulting charge density at TDC was 11.1 kg/m^3.

Table 8-4. Engine operating condition for the baseline RCCI optical engine experiments.

Engine speed	1200 rpm
Gross IMEP	4.2 bar
Intake temperature	90°C
Intake pressure	1.1 bar abs.
Inlet oxygen concentration	21 vol. %
GDI injection pressure	100 bar
CR injection pressure	600 bar
GDI SOI (command)	-240° ATDC
CR SOI 1/2 (actual)	-57°/-37° ATDC
Actual GDI DOI	36° CA
Actual CR DOI1/DOI2	7°/4° CA
Total injected fuel mass	62 mg
iso-octane mass (GDI)	66%
n-heptane mass (CR)	34%
Quantity of injected fuel in CR Inj. 1	12.6
Quantity of injected fuel in CR Inj. 2	8.4
Premixed (iso-octane) equivalence ratio	0.27
Overall equivalence ratio	0.42
Nom. motored TDC density	11.1 kg/m3
Nom. motored TDC temperature	835 K

8.2 Conventional Data acquisition

Cylinder pressure was measured with an AVL QC43D piezoelectric transducer at ¼° crank angle increments and the measurements were set to match (pegged to) the intake pressure near bottom dead center (BDC). The apparent heat-release rate (AHRR) was calculated from the measured pressure data using the standard first-law analysis (e.g., Heywood [87]) with constant gas properties. Prior to calculating the AHRR, the cylinder pressure data were smoothed using a

Fourier series low-pass filter with a Gaussian roll-off function having a transmission of 100% from 0 to 800 Hz and dropping to 1% at 3360 Hz.

8.3 Optical Diagnostics

8.3.1 High Speed Combustion Luminosity Imaging

Figure 8-2 shows the experimental setup used to record high speed combustion luminosity. Crank-angle resolved combustion luminosity was recorded with an unintensified Phantom 7.1 complementary metal oxide semiconductor (CMOS) high-speed camera (HSC). Unless otherwise indicated, a 50-mm glass Nikkor lens with the aperture fully open (f/1.2) was used. High speed combustion luminosity was recorded in two locations: with the camera viewing upward through the piston crown window and with the camera viewing downward into the squish region through the cylinder head window. The unintensified CMOS camera is not sensitive in the UV range; accordingly, OH* does not contribute to the recorded combustion luminosity. Furthermore, a combination of a 500 nm short-wave pass (SWP) filter and a BG39 colored glass filter were used to reject long-wavelength (green through IR) soot luminosity (if present). The recorded luminosity is likely chemiluminescence from CH_2O^*, HCO*, CH*, and CO_2^* and broadband emission from the CO continuum [13, 113]. The HSC images were acquired with a resolution of 512 x 512 pixels and the exposure time for each frame was 125 μs. The long exposure time was required to collect reasonable light levels with the non-intensified HSC used in this study. Although the long exposure time results in a small amount of smearing for cases showing rapid energy release, the smearing does not influence the conclusions of the study.

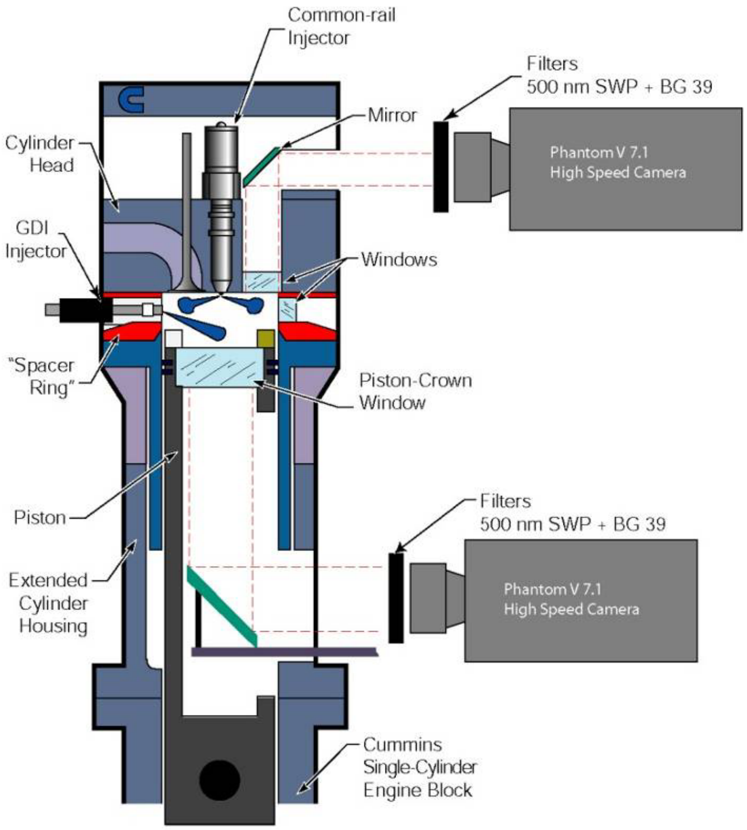

Figure 8-2. Schematic of the optically accessible research engine showing the camera setup for the high-speed chemiluminescence imaging study.

8.3.2 Fuel Tracer Fluorescence

Quantitative fuel-vapor concentrations were measured using toluene fuel-tracer fluorescence. The toluene fuel-tracer fluorescence study was conducted at the same thermodynamic conditions as those presented in Table 8-4; however, to avoid complications from oxygen quenching of the toluene fluorescence, the intake was supplied with 100% nitrogen. Further, HPLC n-heptane doped with 1% toluene was used in both the GDI and common-rail fuel systems for quantitative fuel distribution measurements. Previous work (e.g., Genzale et al. [111]) showed that this toluene concentration provided a good balance between signal strength and attenuation of the laser light. The same toluene-doped n-heptane was used in both fuel systems (for the non-combusting conditions) to avoid uncertainties in the toluene fluorescence yield in different solvents.

Figure 8-3 shows the laser sheet and imaging setup for the toluene fluorescence study. The toluene fluorescence was excited by the 266-nm output of a frequency-quadrupled Nd:YAG laser. The laser beam was formed into a thin sheet (less than 1 mm thick) using a combination of a negative cylindrical lens (f = -50 mm) and positive plano-spherical lens (f = 500 mm). The low-intensity tails on either end of the sheet were clipped to leave the center of the beam, with relatively uniform intensity. After being clipped, the sheet passing through the window was approximately 31 mm wide with a remaining energy of 26 mJ per pulse.

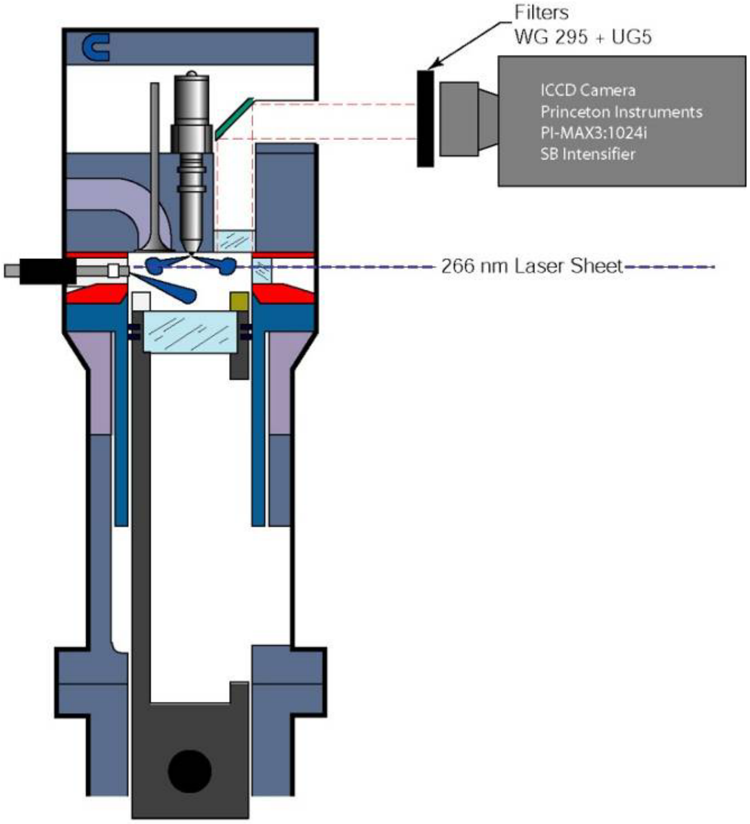

Figure 8-3. Schematic of the optically accessible research engine showing the camera setup for the toluene fuel tracer fluorescence imaging.

Images were acquired at two laser sheet heights. Figure 8-4 shows a schematic of the two laser sheet setups. Early cycle images of the mixing process (from -50° ATDC to -21° ATDC) were acquired with the laser sheet located 10 mm below the firedeck[9] as indicated in Figure 8-4 (a). Notice that these images were acquired with the camera (discussed below) viewing downward into the squish region (i.e., above the piston bowl rim). At -21° ATDC the

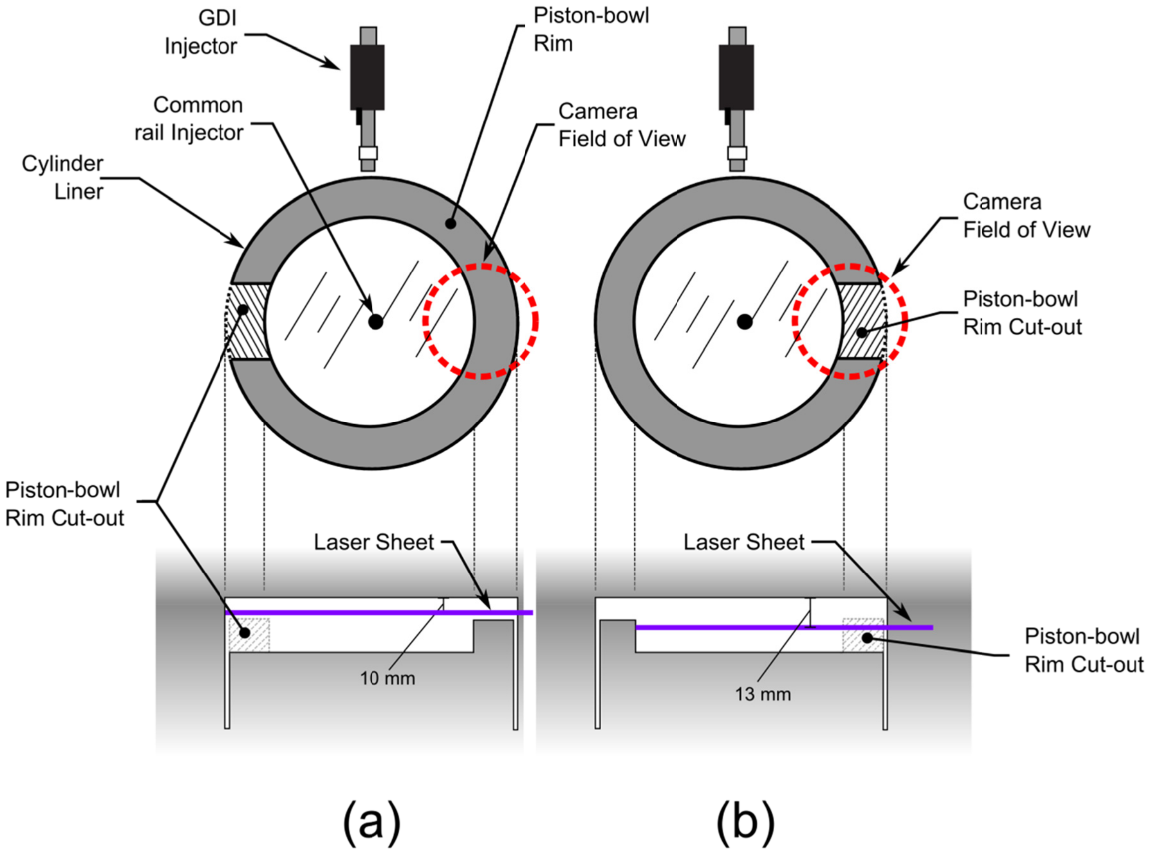

Figure 8-4. Laser sheet setup for the fuel tracer fluorescence imaging study. (a) Laser sheet location for the early cycle images acquired above the piston bowl-rim. (b) Laser sheet location for the near TDC images acquired inside of the cutout in the piston bowl-rim. The camera field of view is indicated by the red dashed line.

---

[9] The cross optical access window narrows at 10 mm below the firedeck; thus, this is effectively the highest imaging location possible using the full width of the laser sheet.

piston bowl rim clips the laser sheet and imaging above the piston bowl rim is not possible. To allow the laser sheet to enter the combustion chamber up to TDC, the piston bowl rim cutout was rotated 180° into the camera field of view. Images after -21° ATDC were acquired inside of this cutout as indicated in Figure 8-4 (b). The images after -21° ATDC were acquired with a laser sheet height of 13 mm below the firedeck.

A blue-optimized, intensified CCD camera (Princeton Instruments PI-MAX3:1024i SB) with a 55 mm f/3.5 UV lens with the aperture fully open imaged the resulting florescence viewing downward through the cylinder head window (see Figure 8-3 and Figure 8-4). A WG295 long-wave pass (LWP) filter helped to isolate the toluene fluorescence (265-330 nm) from scattered laser light. Additionally, a UG5 UV-bandpass filter (passband in the range of 220 to 400 nm) blocked red-shifted fluorescence from motor oil and other sources [12].

Quantitative fuel-vapor concentration measurements require calibration of the fluorescence signals with a known fuel/tracer concentration. In this work, calibration images at a known fuel/tracer concentration were obtained by injecting toluene-doped n-heptane, using the common-rail injector, near TDC of the intake stroke. In similar studies (e.g., Musculus et al. [114]) early-cycle injections of low boiling-range fuels have been shown to yield acceptably homogenous mixtures during the compression stroke. Indeed, the calibration images from this study (e.g., Figure 8-5) appear reasonably uniform. Although the calibration images appear nearly homogeneous, it is possible that non-uniformities exist outside of the camera field of view. These non-uniformities, if present, introduce uncertainty into the vapor fuel concentration measurements of this study, though it is not possible to quantify this level of uncertainty in the present work. Further, with the early-cycle injection used in this study, some liquid may impinge on the combustion chamber surfaces; however, the intake temperature and coolant temperature were set to near the atmospheric boiling point of n-heptane. Thus, it is likely that any liquid impinging on a combustion chamber surface would rapidly vaporize. However, should liquid fuel remain at the imaging time, the fuel vapor concentration measurements would be biased towards higher fuel concentrations.

Fuel-vapor concentrations were measured for separate injections from both the common-rail and GDI fuel systems. At each crank angle of interest, images were acquired in sets of four. Between each image, the engine was motored (without supplying fuel) for 9 cycles to scavenge residual fuel from the combustion chamber. The first image had no fuel injection and recorded background fluorescence interference–likely due to residual lubrication oil excited by scattered laser light [12, 86]. The second image provided a flat-field calibration at a known toluene/fuel concentration as previously discussed. The third and fourth images recorded fluorescence from the fuel injected through the GDI only and common-rail injector only, respectively. This four-image sequence was repeated 40 times at each crank angle of interest. After the image acquisition sequence, the optics were cleaned and the procedure was repeated for the next operating condition. Figure 8-5 shows a representative image sequence.

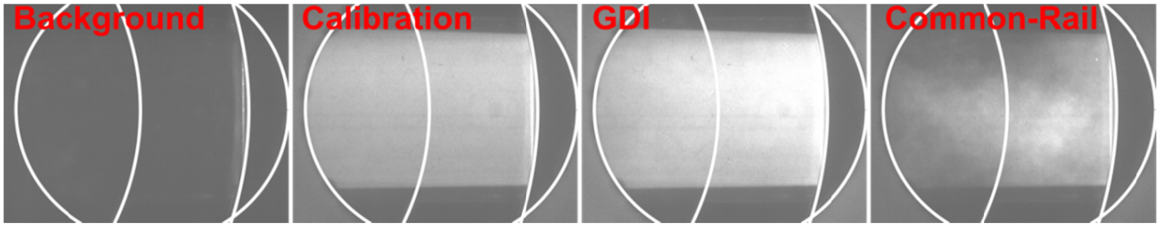

Figure 8-5. Typical image acquisition sequence for the toluene fuel-tracer PLIF diagnostic. The images were acquired at -5° ATDC.

To extract quantitative information using LIF, the photophysics of the LIF signal must be understood. The engine was operated using 100% N_2 for the fluorescence measurements to avoid the collisional quenching by oxygen, but two primary concerns remain: temperature dependence of the fluorescence quantum yield and absorption cross section, and potential pressure dependence due to collisional quenching with N_2 and fuel [115].

In a review paper, Schulz et al. [115] showed that, under 266 nm excitation, the absorption cross section increases by more than a factor of three when the temperature is increased from 300 to 1000 K. Further, the fluorescence quantum yield over the same temperature range decreases by two orders of magnitude. At the image acquisition time, the temperatures of the calibration and raw data images are slightly different due to differences in the fuel concentrations (i.e., differences in the evaporative cooling and in the compression heating). Therefore, it is important to correct the images for temperature prior to conversion to a fuel concentration. The temperature dependence of toluene fluorescence was evaluated under well-mixed conditions (i.e., common-rail fuel injection at -345° ATDC) over a range of temperatures. Figure 8-6 shows the relative toluene fluorescence yield evaluated over a range of in-cylinder temperatures from 550 K to 940 K during the compression stroke, corrected for changing charge density. Following the work of Musculus et al. [114], an offset exponential was fit to the data and used as a calibration curve.

Similar to the temperature dependence, the pressure dependence was evaluated over a range of conditions. Consistent with the findings of Musculus et al. [114], the toluene LIF signal was shown to be independent of pressure after temperature corrections were applied.

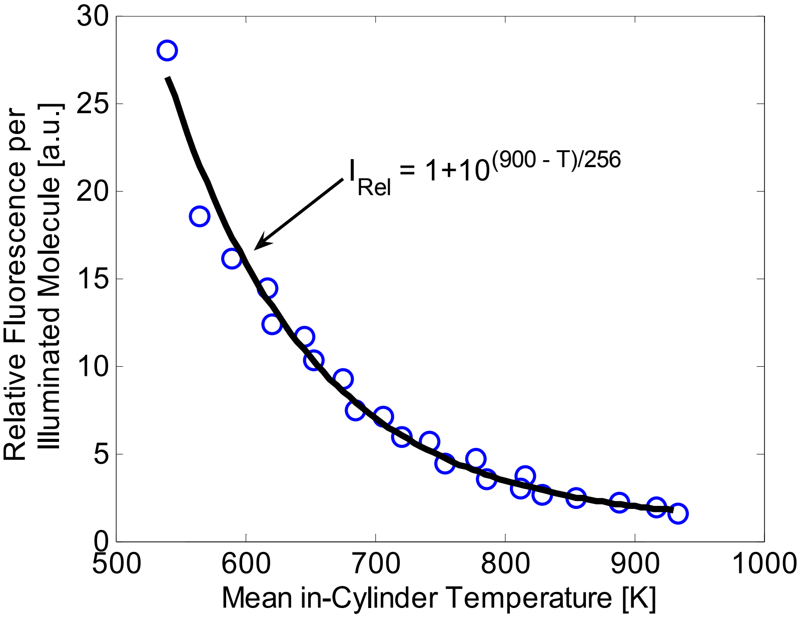

Figure 8-6. Relative toluene fluorescence as a function of mean in-cylinder temperature. The fueling was held constant at 39 mg/inj.

With the pressure and temperature dependence known, the images were processed as discussed below. Initially, the fuel distribution was calculated by assuming a uniform temperature distribution at the image acquisition time. The temperature fields of the calibration and data images (i.e., GDI or CR images) are different due to evaporative cooling and changes in the specific heats of the mixture due to the differences in fuel concentrations. To account for the temperature dependence of toluene fluorescence, the fluorescence intensity of each data image was corrected for the local temperature difference from the calibration image by

$$I_{corrected\_pixel} = I_{data\_raw\_pixel} \frac{I_{rel}\left(T_{cal}\right)}{I_{rel}\left(T_{data\_pixel}\right)}, \qquad \textbf{(8-1)}$$

where $I_{corrected\_pixel}$ is the corrected fluorescence intensity of the data image, $I_{data\_raw\_pixel}$ is the local fluorescence intensity of the GDI or common-rail image, $I_{rel}(T_{cal})$ was calculated from the temperature calibration curve given in Figure 8-6 at the average temperature of the calibration image, and $I_{rel}(T_{data\_pixel})$ was calculated from the temperature calibration curve at the local temperature of the data image. Then, the fuel distribution was calculated by normalizing the corrected fluorescence intensity by the flat field calibration image as shown in Eq. 8-2.

$$n_{data} = n_{calibration} \frac{I_{corrected\_pixel}}{I_{calibration\_pixel}} \qquad \textbf{(8-2)}$$

In Eq. 8-2, n_{data} is the local fuel vapor molar density and $n_{calibration}$ is fuel vapor molar density of the calibration image.

The above procedure provides an initial estimate of the fuel distribution. The final fuel distribution was calculated iteratively as outlined in Figure 8-7. First, the temperature of the N_2 charge at BDC was adjusted from the intake stream temperature to account for heat transfer during induction according to the procedure of Sjöberg et al. [116]. Second, the rise in temperature of the charge of N_2 due to compression from BDC to the start of injection (SOI) timing was calculated by numerical integration assuming adiabatic compression according to the measured pressure rise. The compression calculation accounted for variable specific heats. In this way, the resulting temperature represents the adiabatic core of the charge. Third, the fuel was assumed to be injected and mixed at the SOI timing. The charge of N_2 and fuel was then compressed from the SOI timing to the image timing assuming that the fuel distribution remains frozen. Although the real fuel distribution is not actually frozen, this simplification in the calculation provides a method to account for the temperature distribution resulting from fuel vaporization and the different heat capacities of N_2 and n-heptane. Hwang et al. [22] showed the importance of considering the change in temperature due to evaporative cooling and differences in compression heating due to the different specific heats of different equivalence ratio zones. In their work, they showed that neglecting these temperature corrections caused the peak

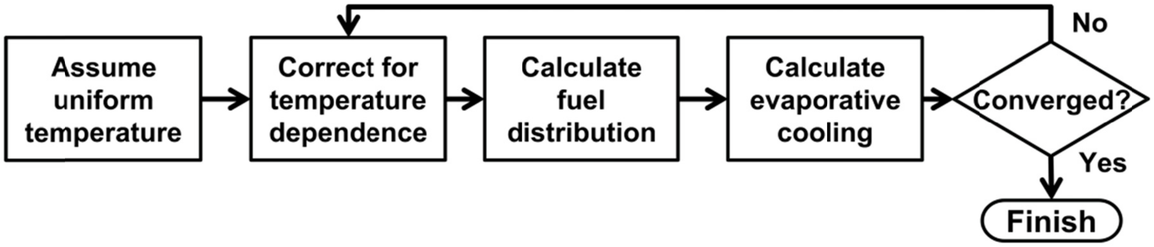

Figure 8-7. Image processing procedure for toluene fuel tracer fluorescence imaging.

equivalence ratio to be over-predicted by 38%, thus limiting the usefulness of the diagnostic. This iterative procedure was looped until convergence was obtained in the fuel distribution.

To improve the signal-to-noise ratio (SNR) of the images, the fuel distributions of the GDI and common-rail injections were ensemble averaged over 40 images. The average fuel-distribution maps were generated by combining the GDI and common-rail fuel concentration measurements. Of particular interest to this study are the relative concentrations of fuel from the GDI and common-rail fuel streams. Thus, the PRF number is defined as

$$PRF = 100 \frac{m_{GDI} / \rho_{\text{iso-octane}}}{m_{GDI} / \rho_{\text{iso-octane}} + m_{CR} / \rho_{\text{n-heptane}}}, \qquad \textbf{(8-3)}$$

where the m_{GDI} is the measured vapor-fuel mass from the GDI images corrected for the difference in molecular weight of iso-octane and n-heptane, m_{CR} is the mass of n-heptane measured from the common-rail (CR) injection images, and $\rho_{\text{iso-octane}}$ and $\rho_{\text{n-heptane}}$ are the densities of liquid iso-octane and n-heptane, respectively. This definition of PRF number is equivalent to a volume percent (by liquid) of iso-octane in the fuel blend for each pixel. The PRF number can be interpreted as a local octane number.

In order to use the fuel distribution measurements to explain the differences in the combustion characteristics, the uncertainty of the measurement must be addressed. For the present study, the precision of the measurement is of more interest than the absolute accuracy. That is, the gradients in PRF number and equivalence ratio are of more interest than the absolute value of PRF or equivalence ratio. The precision of the measurement was estimated using the calibration images. Each single-shot calibration image was processed to calculate a 95% confidence interval on the mean intensity of each pixel. The confidence intervals at each pixel were averaged to give a single number representing the relative error in each image. This error accounts for shot-to-shot variations in the mixture distribution, shot-to-shot variations in the laser sheet intensity profile, shot-to-shot variations in the injected fuel mass, and camera/shot noise. The equivalence ratio and PRF images are calculated by summing the GDI and common-rail images (see Eq. 8-3); therefore, the combined precision error for these images can be calculated by summing the error in quadrature to give a relative error in the equivalence ratio and PRF images of ~7%. For example, a PRF 50 mixture with an equivalence ratio of 0.5 has error bounds of ±4 PRF and $\pm 0.04\phi$.

8.3.3 Combined 355 PLIF, OH PLIF, and High Speed Combustion Luminosity Imaging

The CFD modeling presented in Chapter 5 suggests that tracking formaldehyde and OH will provide further details of the RCCI combustion evolution. Accordingly, PLIF imaging was used to track formaldehyde and OH throughout the combustion process. Additionally, the remaining light was imaged with the high-speed camera. Figure 8-8 shows the experimental setup. The diagnostics and imaging setup are discussed below.

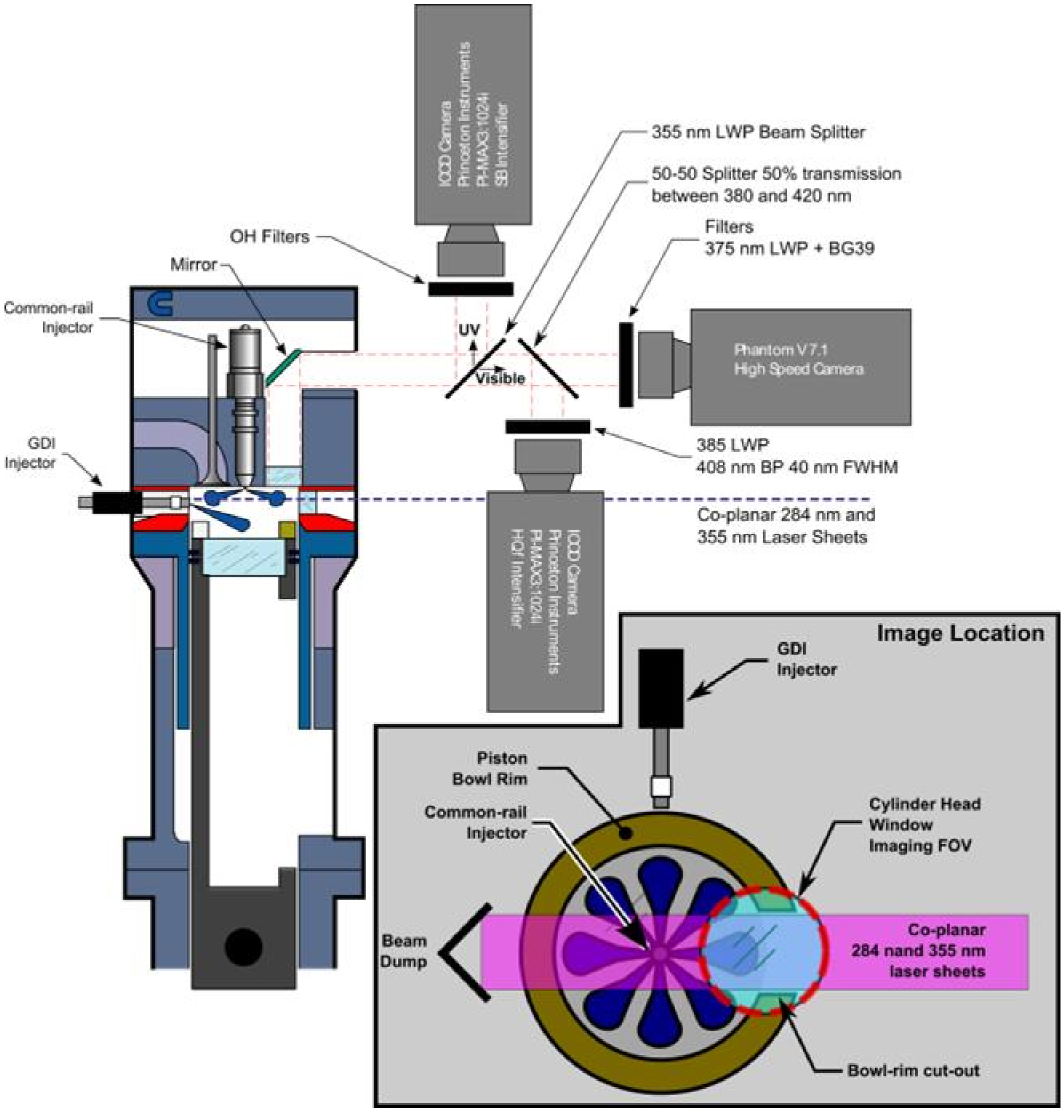

Figure 8-8. Imaging setup for simultaneous 355 PLIF, OH PLIF, and high-speed chemiluminescence.

8.3.3.1 355 nm PLIF (Formaldehyde)

Formaldehyde fluorescence was excited by the 355 nm output of a frequency tripled Nd:YAG laser. The 355 nm beam was formed into a thin sheet (less than 1 mm thick) using a combination of a negative cylindrical lens (f = -50 mm) and positive plano-spherical lens (f = 500 mm). The resulting fluorescence was imaged using an intensified CCD camera with a 105 mm glass lens viewing downward through the cylinder head window indicated in Figure 8-8. All 355 PLIF images were acquired with a camera gate width of 50 ns. A 385 nm long wave pass

(LWP) filter was used to block elastically scattered laser light and a 40 nm wide band-pass filter (BPF) centered at 408 nm isolated the fluorescence signal from other species excited by 355 nm light. Note that polycyclic aromatic hydrocarbons (PAH) also fluoresce under 355 nm excitation; however, PAH is generally a product of rich combustion and the fuel distribution measurements show that, at the operating conditions of this study, local equivalence ratios are lean of stoichiometric. Therefore, it is expected that the observed fluorescence is due primarily to formaldehyde.

8.3.3.2 OH PLIF

The OH fluorescence diagnostic is discussed in detail by Dec et al. [117]; thus, only a brief description is given here. OH fluorescence was excited by pumping the $Q_1(9)$ and $Q_2(8)$ lines of the (1,0) band of the A→X transition near 284 nm. The 284 nm beam was created using an optical parametric oscillator (OPO) pumped by the 355 nm output of a second Nd:YAG laser and formed into a sheet using the same optics discussed above. The resulting fluorescence–from the (0,0) and (1,1) vibrational bands in the 308 nm to 320 nm range–was imaged using a second intensified CCD camera (Princeton Instruments PIMAX) with a blue optimized intensifier (SB) and a 105 mm UV lens. Three filters were used to isolate OH fluorescence and reject scattered laser light. The filter selection is discussed in detail by Dec et al. [117]. A 16 nm wide band-pass filter (BPF) centered at 312 nm was used to isolate OH fluorescence. A 305 nm LWP filter was used to block scattered 284 nm laser light and a 355 nm short wave pass (SWP) filter was used to reject fluorescence from other species. It was found that the array of the SB intensified camera does not become fully operational until the camera gate was set to a value longer than 280 nm; thus, in this work all OH PLIF images were acquired with a gate of 300 ns.

Other species (e.g., PAH) also fluoresce in the 308-320 nm range. However, OH has very narrow excitation lines and tuning the wavelength of the laser slightly off of the OH band results in an order of magnitude decrease in the OH signal level. The narrow OH line can be used to verify that the signal is due to OH fluorescence. Images were acquired (from different cycles) with the laser tuned to the OH line (near 284.01 nm) and slightly off the OH line (near 283.9 nm). Comparison of the online and offline images showed that the signal level drops by nearly an order of magnitude when the laser is tuned off the OH line. That is, the recorded florescence signal is dominated by OH fluorescence. An example comparison is shown in Figure 8-9.

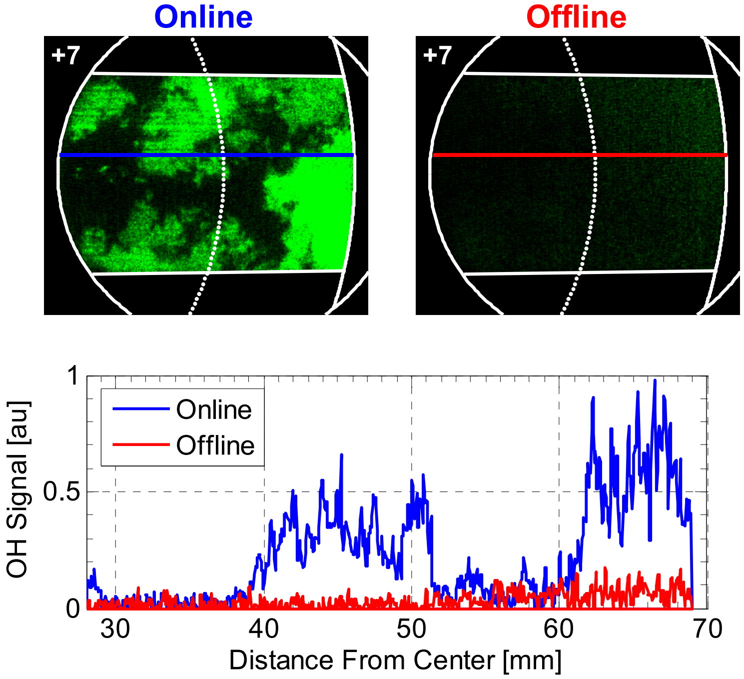

Figure 8-9. Comparison of images with the laser tuned to the OH line (near 284.01 nm) and off of the OH line (near 283.9 nm) images. The line-plot on the bottom shows a slice from the online (blue) and offline (red) images.

8.3.3.3 High Speed Imaging

A third camera was used to collect the remaining light. This high-speed digital camera used a 105 nm glass lens and recorded line-of-sight integrated natural luminosity (composed primarily of chemiluminescence). Scattered laser light was blocked with a 375 nm LWP filter and a BG39 was used to reject long-wavelength soot luminosity (if present). The exposure time for each frame was 125 μs. The long exposure time was required to collect reasonable light levels with the non-intensified HSC used in this study.

8.3.3.4 Laser Sheets and Image setup for Combined CH_2O PLIF, OH PLIF, and High Speed Combustion Luminosity Imaging

The 284 and 355 nm sheets were overlapped and directed horizontally into the combustion chamber at a height of 13 mm below the firedeck. The tails on either end of the sheet were clipped to improve the uniformity of the laser sheet intensity distribution. After being clipped, both sheets were approximately 31 mm wide and the recorded laser energies were 7 and 33 mJ per pulse for the 284 and 355 nm sheets, respectively. To allow imaging near TDC, a portion of the piston bowl rim was removed and images were acquired inside of the bowl-rim cutout as indicated in Figure 8-8. All three cameras view downward through the cylinder head window. The camera field-of-view (FOV) is shown in Figure 8-8.

8.3.3.5 Selection of Representative Single-Cycle Images

Due to speed limitations of the pulsed lasers, only one 355 and OH image can be acquired per cycle. With this limitation in mind, 20 combined OH and 355 PLIF images from 20 different engine cycles were acquired at each crank angle of interest. Several methods can be used to select a representative image. Genzale et al. [118] applied a pattern recognition technique to select the single-shot image most similar to all other single-shot images. Under conventional diesel-like conditions, where the heat release rate is nearly identical from cycle-to-cycle, this method makes sense; however, under premixed conditions, the heat release rate can vary from cycle-to-cycle even under stable operation. To illustrate the variation heat release rate, Figure 8-10 shows a comparison of the average and single-cycle AHRR for 20 cycles under RCCI operation with the COV of IMEP near 2%.

Although the general features of the heat release are consistent from cycle-to-cycle, differences are evident. The variations in heat release rate are likely due to shot-to-shot variations in the fuel delivery, variations in the fuel distribution, and/or variations in the charge gas temperature distribution (recall that the CFD modeling of Section 5.4 showed that CA50 was most sensitive to temperature and fuel reactivity). It is desirable to select images from a cycle showing a heat release rate similar to the mean heat release rate for a given operating condition;

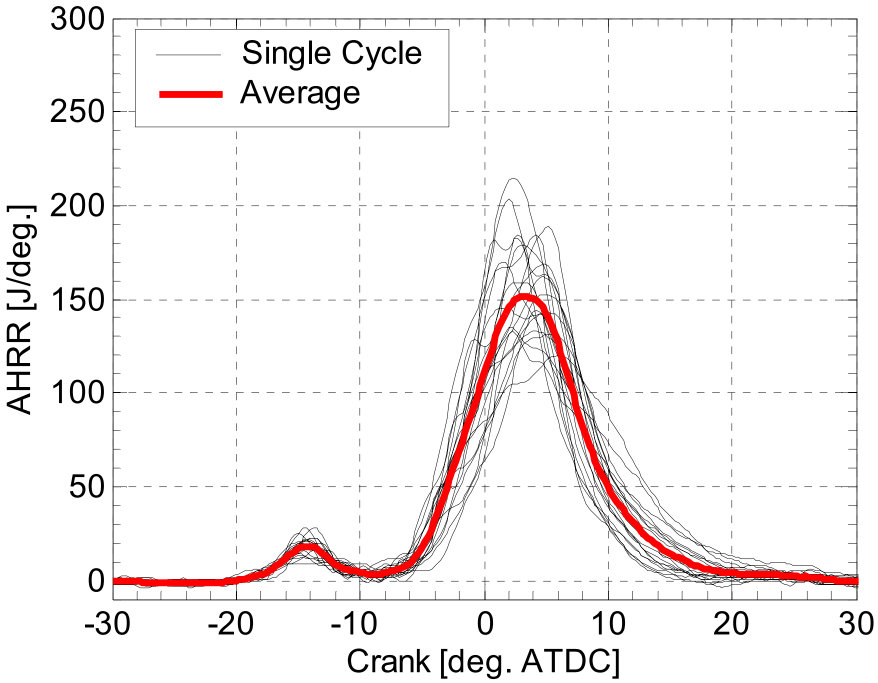

Figure 8-10. Comparison of single-cycle (thin black lines) and average (thick red line) AHRR under stable RCCI operation.

therefore, the images presented are from the cases showing heat release rates most similar to the ensemble averaged AHRR. The selected cycles have the minimum sum of the squared differences between the single-cycle and ensemble averaged AHRR[10].

8.3.4 Laser Ignition

To help isolate the mechanism of reaction zone growth and the role of flame propagation, laser ignition was used to probe the ignitability of various regions throughout the chamber. The resulting combustion luminosity was imaged using the high-speed digital camera. The experimental setup for the laser ignition study is shown in Figure 8-11. The 532 nm output of an Nd:YAG laser was used as an ignition source to probe the ignitability of various regions throughout the chamber. The laser energy was controlled by passing the beam through a half wave plate followed by a polarizer. This setup allows independent control over the beam uniformity and laser power. That is, the laser was tuned to achieve a uniform beam near the maximum laser power and the beam energy was set by adjusting the rotation of the half wave plate. The beam was then passed through a 250 mm plano-spherical lens to focus the laser light. Although the long-focal length lens used for plasma generation is not ideal, it was not possible to use a short focal length lens due to the physical layout of the engine.

The laser energy was steadily increased to achieve consistent plasma formation. At engine conditions, consistent plasma formation was found when the laser energy was greater than 57 mJ/pulse. Although the present study was only concerned with achieving plasma formation as a diagnostic (i.e., no attempt to lower the required laser energy was made) it is worthwhile to point out that this value of laser energy is much higher than values reported in the

---

[10] The average heat release rate was calculated from 12 sets of 120 fired cycles (i.e., 1440 cycles). Although all 1440 cycles were used to calculate the average AHRR, averaging more than 20 cycles only resulted in minor changes in the average AHRR.

literature (e.g., Genzale et al. [119]). The higher laser energy is likely due to the long focal length lens used in the present study.

The resulting combustion progression was imaged using the HSC discussed in Section 8.3.1. A 500 nm SWP filter was used to block scattered laser light and to be consistent with the previous experiments, a BG39 was used to block long-wavelength soot luminosity (if present). The camera viewed upward through the flat piston crown window. The FOV is limited by the edge of the piston bowl rim.

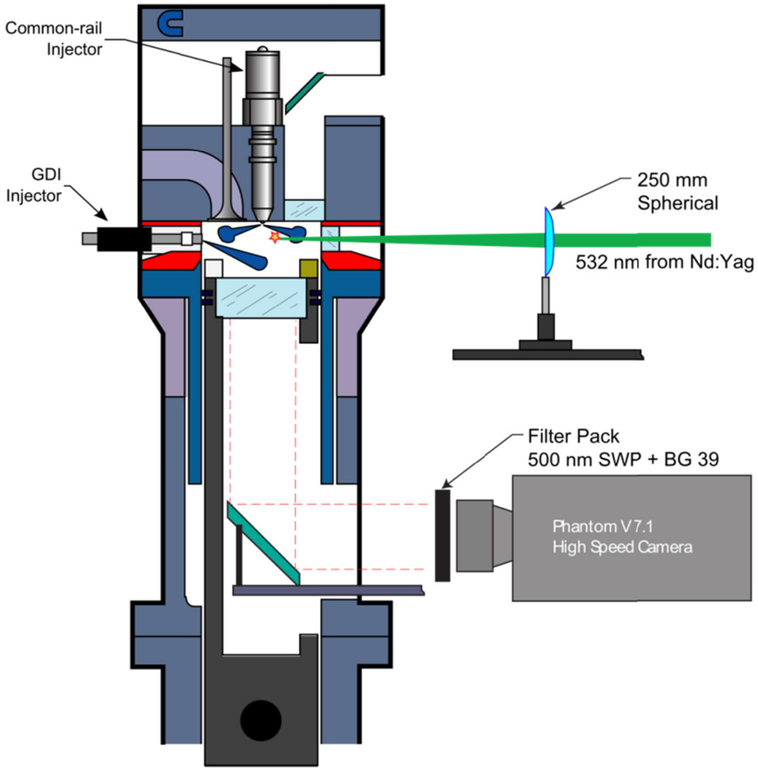

Figure 8-11. Engine setup showing laser ignition using the 532 nm output of an Nd:Yag laser focused with a 250 mm spherical lens.

Chapter 9

Investigation of RCCI Combustion Using Multiple Optical Diagnostics

In this chapter RCCI combustion is investigated in a heavy-duty, single cylinder, optically accessible research engine. The ignition process and combustion zone development are studied using high-speed chemiluminescence imaging, CH_2O PLIF, and OH PLIF. The fuel distribution prior to ignition is evaluated using toluene fuel-tracer PLIF. There are two main objectives to this work. First, provide validation of the model predicted description of the RCCI combustion process presented in Chapter 5. Second, develop a fundamental understanding of the dominant mechanisms controlling ignition and reaction zone growth.

9.1.1 Cylinder Pressure and Heat Release Rate

Figure 9-1 shows the measured cylinder pressure, common-rail fuel injector rate of injection (ROI), and apparent heat release rate. The first common-rail injection of n-heptane begins at -57° ATDC. Near -40° ATDC the evaporative cooling and an increase in the heat capacity of the charge resulting from the GDI and first common-rail injections causes the cylinder pressure recorded on the fired cycle to fall slightly below that of the motored trace. At -37° ATDC, the second common rail injection begins and the associated evaporative cooling causes the pressure to further drop below the motored trace. Around -19° ATDC, low-temperature reactions push the apparent heat release rate above zero. The energy release from these low-temperature reactions reaches a peak near -13° ATDC and by -11° ATDC enough energy has been released from low-temperature reactions to raise the cylinder pressure above the motored pressure. Because iso-octane is a single stage fuel[11] (i.e., it generally does not exhibit low temperature heat release) it is expected that the observed low-temperature heat release is primarily the result of n-heptane decomposition. Recall that a similar conclusion was found in the preliminary RCCI development outlined in Chapter 4. Furthermore, Puduppakkam et al. [62] used CFD modeling coupled with a detailed chemical kinetic mechanism (425 species and 3128 reactions) to study RCCI combustion and found that the low temperature heat release was primarily due to n-heptane decomposition. After peaking, the energy release decreases to near zero at -10° ATDC and the heat release curve remains relatively flat until -6° ATDC. The high-temperature heat-release begins near -6° ATDC and peaks near 2° ATDC. The relatively symmetric shape of the high-temperature heat release curve suggests that no mixing controlled combustion is present, consistent with the long ignition dwell. However, in comparison to perfectly mixed conditions, the energy release occurs rather slowly (if the charge were perfectly premixed, chemical kinetics calculations show that the charge would ignite nearly uniformly (volumetrically) and the combustion event would be completed within a few crank angle degrees).

---

[11] Sjöberg et al. [124] have shown that under some conditions (e.g., low engine speed), iso-octane does show low-temperature heat release; however, the present study operates at conditions where iso-octane is expected to behave as a single stage fuel.

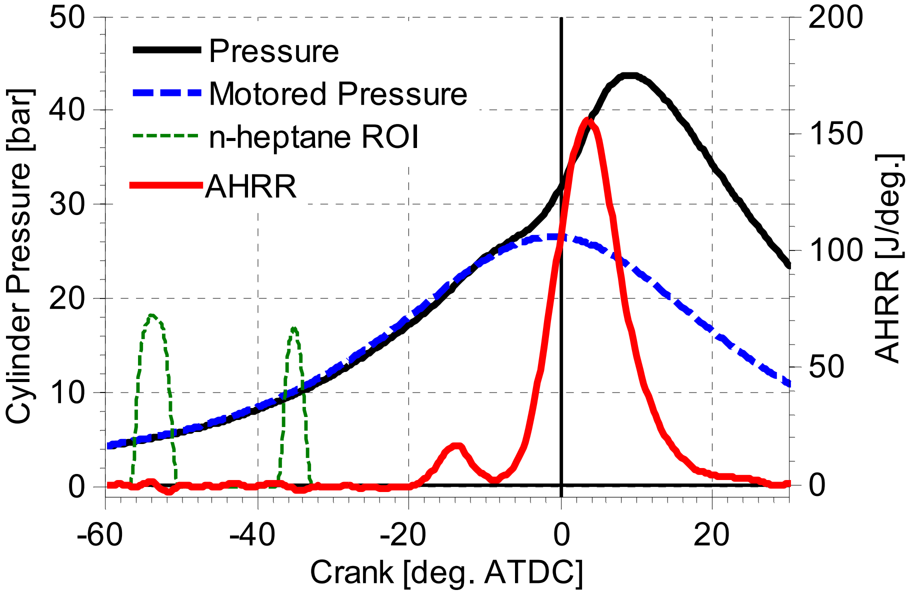

Figure 9-1. Measured cylinder pressure (fired and motored), common-rail (n-heptane) ROI, and apparent heat-release rate. The GDI injection of iso-octane has an SOI timing of -240° ATDC (not shown).

9.1.2 Preliminary Combustion Chemiluminescence Imaging

The purpose of this study is to guide the selection planar diagnostics and gain a preliminary understanding of the RCCI combustion evolution. The operating conditions were presented in Table 8-4. Figure 9-2 shows the field of view (FOV) for each camera setup used for the preliminary combustion chemiluminescence imaging study. The image on the left-hand side shows the recorded luminosity with the HSC viewing upward through the flat piston crown window, while the image on the right-hand side shows the combustion luminosity recorded with the HSC viewing downward through the cylinder head window. Although each pair of bottom-view and top-view images were acquired at the same crank angle, they are from different cycles (only one camera was used), so they are not simultaneous. The time in crank angle degrees after top dead center is shown in the upper left-hand corner of each image. The solid gray line on the piston crown window images shows the inner edge of the piston bowl rim, which also bounds the field of view of the images acquired through the piston crown window. The FOV of the cylinder

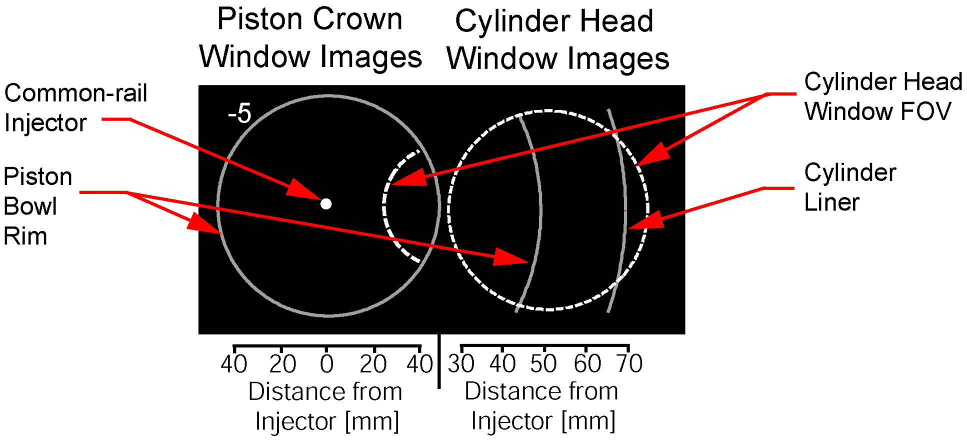

Figure 9-2. Camera field of view for both imaging locations. Note that the cylinder head window images are enlarged by a scale factor of 1.7 to more clearly show the ignition process.

head window images is shown by the white dashed line on both images. Notice that approximately 1/3 of the FOV of the cylinder head window images overlaps with the FOV of the piston crown window. The images acquired through the cylinder-head window view downward onto the top of the piston bowl rim, as indicated by the solid gray lines.

Selected high-temperature combustion chemiluminescence images are shown in Figure 9-3. The presented images are selected from a single cycle that had an AHRR most similar to the ensemble-average AHRR in Figure 9-1. The appearance of chemiluminescence in the downstream region of the jet between -5° and -7° ATDC coincides with the transition to second-stage combustion (i.e., high-temperature ignition). Small ignition pockets are initially observed in two locations, inside the edge of the piston bowl rim, and in the squish region (i.e., above the piston bowl-rim). These ignition zones grow for several crank angles while more ignition pockets continue to appear. The separate ignition pockets then merge into larger, more coherent reaction zones. By -1° ATDC, the squish window image is nearly filled with combustion luminosity[12]. The remainder of the images show that the reaction zones move steadily back upstream towards the centrally mounted common-rail injector. Notice that careful inspection of the reaction zones shows that small auto-ignition pockets appear ahead of the main reaction zone. This suggests that the mechanism for reaction zone movement is sequential auto-ignition; however, more work is required to definitively determine the dominant mechanism of reaction zone growth (discussion of the role of flame propagation is presented in Section 9.1.7).

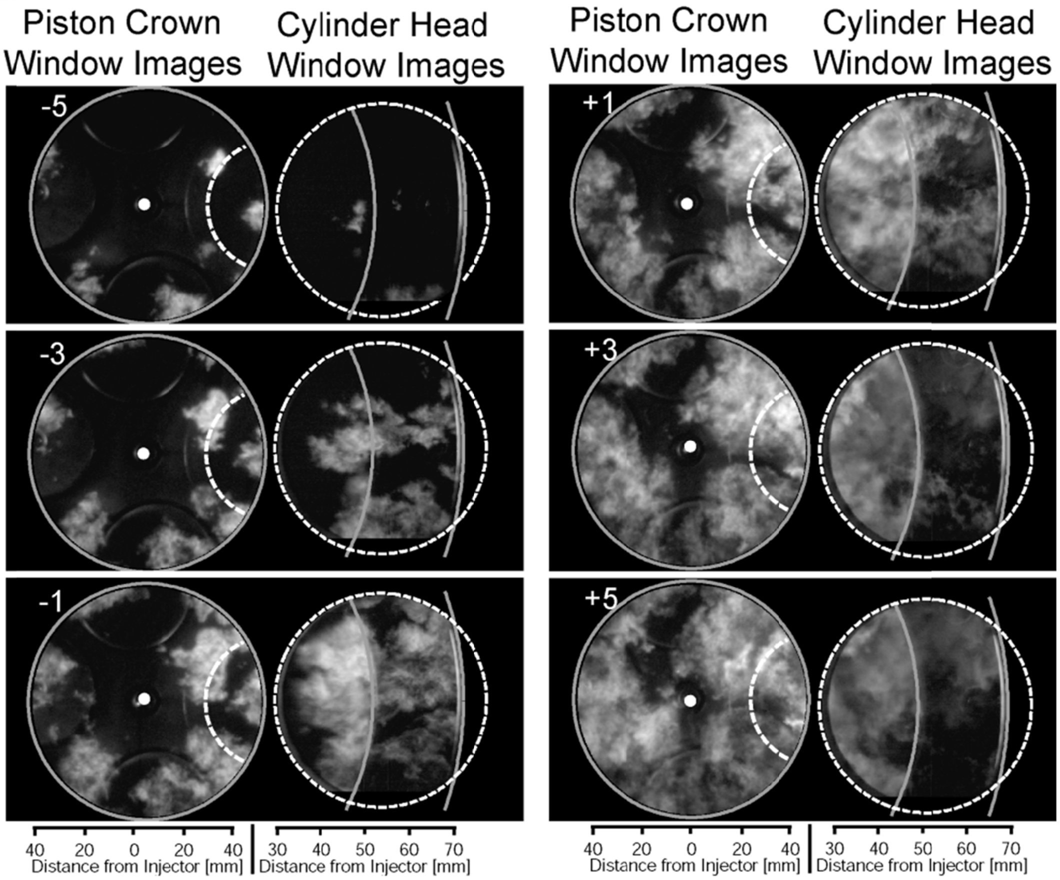

Figure 9-3. High-speed camera image sequence of RCCI combustion. The images on the left-hand side were acquired with the HSC viewing upward through the flat piston crown window, while the images on the right-hand side were acquired looking downward through the cylinder head window. Note that two sets of images were not acquired simultaneously. See Figure 9-2 for a description of the image layout.

---

[12] Note that the presented images are integrated in the line-of-sight; therefore, it is not possible to determine the level of combustion luminosity into the page (i.e., it is possible that the observed luminosity is occurring at different distances orthogonal to the firedeck).

9.1.3 Fuel Distribution

The preliminary chemiluminescence imaging study showed that ignition generally occurs in the squish region (i.e., in the field-of-view of the cylinder head window); therefore, the remaining PLIF imaging studies will focus on the squish region. The toluene fluorescence diagnostic (see Section 8.3.2 for a description of the fuel tracer fluorescence diagnostic) was used to measure the fuel distribution prior to ignition. The PRF maps were acquired with the ICCD camera viewing downward through the cylinder head window. Figure 9-4 shows the location of the laser sheet used for the toluene fuel tracer PLIF imaging with respect to the common-rail fuel injector.

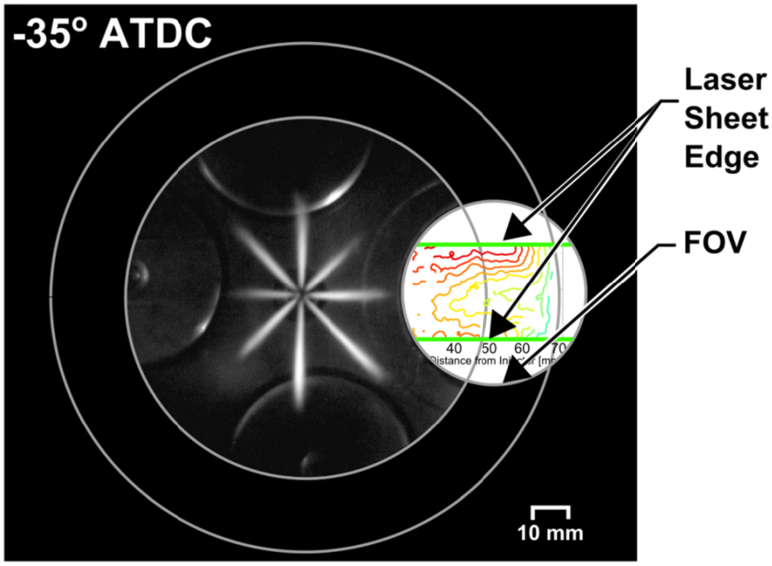

Figure 9-4. Field of view (FOV) for toluene fuel-tracer PLIF imaging. The image shows an overlay of the liquid fuel illuminated by a high-power LED and the resulting PRF map generated from the toluene fuel-tracer PLIF imaging at -35° ATDC.

Figure 9-5 shows the 40 cycle ensemble-averaged PRF maps at several times during the common-rail injection event. The solid gray line on the left-hand side of each PRF map shows the edge of the cylinder-head window FOV. The middle gray line on the PRF maps shows the location of the piston bowl rim and the gray line on the right-hand side of each image shows the

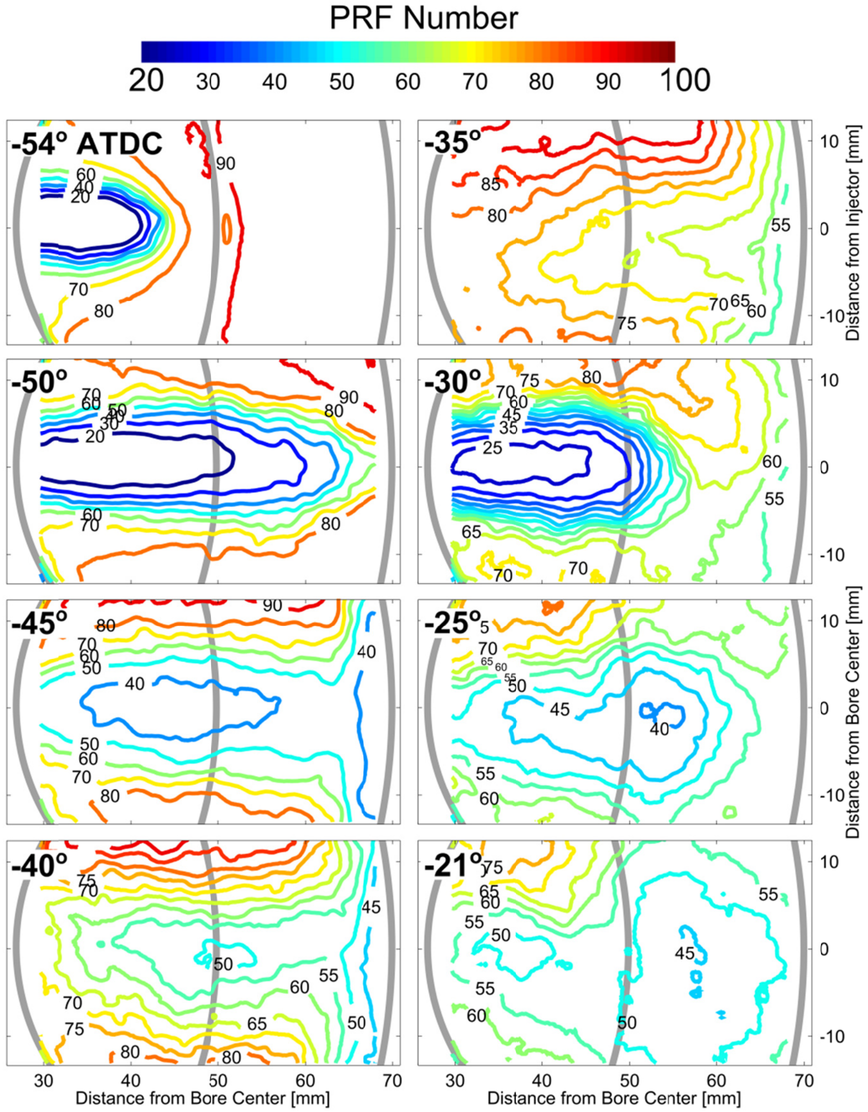

Figure 9-5. Sequence of ensemble-averaged PRF maps at several times during the common-rail injection event. The time in crank angle degrees after TDC is shown in the upper left hand corner of each image. The PRF maps were generated from vapor fuel concentration measurements with the camera viewing downward through the cylinder head window.

location of the cylinder liner. The laser sheet enters from the right-hand side of each image. The fuel enters the field of view of the cylinder head window images around -54° ATDC. Note that at this time, the HSC images (not shown) indicate that liquid fuel is present in the FOV; thus, the fuel concentration measurements at this crank angle are likely biased by fluorescence and scattering from liquid fuel, and should be considered as upper bounds. Shortly later, at -50° ATDC, the first common-rail injection is nearly complete and the fuel-tracer PLIF images show that the vapor fuel has penetrated nearly to the cylinder liner.

By -45° ATDC the vapor fuel from the first injection has penetrated to the liner and is beginning to spread along the cylinder wall. Although the fuel injection is over, momentum causes the vapor fuel to continue to penetrate, entraining ambient gas (air and iso-octane), and the PRF number in the upstream portion begins to rapidly decrease. Post injection mixing continues and shortly before the fuel vapor from the second common-rail injection enters the FOV (i.e., the images at -40° and -35° ATDC), the minimum PRF number in the plane of the laser sheet is 55 to 60.

At -30° ATDC, the fuel jet from the second injection enters the FOV and mixes with the fuel from the GDI and first common-rail injection. Because of slower penetration due to the higher ambient densities for the second injection, by the time vapor fuel enters the FOV of the cylinder head window, the fuel injection process is complete. Similar to the first injection, the vapor-fuel jet continues to penetrate after the end of injection; however, now the jet is entraining not only nitrogen (air in the case of combusting conditions) and iso-octane, but also n-heptane from the first injection. Because the n-heptane concentration tends to increase away from the nozzle (i.e., towards the liner), the PRF number of the entrained fuel tends to decrease as the jet moves downstream. By -25° ATDC the ensemble-averaged PRF number in head of the jet from the second common-rail injection has increased to around 50 (i.e., a 50 – 50 blend of iso-octane and n-heptane). Notice that outside of the region influenced by the second fuel injection, much of the fuel from the first common-rail injection has mixed to create a relatively uniform mixture (on average) in the squish region around a PRF number of 65; however, in the upstream region, between the fuel jets, locations exists that are more dominated by the premixed iso-octane (on average). The final fuel-tracer PLIF image above the piston bowl rim was recorded at -21° ATDC (recall that the optical access window in the cylinder liner becomes blocked by the piston bowl rim at crank angles later than -21° ATDC). At this time, a small region in the downstream portion of the jet is at a PRF number near 45 and the PRF number increases on either side of the jet as well as upstream towards the injector.

Images up to -5° ATDC were acquired inside of the cutout in the piston bowl rim (the imaging layout is shown in Figure 8-4 (b)). Figure 9-6 shows the equivalence ratio and PRF (octane number) distributions at several times during the LTHR and near the onset of second stage combustion. Although the PRF maps shown in Figure 9-6 are acquired inside of a cutout in the piston bowl rim on a plane 3 mm lower than those shown in Figure 9-5, the PRF maps of both imaging locations are very similar at -21° ATDC. As expected from the previous fuel PLIF imaging sequence, Figure 9-6 shows that the charge continues to mix between -21° and -5° ATDC. The region of highest reactivity (lowest PRF number and highest equivalence ratio) remains located in the downstream portion of the jet, near the liner. The fuel reactivity decreases with decreasing distance from the center of the combustion chamber.

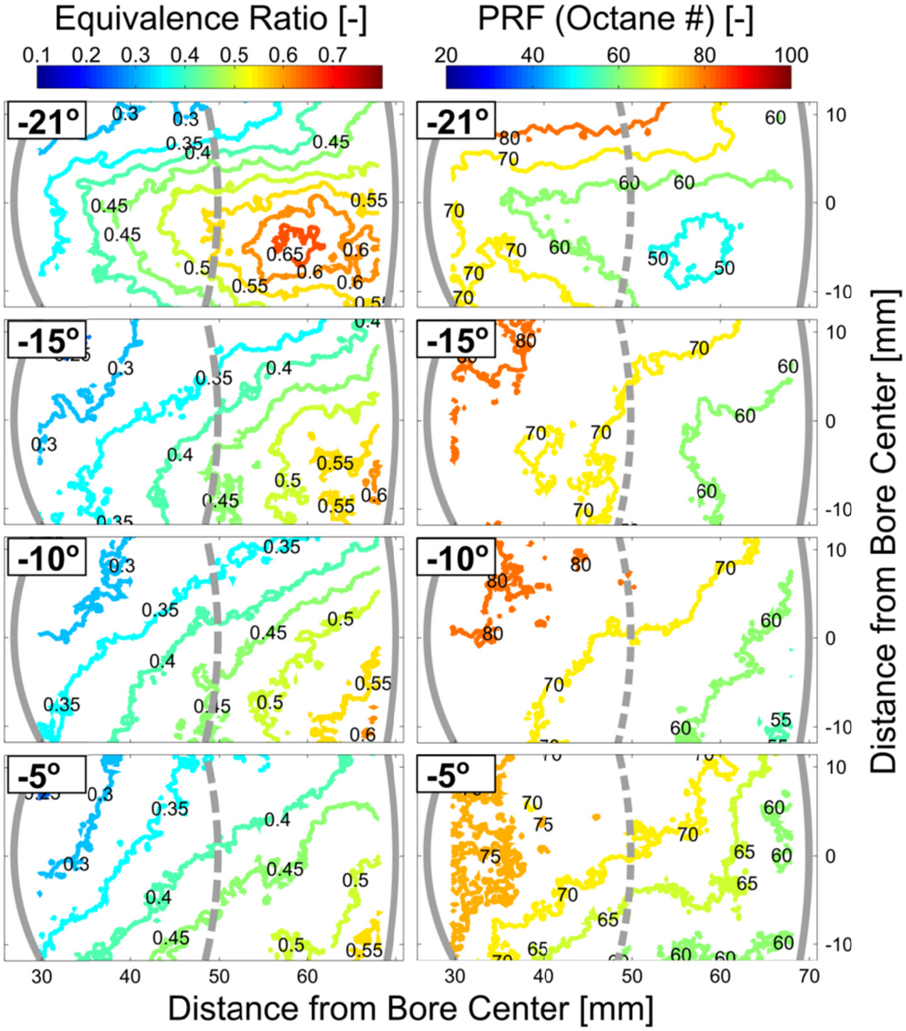

Figure 9-6. PRF (octane number) map at several times prior to ignition. The laser sheet is located 13 mm below the firedeck.

9.1.4 Simultaneous CH_2O PLIF, OH PLIF, and High Speed Combustion Luminosity Imaging

The preliminary high-speed imaging provides an excellent overview of the combustion process and allows the progression of the reaction zone to be observed in a single-cycle. However, the HSC provides a two-dimensional projection of the three-dimensional reaction zone, and the images must be interpreted with caution. Further, no information regarding the progression of the controlling kinetics can be obtained from the HSC. In this section, the CH_2O

PLIF and OH PLIF are added to the high-speed imaging to provide a more detailed description of the combustion process. See Section 8.3.3 for a discussion of the optical diagnostics.

An example 355 PLIF, OH PLIF, and high speed chemiluminescence image is shown in Figure 9-7. The leftmost image shows the selected single-cycle combined 355 (CH_2O) PLIF and OH PLIF. The 355 PLIF signal is false colored red and the OH PLIF signal is false colored green. The center image shows the 20 cycle ensemble averaged 355 PLIF and OH PLIF. The rightmost image shows the recorded combustion luminosity (likely composed primarily of chemiluminescence) corresponding to the single-cycle 355 and OH PLIF image. Several lines are drawn on the images to aid in orientation. The solid white line on the left-hand side of each image shows inner edge of the cylinder head window. The dashed line near the center of each image shows the location of the inner edge of the piston bowl rim; however, recall that a portion of the piston bowl rim was removed to allow the laser to enter the combustion chamber near TDC. The solid white line on the right-hand side of each image shows the edge of the cylinder liner. On the PLIF images, the nearly horizontal white lines show the edges of the laser sheets. The white number in the upper left hand corner of the single-cycle 355 PLIF and OH PLIF image shows the time (in crank angle degrees after TDC) at which the image was acquired. The number in green on the lower left hand corner shows the gain settings of the OH PLIF camera and the number in red shows the gain settings of the 355 PLIF camera. Note that the cameras had sufficient dynamic range such that the gain settings were held constant throughout the study.

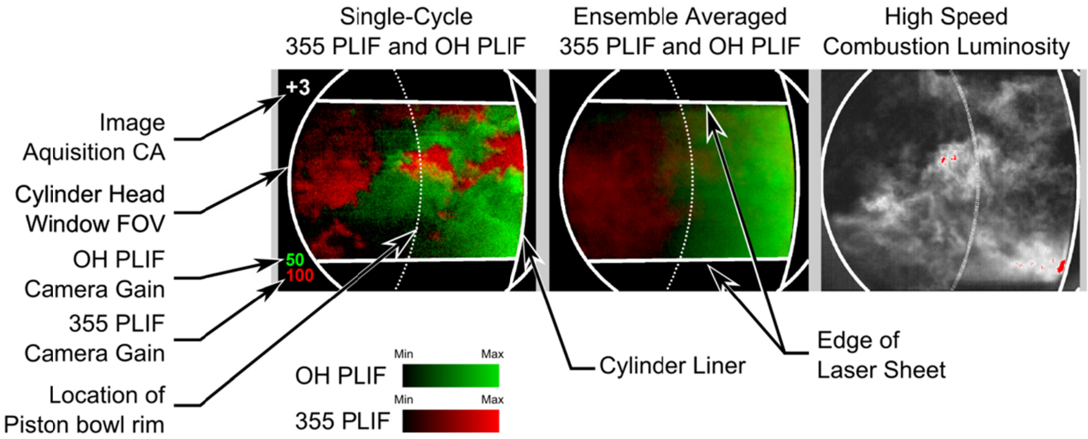

Figure 9-7. Layout of combined 355 PLIF (false colored red), OH PLIF (false colored green), and high speed combustion luminosity image.

Figure 9-8 shows a representative sequence of single-shot and ensemble averaged 355 (CH_2O) PLIF during the low temperature heat release. Note that the images also include OH PLIF; however, no OH fluorescence was detected during the LTHR. The AHRR curve (see Figure 9-1) shows that low temperature heat release begins near -18° ATDC. The corresponding imaging shows that formaldehyde forms first in the region near the center of the piston bowl rim. The fuel tracer PLIF imaging presented in Figure 9-5 and Figure 9-6 showed that the region near the center of the bowl-rim contains the highest concentrations of n-heptane near the time of LTHR. Thus, consistent with the predictions offered by CFD modeling (see Chapter 4), it is thought that the observed low-temperature reactions are primarily due to n-heptane decomposition. By -13° ATDC, the entire field of view is filled with formaldehyde and the ensemble averaged images change little between -13° and -9° ATDC. Notice that several of the single-cycle images show structure to the formaldehyde distribution. For example, at -11° ATDC, the single-cycle image shows that the formaldehyde is primarily constrained to the outer portion of the combustion chamber (i.e., near the liner); however, the ensemble averaged image shows that, on average, formaldehyde is found throughout the entire field of view. Since the -11° ATDC image is prior to the start of second stage combustion and no OH fluorescence is observed, it is thought that the lack of formaldehyde in the upstream (left-hand side of the image) region is due to the fuel distribution rather than formaldehyde consumption.

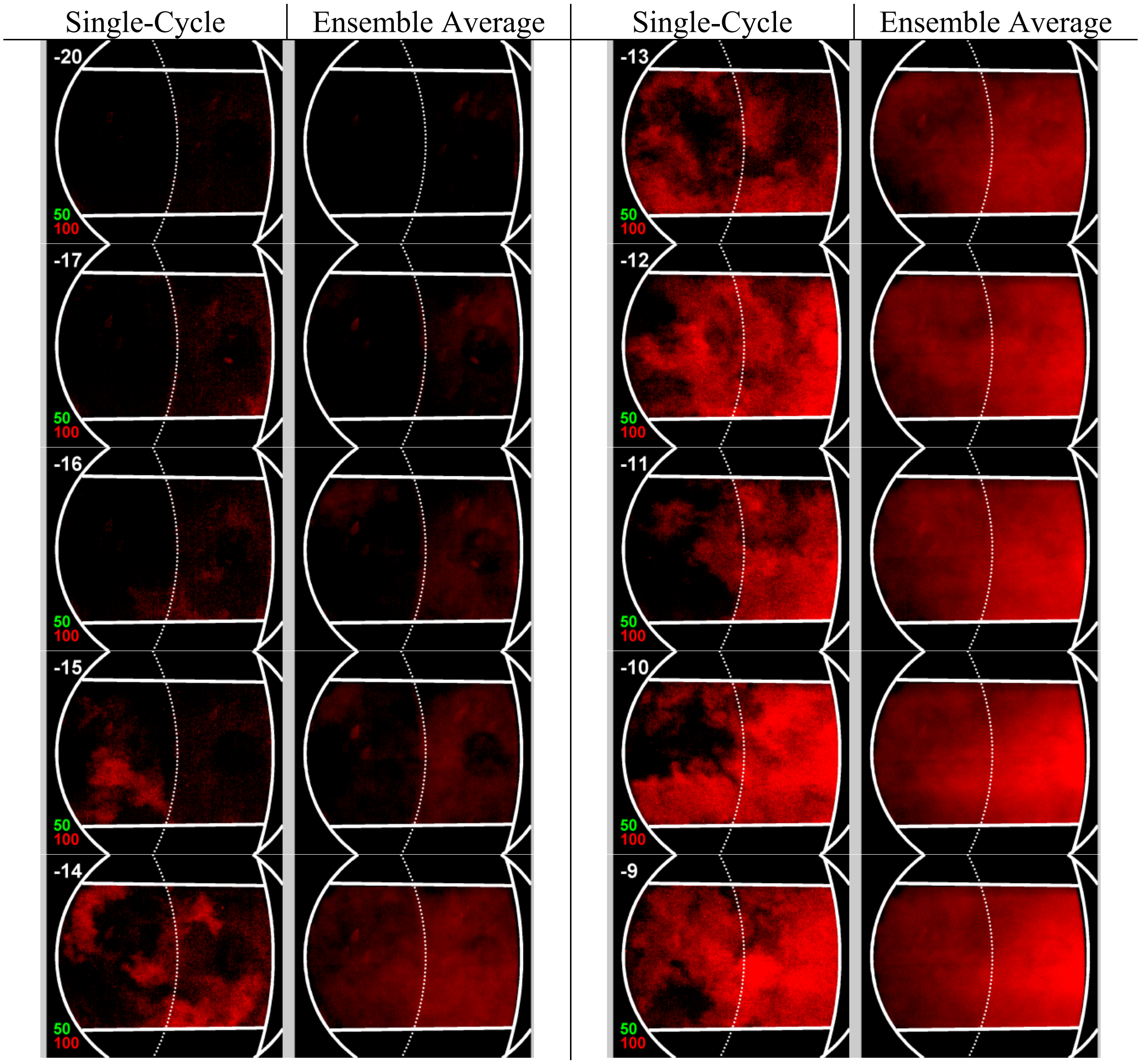

Figure 9-8. Single-cycle and ensemble averaged 355 (false colored red) PLIF and OH PLIF (false colored green) at several crank angles during the low temperature heat release. The numbers in white in the upper left hand corner show the crank angle in degrees after top dead center (ATDC), the numbers in green and red show the camera gain for the OH fluorescence imaging and the 355 fluorescence imaging.

Figure 9-9 shows CH_2O PLIF, OH PLIF, and high-speed chemiluminescence images at several times during the transition to second stage ignition. As previously discussed, after the LTHR the entire field-of-view is filled with formaldehyde. Revisiting the AHRR (shown in Figure 9-1), it can be seen that the transition to second-stage combustion occurs near -6° ATDC. Although no OH formation or CH_2O consumption is observed in the selected image[13] at -6° ATDC, the chemiluminescence image at -6° ATDC shows combustion luminosity in the near liner region. The fact that luminosity is observed in the HSC images, but no evidence of second stage combustion is present in the planar images shows the usefulness of combining the line-of-sight diagnostic (HSC combustion luminosity) with the planar imaging. The first OH fluorescence and consumption of formaldehyde of the presented images is observed at -3° ATDC. In the single-cycle images, OH appears in small pockets throughout the camera field of view. However, the ensemble averaged image at -3° ATDC shows that OH fluorescence is most consistent near the cylinder liner. Notice that the regions with OH fluorescence correspond to the regions showing combustion luminosity; however, not all regions showing combustion luminosity show OH fluorescence. That is, some of the regions showing combustion luminosity are above or below the laser sheet. As the charge transitions to second stage combustion, the OH producing regions become larger and formaldehyde consumption continues. Both the OH and combustion luminosity images show isolated auto-ignition sites, suggesting that the reaction zone moves by sequential auto-ignition. This finding supports the argument proposed in the preliminary high speed chemiluminescence imaging (see Figure 9-3).

---

[13] A few of the single-cycle images show small pockets of OH fluorescence in the images at -6°; however, on average, the OH florescence is not observed.

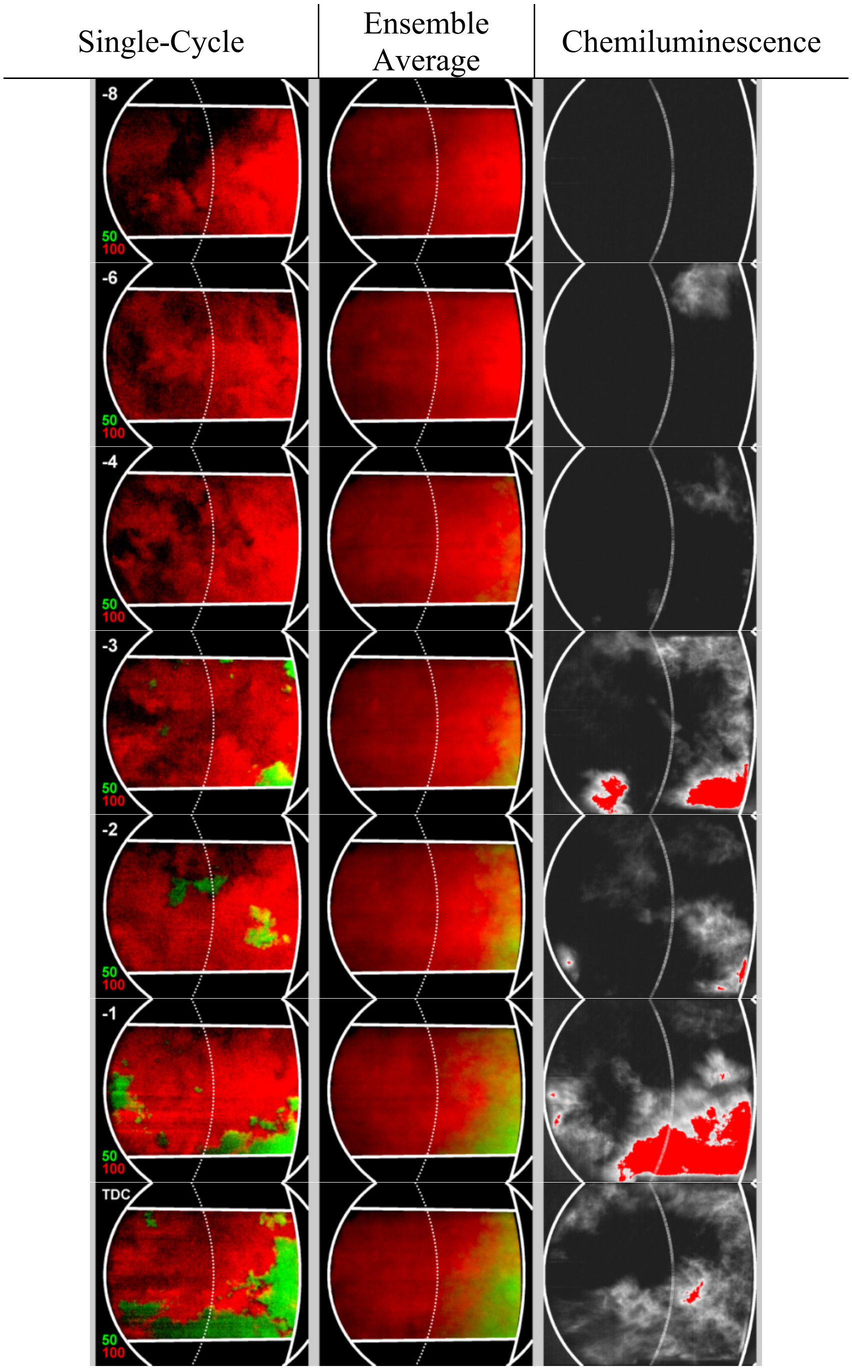

Figure 9-9. Single-cycle and ensemble averaged 355 (false colored red) PLIF and OH PLIF (false colored green) and high-speed chemiluminescence at several crank angles during the transition to second stage combustion. The numbers in white in the upper left hand corner show the crank angle in degrees after top dead center (ATDC), the numbers in green and red show the camera gain for the OH fluorescence imaging and the 355 fluorescence imaging.

Figure 9-10 shows CH_2O PLIF, OH PLIF, and high-speed chemiluminescence images during the high-temperature heat release. As expected the single-cycle images show continued consumption of formaldehyde and appearance of OH. The chemiluminescence images are less useful during the high-temperature heat release, since much of the FOV is filled with chemiluminescence. However, the ensemble averaged CH_2O and OH images show that, on

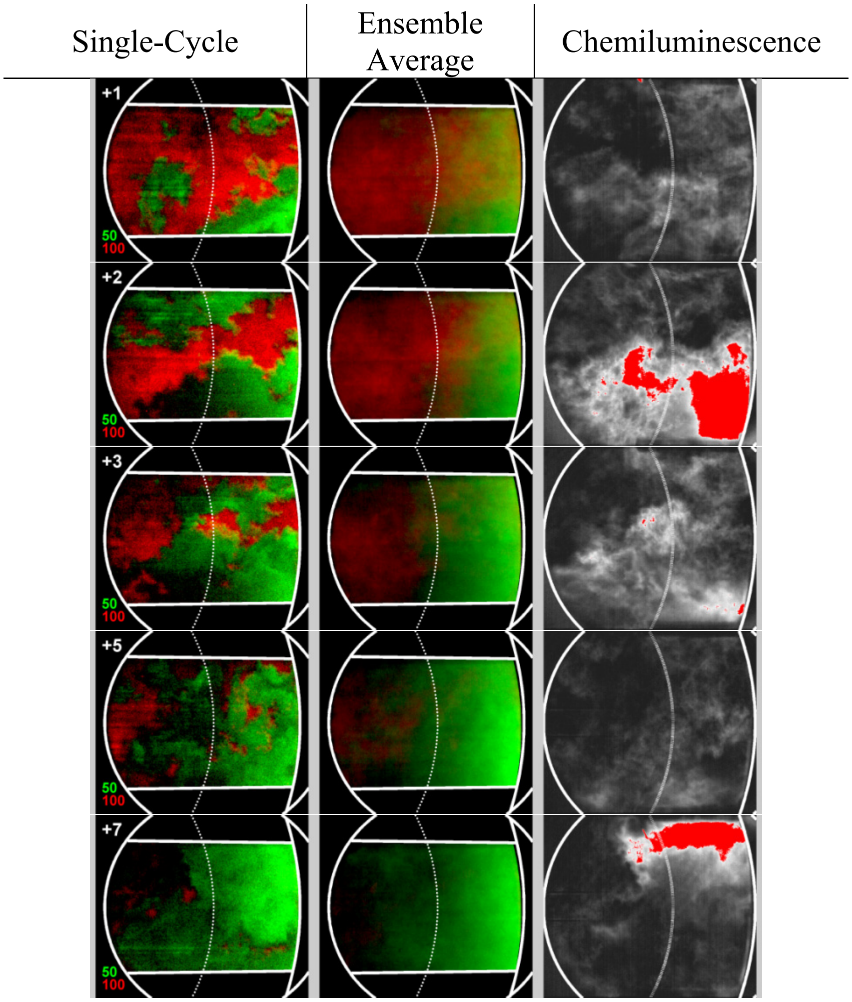

Figure 9-10. Single-cycle and ensemble averaged 355 (false colored red) PLIF and OH PLIF (false colored green) and high-speed chemiluminescence at several crank angles during the high-temperature heat release. The numbers in white in the upper left hand corner show the crank angle in degrees after top dead center (ATDC), the numbers in green and red show the camera gain for the OH fluorescence imaging and the 355 fluorescence imaging.

average (in the plane of the laser sheet), the high-temperature reaction zone grows from the liner towards the center of the combustion chamber. This is consistent with the gradient in fuel distribution obtained from the fuel tracer PLIF imaging (see Figure 9-6).

9.1.5 Analysis of Ignition Location and Reaction Zone Growth Direction

The fuel tracer PLIF measurements (see Figure 9-6) were combined with ignition delay calculations (kinetics modeling) to explain the observed ignition location and direction of reaction zone growth. Recall that the fuel tracer PLIF measurements were focused on ignition, which generally occurs in the field-of-view of the cylinder head window; therefore, measurements of the fuel distribution close to the cylinder centerline were not made. However, a clear trend of decreasing equivalence ratio with decreasing distance from the center of the combustion chamber is evident. With this trend in mind, the fuel distribution in the center of the combustion chamber can be estimated by extrapolating the measured equivalence ratio toward the center of the combustion chamber. Figure 9-11 shows the equivalence ratio averaged in the radial direction as a function of distance from the center of the combustion chamber at -10° ATDC. The -10° ATDC image was chosen since it is the last set of images acquired prior to ignition. Both the total equivalence ratio (i.e., due to the contributions of n-heptane and iso-octane) and the iso-octane only (GDI) equivalence ratio are shown. First, as previously discussed, it can be seen that the iso-octane distribution is not perfectly homogenous. This is expected since the fuel is delivered using a direct injection through the side mounted gasoline direct injector. However, the spread in the iso-octane distribution is reasonably small, ranging from $\phi=0.29$ near the liner to $\phi=0.22$ at 30 mm from the bore center. To estimate the equivalence ratio in the near nozzle region, it is assumed that the iso-octane distribution remains

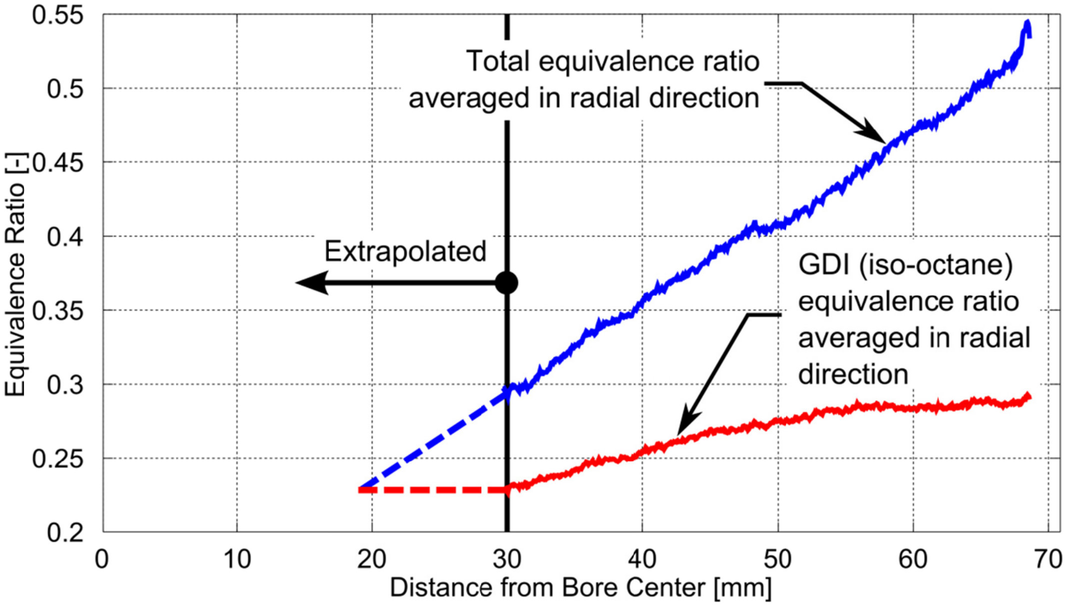

Figure 9-11. Average equivalence ratio in the radial direction as a function distance from the bore center. The blue lines show the total equivalence ratio (i.e., due to the contributions of n-heptane and iso-octane) and the red lines show the iso-octane only (GDI) equivalence ratio. The solid lines are radially averaged measured values and the dashed lines are extrapolated. The standard deviation in the radial direction for the total equivalence ratio is nearly constant at ± 0.06ϕ from the liner to the inner edge of the field of view. Similarly, the standard deviation in the radial direction for the GDI equivalence ratio distribution is ± 0.02ϕ.

constant at the value measured at 30 mm from the bore center (ϕ=0.22). The n-heptane distribution is assumed to continue the linear decrease observed in the measurements.

Similar trends can be extracted from the PRF and temperature distributions. Figure 9-12 shows the corresponding measured and extrapolated PRF and temperature curves (averaged in the radial direction) at -10° ATDC. Note that the extrapolated PRF values were calculated using the extrapolated equivalence ratio values shown in Figure 9-11. The temperature field is calculated as discussed in Section 8.3.2; however, the absolute value of the temperature should be considered an estimate. The extrapolated temperature was assumed to be linear until the PRF value reached 100 at 18 mm from the bore center.

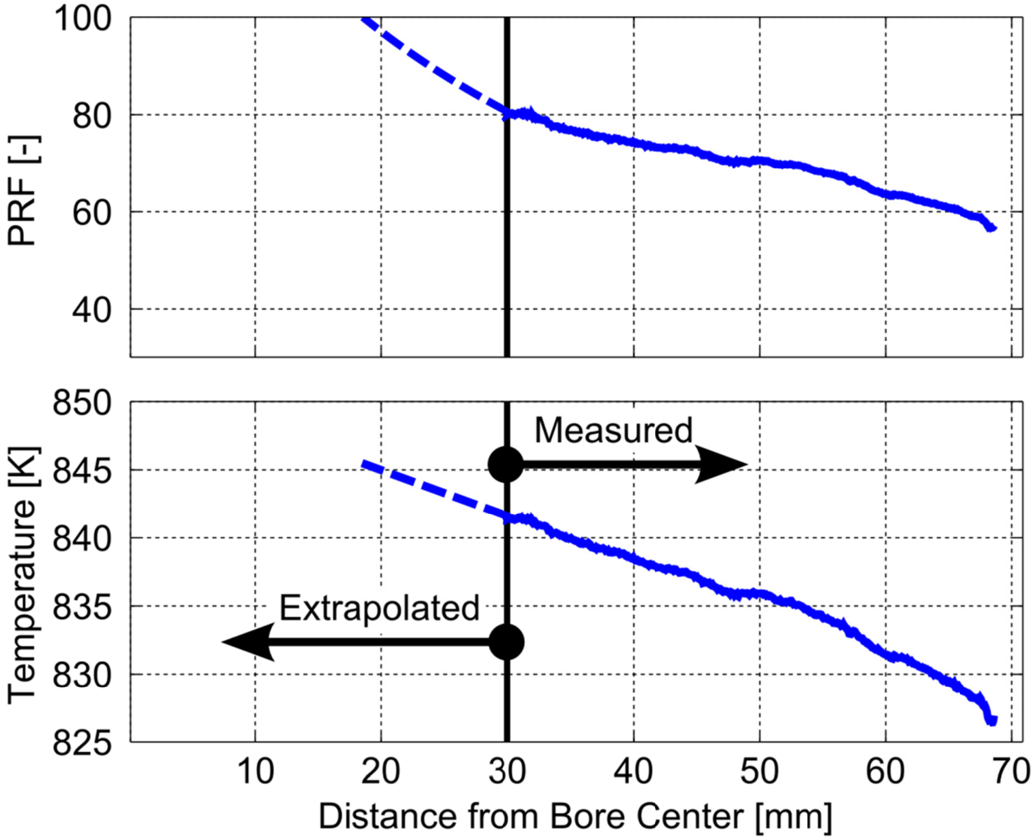

Figure 9-12. Average PRF (octane number) and temperature in the radial direction as a function distance from the bore center. The solid lines are radially averaged measured values and the dashed lines are extrapolated. The standard deviation in the radial direction for the PRF number and temperature are nearly constant at ± 5 PRF and ± 5K from the liner to the inner edge of the field of view.

Figure 9-13 shows the ignition delay, calculated using the Senkin code [47] and the reduced PRF mechanism developed by Ra et al. [58], as a function of distance from the bore center. Figure 9-13 is helpful to interpret the effect of equivalence ratio, PRF, and temperature stratification; however, the results should be interpreted with caution since they represent the ignition delay of an isolated mixture (i.e., with no interaction from the surrounding regions). Even without considering the effects of transport, the ignition delay of the less reactive regions (i.e., higher PRF number or lower equivalence ratio) will decrease due to compression heating. Further, the uncertainty in combining the measured equivalence ratio, PRF, and temperature with the ignition delay calculations is undoubtedly large; however, even with the limitations, the calculations of Figure 9-13 are at least qualitatively in agreement with the OH PLIF and chemiluminescence images. That is, the ignition delay is shortest near the liner and there is a gradient in ignition delay (fuel reactivity) from the liner to the cylinder centerline. Notice that the PRF and equivalence ratio stratification appear to outweigh the temperature stratification. That is, the temperature gradient would suggest that ignition should occur near the center of the chamber (in the hottest region), while PRF and equivalence ratio gradients suggest that ignition should occur in the outer region of the chamber. The relative roles of equivalence ratio stratification, PRF stratification, and temperature stratification are discussed in the next section.

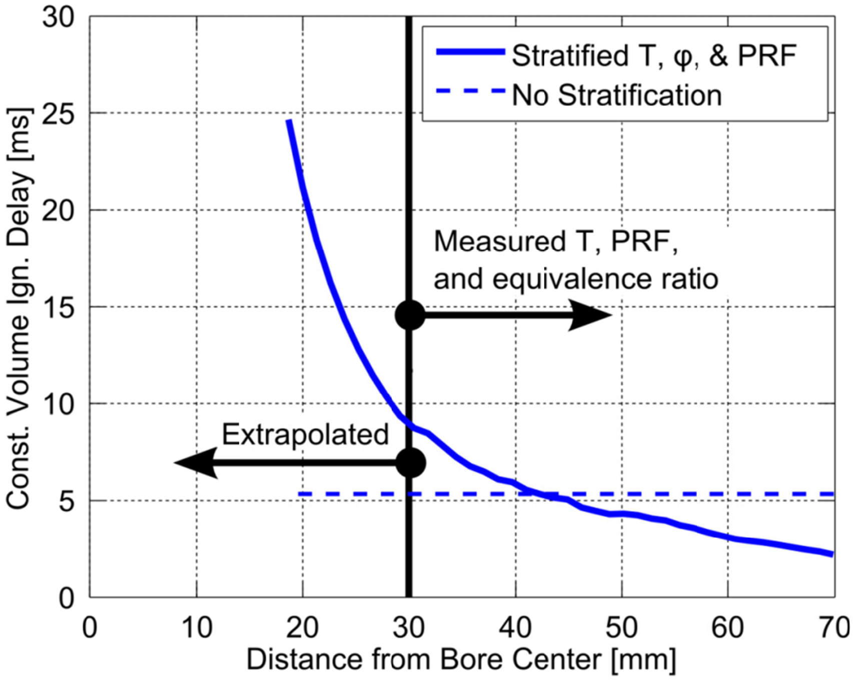

Figure 9-13. Calculated constant volume ignition delay as a function of distance from the bore center.

9.1.6 Relative Roles of Equivalence Ratio and Fuel Reactivity Stratification

The previous discussion and the discussions in derived from CFD modeling in Chapter 5 show that the fuel distribution prior to ignition corresponds well to the ignition location and reaction zone progression. The ignition location correlates with the region with the highest fuel reactivity and the direction of reaction zone growth is controlled by the gradient in fuel reactivity. Dec et al. [10, 12] have showed that the rate of heat release can be controlled by controlling the fuel distribution using a single-fuel (i.e., equivalence ratio stratification). In the RCCI strategy, stratification in PRF (octane number), equivalence ratio, and temperature (due to evaporative cooling and changes in the specific heat ratio) are present. Thus, it is of interest to understand the relative roles of equivalence ratio, PRF, and temperature stratification. The constant volume ignition delay calculations discussed in the previous section were repeated using a 2^3 design of experiments (DOE) to isolate these effects. Table 9-1 shows the design matrix.

Table 9-1. Design matrix used for constant volume ignition delay calculations to isolate the influence of equivalence ratio, PRF, and temperature stratification. The PRF stratification is shown in Figure 9-12, the equivalence ratio stratification is shown in Figure 9-11, and the temperature stratification is shown in Figure 9-12.

Case	PRF	ϕ	Temperature [K]
1	Stratified	Stratified	Stratified
2	Stratified	Stratified	832
3	Stratified	0.37	Stratified
4	Stratified	0.37	832
5	74.3	Stratified	Stratified
6	74.3	Stratified	832
7	74.3	0.37	Stratified
8	74.3	0.37	832

Figure 9-14 shows calculated ignition delays as function of distance from the bore center for each case. Figure 9-15 shows the difference in ignition delay between the least- and most-reactive regions. Case 1 is the same as that presented in Figure 9-13 and the difference between the least- and most-reactive regions is 22.5 ms. Case 2 shows the ignition delay with the temperature stratification removed. As discussed previously, the temperature stratification competes with the equivalence ratio and PRF stratification (i.e., regions with low PRF numbers and high equivalence ratios have low temperatures due to evaporative cooling); therefore, removing the temperature stratification increases the spread between the least- and most-reactive regions to 26 ms. Although the temperature stratification does have a small effect on the ignition delay, Figure 9-15 shows that the ignition delay is dominated by the equivalence ratio and PRF stratification (notice that the case with only temperature stratification (Case 7) has a nearly constant ignition delay, discussed in the next section). Therefore, the remaining discussion will combine cases with and without temperature stratification. Cases 3 and 4 show the ignition delay without equivalence ratio stratification. Removing the equivalence ratio stratification reduces the spread in ignition delay to ~12 ms. Cases 5 and 6 show the ignition delay without PRF stratification. Removing the PRF stratification reduces the ignition delay to ~8 ms.

As previously discussed, the presented change in ignition delay represents the maximum change in ignition delay considering isolated conditions. However, Figure 9-15 shows that, although both equivalence ratio and PRF stratification are important, the PRF stratification has the largest effect on ignition delay. Furthermore, the level of equivalence ratio stratification is limited by the equivalence ratios of ~0.2 to 0.5. On the low side (ϕ=0.2), reactions are too slow and combustion efficiency is poor. On the high side (ϕ=0.5) flame temperatures are high enough to form NOx. The addition of PRF stratification to equivalence ratio stratification allows improved control over the rate of heat release. For a given operating condition, the broadened combustion duration allows the combustion phasing (CA50) to be advanced to improve thermal efficiency with an equal pressure rise rate.

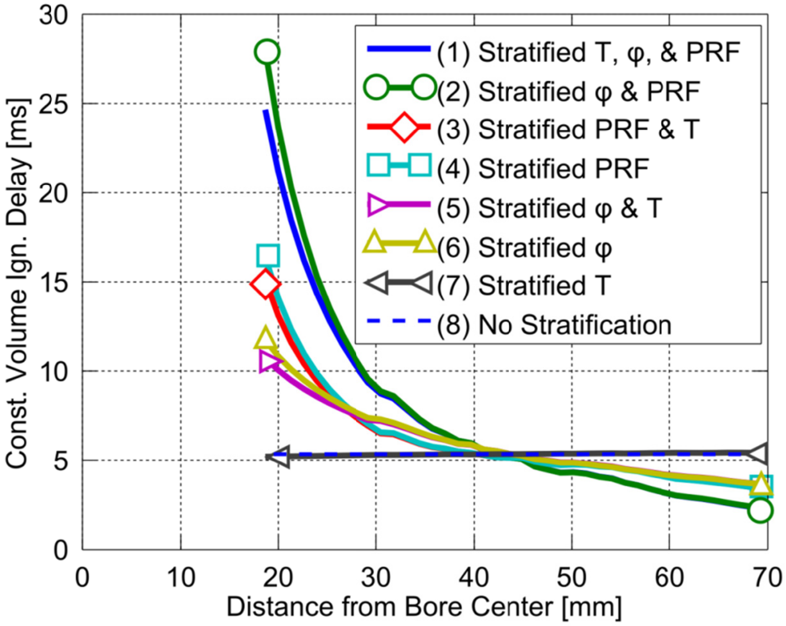

Figure 9-14. Constant volume ignition delay calculations showing the effects of equivalence ratio (φ), PRF, and temperature stratification.

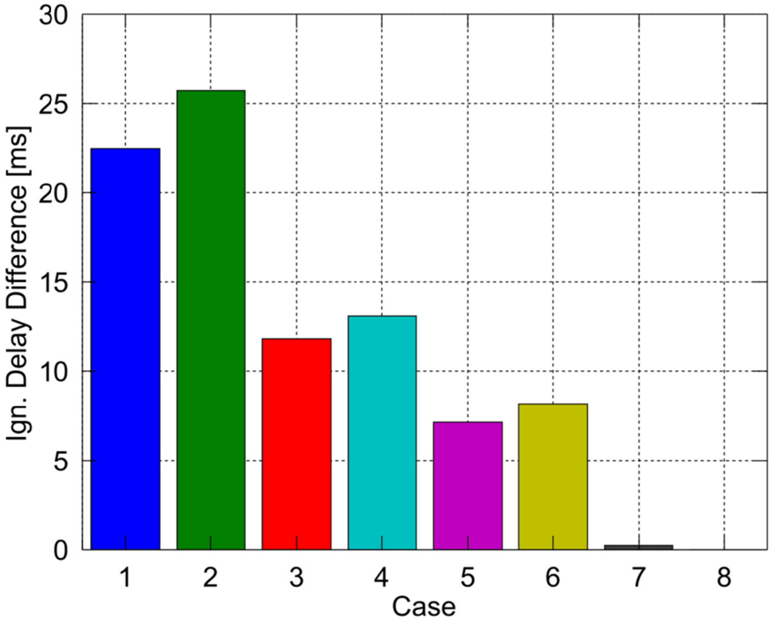

Figure 9-15. Difference between least and most reactive regions for the cases shown in Table 9-1.

Although the ignition delay calculations cannot be directly used to estimate the combustion duration, the relative change in ignition delay between the most- and least- reactive regions in the chamber (see Figure 9-15) is expected to correlate with the change in combustion duration through Eq. 2-1. For example, it is expected that removing the PRF stratification and using equivalences ratio stratification only (i.e., case 5) would shorten the combustion duration by a factor of ~3 (i.e., reducing the CA10 to 90 time 13° to 4°), significantly increasing the rate of heat release, and possibly resulting in unacceptably high pressure rise rate. However, there may also be some portions of the operating map where it is desirable to shorten the combustion duration (e.g., low-load, high-speed operation). Thus, reducing the difference in ignition delay between the most- and least-reactive regions in the combustion chamber (i.e., moving towards case 8 by increasing the mixing between the two fuels) may improve the engine efficiency. The ability to control the heat release rate using reactivity stratification is the focus of Chapter 10.

It is interesting that the temperature stratification only has a minor effect on ignition delay. Notice that, although the temperature gradient is nearly linear, the effect of temperature stratification is largest in the center of the combustion chamber and nearly negligible towards the cylinder liner (see Figure 9-14). Recall that the PRF gradient approximately the inverse of the temperature gradient; thus, it appears that the temperature stratification is most important when the fuel is primarily iso-octane (i.e., a single-stage ignition fuel). To illustrate this, Figure 9-16 shows the change in ignition delay over the temperature gradient shown in Figure 9-14 at a constant equivalence ratio of 0.37 and several different PRF numbers. A positive ignition delay difference means that the ignition delay at the liner (T=826 K) is shorter than the ignition delay at the center of the combustion chamber (T = 845 K). It can be seen that when a PRF fuel is used, the NTC behavior results in a nearly constant ignition delay. The ignition delay is shortest in the cooler regions at PRF blends of 50 and less. As the PRF is increased past 50, the ignition delay is shortest in the higher temperature regions. The effect of temperature stratification is largest when the fuel is neat iso-octane. The NTC behavior of PRF 0 (neat n-heptane), PRF 50, and PRF 100 is shown in Figure 9-17. The combination of Figure 9-16 and Figure 9-17 clearly show that the reason for the negligible temperature stratification effect at this condition is the NTC behavior of the PRF blends.

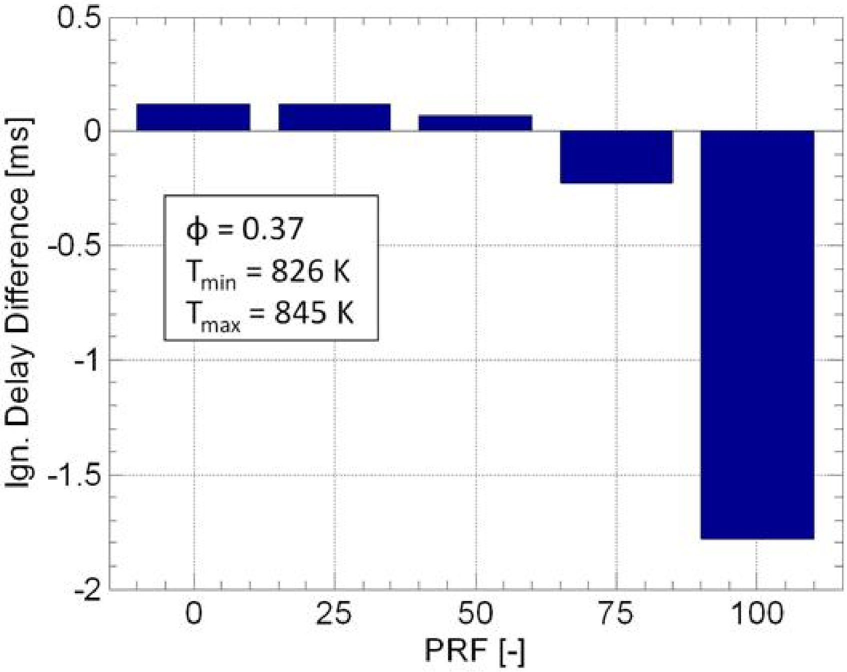

Figure 9-16. Difference in ignition delay from the cylinder liner (T = 826 K) to the center of the combustion chamber (T = 845 K). A positive number should be interpreted as a shorter ignition delay at the liner and longer ignition delay at the center of the combustion chamber.

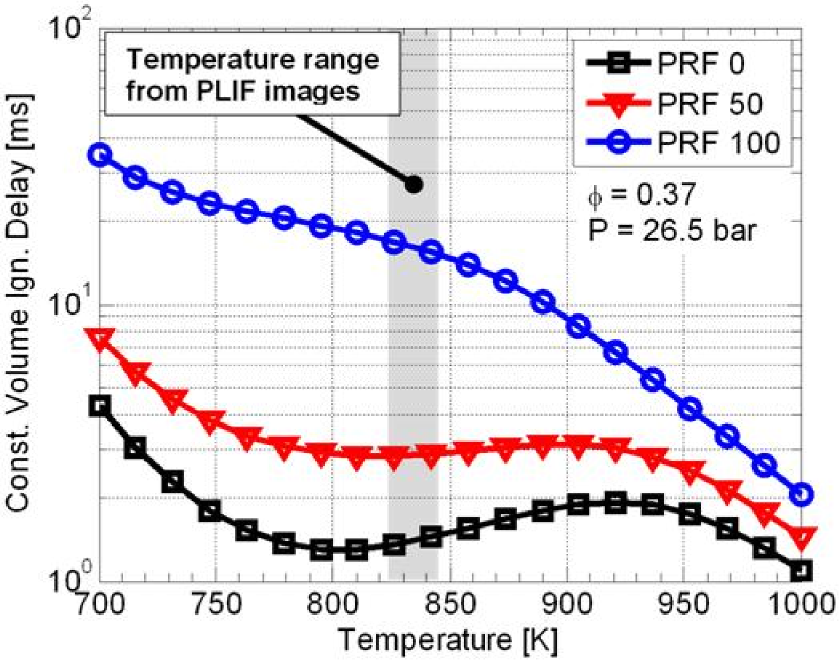

Figure 9-17. Constant volume ignition delay calculations over a range of temperatures at ϕ = 0.37 and a pressure of 26.5 bar. The shaded region shows the temperature range derived from the fuel tracer PLIF images at -10° ATDC.

9.1.7 Role of Flame Propagation

The previous sections show that RCCI combustion features a reaction zone that begins in the outer region of the combustion chamber and moves inward toward the center of the combustion chamber. The CFD modeling of Chapter 5 and the fuel tracer fluorescence imaging combined with the kinetics calculations presented in this chapter show that the ignition location and preferential reaction zone growth direction are controlled by gradients in the fuel reactivity; however, the role of flame propagation is still unclear. In this study, the 532 nm output of an Nd:YAG laser was used as an ignition source to probe the ignitability of various regions throughout the chamber. The resulting combustion luminosity was imaged using a high-speed digital camera. The experimental setup is discussed in Section 8.3.4.

The laser ignition location was swept from the center of the combustion chamber to 30 mm from the injector axis. Figure 9-18 shows the laser ignition locations. Each ignition location

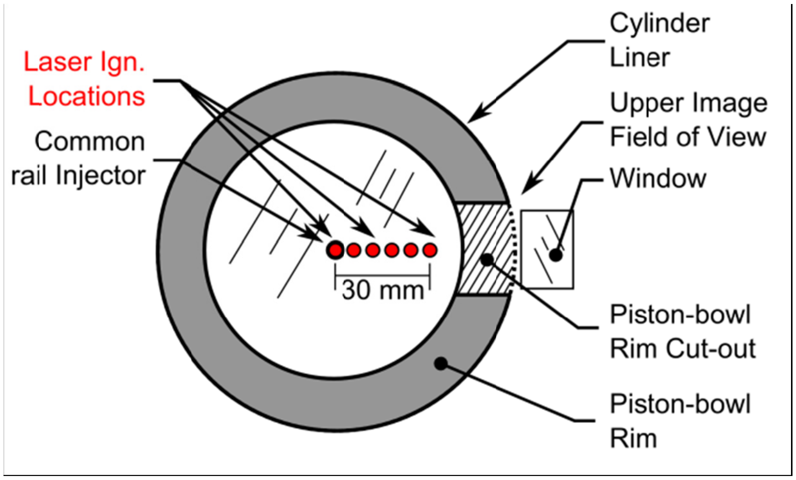

Figure 9-18. Experimental setup for laser ignition study. At each ignition location, 20 laser sparks were recorded.

is 13 mm below the firedeck and all ignition events were at -10° ATDC (slightly before the start-of-high-temperature heat release). At each laser ignition location, 20 firing cycles were recorded.

Figure 9-19, Figure 9-20, and Figure 9-21 show 10 of the 20 image sequences recorded with the laser ignition location at the center of the combustion chamber, 18 mm from the center, and 30 mm from the center, respectively. The images are recorded with the high speed camera viewing upward through the flat piston crown window. The solid white line shows the edge of the piston bowl rim that bounds the field-of-view. The image acquisition time in crank angle degrees after TDC is shown in the upper left-hand corner of each image. The location of laser ignition is indicated by the white dot. To aid in interpretation of the images, an edge-tracking algorithm was applied to the images. The red lines bound the regions showing intensities 20% greater than the background intensity. The intensity cutoff of the edge tracking algorithm is arbitrary; however, the edge tracking is only used to aid in visualization and therefore does not influence the results of the study.

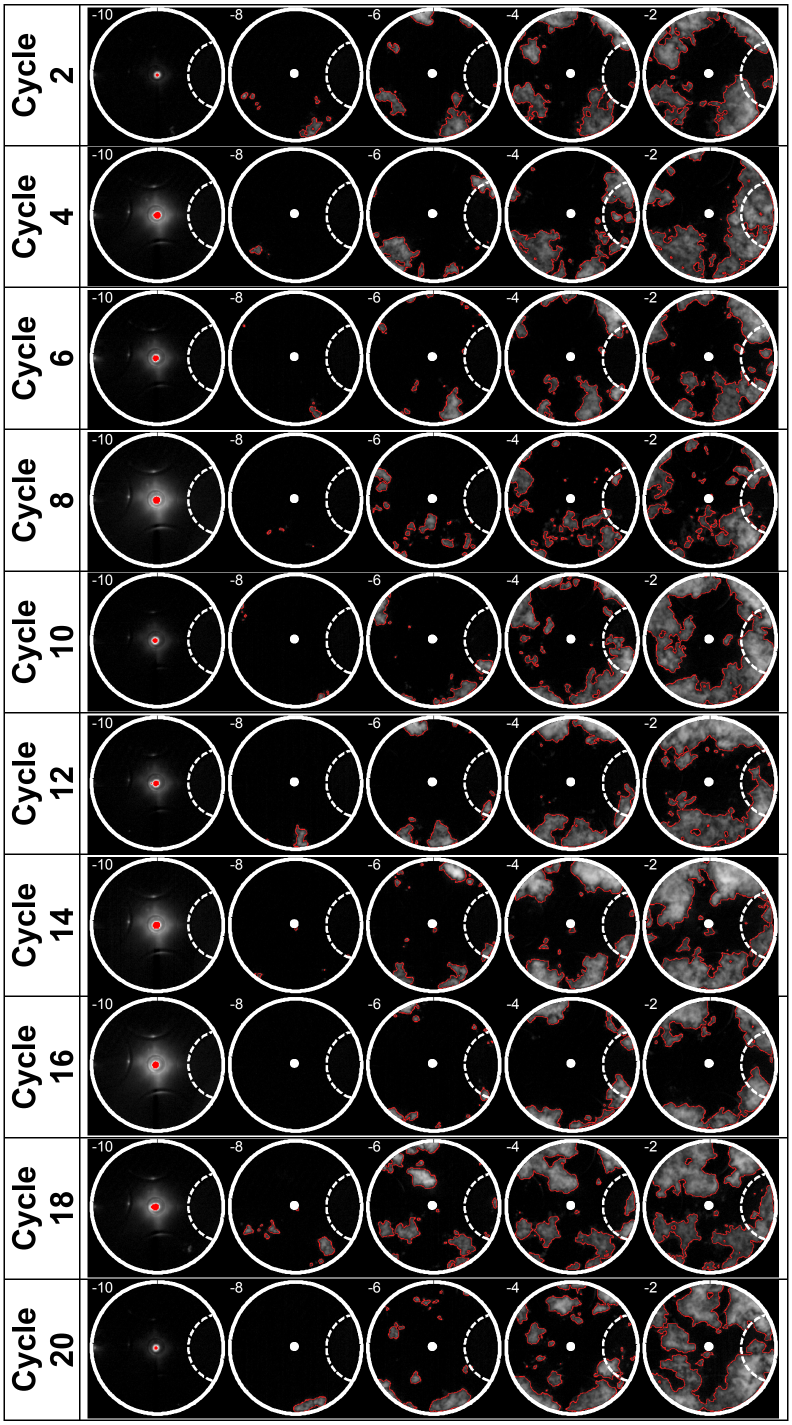

Figure 9-19. High speed chemiluminescence imaging of the RCCI case with the laser ignition location at the center of the combustion chamber. The laser ignition location is indicated by the white dot on the images.

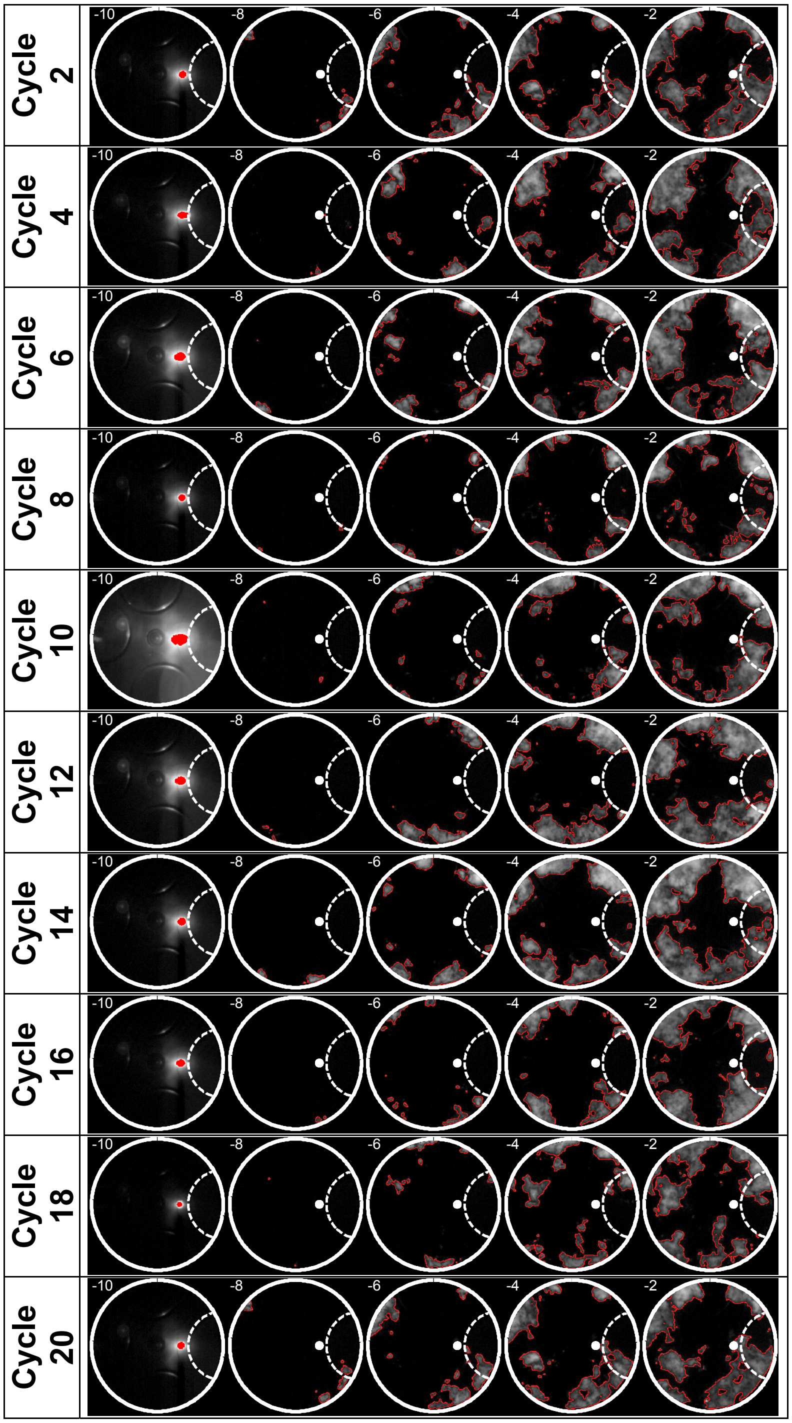

Figure 9-20. High speed chemiluminescence imaging of the RCCI case with the laser ignition location 18 mm from the center of the combustion chamber. The laser ignition location is indicated by the white dot on the images.

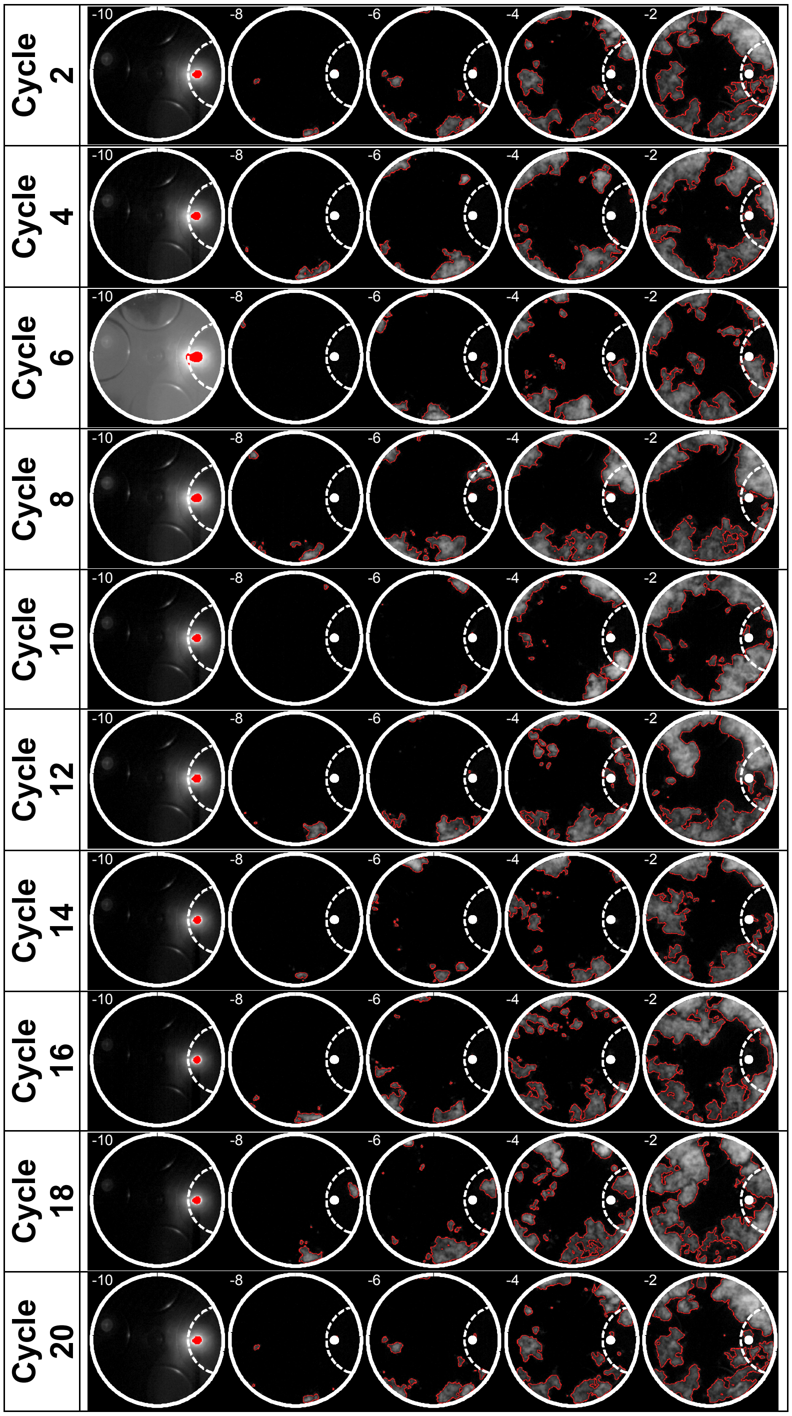

Figure 9-21. High speed chemiluminescence imaging of the RCCI case with the laser ignition location 30 mm from the center of the combustion chamber. The laser ignition location is indicated by the white dot on the images.

At this point, it should be stated that the purpose of this study is only to understand if it is possible to achieve flame propagation. That is, if flame growth is observed from the laser-ignited zone it does not definitively say that the mechanism of reaction zone growth is flame propagation. However, in regions where it is not possible to achieve flame growth from the laser-ignited zone, it is likely that the dominant mechanism of reaction zone growth is not flame propagation. Further, comparing the growth rates of the laser-ignited zones to the growth rates of the zones ignited by auto-ignition can provide evidence of the dominant mechanism of reaction zone growth.

From Figure 9-19 through Figure 9-21, it is clear that not all cycles result in flame growth from the laser ignited zone. However, several cycles do show at least weak flame growth from the laser-ignited zone (e.g., cycle 14 from Figure 9-19, cycle 20 from Figure 9-20, and cycle 10 from Figure 9-21) suggesting that it may be possible to support flame propagation in some regions of the chamber. Figure 9-19 through Figure 9-21 show that the laser ignition process is stochastic. It is desirable to determine the probability of propagating a flame from a laser ignited zone. Chemiluminescence is observed from the laser-ignited zones and from auto-ignition zones; therefore, identifying the cases resulting in flame growth from the laser-ignited zone must be performed manually. Each set of images (high-speed movies) were viewed and the cases showing growth of the auto-ignition zone were recorded. Of course, this manual procedure is subjective; however, after viewing the movies several times, cases with flame growth are clear. Figure 9-22 shows the percent of laser sparks resulting in flame growth. Between the center of the combustion chamber and 18 mm downstream from the injector, approximately 30% of laser-ignited cycles resulted in flame growth. Although flame growth was observed in this region, the laser-ignited zone grew rather slowly and was quickly overtaken by the surrounding reaction zones. These results suggest that for locations between the center of the combustion chamber and 18 mm downstream from the injector axis, flame propagation plays a minimal role in the movement of the reaction zone. As the ignition location was moved away from the center of the combustion chamber, the number of ignition events resulting in flame growth increased and at the 30 mm location approximately 75% of the ignition events result in flame growth. However, even at the 30 mm location, where consistent flame growth was observed, the chemiluminescence images showed the appearance of auto-ignition sites ahead of the main reaction zone. It appears that the bulk reaction zone movement is controlled by the appearance of these auto-ignition sites, rather than the propagation of a continuous flame front. However, the growth rates of the local auto-ignition sites appear to be similar to the growth rate of the laser-ignited zone. This finding suggests that these auto-ignition sites may grow due to a combination of flame propagation and sequential auto-ignition even though the bulk reaction zone movement appears to be the controlled by the sequential appearance of auto-ignition sites.

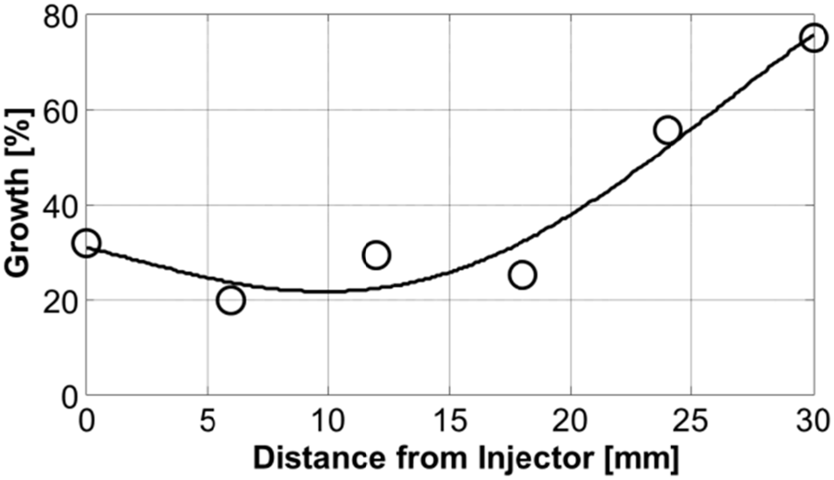

Figure 9-22. Percent of laser sparks resulting in flame growth. Twenty laser sparks were recorded at each location.

To explain the dependence of flame propagation potential on axial location, Figure 9-23 shows a 40 cycle ensemble averaged equivalence ratio map acquired at the laser ignition time (-10° ATDC). The 30 mm laser ignition location is shown by the red outlined circle on the equivalence ratio map. It can be seen that the equivalence ratio increases with increasing distance from the center of the combustion chamber. Thus, the observed dependence of flame growth on ignition location appears to be due to the equivalence ratio stratification. That is, the regions upstream of the 30 mm location are likely too lean to consistently support flame propagation.

The 30 mm laser ignition location is on the edge of the field of view of the cylinder head window. Ideally, the laser ignition location would have been moved all the way to the cylinder liner; however, as the laser ignition location was moved closer to the liner, back reflections of the laser light off the inner surface of the optical access window would damage the window. In Section 9.1.6, the trends in equivalence ratio, PRF (octane number), and temperature were

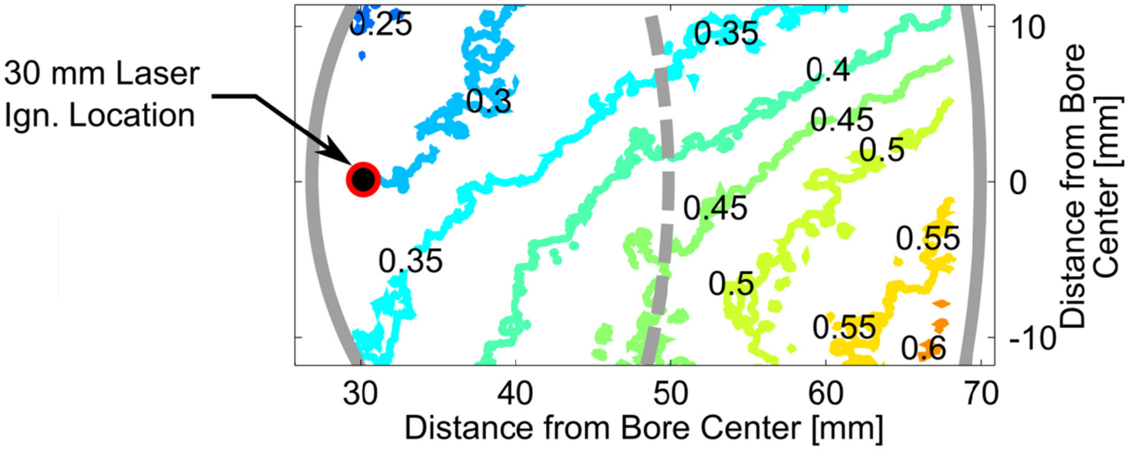

Figure 9-23. Equivalence ratio contour at -10° ATDC acquired using toluene fuel tracer fluorescence. The camera view is downward into the squish region and the laser sheet is located 13 mm below the firedeck.

extrapolated to the cylinder centerline. These data can be further used to estimate the flame speed as a function of distance from the bore center. Figure 9-24 shows the estimated laminar flame speed[14] as a function of distance from the bore center. The laminar flame speed was calculated as discussed in the description of the flame propagation model in Chapter 3. The decrease in flame speed with decreasing distance from the injector is clear and the dependence of flame speed on distance from the center of the combustion chamber correlates with the observed probability of flame propagation.

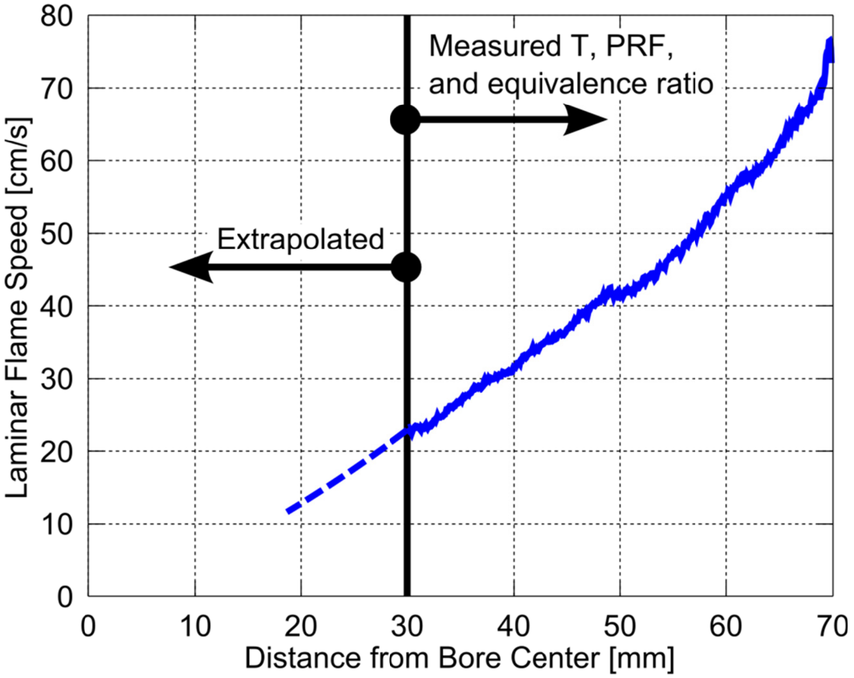

Figure 9-24. Laminar flame speed as a function of distance from the center of the combustion chamber calculated from the radially averaged fuel tracer PLIF measurements and extrapolated values.

---

[14] Of course, turbulence will increase the flame speed; however, the injections occur early in the cycle and CFD modeling shows that the turbulence intensity is nearly uniform in the plane of interest. Thus, the turbulent flame speed will scale with the laminar flame speed and presenting only the laminar flame speed is sufficient.

9.1.7.1 CFD Modeling Considering Flame Propagation

Although the results of the laser ignition study are not conclusive, the study does suggest that, at the present operating conditions, flame propagation may play a role in the outer region of the combustion chamber. The reaction zone movement in the center of chamber appears to be controlled by sequential auto-ignition. CFD modeling was used to further evaluate the roles of flame propagation and distributed auto-ignition. The CFD modeling was performed using the multi-mode combustion model that combines a comprehensive kinetics scheme [58] for volumetric heat release and a level-set-based model for turbulent flame propagation (i.e., the KIVA-Chemkin-G code [55, 68]). To choose between the kinetics solution (Chemkin) and the flame propagation solution (G-Equation), the timescales of flame propagation and kinetics are compared. Figure 9-25 shows a comparison of the measured and predicted cylinder pressure and AHRR with and without the consideration of flame propagation. It can be seen that considering flame propagation has little influence on the bulk combustion characteristics. This is consistent with the chemiluminescence imaging, where it appeared that the bulk reaction zone movement was controlled by the sequential appearance of ignition kernels. However, the laser ignition study showed that locally flame propagation may play a role.

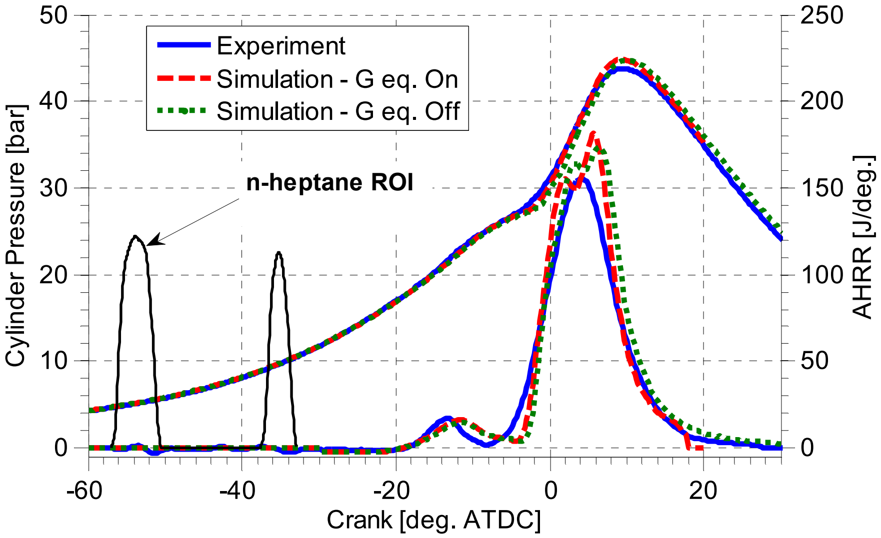

Figure 9-25. Comparison of measured and simulated cylinder pressure and AHRR. The simulations were performed with (G eq. On) and without (G eq. Off) consideration of flame propagation

Figure 9-26 shows the percentage of cells containing a flame and those solved by kinetics and flame propagation and Figure 9-27 shows the locations of the flame surfaces and high temperature regions. It can be seen that initially the few flame-containing cells are almost entirely solved by flame propagation. In the simulations, this consists of the first growth of the auto-ignition zones. As the combustion process proceeds, more auto-ignition sites appear and the kinetics solution begins to dominate. The CFD modeling predictions agree qualitatively with the ignition location and reaction zone growth upstream. The combination of the CFD modeling and chemiluminescence imaging suggests that shortly after the formation of an ignition kernel, flame propagation may play a role in energy release (locally). However, the bulk energy release appears to be dominated by the appearance of ignition kernels.

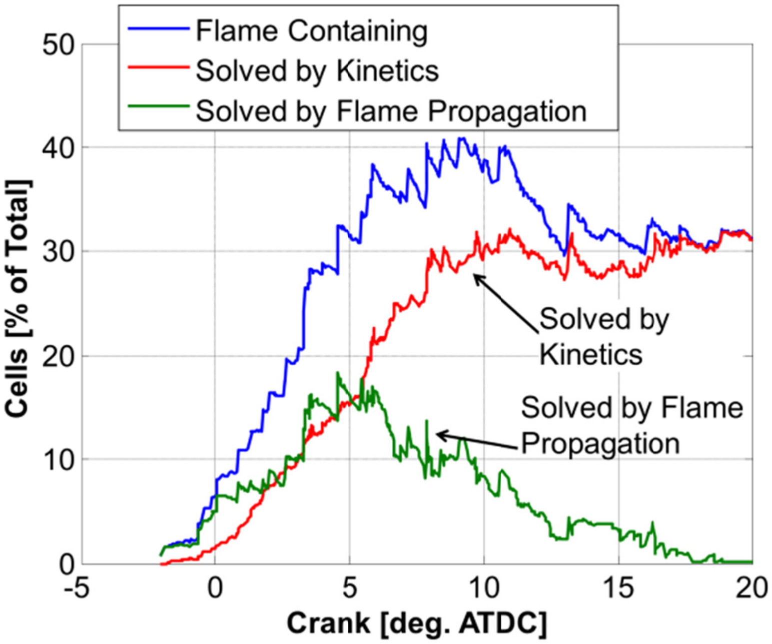

Figure 9-26. CFD solution showing the cells containing a flame, those solved by the flame propagation model, and those solved by kinetics.

The results of this study suggest that at the lean conditions typical of RCCI combustion[15], when flame propagation does play a role, the growth of the flame is very similar to the growth of an auto-ignition front. The present study was performed at a relatively light-load; thus, it can be argued that the results as confined to light load RCCI operation. Recall, however, that the overall equivalence ratio of this case is 0.42. Without using EGR, the peak equivalence ratio to avoid NOx formation is around 0.5 [12]; therefore, it can be concluded that the results are applicable to any RCCI-type strategy operating where low-NOx levels are observed. That is, when low NOx emissions are observed, it is not likely that flame propagation is the dominant mechanism of reaction zone growth. This is not to say that flame propagation results in

---

[15] The present study was repeated at a global equivalence ratio of ϕ=0.8 (see Appendix B: Additional Optical Engine Data). With an equivalence ratio of 0.8, it is found that consistent flame propagation is observed on nearly every cycle.

increased NOx emissions, but rather, regions that support strong flame propagation require equivalence ratios that result in flame temperatures above the NOx formation threshold.

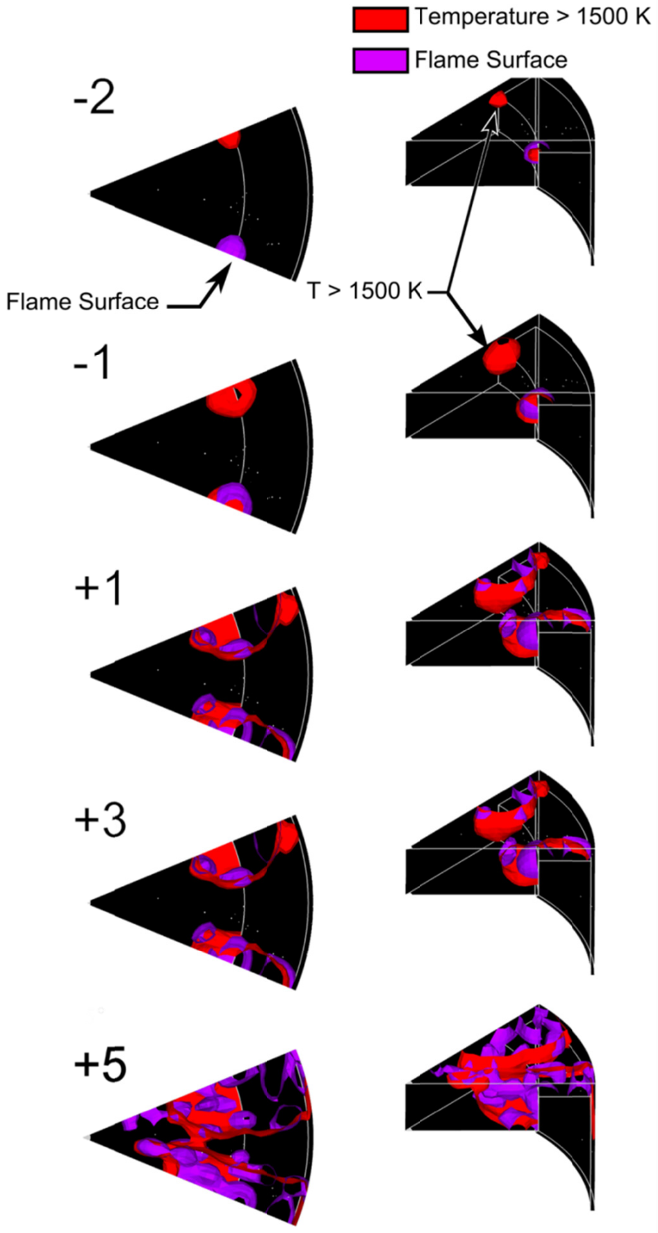

Figure 9-27. CFD modeling showing the flame surface (purple iso-surface) and region with temperature greater than 1500 K.

9.1.8 Evaluation of the CFD model predicted RCCI combustion evolution

Section 9.1.7 suggested that kinetics is the dominant factor controlling the RCCI combustion evolution. This finding supports the preliminary CFD modeling performed without considering flame propagation. This finding is consistent with the description of the RCCI combustion process proposed in Chapter 5. To further evaluate the validity of the description presented in Chapter 5, the model predicted species evolutions are compared to those derived from the PLIF measurements.

To make a qualitative comparison between the CFD modeled species evolutions and those from the PLIF images presented in the Section 9.1.4, the total CH_2O and OH fluorescence (normalized) is compared to the CFD model predicted species evolutions. Figure 9-28 shows the evolution of iso-octane, n-heptane, formaldehyde (CH_2O), and OH predicted by the CFD modeling and the normalized CH_2O and OH fluorescence from the single shot (SS) and average (Ave.) PLIF images. Although the comparison is not quantitative, the CH_2O and OH evolutions derived from the PLIF images agree well with the predicted species evolutions. The good agreement provides confidence in the model predictions and validation for the CFD based explanation of the RCCI combustion process discussed in Chapter 5.

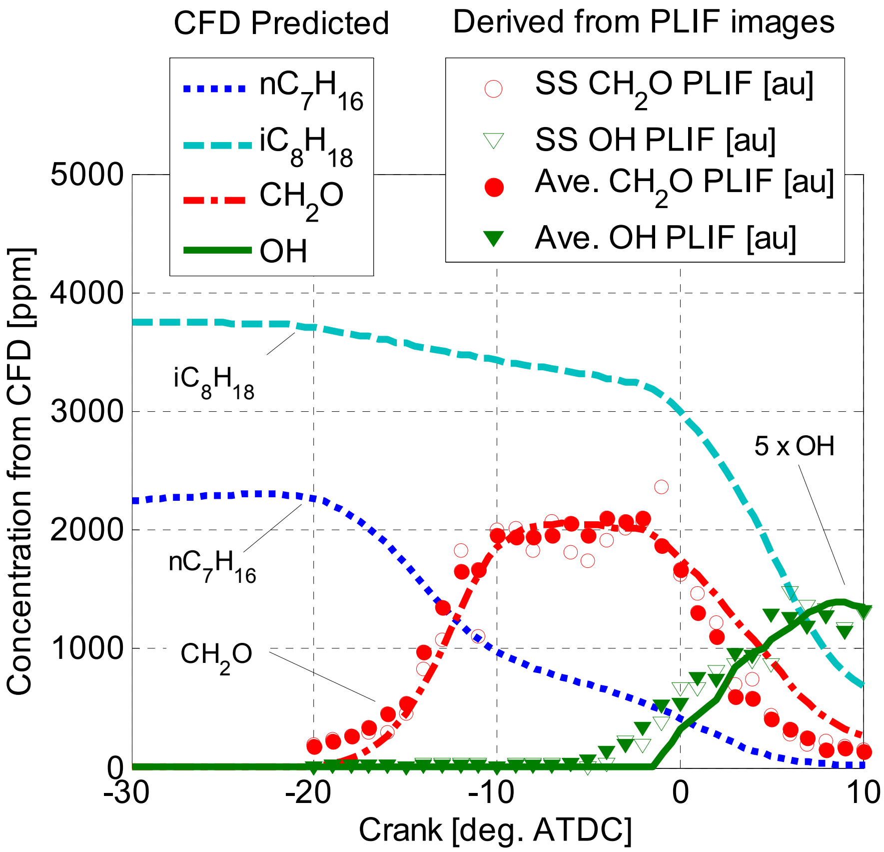

Figure 9-28. Evolution of iso-octane (light-blue), n-heptane (dark blue), formaldehyde (red), and OH (green) predicted by the CFD modeling (lines) compared with the CH_2O and OH evolutions derived from the PLIF images (symbols). The open symbols are from the single-shot images and the filled symbols are from the average images.

CFD modeling was only performed on a sector mesh and the cutout in the piston bowl rim was not modeled; therefore, direct comparisons of the species locations are not possible. However, the general locations of the CH_2O and OH can be compared to the planar imaging. Figure 9-29 shows a comparison of the CFD predicted iso-surfaces of n-heptane, CH_2O, and OH with the CH_2O and OH PLIF images. Note that since iso-octane completely fills the chamber in many of the images, the iso-octane iso-surface is excluded from Figure 9-29 for clarity. The buildup in CH_2O in both the experiments and simulations occurs in the outer region of the combustion chamber (i.e., in the squish in the simulations and in the cutout in the experiments).

This location corresponds to the region with the highest concentration of n-heptane early in the cycle. Likewise, the transition to second stage combustion (i.e., first appearance of OH) occurs in similar location. The overall evolution of RCCI combustion and the general locations of key species appear to be captured well by the simulations, providing additional validation for the description of the combustion evolution presented in Chapter 5.

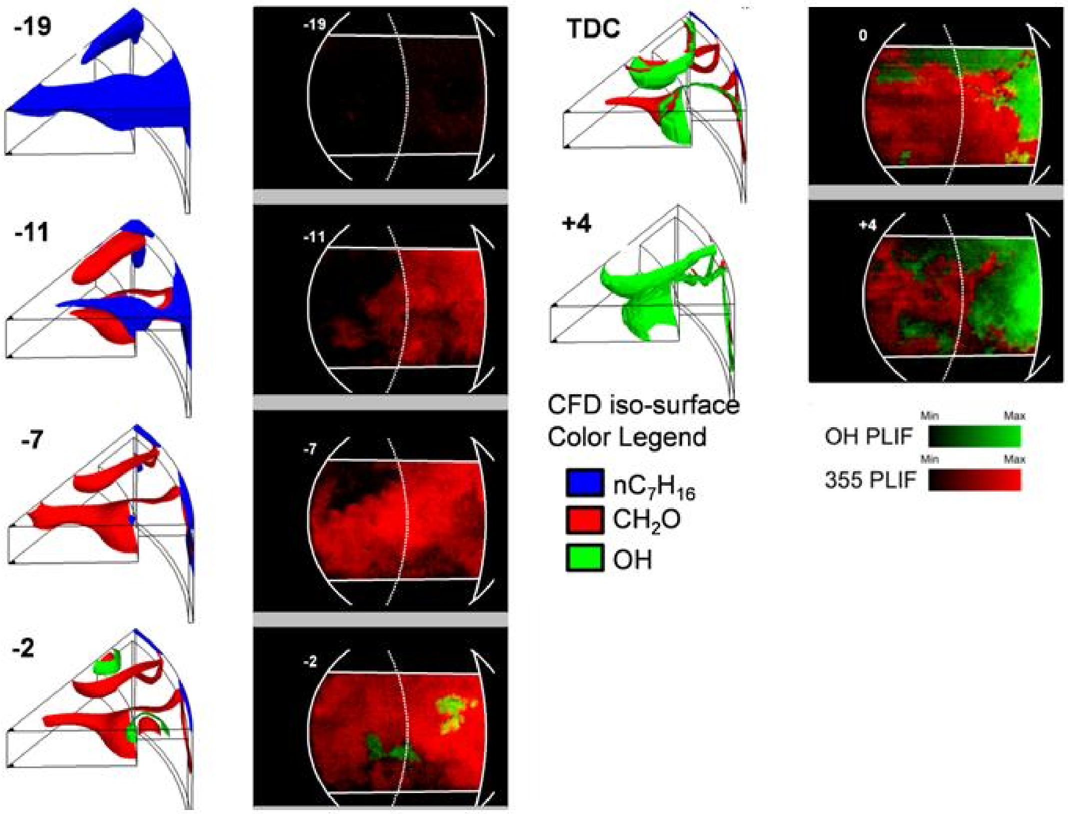

Figure 9-29. Iso-surfaces showing the locations of n-heptane, formaldehyde (CH_2O), and OH predicted by CFD modeling compared with simultaneous CH2O and OH PLIF images.

Chapter 10

Investigation of Fuel Reactivity Stratification as a Method to Control the Heat-Release Rate

In Chapter 9, the combination of optical diagnostics, kinetics modeling, and CFD modeling confirmed that the ignition location and reaction zone growth is dominated by the fuel reactivity stratification and the model predicted description of the combustion process was validated. Additionally, Chapter 9 used kinetics modeling to suggest that controlling the level of fuel reactivity stratification will provide control over the heat release rate. The final chapter expands on the optical engine work of Chapter 9 and explores fuel reactivity stratification as a method to control the rate of heat release for RCCI combustion.

10.1 Operating Conditions

The engine operating conditions are similar to the baseline conditions discussed in Chapter 9 (i.e., 1200 rev/min and 4.2 bar IMEP); however, in this study a single injection of n-heptane is used. The operating conditions are shown in Table 10-1. A sweep of common-rail (n-heptane) start of injection timings was used to generate a range of fuel distributions from well mixed (i.e., early common-rail injection) to stratified (i.e., late common-rail injection)[16]. The intake temperature was adjusted at each injection timing to hold combustion phasing (CA50) fixed at 2° ATDC in order to allow direct comparisons of the combustion rate. This value of

---

[16] The purpose of this work is not to optimize the injection timing, but rather show the influence of fuel reactivity stratification on the heat-release rate. Liquid impingement on the cylinder liner was observed for injection timings earlier than -90° ATDC; however, since n-heptane was used as the common-rail fuel and the intake and coolant temperatures were set near the atmospheric boiling point of n-heptane, it is expected that any liquid impinging on the liner will quickly vaporize. The high-speed imaging showed very little evidence of the “pool fires” characteristic of liquid films. Of course, if diesel fuel were used as the common-rail fuel, it is expected that liquid impingement would be problematic; however, it is likely that, even using diesel fuel, a multiple injection strategy could be used to generate a range of fuel reactivity stratification. Such an investigation, however, is beyond the scope of this study.

CA50 was selected to be comparable to the baseline RCCI case and previous RCCI research (e.g., Hanson et al. [22]).

Table 10-1. Engine operating conditions for the chemiluminescence imaging study and reference operating condition for the toluene fuel tracer fluorescence study. The toluene fluorescence study operated under oxygen-free conditions by supplying the intake with 100% nitrogen.

Engine speed	1200 rpm
Gross IMEP	4.2 bar
Intake temperature	73°C to 100°C
Intake pressure	1.1 bar abs.
Intake flowrate	23.0 g/s
Inlet oxygen concentration	21 vol. %
GDI injection pressure	100 bar
CR injection pressure	600 bar
GDI SOI (command)	-240° ATDC
CR SOI (actual)	-155° to -15° ATDC
Actual GDI DOI	36° CA
Actual CR DOI	9° CA
Total injected fuel mass	64 mg
iso-octane mass (GDI)	64%
n-heptane mass (CR)	36%
Premixed (iso-octane) equivalence ratio	0.27
Overall equivalence ratio	0.42
Overall PRF	64
Nom. motored TDC density	11.1 kg/m^3

10.2 Results and Discussion

10.2.1 Heat-release rate

Figure 10-1 shows the effect of CR SOI timing on the peak apparent heat-release rate. Notice that the peak apparent heat-release rate tends to increase significantly at both early and late CR SOI timings and a minimum is observed near an intermediate CR SOI timing of -50° ATDC. Figure 10-2 shows the ensemble-averaged apparent heat-release rates for cases with CR SOI timings of -145°, -50°, and -15° ATDC. At an early common-rail SOI timing (-145° ATDC) the low-temperature heat release (LTHR) begins around 19° BTDC, reaches a peak near -15° ATDC, and ends at -11° ATDC. Second-stage ignition begins near -4° ATDC and the AHRR

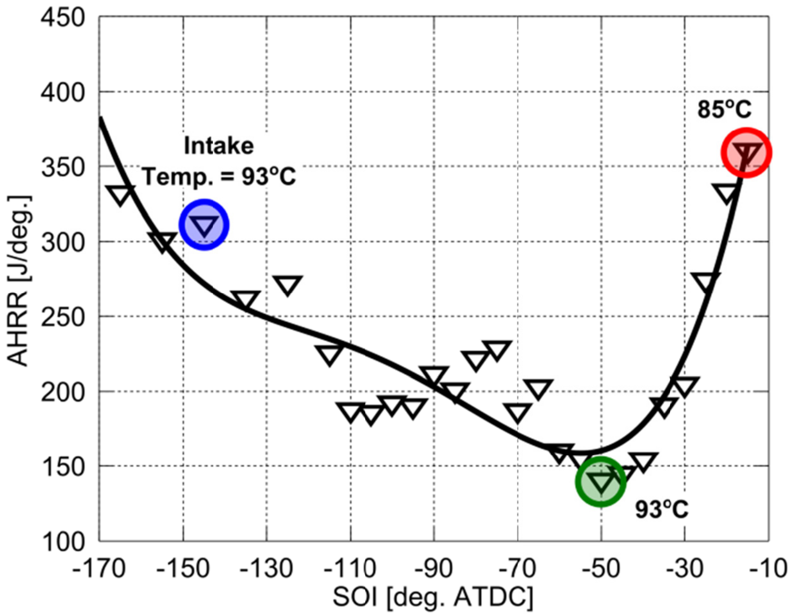

Figure 10-1. Effect of CR SOI timing on the peak AHRR. The colored circles show selected cases for further analysis. The intake temperature was adjusted at each operating condition to hold CA50 constant at 2° ATDC. The intake temperature for each of the selected cases is indicated by the numbers on the plot [121].

peaks around 2° ATDC. Following the peak, the AHRR falls off rapidly until about 7.5° ATDC, followed by a small tail until about 12° ATDC.

Similar to the early-injection timing, the SOI -50° case also shows that LTHR begins near -19° ATDC. The LTHR peaks at -14° ATDC and reaches completion by -10° ATDC. In contrast to the early-injection timing, the delay between the end of LTHR and start of high-temperature heat release (HTHR) is relatively short. HTHR begins at -7° ATDC and proceeds relatively slowly, peaking near TDC. Recall that as was shown in Figure 10-1, the peak AHRR is approximately half that of the earliest or latest injection timing cases. Similar to the slow rise in the AHRR, the end of combustion also occurs at a relatively slow rate.

The latest injection timing case (SOI -15° ATDC) shows that LTHR begins around -5° ATDC and peaks around -3.5° ATDC. The end of LTHR is much less clear for the latest injection timing case. Although the average AHRR trace shows a “dip” near -2° ATDC which could signify the end of LTHR, this feature was not observed for all cycles. Regardless, the latest injection case shows a very quick transition to second-stage ignition followed by a rapid spike in heat release. The peak AHRR occurs at 1.75° ATDC. Following the peak, the heat release falls off rapidly until 6° ATDC. In this case, a long tail on the AHRR curve is observed and heat release remains elevated to later than 20° ATDC. CFD modeling (see Appendix A: Additional Model Validation Cases) suggests that the tail on the heat release curve is due to the regions outside of the n-heptane jet, where the reactions are slow. Indeed, metal-engine experiments [120] performed at a similar condition showed very high hydrocarbon emissions for

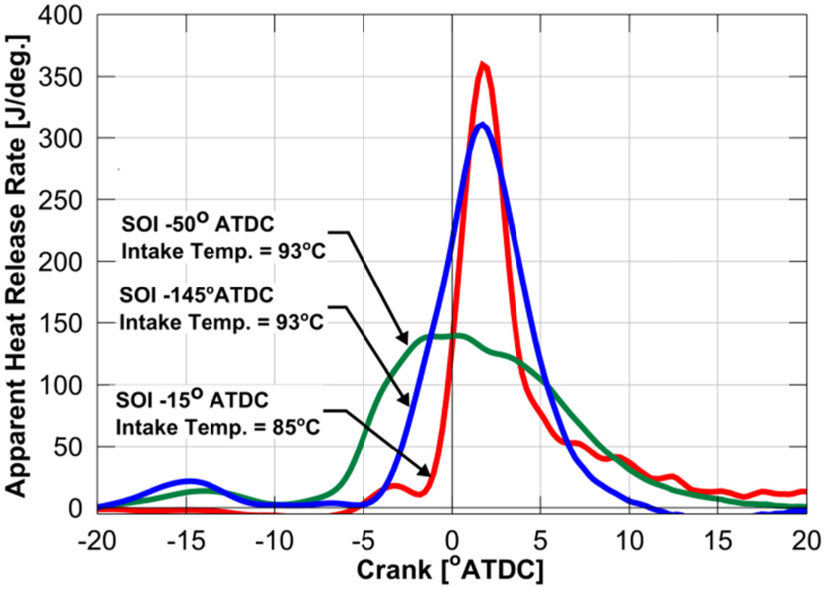

Figure 10-2. Apparent heat-release rates for the selected cases. The SOI timings and intake temperatures for each case are shown on the figure [121].

the late injection timing case. The rapid heat release and weak late cycle burnout of the SOI -15° case show that operation in the RCCI mode with near TDC injection timings will likely result in poor engine performance due to high combustion rates and low combustion efficiency.

10.2.2 Combustion Luminosity Images

To understand the observed differences in the AHRR curves for the different injection timings, high-speed camera sequences showing high-temperature chemiluminescence were recorded. The image sequences for the three selected injection timings are shown in Figure 10-3. The camera settings were held fixed for all operating conditions. The images are acquired with the high-speed camera viewing upward through the flat piston crown window and the imaging setup is discussed in Section 8.3.1. The number in the upper left-hand corner of each image shows the crank angle at which the image was acquired. The first image in each sequence shows the CR fuel spray illuminated by a high-powered LED at 3 degrees after SOI (ASOI). The piston bowl-rim has a cutout at the three o'clock position to allow laser access for the fuel-tracer fluorescence diagnostic (see Figure 8-4 (b)). Similar to the HSC sequence presented in Chapter 9, the image sequences presented here are from a representative single cycle that has the heat release most similar to the ensemble averaged AHRR curve. Comparison between the single-cycle and ensemble average heat-release rates are shown at the top of each image sequence.

Discussion of the combustion luminosity images begins with the SOI -145° case. The spray penetration for such early injection into low-density gases is quite long, extending nearly to the bowl-rim even with high-volatility n-heptane. Some variation in the penetration among the sprays seems apparent, but the sprays are not illuminated uniformly, so some of the variation in the liquid fuel penetration may be an optical artifact. Ignition is observed near -5° ATDC at several locations on the right half of the field of view. After ignition, the reaction zone grows rapidly, which is consistent with the observed rapid energy release. By -2° ATDC the reaction zone fills approximately half of the field of view. Notice that auto-ignition sites are now visible near the nine o'clock position and by 1° ATDC the luminosity is present nearly all the way across the field-of-view. For the selected case, ignition was first observed on the right-hand side of the chamber. This suggests that on average, either the reactivity of the right side of the chamber is slightly higher than that of the left, or that temperature and/or mixing on the right side of the chamber is different, possibly due to flows associated with the piston bowl-rim cut-out. Not all image sequences showed auto-ignition favoring the right side of the chamber, however. Moreover, the random ignition locations and rapid reaction zone growth suggests little stratification in fuel reactivity.

The second column of Figure 10-3 shows combustion luminosity images for the SOI -50° case. Similar to the early injection timing, the liquid sprays penetration is uneven among the holes, due to non-uniform illumination and/or needle dynamics, but the overall penetration is much shorter at the higher in-cylinder density. Luminosity first appears near the piston bowl rim at -6° ATDC. Additional imaging into the squish region (not presented here for brevity), with the camera viewing downward through the cylinder head window as shown in Figure 8-2, showed that ignition generally occurred in the squish region near -6° ATDC (similar to the split-injection RCCI case discussed in Chapter 9). At -4° ATDC, luminosity is observed from five of the eight fuel jets, and similar to the image at -6° ATDC, luminosity is first observed near the edge of the piston bowl-rim. By 2° ATDC, all eight fuel jets show at least weak luminosity. In contrast to the early injection case, once ignition occurs, the reaction zone does not rapidly progress throughout the chamber, but rather moves at a relatively steady rate from the bowl rim to the center of the chamber. This is observed in the images from TDC to 5° ATDC. The combustion luminosity sequence is very similar to the combustion luminosity sequences observed for the split-injection RCCI case discussed in detail in Chapter 9. The observed broad combustion duration of the SOI -50° case is the result of sequential auto-ignition from the downstream portion of the jet to the center of the combustion chamber.

The third column of Figure 10-3 shows combustion luminosity images for the SOI -15° case. The liquid penetrations for the high-volatility n-heptane sprays are very short at the high charge-density, near-TDC conditions. The injection ends near -6° ATDC (not shown) and luminosity is first observed at -1° ATDC near the piston bowl-rim. Once ignition occurs in the downstream region of a jet, the combustion zone rapidly progresses to fill the jet. The rapid progression of combustion throughout the jet suggests that much of the jet has a similar ignitability. This is in contrast to the previous case (i.e., the SOI -50° ATDC case) where it was shown that the reaction zone moved slowly from the bowl rim to the center of the chamber. By TDC, seven of the eight jets display strong luminosity. Note that at TDC, luminosity for the one o'clock jet is much weaker than for the other jets. Such asymmetric ignition from jet-to-jet is typical, with different jets igniting late on different cycles. At 1° ATDC, high-intensity luminosity fills all eight jets. The late-SOI case has much higher intensity than the two other selected cases, which saturates the camera in the downstream portion of each jet. Due to the relatively late SOI timing, the strong luminosity is most likely due to natural soot incandescence from fuel-rich regions. Metal engine experiments [120] operated at a similar condition showed a significant increase in engine-out NOx and soot emissions as the injection timing was retarded to

-15° ATDC. Further, notice that the highest intensity regions are confined to the fuel jets and weaker luminosity is observed between the jets. The weaker luminosity is likely due to chemiluminescence in the premixed iso-octane. At 4° ATDC the total luminosity begins to decrease and the brightest regions are confined to the downstream portion of the jet (i.e., near the piston bowl rim), and strong luminosity is observed near the piston bowl rim late into the expansion stroke (not shown).

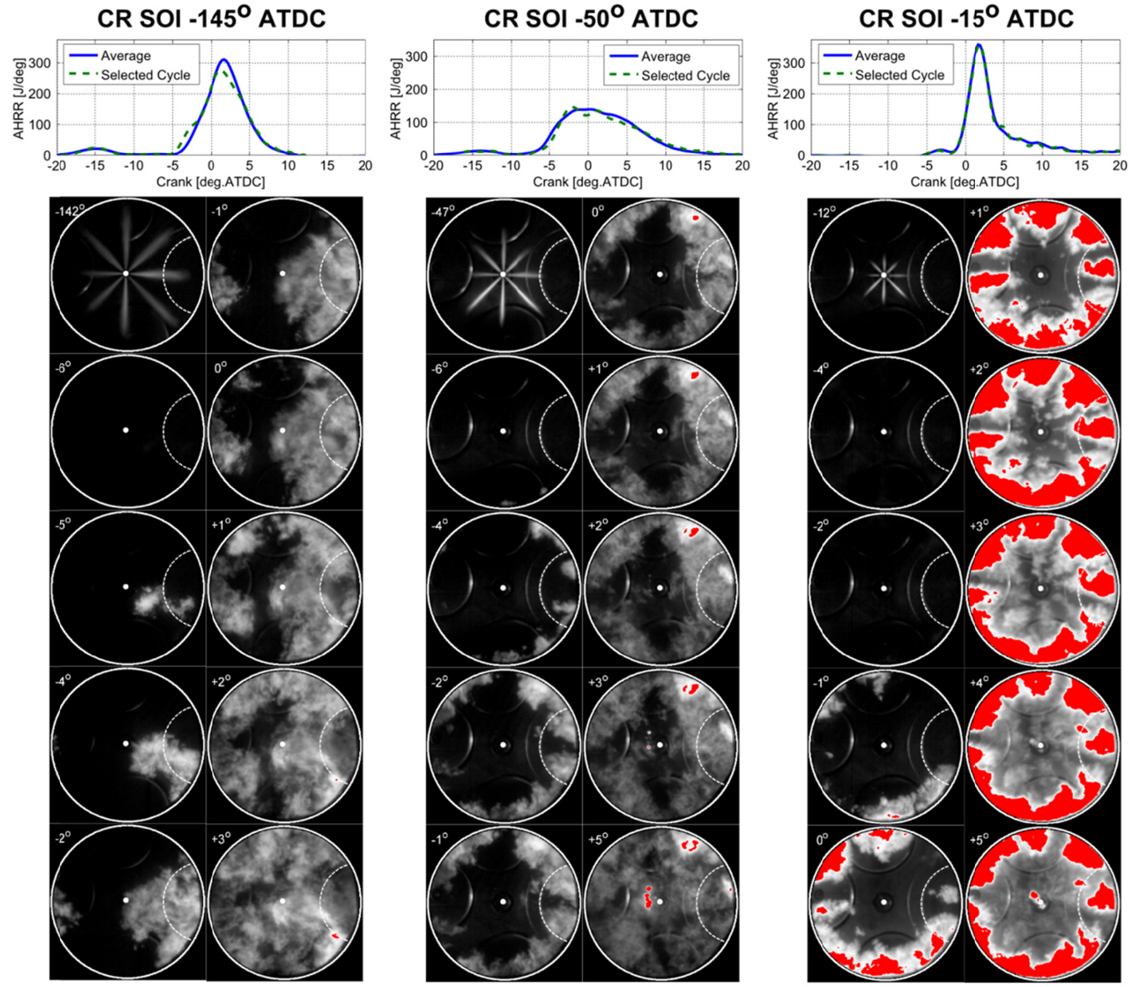

Figure 10-3. High speed movie sequence showing liquid fuel sprays and natural luminosity for the cases with common-rail SOI timings of -155°,-50°, and -15° ATDC. The number in the upper left-hand corner of each image shows the crank angle at which the image was acquired. The camera settings are the same for each operating condition. Regions colored red indicate saturation [121].

10.2.3 Mixing Measurements

The high-speed combustion luminosity imaging in Figure 10-3 shows distinctly different combustion events for the early-, mid- , and late-SOI timings. The differences in combustion characteristics are likely due to differences in the mixing times of the three cases. That is, the early-SOI timing results in rapid energy release due to an under-stratified charge and the late-SOI timing results in rapid energy release due to an over-stratified charge. From a practical perspective, these two limiting cases suggest controlling charge stratification using two fuels with different auto-ignition characteristics can be used to control PCI combustion heat release. To understand the influence of fuel reactivity stratification, the fuel tracer fluorescence diagnostic was used to evaluate the mixture stratification (both PRF and equivalence ratio) for the three cases previously discussed. In general, ignition occurred in the downstream portion of the jet near the bowl wall. The close proximity to the bowl wall, and the work presented in Chapter 9, suggests that ignition may occur in the squish region. Therefore, the fuel tracer fluorescence images were recorded with the camera viewing downward through the cylinder head window and into the squish region, as described in Figure 8-3.

The fuel distributions are compared at -5° ATDC (i.e., near the onset of high-temperature heat release). The ensemble-averaged fuel distributions are discussed first and are then compared to single-shot images to highlight local phenomena controlling the combustion characteristics.

Figure 10-4 shows the ensemble-averaged PRF and equivalence ratio distributions at -5° ATDC for the three selected cases. To improve the interpretation of the PRF and equivalence ratio distributions, Figure 10-5 shows the corresponding average PRF and equivalence ratio as a function of axial distance from the injector. The solid lines show the average in the radial

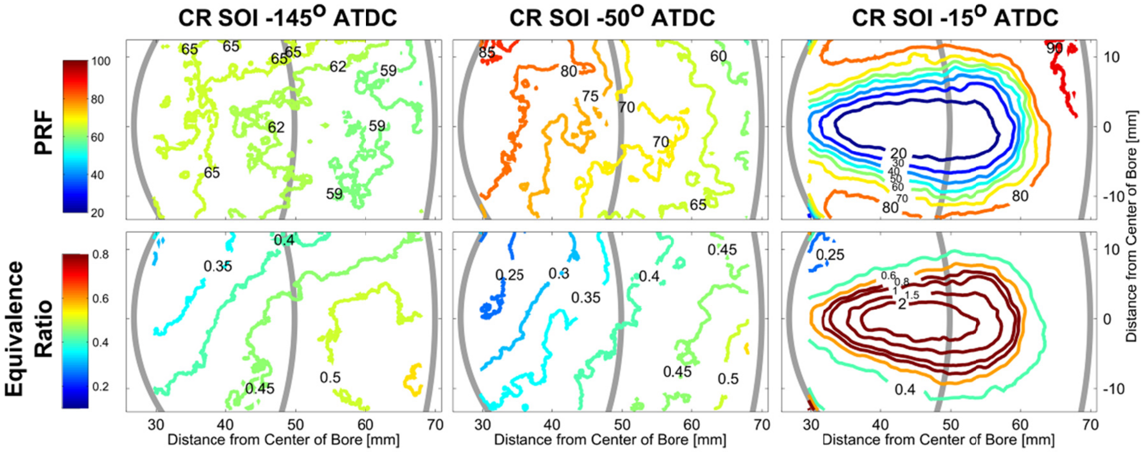

Figure 10-4. Ensemble-averaged PRF and equivalence ratio distributions acquired at -5° ATDC for cases with injection timings of -145°, -50°, and -15° ATDC [121].

direction (y-direction in the PRF and equivalence ratio maps of Figure 10-5) and the shading shows one standard deviation on each side of the mean value. Because the low-temperature reactions occur prior to the image acquisition time, it is likely that, under combusting conditions, much of the n-heptane will be consumed by -5° ATDC (see the CH_2O PLIF imaging of Chapter 9). Thus, the fuel distributions at this time correspond to a representative mixture distribution that tracks the fuel species present earlier in the cycle.

The SOI -145° case shows a relatively small distribution in PRF number, with a range of PRF numbers from 59 to 65. However, the equivalence ratio map shows that a gradient in equivalence ratio is still present. The maximum equivalence ratio, $\phi = 0.55$, is located near the cylinder liner. Figure 10-5 shows that this gradient is primarily in the axial jet direction. The gradient in equivalence ratio is the result of the axial gradients in the equivalence ratio from the common-rail fuel distribution, and to a smaller extent, the equivalence-ratio gradient of the GDI distribution. It is possible that the apparent gradient in equivalence ratio (and PRF number) is

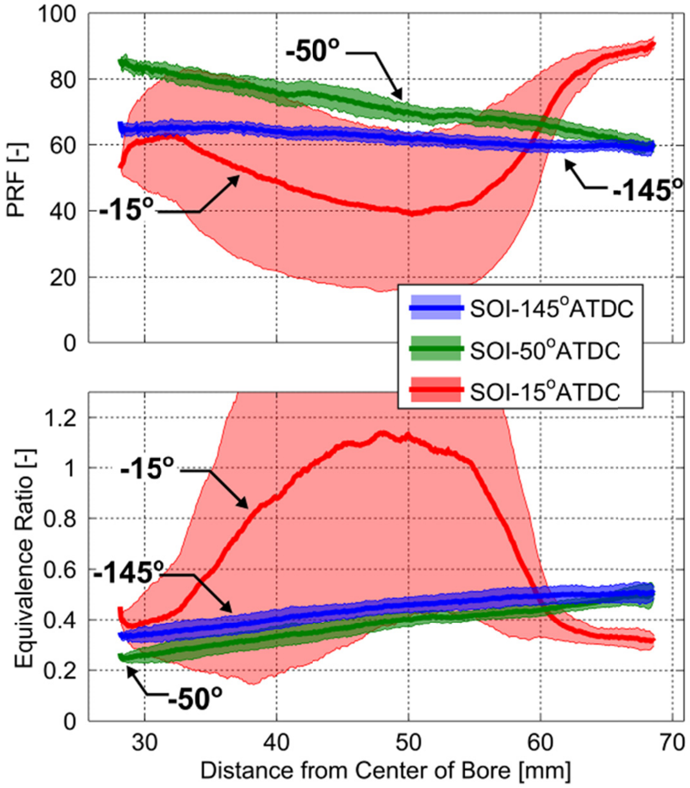

Figure 10-5. Average PRF and equivalence ratio at -5° ATDC as a function of axial distance from the common-rail injector. The solid lines show the average equivalence ratio at each axial distance from the common-rail injector and the shading shows ± one standard deviation (i.e., showing a measure of the spread in the radial direction) [121].

partially the result of attenuation of the laser sheet. However, the calibration images showed only weak attenuation along the laser sheet. Additionally, the calibration procedure accounts for laser sheet attenuation to the degree that it occurs in the calibration image.

Retarding the n-heptane injection timing to -50° ATDC increases the stratification of both equivalence ratio and PRF number. The PRF range spans from 60 in the downstream region of the jet, near the cylinder liner, to around 85 near the front edge of the field-of-view (~30 mm from the common-rail injector). The equivalence ratio ranges from a maximum of $\phi = 0.55$ near the liner to a minimum of $\phi = 0.25$ in the upstream region. Notice that, compared to the SOI -145° case, the equivalence ratios are shifted to lower values and the PRF numbers are shifted to higher values for the SOI -50° case. This shift is due to the limited imaging area rather than a difference in the overall equivalence ratio or PRF number. That is, the increased stratification of the SOI-50° case results in less fuel in the laser sheet (evidently more fuel is located outside of the sheet). Although this limited imaging area makes it difficult to compare the magnitudes of the equivalence ratios and PRF numbers from case-to-case, gradients in equivalence ratio and PRF number can be evaluated from the slope of the curves in Figure 10-5. Further, since the intake temperature was changed at each condition to maintain a constant CA50, the magnitudes of the PRF number are less important than the gradients in the PRF number. Retarding the injection timing from -145° to -50° ATDC causes the slope of the PRF and equivalence ratio distributions to become steeper (i.e., relative to the region closer to the common-rail injector, the near-liner region becomes richer and more reactive). Hence, with the later common-rail injection, the mixing times are reduced such that the n-heptane is less uniformly mixed throughout the chamber and gradients in both PRF number and equivalence ratio are greater. The increase in equivalence ratio and PRF stratification is consistent with the reduction in the peak AHRR of the SOI -50° case.

The primary difference between the SOI -145° and -50° cases is the level of fuel reactivity stratification in the axial jet direction. In contrast, the SOI -15° case shows a much different fuel distribution. The earlier SOI cases had sufficient time to “mix-out” the gradients in the radial jet direction. However, the SOI -15° case shows strong gradients both in the axial and radial directions and a fuel distribution typical of a diesel jet – notice the large deviation from the axial average for the SOI -15° case shown in Figure 10-5. The peak equivalence ratio of the ensemble-averaged images at -5° ATDC is greater than $\phi = 2.6$[17]. The high equivalence ratio region in the center of the jet corresponds to the region where high intensity luminosity was observed in the combusting cases, providing evidence that the bright regions in the luminosity images are the result of natural soot incandescence. Similar to the equivalence ratio distribution, the PRF distribution of the SOI -15° case is broad with a maximum PRF number approaching 100 (i.e., neat iso-octane outside of the n-heptane jet) and a minimum PRF number of ~10 near the jet center. Although the PRF gradient of the SOI -15° case is much larger than that of the SOI -50° case, the SOI -15° case shows more rapid heat release and a peak heat-release rate similar to that of the earliest injection timing case. Thus, increasing the gradient in PRF number does not always decrease the peak heat-release rate. In fact, the present study shows that over stratification significantly increases the peak heat-release rate.

In Chapter 9 ignition delay calculations were used to help explain the dependence of the ignition location and direction of reaction zone growth on the fuel distribution prior to ignition. A similar procedure is applied here; however, since the SOI-15° case has strong gradients in both the axial and radial directions, the ignition delay calculations cannot be reduced to one-dimension as in Chapter 9. Thus, the ignition delay calculations are applied to the full fuel tracer PLIF images. First, constant volume ignition delay calculations were performed over a range of temperatures, equivalence ratios, and PRF numbers to create a lookup table of ignition delay. Figure 10-6 shows an example set of ignition delay calculations.

---

[17] Note that the maximum equivalence ratio was capped at ten times the equivalence ratio of the calibration images. Therefore, the peak equivalence ratio in the images is shown to be 2.6; however, small regions have slightly higher equivalence ratios.

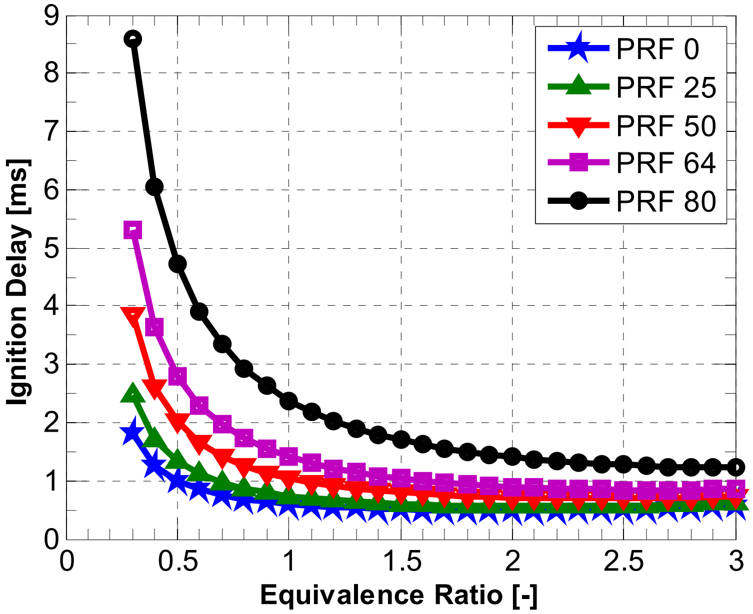

Figure 10-6. Constant-volume ignition delay calculations illustrating the effect of equivalence ratio and PRF number on ignition delay. The initial conditions correspond to representative TDC conditions from the current experiments (initial pressure = 27 bar, initial temperature = 837 K, and 21% intake oxygen concentration) [121].

The ignition delay was then mapped to the PLIF images using the measured temperature, equivalence ratio, and PRF number. Figure 10-7 shows the calculated ignition delay for each case. As previously discussed, the absolute values of ignition delay should be considered upper limits corresponding to reactions occurring in isolation (i.e., with no communication to the surrounding regions). Further, the values of ignition delay do not consider prior processes that would shorten the ignition delay (e.g., low temperature reactions that would have occurred before -5° ATDC). Finally, since the ignition delay maps are calculated from the combination of PLIF measurements and kinetics modeling, the uncertainty in the ignition delay values is large. Although, the ignition delay maps must be interpreted with caution, they provide additional insight into the mechanisms controlling the energy release.

Similar to the PRF and equivalence ratio maps, the ignition delay map of the SOI -145° case shows a relatively small change in ignition delay from the most- to least-reactive regions. This is consistent with the observed volumetric combustion and rapid energy release. The SOI -50° case shows a larger span of ignition delay with the shortest ignition delay corresponding to the area with the lowest PRF number and highest equivalence ratio. Consistent with the analysis presented in Chapter 9, the gradient in ignition delay is consistent with the gradient in the PRF number, equivalence ratio, and the observed direction of reaction zone growth. Finally, the SOI -15° case shows a nearly constant ignition delay inside of the n-heptane jet and much longer ignition delay outside of the jet. The ignition delay calculations are consistent with the high rate of energy release and observed rapid luminosity throughout the jet cross section (see Figure 10-3). Inside of the n-heptane jet, the mixture is near stoichiometric or richer (see Figure 10-4). The constant volume ignition delay calculations (see Figure 10-6) show that mixtures with equivalence ratios greater than 0.6[18] have very similar ignition delays. Thus, at the present operating conditions, controlled energy release appears to be most achievable when the peak equivalence ratio is 0.6 or less.

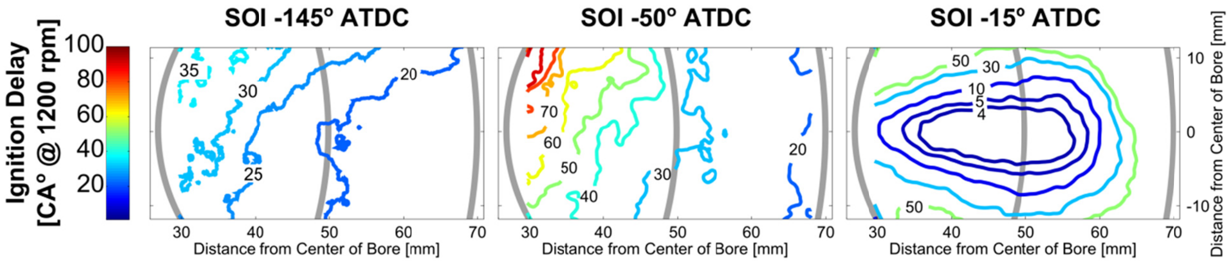

Figure 10-7. Constant volume ignition delay calculations mapped to the PLIF images shown in Figure 10-4. The contours show ignition delay in crank angle degrees at 1200 rpm. The ignition delay maps are shown at -5° ATDC [121].

---

[18] At these operating conditions the ignition delay begins to increase around $\phi = 5$; however, the quantity of fuel at such high equivalence ratios in the present study is likely negligible.

This study confirms that the rate of energy release can be controlled by controlling the stratification in the fuel reactivity using in-cylinder fuel blending. However, the study also shows that care must be taken to avoid over- and under-stratified operation, both of which can result in rapid energy release and excessive pressure rise rate.

Chapter 11 Conclusions and Future Work

This chapter provides a brief summary of the results related to each objective and discusses directions for future work.

11.1 Summary of RCCI Development

An alternative combustion mode (RCCI combustion) using in-cylinder blending of two fuels with different auto-ignition characteristics was proposed. RCCI is shown to address two of the primary problems limiting the widespread application of PCI combustion strategies: combustion phasing control and rate of heat release control. It was found that, at the conditions evaluated in this study, the combustion phasing can be controlled by adjusting the ratio of the amount of the two fuels used. In contrast with control mechanisms relating to the air system (e.g., EGR), the relative ratios of the fuels can be adjusted on a cycle-to-cycle basis. Further, by introducing stratification in fuel reactivity, it was found that the rate of heat release can be controlled.

A genetic algorithm was coupled to the CFD modeling to develop a charge preparation strategy using a port-fuel-injector for the low-reactivity fuel and conventional common-rail injector for the high-reactivity fuel. The results of the RCCI development study show that the highly-dilute nature of RCCI allows for very low engine-out NOx emissions and low fuel consumption (GIE greater than 50%).

11.2 Summary of RCCI emissions and performance characteristics

A combination of CFD modeling and metal engine experiments were used to assess the emissions and performance characteristics of RCCI combustion. The following conclusions can be drawn from this investigation:

1) In both light- and heavy-duty engines RCCI shows extremely low engine out NOx and soot emissions. It is possible to meet 2010 NOx targets in-cylinder over a wide range of conditions.
2) The GIE of heavy-duty RCCI is greater than 49% from 4 bar to 15 bar IMEP. By controlling the combustion phasing (through adjustments to the gasoline-to-diesel ratio) and introducing spatial stratification in fuel reactivity, acceptable ringing intensity (combustion noise) is achievable over this range of loads.
3) Compared to conventional diesel combustion, heavy-duty RCCI shows 11.5% higher GIE (i.e., 5.6% more of the fuel energy is converted to work) at the mid-load operating point evaluated. The increase in GIE is explained primary by lower heat transfer losses. The heat transfer losses are reduced by avoiding near stoichiometric regions and by keeping high temperature regions away from heat transfer surfaces. Further, at identical initial conditions, heavy-duty RCCI shows two orders of magnitude lower NOx emissions and 5 times lower soot emissions.
4) Single-cylinder engine experiments were used to adapt the RCCI concept to an automotive-type light-duty engine and comparisons were made between the engine platforms. It was found that with only small changes in the injection parameters, the combustion characteristics of the heavy-duty engine can be adequately reproduced in the light-duty engine. Similar to the heavy-duty RCCI operation, the light-duty engine is capable of achieving very low NOx and soot emissions (NOx less than 0.05 g/kW-hr and soot below 0.01 g/kW-hr) and acceptable combustion noise. However, it was found that the GIE of the light-duty engine is 5% to 7% lower than the

heavy-duty engine at similar conditions. The results showed that two factors contribute to the lower GIE of the light-duty engine: higher heat transfer losses and lower combustion losses. The increased heat transfer losses are due to the higher surface area-to-volume ratio, piston material (the heavy-duty engine uses a steel piston and the light-duty engine uses an aluminum piston), and higher swirl ratio. The combustion efficiency appears to be primarily related to the ring-pack geometry. CFD modeling showed that lowering the swirl ratio of the light-duty engine and increasing the surface temperatures (approximating the use of a steel piston) significantly reduces the heat transfer losses and improves the GIE. The lower heat transfer losses also result in higher temperatures and improved combustion efficiency.

5) Light-duty RCCI was compared to conventional diesel combustion at five operating points representative of the light-duty drive cycle. The results show that RCCI is capable of meeting NOx targets (equivalent to Tier 2-Bin 5) without NOx aftertreatment. A method to compare the combustion modes considering the impact of urea (DEF) consumption was proposed. The comparisons show that even when the DEF consumption not considered, the lower heat transfer losses of RCCI result in a 4% improvement in fuel consumption. When the DEF consumption is considered, RCCI shows a 7.3% improvement in fuel consumption.

11.3 Summary of the key processes controlling RCCI combustion

The dominant processes controlling RCCI combustion were explained using a combination of CFD modeling and optical engine experiments. The following conclusions can be drawn from the CFD analysis of RCCI combustion:

1) The locations of formaldehyde prior to second stage combustion track well with the early-cycle diesel fuel distribution. During LTHR, the diesel fuel concentration decreases by nearly an order of magnitude while the gasoline concentration remains nearly constant.
2) The ignition location is controlled by the location of the highest concentration of high reactivity fuel (e.g., diesel fuel) and that the combustion process proceeds in a staged event from regions of high to low fuel reactivity.
3) This staged combustion event extends the combustion duration, providing control over the heat release rate.
4) Simulations without consideration of flame propagation are able to capture the heat release characteristics of RCCI over a range of conditions.

A suite of optical diagnostics were applied to an engine operating in the dual-fuel combustion mode to evaluate the model predictions and develop a more fundamental understanding of RCCI combustion. The following conclusions can be drawn from the optical engine experiments.

1) High-speed chemiluminescence imaging shows that ignition occurs in the outer region of the combustion chamber (near the cylinder liner) at the light-load condition evaluated. The reaction zone grows inward toward the center of the chamber.
2) The reaction zone movement appears to be controlled by the occurrence of isolated auto-ignition pockets, rather than propagation of a continuous reaction zone.
3) Simultaneous formaldehyde PLIF and OH PLIF shows that the downstream region of the jet goes through a two-stage combustion event. During LTHR, much the outer

region of the combustion chamber fills with formaldehyde due to fuel decomposition. The appearance and consumption of formaldehyde is consistent with the CFD model predictions. Similar to the chemiluminescence imaging, the OH PLIF imaging shows that ignition occurs in outer region of the chamber. The temporal appearance of OH is consistent with CFD model predictions.

5) Fuel tracer fluorescence imaging shows that the preferential ignition location corresponds to the region with the highest concentration of n-heptane early in the cycle (consistent with the CFD modeling predictions). The direction of reaction zone growth is consistent with the direction of decreasing fuel reactivity (i.e., increasing octane number and decreasing equivalence ratio). Combining kinetics calculations with the fuel tracer PLIF imaging shows that the level of PRF (octane number) stratification has a larger effect on the combustion duration than equivalence ratio or temperature stratification. Further, it was found that the energy release rate could be controlled by controlling the level of fuel reactivity stratification.
6) The laser ignition study suggests that, at the lean conditions typical of RCCI combustion, flame propagation only plays a minor role in the heat release. It appears that flame propagation may play a role locally; however, the bulk reaction zone movement and energy release is controlled by sequential auto-ignition.
7) In general, the results of the optical diagnostics confirm the model predicted combustion evolution. Further, the optical engine experiments confirm that accurate modeling of RCCI combustion can be performed without consideration of flame propagation.

11.4 Recommendations for Future Work

11.4.1 Improvement of Low-Load RCCI Performance in the Light-duty Engine

RCCI achieves very high GIE at mid-load conditions; however, the combustion efficiency can be poor at light load conditions. Since much of the light-duty drive cycle is focused on low-load operation, the poor combustion efficiency at light-load limits the efficiency advantages over CDC operation. Below are several suggestions to improve light-load combustion efficiency:

1) All of the RCCI experiments presented in this work were performed using 91 octane gasoline to allow the highest load operation to be achieved; however, the light-duty engine should focus on low-load operation. Thus, operating on 87 octane gasoline (or lower) may improve light-load combustion efficiency.
2) The simulations show that the higher heat transfer losses of the light-duty engine tend to result in lower combustion efficiency. Thus, partially (or fully) insulating the piston may improve the combustion efficiency.

11.4.2 Extension of the RCCI load range in the heavy-duty engine

The present research focused on mid-load operation in both engines; however, a significant portion of the heavy-duty drive cycle is weighted towards high-load conditions. Several methods to achieve operation over the full load range are discussed below:

1) The compression ratios used in the present work were not optimized for RCCI operation. Reducing the compression ratio in the heavy-duty engine is expected to allow higher load operation. However, the performance at low load and high-speed may suffer. Thus, an optimization considering the effect of compression ratio should be performed at two conditions: low speed-high load (e.g., A100) and high speed-low

load (e.g., C25). These two conditions will provide bounds on the upper and lower limit of the compression ratio.

2) Sun et al. [122] proposed a split heat release strategy where the first heat release event resulted from premixed fuel (i.e., HCCI) and the second heat release event was a diffusion combustion process resulting from a direct injection after TDC. This strategy could be applied to RCCI as a method to extend the load range. That is, RCCI operation with a single-heat release could be used from low load up to approximately 15 bar IMEP (as was demonstrated in this work). To achieve full load operation, a third injection of diesel fuel could be added after TDC. Since the final injection of diesel fuel will burn in a diffusion flame, acceptable pressure rise rate can be maintained. Further, if the diesel fuel is injected after the premixed energy release, the oxygen concentration can be lowered enough to avoid forming NOx. The primary difficulty in this strategy is minimizing engine out soot. Since the second energy release occurs in a high-temperature, low-oxygen concentration condition, higher soot levels may require soot aftertreatment.

11.4.3 Additional RCCI Performance Considerations

1) This work has shown that, as expected, RCCI is strongly influenced by the intake conditions; however, it was found that the fuel blend (e.g., gasoline percentage) can be used to control combustion phasing on a cycle-to-cycle basis. Transient operation is a limiting factor for most PCI-type strategies; thus, it would be interesting to evaluate the possibility of using RCCI during transient operation. The changes in combustion phasing have been shown to be captured adequately using coarse grid

HCCI simulations in KIVA or even single-zone, homogeneous reactor simulations. Thus, a preliminary study could be conducted by coupling a single-zone model to a cycle-simulation model (e.g., GT-Power).

2) Even at mid-load conditions, the combustion efficiency of RCCI is approximately 2% of the fuel energy lower than conventional diesel combustion. The metal engine experiments show that UHC emissions generally account for the majority of incomplete combustion products. Further, the CFD simulations show that most of the late-cycle UHC emissions reside in the ring-pack crevice volume. Thus, it would be interesting to replace the port-fuel-injected gasoline (i.e., premixed gasoline) with an optimized direct-injection of gasoline. Additionally, since high-pressure injection of diesel fuel is not needed, the diesel fuel may be delivered through a GDI injector (as demonstrated in Kokjohn et al. [17]). This would allow the gasoline to be delivered through the common-rail injector and allow the possibility of gasoline PCI combustion (e.g., using the strategy of Kalghatgi et al. [35-37]) at high-load.

11.4.4 CFD Model Development

The CFD models used in this study were shown to adequately capture the combustion characteristics over a range of conditions from conventional diesel combustion to RCCI; however, areas of model improvement remain. These are discussed below.

1) The comparison of the heavy- and light-duty engines suggested that a primary source of increased heat transfer losses in the light-duty engine is the piston material. It would be interesting to add a conjugate heat transfer model to the current

KIVA-CHEMKIN code and provide more detailed descriptions of the material effects.

2) The soot model used in this study (two-step) is generally not predictive and requires tuning to capture the soot levels at different operating conditions. In the present study, most of the operating conditions focused on mid-load RCCI, where measured soot levels are low. Thus, the soot model did not cause significant difficulty interpreting the results. However, it is expected that near TDC injections will be required to achieve full load RCCI. In this case soot modeling may be problematic since the first stage heat release may be very premixed (i.e., RCCI-like) and the second stage heat release may be diesel-like. Thus, to model these cases the soot model must be improved. Vishwanathan et al. [123] developed an improved soot model considering four steps: soot inception (i.e., PAH formation), surface growth, soot coagulation, and soot oxidation. It would be interesting to compare the predictions of this soot model to the RCCI and CDC cases presented in this work.

11.4.5 Additional Optical Engine Experiments

The laser ignition study presented in this research provides a preliminary investigation of the role of flame propagation in RCCI combustion; however, the laser ignition location was limited by the physical setup of the engine (recall that the laser ignition location could not be moved into the squish region without damaging the optical access window). It would be interesting to design a new window such that the focusing lens is incorporated into the window (see e.g., Genzale et al. [119]). This would allow the laser ignition location to be moved significantly closer to the liner and allow ignition in the squish region.

References

1. Bilger, R. W., Libby, P. A., and Williams, F. A. *Turbulent Reacting Flows*. Springer Verlag, New York, 1980.

2. Kim, J., Park,S. W., and Reitz,R. D., "Improvements in the Performance and Pollutant Emissions for Stoichiometric Diesel Combustion Engines using a Two-Spray-Angle Nozzle," *Journal of Automobile Engineering*, 224(8):1113-1122., 2010, doi:0.1243/09544070JAUTO1457

3. Theis, J. R., Ura,J. A., Li,J. J., Surnilla,G. G., Roth,J. M., and Goralski Jr.,C. T., "NOx Release Characteristics of Lean NOx Traps during Rich Purges," SAE Technical Paper 2003-01-1159, 2003, doi:10.4271/2003-01-1159.

4. Johnson, T., "Diesel Emissions in Review," *SAE Int. J. Engines*, 4(1):143-157, 2011, doi:10.4271/2011-01-0304.

5. Turns, S. R., "An Introduction to Combustion: Concepts and Applications," Second Edition, McGraw-Hill, New York, 2000.

6. Manente, V., Tunestal, P., Johansson, B., and Cannella, W., "Effects of Ethanol and Different Type of Gasoline Fuels on Partially Premixed Combustion from Low to High Load," SAE Technical Paper 2010-01-0871, 2010, doi:10.4271/2010-01-0871.

7. Manente, V., Johansson, B., Tunestal, P., and Cannella, W., "Influence of Inlet Pressure, EGR, Combustion Phasing, Speed and Pilot Ratio on High Load Gasoline Partially Premixed Combustion," SAE Technical Paper 2010-01-1471, 2010, doi:10.4271/2010-01-1471.

8. Manente, V., Johansson, B., Tunestal, P., and Cannella, W., "Effects of Ethanol and Different Type of Gasoline Fuels on Partially Premixed Combustion from Low to High Load," SAE Technical Paper 2010-01-0871 , 2010.

9. Manente, V., Tunestal, P., and Johansson, B., "Gasoline Partially Premixed Combustion, the Future of Internal Combustion Engines?," *International Journal of Engine Research*, 12(3):194-208, 2011, doi:10.1177/1468087411402441

10. Dec , J. E., Yang ,Y., and Dronniou, N., "Boosted HCCI - Controlling Pressure-Rise Rates for Performance Improvements using Partial Fuel Stratification with Conventional Gasoline," *SAE Int. J. Engines*, 4(1):1169-1189, 2011, doi:10.4271/2011-01-0897.

11. Yang, Y., Dec,J. E., Dronniou, N., and Sjöberg, M., "Tailoring HCCI Heat-Release Rates with Partial Fuel Stratification: Comparison of Two-Stage and Single-Stage-Ignition Fuels," *Proceedings of the Combustion Institute,* 33(2):3047-3055, 2011, http://dx.doi.org/10.1016/j.proci.2010.06.114.

12. Hwang, W., Dec, J. E., and Sjöberg, M., "Fuel Stratification for Low-Load HCCI Combustion: Performance and Fuel-PLIF Measurements," *SAE Transactions*, 3(116): 1437-1460, SAE Technical Paper 2007-01-4130, 2007, doi:10.4271/2007-01-4130.

13. Dec, J. E., Hwang, W., and Sjöberg, M. "An Investigation of Thermal Stratification in HCCI Engines Using Chemiluminescence Imaging," SAE Technical Paper 2006-01-1518, 2006, doi:10.4271/2006-01-1518.

14. Sjoberg, M., Dec, J. E., and Cernansky, N. P., "Potential of Thermal Stratification and Combustion Retard for Reducing Pressure-Rise Rates in HCCI Engines, Based on Multi-Zone Modeling and Experiments," SAE Technical Paper 2005-01-0113, 2005, doi:10.4271/2005-01-0113.

15. Sjoberg, M. and Dec, J. E., "Smoothing HCCI Heat-Release Rates Using Partial Fuel Stratification with Two-Stage Ignition Fuels," SAE Technical Paper 2006-01-0629, 2006, doi:10.4271/2006-01-0629.

16. Kokjohn, S. L., Swor, T. A., Andrie, M. J., and Reitz, R. D., "Experiments and Modeling of Adaptive Injection Strategies (AIS) in Low Emissions Diesel Engines," *SAE Int. J. Engines*, 2(1):16-32, 2009, doi:10.4271/2009-01-0127.

17. Kokjohn, S. L., Splitter, D. A., Hanson, R.M., and Reitz, R. D., "Experiments and Modeling of Dual Fuel HCCI and PCCI Combustion using in-Cylinder Fuel Blending. *SAE Int. J. Engines*, 2(2):24-39, 2010, doi:10.4271/2009-01-2647.

18. Hanson, R. M., Kokjohn, S. L., Splitter, D. A., and Reitz, R. D., "An Experimental Investigation of Fuel Reactivity Controlled PCCI Combustion in a Heavy-Duty Engine," *SAE Int. J. Engines*, 3(1):700-716, 2010, doi:10.4271/2010-01-0864.

19. Splitter, D. A., Hanson, R. M., Kokjohn, S. L., and Reitz, R. D. "Reactivity Controlled Compression Ignition (RCCI) Heavy-Duty Engine Operation at Mid-and High-Loads with Conventional and Alternative Fuels," SAE Technical Paper 2011-01-0363, 2011, doi:10.4271/2011-01-0363.

20. Kokjohn, S. L. and Reitz, R. D.,"A Comparison of Conventional Diesel and RCCI Combustion using Detailed CFD Modeling," 21st International Multidimensional Engine Modeling User's Group Meeting, April 11th, 2011.

21. Kokjohn, S. L., Hanson, R. M., Splitter, D. A., and Reitz, R. D., "Fuel Reactivity Controlled Compression Ignition (RCCI) Combustion in Light- and Heavy-Duty Engines," *SAE Int. J. Engines* 4(1):360-374, 2011, doi:10.4271/2011-01-0357.

22. Hanson, R. M., Kokjohn, S. L., Splitter, D. A., and Reitz, R. D., "Fuel Effects on Reactivity Controlled Compression Ignition (RCCI) Combustion at Low Load," *SAE Int. J. Engines* 4(1):394-411, 2011, doi:10.4271/2011-01-0361.

23. Caton, J. A. "Thermodynamic Advantages of Low Temperature Combustion (LTC) Engines Using Low Heat Rejection (LHR) Concepts," SAE Technical Paper 2011-01-0312, 2011, doi:10.4271/2011-01-0312.

24. Neely, G. D., Sasaki, S., Huang, Y., Leet, J. A., and Stewart, D. W. "New Diesel Emission Control Strategy to Meet US Tier 2 Emissions Regulations," SAE Technical Paper 2005-01-1091, 2005, doi:10.4271/2005-01-1091.

25. Kamimoto, T. and Bae, M. "High Combustion Temperature for the Reduction of Particulate in Diesel Engines," SAE Technical Paper 880423, 1988, doi:10.4271/880423.

26. Akihama, K., Takatori, Y., Inagaki, K., Sasaki, S., and Dean, A. M. Akihama, K., Takatori, Y., Inagaki, K., Sasaki, S. et al., "Mechanism of the Smokeless Rich Diesel Combustion by Reducing Temperature," SAE Technical Paper 2001-01-0655, 2001, doi:10.4271/2001-01-0655.

27. Park, S. W. and Reitz, R. D., "Numerical Study on the Low Emission Window of Homogeneous Charge Compression Ignition Diesel Combustion," Combustion Science and Technology, 179(11):2279-2307, 2007, doi:10.1080/00102200701484142.

28. Onishi, S., Hong Jo, S., Shoda, K., Jo, P., and Kato, S., "Active Thermo-Atmosphere Combustion (ATAC) - A New Combustion Process for Internal Combustion Engines," SAE Technical Paper 790501, 1979, doi:10.4271/790501.

29. Najt, P. M. and Foster, D. E., "Compression-Ignited Homogeneous Charge Combustion," SAE Technical Paper 830264, 1983, doi:10.4271/830264.

30. Yamaguchi, J. "Honda Readies Activated Radical Combustion Two-Stroke Engine for Production Motorcycle," *Automotive Engineering*, 1997, (January).

31. Hasegawa, R. and Yanagihara, H., "HCCI Combustion in DI Diesel Engine ," SAE Technical Paper 2003-01-0745, 2003, doi:10.4271/2003-01-0745.

32. Marriott , C. D., Kong ,S.-C., and Reitz ,R. D., "Investigation of Hydrocarbon Emissions from a Direct Injection-Gasoline Premixed Charge Compression Ignited Engine," SAE Technical Paper 2002-01-0419, 2002, doi:10.4271/2002-01-0419.

33. Marriott , C. D. and Reitz ,R. D., “Experimental Investigation of Direct Injection-Gasoline for Premixed Compression Ignited Combustion Phasing Control,” SAE Technical Paper 2002-01-0418, 2002, doi:10.4271/2002-01-0418.

34. Aroonsrisopon, T., Werner, P., Waldman , J. O., Sohm, V., Foster,D. E., Morikawa, T., and Iida ,M., “Expanding the HCCI Operation With the Charge Stratification,” SAE Technical Paper 2004-01-1756, 2004, doi:10.4271/2004-01-1756.

35. Kalghatgi, G. T., Risberg, P., and Ångström, H. “Partially Pre-Mixed Auto-Ignition of Gasoline to Attain Low Smoke and Low NOx at High Load in a Compression Ignition Engine and Comparison with a Diesel Fuel,” SAE Technical Paper 2007-01-0006, 2007, doi:10.4271/2007-01-0006.

36. Kalghatgi, G. T., Risberg, P., and Angstrom, H., “Advantages of Fuels with High Resistance to Auto-ignition in Late-injection, Low-temperature, Compression Ignition Combustion,” SAE Technical Paper 2006-01-3385, 2006, doi:10.4271/2006-01-3385.

37. Kalghatgi, G. T. “Auto-Ignition Quality of Practical Fuels and Implications for Fuel Requirements of Future SI and HCCI Engines,” SAE Technical Paper 2005-01-0239, 2005, doi:10.4271/2005-01-0239.

38. Liu, H., Yao,M., Zhang, B., and Zheng, Z., “Effects of Inlet Pressure and Octane Numbers on Combustion and Emissions of a Homogeneous Charge Compression Ignition (HCCI) Engine,” *Energy & Fuels*, 22(4):2207-2215, 2008, doi:10.1021/ef800197b.

39. Opat, R., Ra, Y., Gonzalez, M. A., Krieger, R., Reitz, R. D., Foster, D. E., Siewert, R., and Durrett, R., “Investigation of Mixing and Temperature Effects on HC/CO Emissions for Highly Dilute Low Temperature Combustion in a Light Duty Diesel Engine,” SAE Technical Paper 2007-01-0193, 2007, doi:10.4271/2007-01-0193.

40. Martin , G. C., Mueller ,C. J., Milam ,D. M., Radovanovic ,M. S., and Gehrke ,C. R. “Early Direct-Injection, Low-Temperature Combustion of Diesel Fuel in an Optical Engine Utilizing a 15-Hole, Dual-Row, Narrow-Included-Angle Nozzle,” *SAE Int. J. Engines* 1(1):1057-1082, 2009, doi:10.4271/2008-01-2400.

41. Aroonsrisopon, T., Foster, D., Morikawa, T., and Iida, M., “Comparison of HCCI Operating Ranges for Combinations of Intake Temperature, Engine Speed and Fuel Composition,” SAE Technical Paper 2002-01-1924, 2002, doi:10.4271/2002-01-1924.

42. Yao , M., Zheng ,Z., Zhang ,B., and Chen ,Z., “The Effect of PRF Fuel Octane Number on HCCI Operation,” SAE Technical Paper 2004-01-2992, 2004, doi:10.4271/2004-01-2992.

43. Bessonette, P. W., Schleyer, C. H., Duffy, K. P., Hardy, W. L., and Liechty, M. P. ,"Effects of Fuel Property Changes on Heavy-Duty HCCI Combustion," SAE Technical Paper 2007-01-0191, 2007, doi:10.4271/2007-01-0191.

44. Zheng, Z., Yao ,M., Chen ,Z., and Zhang ,B. , "Experimental Study on HCCI Combustion of Dimethyl Ether(DME)/Methanol Dual Fuel," SAE Technical Paper 2004-01-2993, 2004, doi:10.4271/2004-01-2993.

45. Inagaki, K., Fuyuto, T., Nishikawa, K., Nakakita, K., and Sakata, I., "Dual-Fuel PCI Combustion Controlled by In-Cylinder Stratification of Ignitability," SAE Technical Paper 2006-01-0028, 2006, doi:10.4271/2006-01-0028.

46. Ra, Y. and Reitz, R. D., "A Combustion Model for IC Engine Combustion Simulations with Multi-Component Fuels," *Combustion and Flame* , 158(1): 69-90, 2011, http://dx.doi.org/10.1016/j.combustflame.2010.07.019

47. Lutz, A. E., Kee, R. J., and Miller, J. A., "SENKIN: A FORTRAN Program for Predicting Homogeneous Gas Phase Chemical Kinetics with Sensitivity Analysis," SAND 89-8009, 1988.

48. Dahl , D., Andersson ,M., Berntsson ,A., Denbratt ,I., and Koopmans ,L. , "Reducing Pressure Fluctuations at High Loads by Means of Charge Stratification in HCCI Combustion with Negative Valve Overlap," SAE Technical Paper 2009-01-1785, 2009, doi:10.4271/2009-01-1785.

49. Dec , J. E. and Hwang ,W., "Characterizing the Development of Thermal Stratification in an HCCI Engine Using Planar-Imaging Thermometry," *SAE Int. J. Engines* 2(1):421-438, 2009, doi:10.4271/2009-01-0650.

50. Zeldovich, Y. B., "Regime Classification of an Exothermic Reaction with Non-uniform Initial Conditions," *Combust. Flame* , 1980, 39(2): 211-214, http://dx.doi.org/10.1016/0010-2180(80)90017-6.

51. Chen, J. H., Hawkes, E. R., Sankaran, R., Mason, S. D., and Im, H. G., "Direct Numerical Simulation of Ignition Front Propagation in a Constant Volume with Temperature Inhomogeneities: I. Fundamental Analysis and Diagnostics," *Combust. Flame*, 2006, 145(1-2):128-144, doi:10.1016/j.combustflame.2005.09.017

52. Amsden, A. A. KIVA-3V, Release 2, Improvements to KIVA-3V. *LA-UR-99-915*, 1999, LA-UR-99-915.

53. Beale, J. C. and Reitz, R. D., "Modeling Spray Atomization with the Kelvin-Helmholtz/Rayleigh-Taylor Hybrid Model," *Atomization and Sprays* , 1999, 9(6):623-650.

54. Kong, S.-C., Sun, Y., and Reitz, R. D., “Modeling Diesel Spray Flame Lift-Off, Sooting Tendency and NOx Emissions using Detailed Chemistry with a Phenomenological Soot Model,” *J. Eng. Gas Turbines Power*, 129:245-251, 2007.

55. Singh , S., Liang, L., Kong, S.-C., and Reitz, R. D., “Development of a Flame Propagation Model for Dual-Fuel Partially Premixed Compression Ignition Engines,” *International Journal of Engine Research* , 7(1) 65-76, 2006, DOI: 10.1243/146808705X7464.

56. Abani, N., Kokjohn, S. L., Park, S. W., Bergin, M., Munnannur, A., Ning, W., Sun, Y., and Reitz, R. D., “An Improved Spray Model for Reducing Numerical Parameter Dependencies in Diesel Engine CFD Simulations,” SAE Technical Paper 2008-01-0970, 2008, doi:10.4271/2008-01-0970.

57. Abani, N., Munnannur, A., and Reitz, R. D., “Reduction of Numerical Parameter Dependencies in Diesel Spray Models,” *J. Eng. Gas Turbines Power*, 130(3):9 pages, 2008.

58. Ra, Y. and Reitz, R. D., “A Reduced Chemical Kinetic Model for IC Engine Combustion Simulations with Primary Reference Fuels,” *Combustion and Flame* , 155(4):713-738, 2008, doi:10.1016/j.combustflame.2008.05.002.

59. Han, Z. and Reitz, R. D. “Turbulence Modeling of Internal Combustion Engines using RNG k-ε Models,” *Combustion Science and Technology*, 1995, 106(4-6) 267-295.

60. Ra, Y., Yun, J. E., and Reitz, R. D., “Numerical Simulation of Gasoline-Fuelled Compression Ignition Combustion with Late Direct Injection,” *Int. J. Veh. Des.*, 50(1):3-34, 2009, doi:10.1504/IJVD.2009.024966

61. Kokjohn, S. L., Hanson, R. M., Splitter, D. A., and Reitz, R. D., “Fuel Reactivity Controlled Compression Ignition (RCCI): A Pathway to Controlled High-Efficiency Clean Combustion,” *International Journal of Engine Research*, 12(3):209-226, 2011, doi:10.1177/1468087411401548

62. Puduppakkam, K. V., Liang, L., Naik, C. V., Meeks, E., Kokjohn, S. L., and Reitz, R. D., “Use of Detailed Kinetics and Advanced Chemistry-Solution Techniques in CFD to Investigate Dual-Fuel Engine Concepts,” *SAE Int. J. Engines* 4(1):1127-1149, 2011, doi:10.4271/2011-01-0895.

63. Singh, S., Musculus,M. P. B., and Reitz, R. D., “Mixing and Flame Structures Inferred from OH-PLIF for Conventional and Low-Temperature Diesel Engine Combustion,” *Combustion and Flame*, 156(10):1898-1908, 2009, doi:10.1016/j.combustflame.2009.07.019

64. Peters, N., “Turbulent Combustion,” Cambridge University Press, Cambridge, New York, 2000.

65. Tan, Z. and Reitz, R. D., “Ignition and Combustion Modeling in Spark-Ignition Engines using a Level Set Method,” *SAE Transactions Journal of Engines*, 112(3):1028-1040, 2003, doi:10.4271/2006-01-0243.

66. Halstead, M. P., Kirsch, L. J., and Quinn, C. P. “The Autoignition of Hydrocarbon Fuels at High Temperatures and Pressures Fitting of a Mathematical Model,” *Combustion and Flame*, 30:45-60, 1977, http://dx.doi.org/10.1016/0010-2180(77)90050-5,

67. Kong, S-C., Han, Z., and Reitz, R. D., “The Development and Application of a Diesel Ignition and Combustion Model for Multidimensional Engine Simulations,” *SAE Transactions Journal of Engines*, 104:502-518, 1995, doi:10.4271/950278.

68. Liang, L. and Reitz, R. D., “Spark Ignition Engine Combustion Modeling Using a Level Set Method with Detailed Chemistry,” SAE Technical Paper 2006-01-0243, 2006, doi:10.4271/2006-01-0243.

69. Metghalchi, M. and Keck, J. C., “Burning Velocities of Mixtures of Air with Methanol, Isooctane, and Indolene at High Pressures and Temperatures,” *Combustion and Flame*, 48:191-210, 1982.

70. Yang , S. and Reitz ,R. D., “Integration of a Continuous Multi-Component Fuel Evaporation Model with an Improved G-Equation Combustion and Detailed Chemical Kinetics Model with Application to GDI Engines,” SAE Technical Paper 2009-01-0722, 2009, doi:10.4271/2009-01-0722.

71. Hiroyasu, H. and Kadota, T., “Models for Combustion and Formation of Nitric Oxide and Soot in DI Diesel Engines,” SAE Technical Paper 760129, 1976, doi:10.4271/760129.

72. Nagle, J. and Strickland-Constable, R. F., “Oxidation of Carbon Between 1000-2000 C”, Proc. of the Fifth Carbon Conf., Vol.1, 1962.

73. Liu, Y., Tao,F., Foster, D. E., and Reitz, R. D., “Application of A Multiple-Step Phenomenological Soot Model to HSDI Diesel Multiple Injection Modeling,” SAE Technical Paper 2005-01-0924, 2005, doi:10.4271/2005-01-0924.

74. Prikhodko, V. Y., Curran, S. J., Barone, T. L., Lewis, S. A., Storey, J. M., Cho, K., Wagner, R. M., and Parks, J. E., “Emission Characteristics of a Diesel Engine Operating with in-Cylinder Gasoline and Diesel Fuel Blending,” *SAE International Journal of Fuels and Lubricants*, 3(2):946-955, 2010, doi:10.4271/2010-01-2266.

75. Sun, Y., “Diesel Combustion Optimization and Emissions Reduction using Adaptive Injection Strategies (AIS) with Improved Numerical Models,” *PhD Thesis in Mechanical Engineering, University of Wisconsin-Madison*, 2007.

76. Smith, G.P., Golden, D.M., Frenklach, M., Moriarty, N.W., Eiteneer, B., Goldenberg, M., Bowman, C.T., Hanson, R.K., Song, S., Gardiner, Jr., W.C., Lissianski, V.V., and Qin, Z., "GRI-Mech," http://www.me.berkeley.edu/gri_mech/.

77. Abraham, J., "What is Adequate Resolution in the Numerical Computations of Transient Jets?" SAE Technical Paper 970051, 1997, doi:10.4271/970051.

78. Munnannur, A., "Droplet Collision Modeling in Multi-Dimensional Engine Spray Computations," *PhD Thesis in Mechanical Engineering, University of Wisconsin-Madison*, 2007.

79. O'Rourke, P. J. and Amsden, A. A. "A Spray/Wall Interaction Submodel for the KIVA-3 Wall Film Model," SAE Technical Paper 2000-01-0271, 2000, doi:10.4271/2000-01-0271.

80. O'Rourke, P. J. and Amsden, A. A., "A Particle Numerical Model for Wall Film Dynamics in Port-Injected Engines," SAE Technical Paper 961961, 1996, doi:10.4271/961961.

81. Senecal, P. K. and Reitz, R. D., "Simultaneous Reduction of Engine Emissions and Fuel Consumption Using Genetic Algorithms and Multi-Dimensional Spray and Combustion Modeling," SAE Technical Paper 2000-01-1890, 2000, doi:10.4271/2000-01-1890.

82. Shi, Y. and Reitz, R. D., "Assessment of Optimization Methodologies to Study the Effects of Bowl Geometry, Spray Targeting and Swirl Ratio for a Heavy-Duty Diesel Engine Operated at High-Load," *SAE Int. J. Engines* 1(1):537-557, 2009, doi:10.4271/2008-01-0949.

83. Deb, K., A. Pratap, S. Agarwal, and T. Meyarivan, "A Fast and Elitist Multiobjective Genetic Algorithm: NSGA-II," IEEE Transactions on Evolutionary Computation, 2, 2002, pp. 182-197.

84. Kokjohn, S. L. and Reitz, R. D. "Investigation of the Roles of Flame Propagation, Turbulent Mixing, and Volumetric Heat Release in Conventional and Low Temperature Diesel Combustion," *J. Eng. Gas Turbines Power,* 133, 2011, DOI:10.1115/1.4002948

85. Dec, J. E., "A Conceptual Model of DI Diesel Combustion Based on Laser-Sheet Imaging," SAE Transactions, 106(3):1319-1348, 1997, doi:10.4271/970873.

86. Musculus, M. P. B., "Multiple Simultaneous Optical Diagnostic Imaging of Early-Injection Low-Temperature Combustion in a Heavy-Duty Diesel Engine," SAE Technical Paper 2006-01-0079, 2006, doi:10.4271/2006-01-0079.

87. Heywood, J. B. "Internal Combustion Engine Fundamentals," McGraw-Hill, 1988.

88. Lachaux, T. and Musculus, M. P. B., "In-Cylinder Unburned Hydrocarbon Visualization during Low-Temperature Compression-Ignition Engine Combustion using Formaldehyde PLIF," *Proceedings of the Combustion Institute*, 2007, 31(2) 2921-2929.

89. Glewen, W., Meyer ,C., Foster , D., Andrie, M. J., and Krieger ,R., "Sources and Tradeoffs for Transient NO and UHC Emissions with Low Temperature Diesel Combustion," SAE Technical Paper 2011-01-1356, 2011, doi:10.4271/2011-01-1356.

90. Swor, T. A., Kokjohn, S. L., Andrie, M. J., and Reitz, R. D., "Improving Diesel Engine Performance using Low and High Pressure Split Injections for Single Heat Release and Two-Stage Combustion," SAE Technical Paper 2010-01-0340, 2010, doi:10.4271/2010-01-0340.

91. Lin, Y. and Zhang, H. H., "Component Selection and Smoothing in Smoothing Spline Analysis of Variance Models," *Institute of Statistics Mimeo Series 2556 NUCS*, 2003.

92. Genzale , C. L., Reitz ,R. D., and Wickman, D. D., "A Computational Investigation into the Effects of Spray Targeting, Bowl Geometry and Swirl Ratio for Low-Temperature Combustion in a Heavy-Duty Diesel Engine," SAE Technical Paper 2007-01-0119, 2007, doi:10.4271/2007-01-0119.

93. Shi, Y. and Reitz, R. D. "Optimization of a Heavy-Duty compression–ignition Engine Fueled with Diesel and Gasoline-Like Fuels," *Fuel*, 89(11):3416-3430, 2010, http://dx.doi.org/10.1016/j.fuel.2010.02.023.

94. Dempsey , A. B. and Reitz, R. D., "Computational Optimization of a Heavy-Duty Compression Ignition Engine Fueled with Conventional Gasoline," *SAE Int. J. Engines*, 4(1):338-359, 2011, doi:10.4271/2011-01-0356.

95. Dempsey , A. B. and Reitz, R. D., "Computational Optimization of Reactivity Controlled Compression Ignition in a Heavy-Duty Engine with Ultra Low Compression Ratio," *SAE Int. J. Engines*, 4(2):2222-2239, 2011, doi:10.4271/2011-24-0015

96. Hanson, R. M., "Experimental Investigation of Fuel Effects on Low Temperature Combustion in a Heavy-Duty Compression-Ignition Engine," *MS Thesis in Mechanical Engineering, University of Wisconsin-Madison*, 2010.

97. Splitter, D. A. Experimental Investigation of Fuel Reactivity Controlled Combustion in a Heavy-Duty Internal Combustion Engine. *MS Thesis in Mechanical Engineering, University of Wisconsin-Madison*, 2010.

98. Curran , S., Prikhodko ,V., Cho ,K., Sluder ,C., Parks ,J., Wagner ,R., Kokjohn ,S. L., and Reitz ,R. D., "In-Cylinder Fuel Blending of Gasoline/Diesel for Improved Efficiency and Lowest Possible Emissions on a Multi-Cylinder Light-Duty Diesel Engine," SAE Technical Paper 2010-01-2206, 2010, doi:10.4271/2010-01-2206.

99. Splitter, D. A., Hanson, R. M., Kokjohn, S. L., Rein, K., Sanders, S., and Reitz, R. D., "An Optical Investigation of Ignition Processes in Fuel Reactivity Controlled PCCI Combustion," SAE Int. J. Engines 3(1):142-162, 2010, doi:10.4271/2010-01-0345.

100. Kokjohn, S. L. and Reitz, R. D., "A Computational Investigation of Two-Stage Combustion in a Light-Duty Engine," *SAE Int. J. Engines* 1(1):1083-1104, 2009, doi:10.4271/2008-01-2412.

101. Dec, J. E. and Yang, Y., "Boosted HCCI for High Power without Engine Knock and with Ultra-Low NOx Emissions - Using Conventional Gasoline," *SAE Int. J. Engines* 3(1):750-767, 2010, doi:10.4271/2010-01-1086.

102. Eng, J., "Characterization of Pressure Waves in HCCI Combustion," SAE Technical Paper 2002-01-2859, 2002, doi:10.4271/2002-01-2859.

103. DieselNet, "Emission Standard," www.dieselnet.com, 2011.

104. McBride, B. and Gordon, S., "Computer Program for Calculation of Complex Chemical Equilibrium Compositions, Rocket Performance, Incident and Reflected Shocks, and Chapman-Jouguet Detonations," 1971, NASA SP-273.

105. Tess, M. J., "Diesel Engine Combustion Size Scaling at Medium Load without EGR," *MS Thesis in Mechanical Engineering, University of Wisconsin-Madison*, 2010.

106. Splitter, D. A., Wissink, M., Kokjohn, S. L., and Reitz, R. D., "Effect of Compression Ratio and Piston Geometry on RCCI Load Limits and Efficiency," SAE Technical Paper 2012-01-0383, 2012,

107. Shi, Y. and Reitz, R.D., "Study of Diesel Engine Size-Scaling Relationships Based on Turbulence and Chemistry Scales," SAE Technical Paper 2008-01-0955, 2008, doi:10.4271/2008-01-0955

108. Kenney , T. E., Gardner ,T. P., Low ,S. S., Eckstrom, J. C., Wolf ,L. R., Korn, S. J., and Szymkowicz, P. G., "Overall Results: Phase I Ad Hoc Diesel Fuel Test Program," SAE Technical Paper 2001-01-0151, 2001, doi:10.4271/2001-01-0151.

109. Hanson, R. M., *PhD Thesis, University of Wisconsin-Madison*, 2013 (In Progress).

110. Cooper, B., Penny, I., Beasley, M., Greaney, A., and Crump, J., "Advanced Diesel Technology to Achieve Tier 2 Bin 5 Emissions Compliance in US Light-Duty Diesel Applications," SAE Technical Paper 2006-01-1145, 2006, doi:10.4271/2006-01-1145.

111. Genzale, C., Reitz, R. D., and Musculus, M. P. B. "Effects of Piston Bowl Geometry on Mixture Development and Late-Injection Low-Temperature Combustion in a Heavy-Duty Diesel Engine," *SAE Int. J. Engines* , 1(1):913-937, 2008, doi:10.4271/2008-01-1330.

112. Musculus, M. P. B., "On the Correlation between NOx Emissions and the Diesel Premixed Burn," SAE Technical Paper 2004-01-1401, 2004, doi:10.4271/2004-01-1401.

113. Hultqvist, A., Christensen, M., Johansson, B., Franke, A., Richter, M., and Aldén, M., "A Study of the Homogeneous Charge Compression Ignition Combustion Process by Chemiluminescence Imaging," SAE Technical Paper 1999-01-3680, 1999, doi:10.4271/1999-01-3680.

114. Musculus, M. P. B., Lachaux, T., Pickett, L. M., and Idicheria, C. A., "End-of-Injection Over-Mixing and Unburned Hydrocarbon Emissions in Low-Temperature-Combustion Diesel Engines," *SAE Transactions*, 116(3):515-541, 2007, doi:10.4271/2007-01-0907.

115. Schulz, C. and Sick, V., "Tracer-LIF Diagnostics: Quantitative Measurement of Fuel Concentration, Temperature and fuel/air Ratio in Practical Combustion Systems" *Progress in Energy and Combustion Science*, 31(1):75-121,2005, http://dx.doi.org/10.1016/j.pecs.2004.08.002.

116. Sjöberg, M. and Dec ,J. E., "An Investigation of the Relationship between Measured Intake Temperature, BDC Temperature, and Combustion Phasing for Premixed and DI HCCI Engines," *SAE Transactions* , 113(3):1271-1286, 2004, doi:10.4271/2004-01-1900.

117. Dec, J. E. and Coy ,E. B., "OH Radical Imaging in a DI Diesel Engine and the Structure of the Early Diffusion Flame," SAE Technical Paper 960831, 1996, doi:10.4271/960831.

118. Genzale, C. L., "Optimizing Combustion Chamber Design for Low-Temperature Diesel Combustion," *PhD Thesis in Mechanical Engineering, University of Wisconsin-Madison*, 2009.

119. Genzale, C. L., Pickett, L. M., Hoops ,A. A., and Headrick, J. M., "Laser Ignition of Multi-Injection Gasoline Sprays," SAE Technical Paper 2011-01-0659, 2011, doi:10.4271/2011-01-0659.

120. Splitter, D. A., Hanson, R. M., Kokjohn, S. L., Wissink, M., and Reitz, R. D., "Injection Effects in Low Load RCCI Dual-Fuel Combustion," SAE Technical Paper 2011-24-0047, 2011, doi:10.4271/2011-24-0047.

121. Kokjohn, S. L., Musculus, M. P. B., Reitz, R. D., Splitter, D. A., "Investigation of Fuel Reactivity Stratification for Controlling PCI Heat-Release Rates Using High-Speed Chemiluminescence Imaging and Fuel Tracer Fluorescence", SAE Technical Paper 2012-01-0375, 2012.

122. Sun, Y. and Reitz, R. D., "Adaptive Injection Strategies (AIS) for Ultra-Low Emissions Diesel Engines," SAE Technical Paper 2008-01-0058, 2008, doi:10.4271/2008-01-0058.

123. Vishwanathan, G. and Reitz ,R. D., “Development of a Practical Soot Modeling Approach and its Application to Low-Temperature Diesel Combustion. Combustion Science and Technology,” 182(8):1050-1082, 2010, doi:10.1080/00102200903548124.

124. Sjöberg, M. and Dec, J. E., “Effects of Engine Speed, Fueling Rate, and Combustion Phasing on the Thermal Stratification Required to Limit HCCI Knocking Intensity,” SAE Technical Paper 2005-01-2125, 2005, doi:10.4271/2005-01-2125.

Appendix A: Additional Model Validation Cases

The main text included several sets of comparisons between the model predictions and metal and optical engine experiments. Additional model validation data are shown here. These model validation cases support the conclusions presented in the main text; however, no new information is derived from the cases. Thus, they are included here with brief descriptions.

A.1 Sandia Heavy-Duty Optical Engine

A.1.1 SOI Timing Sweep - Combustion Simulations

Simulation results are compared to the SOI timing sweep presented in Chapter 10. The operating conditions are shown in Table 10-1. A comparison of the measured and predicted peak AHRR is shown in Figure A-1 and a comparison of the cylinder pressure and AHRR is shown in Figure A-2. Similar to the comparisons shown in the text, the simulations are capable of capturing the combustion characteristics well over a range of conditions.

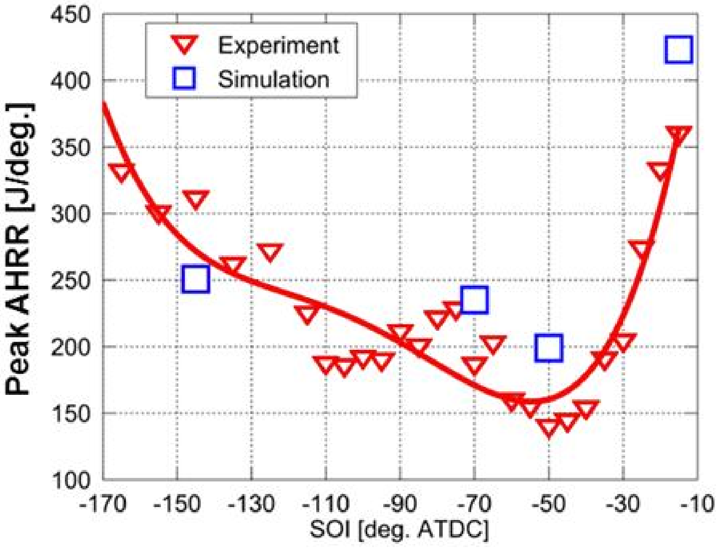

Figure A-1. Comparison of measured and predicted peak AHRR over the SOI timing sweep.

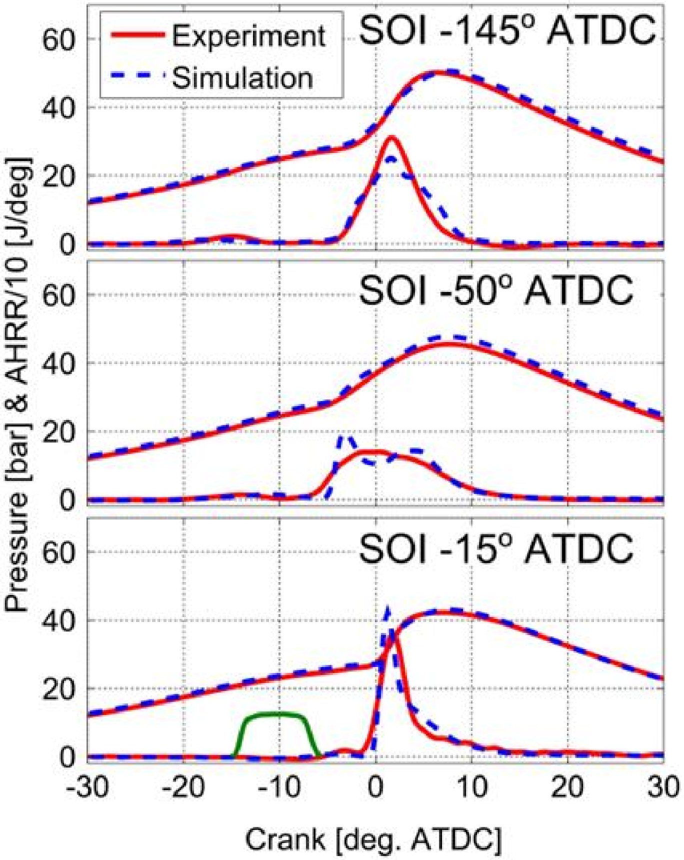

Figure A-2. Comparison of cylinder pressure and AHRR at several selected SOI timings.

CFD modeling (KIVA-Chemkin) is used to evaluate the source of the tail on the heat release curve of the SOI-15° case. Figure A-3 shows a comparison of the measured and predicted AHRR. Two sets of simulation results are presented. First, the baseline simulation results are compared to the experiments to show that the simulations are able to reproduce the combustion characteristics. It can be seen that case titled “Simulation – Baseline” adequately captures the AHRR of the measurements. Next, the simulations were repeated using exactly the same conditions as the “Simulation – Baseline” case, but with the iso-octane chemistry removed from the kinetics mechanism. The thermodynamic conditions (e.g., temperature and equivalence ratio) are identical between the two cases prior to ignition; however, iso-octane does not participate in chemistry. It can be seen that when iso-octane chemistry is removed, the tail on the heat release curve is nearly completely eliminated.

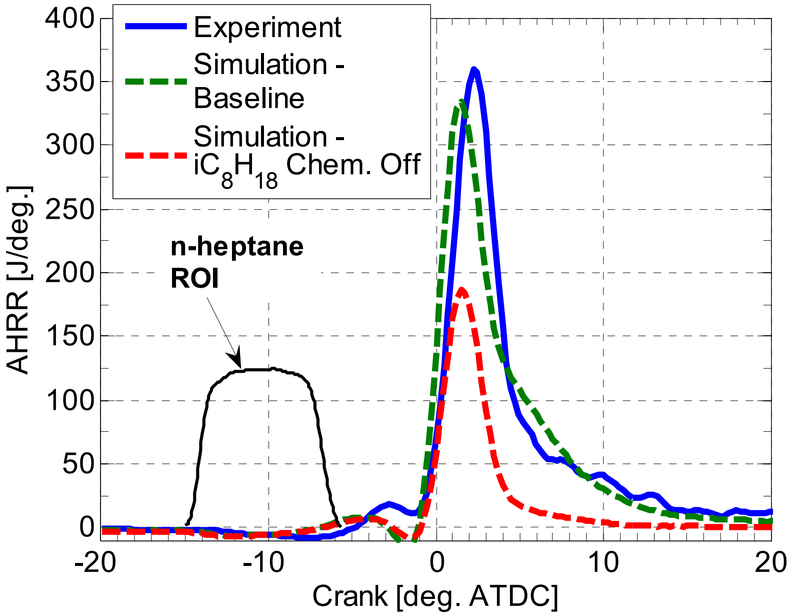

Figure A-3. Comparison of measured and predicted AHRR for the SOI-15° case. The blue curve shows the measured AHRR, the red curve shows the baseline simulation results, and the green line shows the simulation results with iso-octane chemistry turned off.

Appendix B: Additional Optical Engine Data

The main text included several sets of optical engine experiments. Although these data are useful, they were excluded from the main text for brevity. Thus, they are included here with brief descriptions.

B.1 Laser Ignition Study at $\phi=0.8$

To further explore flame propagation in a dual-fuel combustion mode, the operating conditions were adjusted to achieve An additional laser ignition study was performed. In this study the intake flow rate was reduced to half of the baseline case to increase the equivalence ratio to 0.8. To achieve stable combustion, an a single direct-injection of n-heptane was used with an SOI timing of -20° ATDC. The operating conditions are shown in Table B-1 and the cylinder pressure and AHRR is shown in Figure B-1.

Table B-1. Engine operating condition for the high-equivalence ratio laser ignition study

Engine speed	1200 rpm
Gross IMEP	4.2 bar
Intake temperature	140°C
Intake pressure	0.55 bar abs.
Inlet oxygen concentration	21 vol. %
GDI injection pressure	100 bar
CR injection pressure	600 bar
GDI SOI (command)	-240° ATDC
CR SOI 1/2 (actual)	-20° ATDC
Actual GDI DOI	36° CA
Actual CR DOI1/DOI2	9.3° CA
Total injected fuel mass	62 mg
iso-octane mass (GDI)	66%
n-heptane mass (CR)	34%
Quantity of injected fuel in CR Inj. 1	21.8
Premixed (iso-octane) equivalence ratio	0.54
Overall equivalence ratio	0.84
Nom. motored TDC density	11.1 kg/m3
Nom. motored TDC temperature	835 K

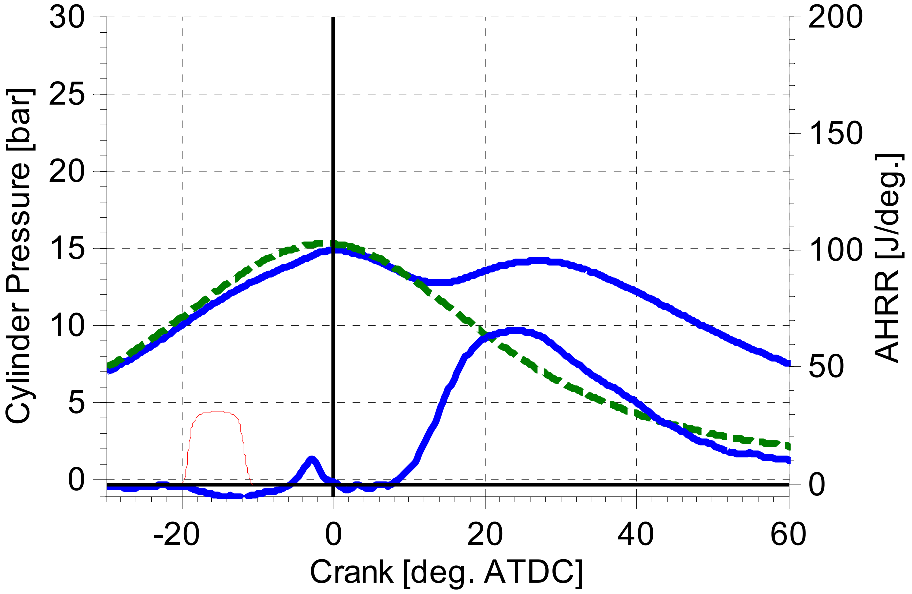

Figure B-1. Cylinder pressure and AHRR for high equivalence ratio case where flame propagation dominates.

Figure B-2 shows a combustion luminosity sequence for the case were flame propagation dominates and the baseline case, where auto-ignition dominates. In both cases, the laser ignition location is 30 mm from the center of the combustion chamber. The combustion phasing is ~10° later for the higher equivalence ratio case; thus, the laser ignition timing is retarded by 10° from the baseline case (i.e., the laser ignition timing is at TDC). Although the operating conditions are different from the baseline condition, Figure B-2 clearly shows that the growth rate of the laser ignited zone for the high-equivalence ratio case is much closer to that of the surrounding reaction zones than the low equivalence ratio baseline case.

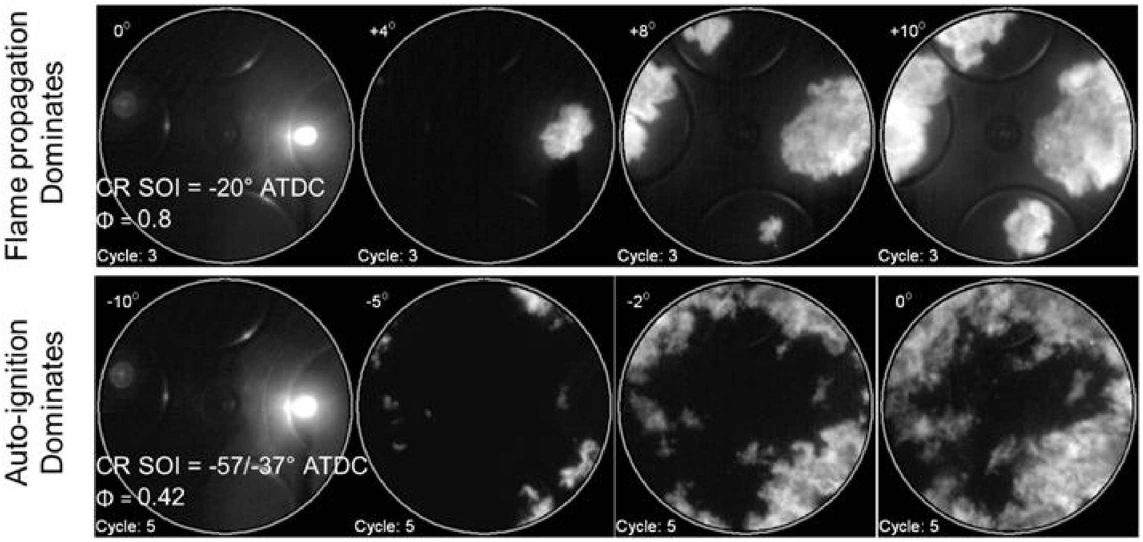

Figure B-2. Comparison of laser ignition study showing a case where flame propagation dominates and a case where auto-ignition dominates.

Figure B-3 shows the equivalence ratio and PRF maps at several times for the case showing consistent flame propagation. The equivalence ratio near the laser ignition location at TDC is ~0.6 to 0.8. The images were acquired with the ICCD camera viewing downward through the cylinder head window (see Figure 8-3). All images were acquired on a plane 13 mm below the firedeck inside of the cutout in the piston bowl rim. The imaging setup is described in Figure 8-4 (b).

Figure B-4 shows a sequence of simultaneous CH_2O PLIF and OH PLIF acquired during the early stages of the high temperature heat release for high equivalence ratio case of in Table B-1 (i.e., the case from the laser ignition study with ϕ=0.8). Note that laser ignition was not used in the images presented in Figure B-4 (i.e., ignition occurs due to the direct-injected n-heptane). It can be seen that the OH producing zone is continuous and the reaction zone appears to move as a continuous front, suggesting that flame propagation may play a role in this case and supporting the conclusion of the laser ignition study.

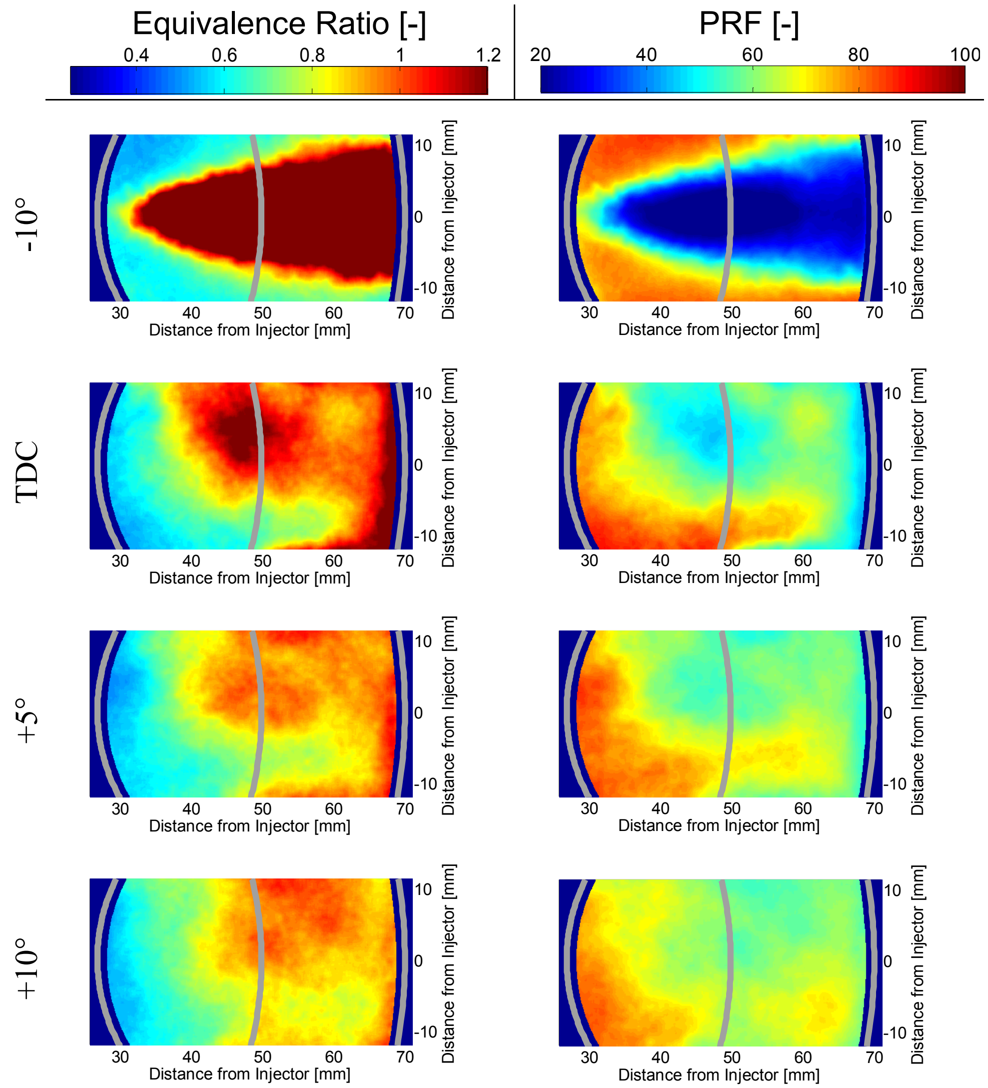

Figure B-3. Equivalence ratio and PRF maps at several times during the cycle for the case from the laser ignition study at ϕ=0.8.

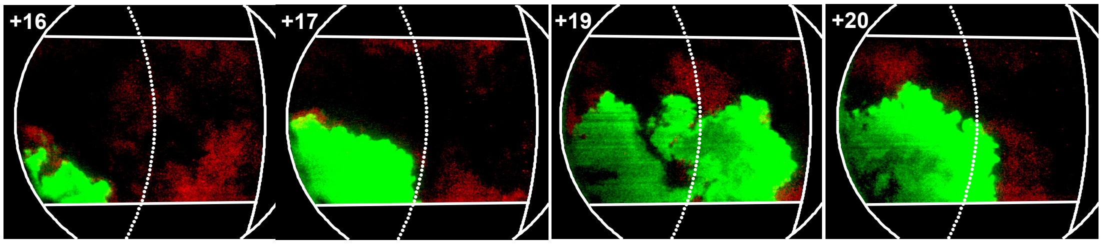

Figure B-4. Simultaneous CH_2O PLIF (false colored red) and OH PLIF (false colored green) for the high equivalence ratio case. The gain on the OH camera is 50 for all images and the gain on the CH2O camera is 100 for all images.

B.2 Effect of Temperature and PRF Blend

In this study, the global PRF number (i.e., the percent iso-octane) was swept from 56% to 91%. To allow comparisons at a fixed combustion phasing, the intake temperature was adjusted at each condition to hold CA50 constant at 2° ATDC. Table B-2 shows a summary of the operating conditions and Figure B-5 shows the tradeoff between iso-octane percent and intake temperature.

Table B-2. Engine operating condition for the intake temperature vs. PRF number sweep.

Engine speed	1200 rpm
Gross IMEP	4.2 bar
Intake temperature	80°C to 170°C
Intake pressure	1.1 to 1.3 bar abs.
Intake flowrate	23.0 g/s
Inlet oxygen concentration	21 vol. %
GDI injection pressure	100 bar
CR injection pressure	600 bar
GDI SOI (command)	-240° ATDC
CR SOI (actual)	-50° ATDC
Actual GDI DOI	36° CA
Actual CR DOI	9° CA
Total injected fuel mass	64 mg
iso-octane mass (GDI)	64%
n-heptane mass (CR)	36%
Premixed (iso-octane) equivalence ratio	0.27
Overall equivalence ratio	0.42
Overall PRF	56 to 91
Nom. motored TDC density	11.1 kg/m^3

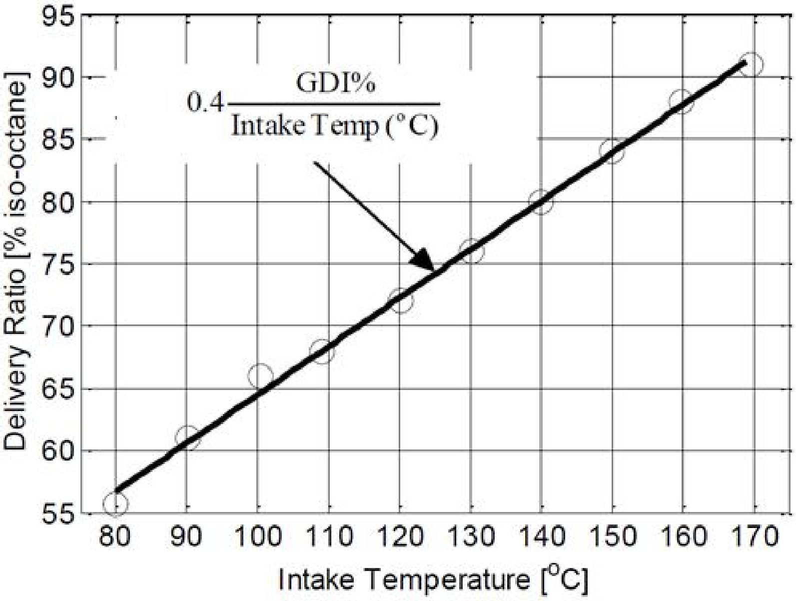

Figure B-5. Tradeoff between iso-octane percent and intake temperature.

Figure B-6 shows a comparison of the AHRR over the iso-octane percentage sweep. The AHRR curves show a distinct two-peak behavior during high-temperature combustion. As the iso-octane percentage is increased, the first peak drops and the second peak increases. The first peak is likely due to the mixture of n-heptane and iso-octane inside the fuel jet (i.e., the PRF burn) and the second peak is likely primarily iso-octane.

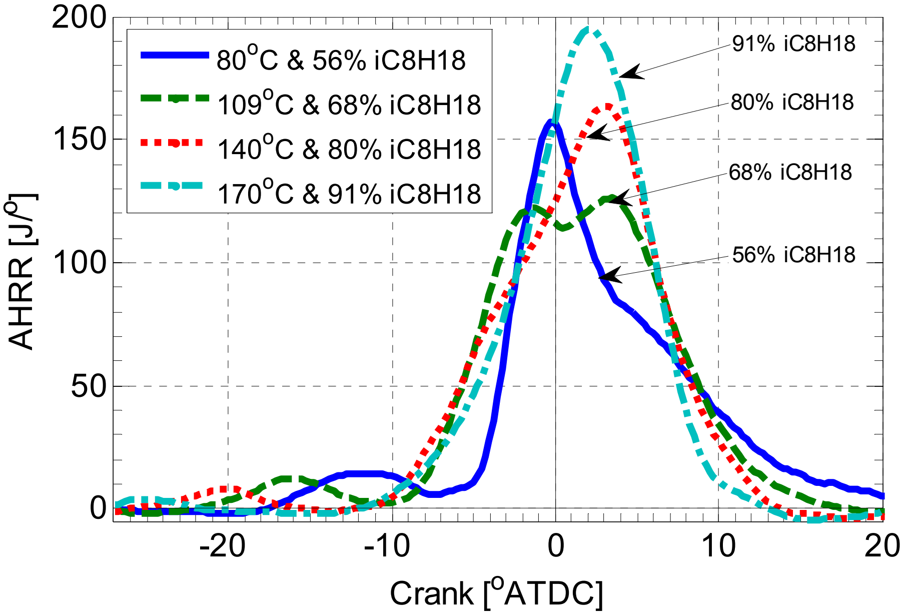

Figure B-6. Effect of iso-octane percentage (PRF number) on AHRR.

B.3 SOI Sweep Fuel Distributions from -21° ATDC to TDC

Fuel distribution measurements at -5° ATDC for several SOI timings were presented in Chapter 10. Figure B-7 and Figure B-8 show additional equivalence ratio and PRF maps at several crank angles from -21° ATDC to TDC. Note that two images at -21° are shown for each SOI timing: one on a plane 10 mm below the firedeck and another on a plane 13 mm below the firedeck. The images from -15° ATDC to TDC are on a plane 13 mm below the firedeck. The imaging location is shown in Figure 8-4 (b).

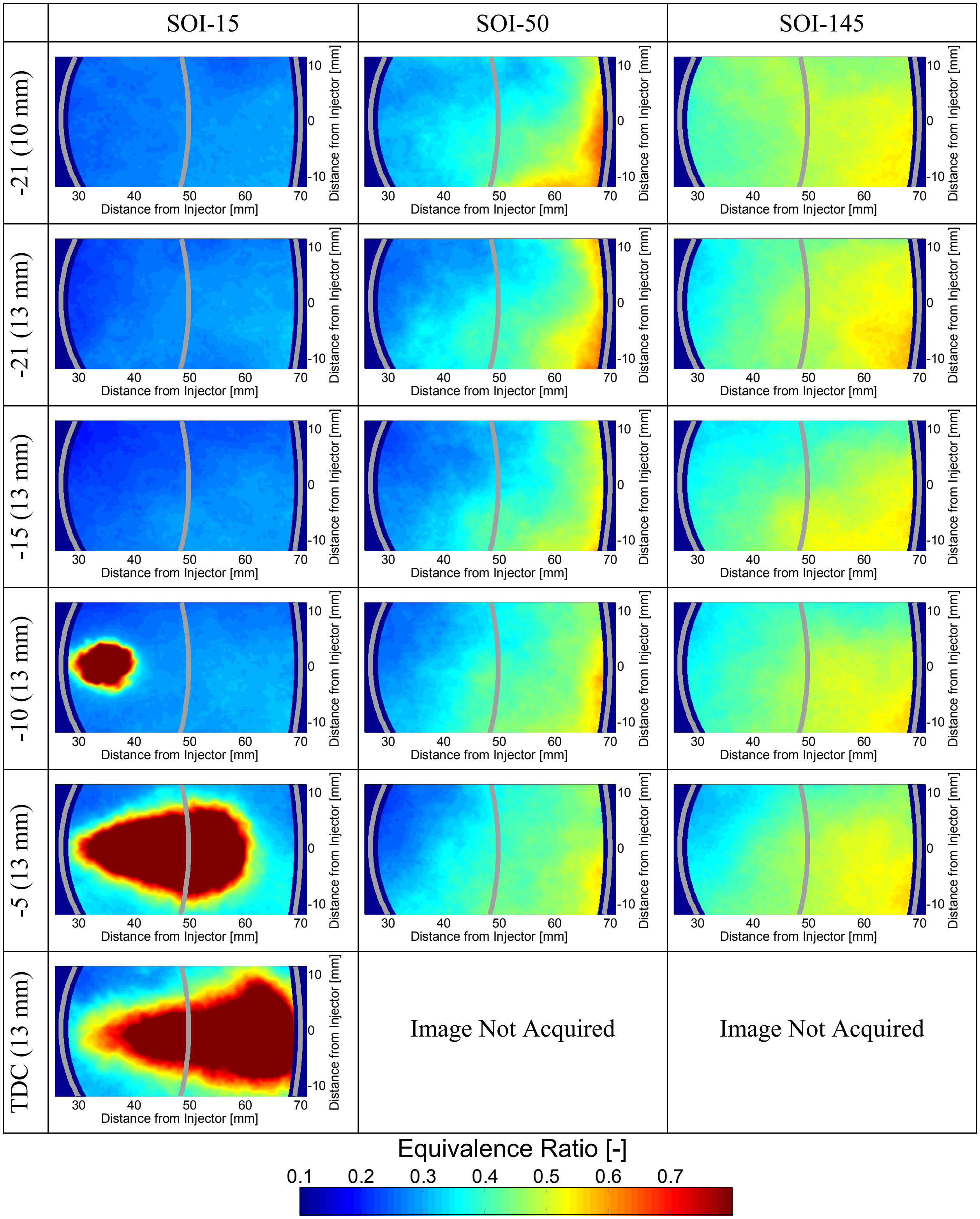

Figure B-7. Equivalence ratio maps from -21° ATDC to TDC for SOI timings of -15°, -50°, and -145° ATDC.

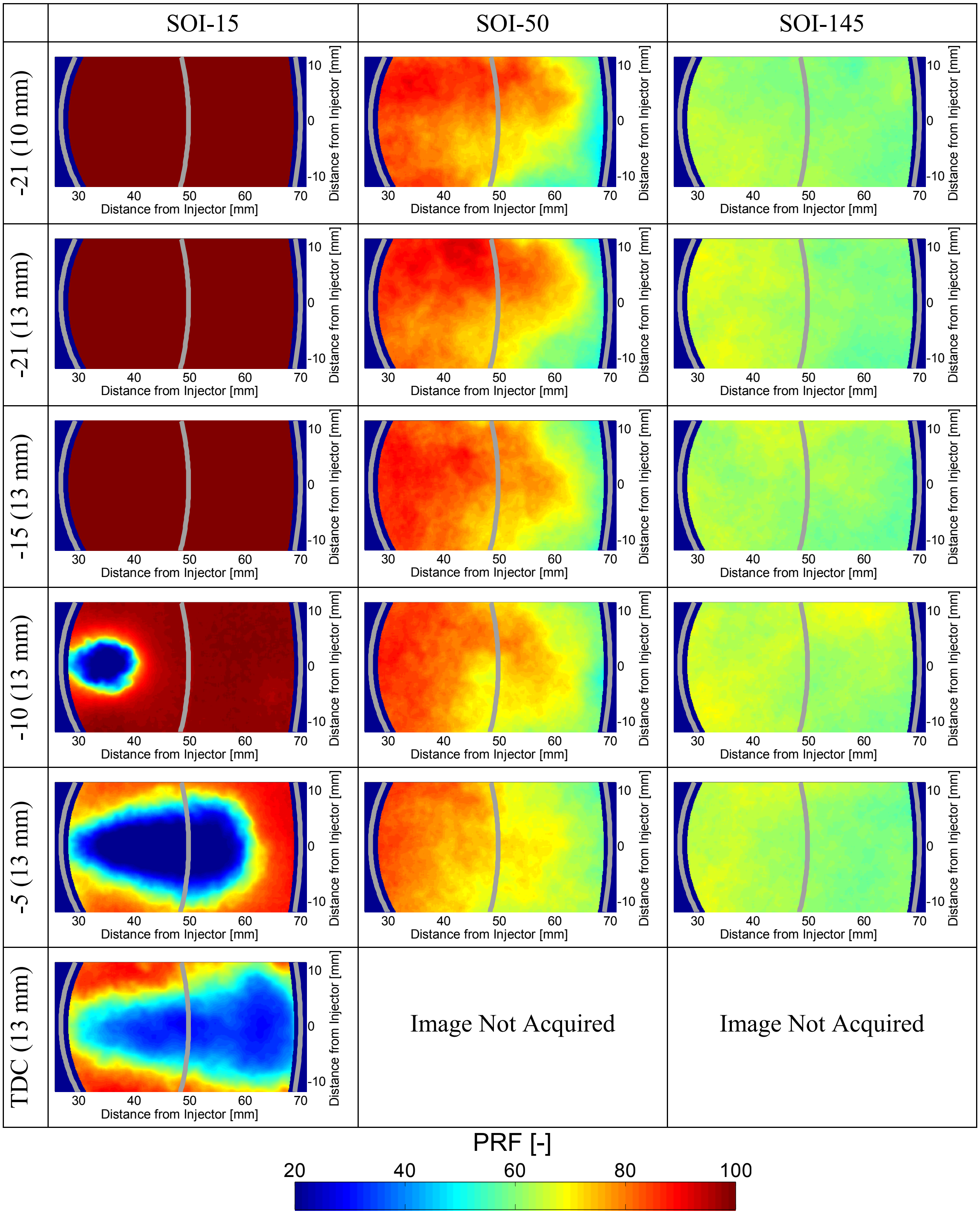

Figure B-8. PRF maps from -21° ATDC to TDC for SOI timings of -15°, -50°, and -145° ATDC.